University of Massachusetts Amherst
ScholarWorks@UMass Amherst

Doctoral Dissertations 1896 - February 2014

1-1-2007

Multiwavelength study of parsec scale outflows associated with low mass young stellar objects.

Irena Stojimirovic
University of Massachusetts Amherst

Follow this and additional works at: https://scholarworks.umass.edu/dissertations_1

Recommended Citation

Stojimirovic, Irena, "Multiwavelength study of parsec scale outflows associated with low mass young stellar objects." (2007). *Doctoral Dissertations 1896 - February 2014*. 2007.
https://doi.org/10.7275/cra8-rc37 https://scholarworks.umass.edu/dissertations_1/2007

This Open Access Dissertation is brought to you for free and open access by ScholarWorks@UMass Amherst. It has been accepted for inclusion in Doctoral Dissertations 1896 - February 2014 by an authorized administrator of ScholarWorks@UMass Amherst. For more information, please contact scholarworks@library.umass.edu.

UMASS/AMHERST
312066 0310 4632 3


University of
Massachusetts
Amherst

LIBRARY

Digitized by the Internet Archive
in 2015

https://archive.org/details/multiwavelengths00stoj

This is an authorized facsimile, made from the microfilm master copy of the original dissertation or master thesis published by UMI.

The bibliographic information for this thesis is contained in UMI's Dissertation Abstracts database, the only central source for accessing almost every doctoral dissertation accepted in North America since 1861.

UMI® Dissertation Services

From:ProQuest COMPANY

300 North Zeeb Road
P.O. Box 1346
Ann Arbor, Michigan 48106-1346 USA

800.521.0600 734.761.4700
web www.il.proquest.com

Printed in 2007 by digital xerographic process
on acid-free paper

MULTIWAVELENGTH STUDY OF PARSEC SCALE OUTFLOWS ASSOCIATED WITH LOW MASS YOUNG STELLAR OBJECTS

A Dissertation Presented

by

IRENA STOJIMIROVIC

Submitted to the Graduate School of the
University of Massachusetts Amherst in partial fulfillment
of the requirements for the degree of

DOCTOR OF PHILOSOPHY

May 2007

Astronomy

UMI Number: 3275737

INFORMATION TO USERS

The quality of this reproduction is dependent upon the quality of the copy submitted. Broken or indistinct print, colored or poor quality illustrations and photographs, print bleed-through, substandard margins, and improper alignment can adversely affect reproduction.

In the unlikely event that the author did not send a complete manuscript and there are missing pages, these will be noted. Also, if unauthorized copyright material had to be removed, a note will indicate the deletion.

UMI®

UMI Microform 3275737

Copyright 2007 by ProQuest Information and Learning Company.

All rights reserved. This microform edition is protected against unauthorized copying under Title 17, United States Code.

ProQuest Information and Learning Company
300 North Zeeb Road
P.O. Box 1346
Ann Arbor, MI 48106-1346

© Copyright by Irena Stojimirovic 2007

All Rights Reserved

MULTIWAVELENGTH STUDY OF PARSEC SCALE OUTFLOWS ASSOCIATED WITH LOW MASS YOUNG STELLAR OBJECTS

A Dissertation Presented

by

IRENA STOJIMIROVIC

Approved as to style and content by:

Gopal Narayanan, Chair

Ronald L. Snell, Member

Suzan Edwards, Member

Mark Heyer, Member

Guy Blaylock, Member

Ronald L. Snell, Department Chair
Astronomy

MULTIWAVELENGTH STUDY OF PARSEC SCALE OUTFLOWS ASSOCIATED WITH LOW MASS YOUNG STELLAR OBJECTS

A Dissertation Presented

by

IRENA STOJIMIROVIC

Approved as to style and content by:

Gopal Narayanan, Chair

Ronald L. Snell, Member

Suzan Edwards, Member

Mark Heyer, Member

Guy Blaylock, Member

Ronald L. Snell, Department Chair
Astronomy Department

EPIGRAPH

There may be times when we are powerless to prevent injustice. but there must never be a time when we fail to protest

Elie Wiesel

ACKNOWLEDGMENTS

More then a three years ago, when I successfully defended my second year project I forgot to thank my advisor Gopal Narayanan for sharing his project with me and teaching me patiently how to take the first steps as a researcher. Without Gopal's support and encouragement I would have never begun and finished this journey and for that I will always be grateful.

I would like to extend a special thanks to Ron Snell with whom I enjoyed working for the past two years. Ron's door was always open for me and he was always prompt with feedback and suggestions for my work. His continuing excitement about research was the real energizer for me. Thanks a lot and I am looking forward for the Fall get-together in the new house!

I am also grateful to Suzan Edwards, Terri Grzybowski, Martin Weinberg, Judy Young and James Lowenthal who always showed interest in my progress and well being; as well as to Mark Heyer for allocating time at 14 m telescope for my Thesis project. I would like to thank Mike Brewer for being kind in situations when the telescope's control systems seemed to be against me, and to Pete Schloerb for financially supporting me for the majority of my Thesis years. During my observational run in Arizona I was lucky enough to meet another astronomer Abby Hedden who was of a great help and became my dear friend, perfect company during Arizona snow storm, conference trips, and beautiful hikes in Yoho National Park.

Many people came and went from UMASS while I was here and some were just wonderful to have around. Dan McIntosh and beautiful Julie made Amherst a nicer place to be - thanks for the unforgettable 30th birthday party, Montreal trip, all the

hikes we did. Jonathan the sailor, Luisito, Adam, Arend, Irena Bozin, Ilija, Danijela, Will, Cara thanks for fun time we had together. Spatial thanks to Jay for taking Abby, Will and me to the top of Mauna Kea and for being a great karaoke partner. Bon Jovi rules!

Living gets easier when there is a person to share it with. I am very fortunate to have Dusan by my side from the war days in Serbia through tough and fun days here in States. I am also fortunate to have my grandma Draga who took care of me when I was little and provided a loving place to live. To our adopted family member Daka a special thanks for always being there for us. To my sister Jelena and Dusan's and my parents, who do not understand much of what we do, but are proud of where we are - it is great to have your support and encouragement. Thanks goes to my best friend Radica for being herself: a patient, wise, and smart woman. Naco, when you are calling I know something is wrong - but we are there for each other in need. I thank Goran, Veljko, Angelina, and Dragana, who have been very important throughout many years in my life and I am just happy to have you all as my base whenever I come back home.

For the inspirations and motivation I'd like to thank Natasa Kandic, Zoran Djindjic and all other activist world-wide who non-violently struggle for democracy, social justice and human rights. Also to Ratomirka Miler, my high school physics and astrophysics teacher who has done an amazing work on preparing me for the path I took. Finally I'd like to dedicate this work to Mrma. There are no words to describe how much we miss you and wish you were here with us.

ABSTRACT

MULTIWAVELENGTH STUDY OF PARSEC SCALE OUTFLOWS ASSOCIATED WITH LOW MASS YOUNG STELLAR OBJECTS

MAY 2007

IRENA STOJIMIROVIC

B.Sc.. BELGRADE UNIVERSITY

Ph.D.. UNIVERSITY OF MASSACHUSETTS AMHERST

Directed by: Professor Gopal Narayanan

A multi-wavelength. multi-telescope observational study of recently discovered parsec-scale Herbig-Haro flows associated with the earliest stages of low mass protostellar formation is presented. Improvements in optical observational capabilities allowed the discovery of the the new class of parsec scale HH flows. Similar improvements at millimeter wavelengths allowed for faster. more sensitive mapping at multiple frequencies of parsec-scale outflows in nearby protostellar regions.

Using the availability of large-format heterodyne arrays at millimeter wavelengths and the availability of "on-the-fly" mapping capabilities at the FCRAO 14 m telescope. a sensitive. fully sampled survey of fifteen parsec-scale HH flows has been completed in ^{12}CO and ^{13}CO J=1→0 over their full extents. A smaller subset of these sources has been observed in ^{12}CO J=3→2 at the HHT 10 m telescope. Com-

plementary optical data are also available for most sources. The use of the combined millimeter and submillimeter CO isotopic transitions allows a better determination of the physical characteristics of outflows, such as mass, energetics, and excitation temperature. The combination of CO and optical data provides morphological relation between different tracers of the shock processes that arise during the interaction of the material launched from the star with its surrounding ambient cloud. By comparing the observational findings to theoretical predictions different outflow entrainment models are distinguished.

The outflow sources L1551 and L1228 are found to possess molecular outflow over the full parsec-scale HH flow extent, whereas outflows in Haro 6-10 and L1617 do not. We also study molecular parsec scale outflows in NGC 2071 region who show only single HH object but are associated with parsec-scale H_2 shocked emission. Comparing the observational characteristics of the outflows to the characteristics of different jet and wind driven theoretical models we find that many outflows have features characteristic of both types of models. The main outflow in L1551 region has M(v) spectral indices and position-velocity features characteristic of the jet entrained outflows, while its low-velocity shell-like morphology is associated with wind models. L1228 is an interesting outflow with two asymmetric outflow lobes. M(V) indices point toward jet entrainment while position-velocity plots are inconclusive. Both outflows in L1228 and L1551 are very energetic and have a strong impact on their host cloud. The outflow activity in the L 1551 has triggered formation of new stars while outflow in L1228 has set its cloud core into motion. Our sensitive mapping allowed us to discover outflow in the Haro 6-10 which has a poor molecular flow with jet-like characteristics. We also report two new outflows in NGC 2071 and we find many features of the main NGC 2071 outflow to be best explained by jet driven models. Since neither theoretical model can produce all of the observed outflow features and both jet and wind features are often present in the same outflows, our results support

the growing notion that there must be a unified model for the outflows where jet and less collimated component are coexistent at all time.

TABLE OF CONTENTS

LIST OF TABLES

LIST OF FIGURES

CHAPTER 1

INTRODUCTION

1.1 Motivation

Low mass stars are formed from (fragmented) gravitationally collapsing rotating molecular cloud cores. Recently a dynamical picture of star formation has emerged (Elmegreen. 2000: Vazquez-Semadeni et al.. 2000: Larson. 2003. e.g.) as opposed to a quasi-static ambipolar diffusion theory (Shu et al.. 1987). In the dynamical scenario. cores are formed in converging flows in highly turbulent molecular clouds. They evolve rapidly. since the shocked converging regions become Jeans unstable and collapse. as opposed to the inside-out slow collapse of the ambipolar diffusion theory. Regardlees if the core collapse was initiated by dynamical or quasi-static scenario. the by product of the collapse is the formation of an accreting disk surrounding a prostostellar source. By gradually accreting gas from the disk. the protostellar source will gain mass and evolve toward the main sequence.

In order for gas from the rapidly rotating disk to settle onto a star. a significant fraction of its angular momentum must be lost. The ejection of gas during the accretion phase of the protostellar life is a key mechanism for removing excess angular momentum from the disk. Therefore. mass loss processes via winds and/or jets are associated with all stages of early stellar evolution. from deeply embedded protostars to visible young stars (Reipurth & Bally. 2001). The most energetic outflow phase occurs in the earliest stages of protostellar collapse (CLASS 0). when the infalling

envelope is still settling into a forming disk and disk accretion rate is high (Pudritz et al., 2006). When the disk disappears in the weak T-Tauri Star phase (CLASS III), the outflow also ceases (Pudritz et al., 2006).

For low-luminosity young stellar objects, there is a general consensus that outflows are driven magnetocentrifugally from open field lines anchored on rapidly rotating circumstellar disks. However, two different theories arise with the distinction being where the field lines are anchored: either near the radius of magnetospherical truncation on the disk (Shu et al., 2000, X-wind theory) or from a wider range in disk radii, distances of 0.1 AU or more (disk wind theory citetkp00. These different outflow launching conditions cannot yet be probed directly by observations. In addition, many details, such as acceleration and collimation mechanisms for the outflows or the nature of mass loss whether it is a steady-state process or more dynamical with powerful short-duration outbursts, remain unresolved.

The ejected matter will accelerate surrounding ambient cloud gas to velocities greater than those of the cloud, thereby creating an *outflow*. The lower rotational levels of CO molecule are collisionally excited at temperatures of only few Kelvins at the densities typically found in molecular clouds. Therefore non-gaussian wing emission of this abundant molecule is the best tracer of outflow activity in the molecular clouds, dubbed the *molecular outflow*. Observations of CO J=1→0 line emission, originally opened up the study of outflows from young stars (e.g. Snell et al., 1980, SLP hereafter) and remain the key tool for understanding outflow activity. Since extinction is the principal barrier to observing the jet launch region, molecular outflows can be useful tools for understanding the underlying star formation process and its accretion history, because they provide a fossil record of the mass loss. Different outflow symmetries, provide clues about the dynamical engine and its environment (Bally et al., 2006).

Outflows manifest themselves in various spectral bands from X-rays to centimeter wavelengths. Optically visible Herbig-Haro (HH) objects were the first identified outflow-ambient gas interaction regions (Herbig, 1950, 1951; Haro, 1952, 1953). Our understanding of HH flows has advanced from nebulous objects randomly found within molecular clouds to short-lived objects with bipolar distribution around driving star which often take a form of highly collimated jets, ending in a bright symmetric bow shock, see Figure 1.1. The advent of large-format CCDs during 1990s, revealed that HH outflows can attain parsec-scale dimensions and that they can be found well beyond the boundaries of their molecular clouds (Reipurth et al., 1997, e.g.). With the launch of the Hubble Space Telescope (HST), the subarc-second structure and cooling layers of dozens of HH objects have been resolved (Bally et al., 2006). In addition to Hα and other Balmer lines, HH objects are identified by the characteristic emission line spectra of forbidden optical lines: [S II], [N II], [Fe II], [O III]. The forbidden line emission is stratify in such way that the species with higher excitation are found closest to the shock front, while the species with lower excitation are found at greatest distances behind the shock front (Reipurth & Bally, 2001). These lines require temperatures of at least several thousand degrees to excite, compared to 10 K typical temperature of dark molecular clouds. Therefore *the location of HH objects identifies the locations of a shocks* and provides insights into the nature of the accretion and ejection processes that govern the formation of star.

While the jet, traced by HH objects, represents the material originating directly from the star, the molecular outflows are ambient cloud material, being pushed away from the vicinity of the star (Stahler & Palla, 2005). Integrated over time, the effect of a wind from a young star is to blow away the material that shrouds it during its earliest evolution. In its interaction with the infalling envelope surrounding the protostar and circumstellar disk, outflows may have a significant effect on the final mass of the forming star (Adams & Fatuzzo, 1996) and consequently the shape of

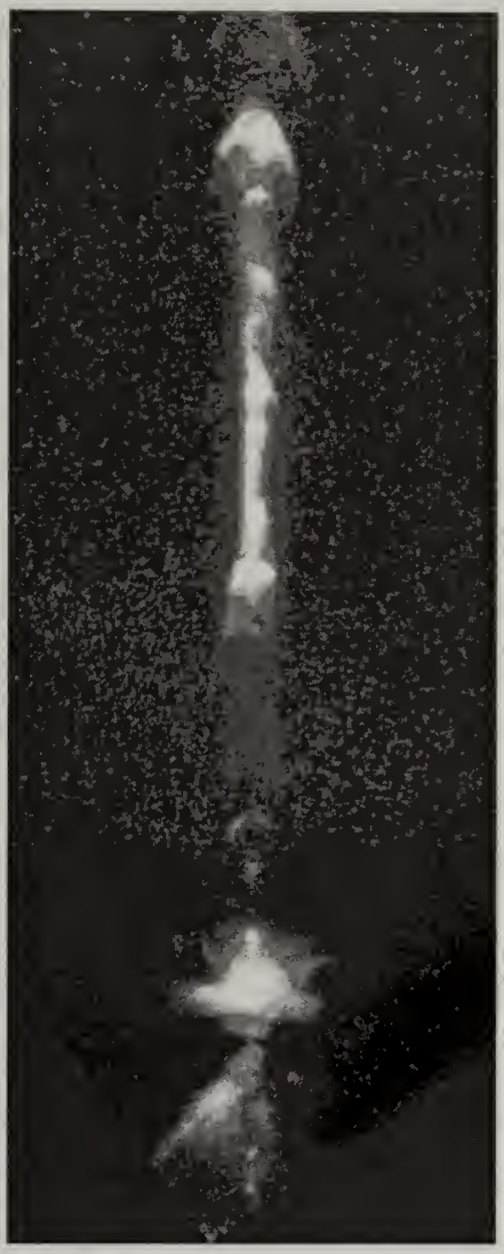

Figure 1.1 HH objects as jet tracers. The HH 111 jet and its source region as imaged by the Hubble Space Telescope in the optical and infrared. The main body of the jet is optically visible, whereas the deeply embedded source region is detected only in the infrared. HH 111 jet is a prototypical examples of straight, knotty jet. Knots represent "internal working surface" which form where faster-moving gas catches up with slower-moving material ejected earlier. The optical image is a composite of Hα (blue) and [SII] (red) emission. Optical traces show characteristic stratification where high-excitation lines, such as Hα peak at the apex of shock front, base of jet and internal knots/working surface while low-excitation lines, such as [SII] peak at the bow shock wings.

Initial Mass Function. During the interaction with the ambient medium, wind and jets carve out cavities, sculpture the cloud and are able to disrupt their parent cloud and regulate star-formation rate within it.

Molecular outflows have dimensions of up to several parsecs, masses one or two orders of magnitude larger than their driving sources, and kinetic energies often exceeding the gravitational binding energy of their host cloud (Bally & Lada, 1983). In the absence of massive stars the energy and momentum deposited by molecular outflows within the molecular cloud can be large enough to dominate the generation of turbulence and cloud motions (Li & Nakamura, 2006; Bally et al., 2006). The combination of CO tracers offers a time-integrated view of the protostar's mass-loss process and probes the total mass and momentum deposited in the surrounding medium by the outflow. Understanding outflow properties over the entire outflow history is critical in determining their impact on the cloud.

1.2 Parsec-Scale Outflows

Until the mid-1990s, the dimensions of HH flows were generally assumed to be around a fraction of a parsec. The ubiquity of parsec-scale HH flows profoundly alters our view of the impact of young stars on their environment. Giant flows trace the stellar wind history over much greater periods of time. With typical flow velocities of about 100 km s^{-1}, the dynamical age of parsec-scale HH flows is a few 10^4 yr, comparable to the main accretion phase for the typical CLASS I protostar. Therefore *the parsec-long chains of HH objects provide a record of the mass ejection (and mass accretion) history of a newborn star over a time-scale comparable to its accretion time.*

Up to now, more than two dozen giant HH flows have been reported in the Orion, Taurus, Cepheus and Perseus molecular cloud complexes (Bally & Devine, 1994; Reipurth et al., 1997; Eisloffel & Mundt, 1997). It thus appears that it is common

for HH flows to attain parsec-scale dimensions. Most giant HH flows contain multiple groups of HH objects along their outflow axes and their symmetry around central object, provides evidence for variability of ejection velocity and orientation of the source jet. The spacing of shocks, their sizes, and their morphological complexity tend to increase with increasing distance from the source. Giant HH flows are capable of heating, ionizing, and dissociating cloud material over parsec scale distances and may play a role in the chemical rejuvenation of clouds and the generation of the turbulent motions observed in molecular clouds as well as the self-regulation of star formation.

So far, in the literature, most of the observations of giant flows have been restricted to the optically revealed components of the flow. The entrained molecular component of these parsec-scale flows have not been adequately studied toward the *full* extent of these optical flows. Only five years ago it would have been impossible to observe a large sample of parsec scale flows at millimeter wavelengths with reasonable amounts of observing time. With the advent of large-format heterodyne focal plane arrays like SEQUOIA (Erickson et al., 1999, Second Quabbin Imaging Array), and the implementation of rapid or on-the-fly (OTF) mapping capabilities at the FCRAO 14 m telescope in 2001, observing capability has been significantly improved. With the SEQUOIA 32-pixel focal plane array on the FCRAO 14 m telescope, observing with the OTF mapping mode, it was possible to make a full square-degree map with resulting signal-to-noise ratio >20 in less then 24 hours. In addition, with the availability of a flexible, dual-channel autocorrelator spectrometer (DCC), we were able to observe CO molecule in two isotopic transitions, which allow us to better estimate the total mass entrained by the outflow, and also to probe deeper into the molecular cloud. We have also searched narrow-band H_α and [S II] optical data on majority of the parsec-scale HH sources (John Bally). We astrometrize such optical images and correlate them against the CO data.

There have been only a few studies of the parsec scale HH flows and complementing molecular outflows in the literature so far (Arce & Goodman, 2001a, 2002; Yu et al., 1999). With a large sample of fifteen parsec-scale sources observed, we can address the question of the mutual relation between these two tracers of the outflow activity. In the past, the prevailing idea of outflow formation was that fast atomic winds, with low collimation, were the primary accelerating agents of molecular outflows (Lada, 1985), while optical jets were considered as parallel phenomena with no dynamical significance, because their momentum transport rate was estimated to be much lower than that of molecular outflows. Over the timescale of parsec scale outflow events, jets have more dynamical significance with total momentum deposition sufficient to drive molecular flows. Naturally, there rises a question whether HH jets play a significant role in formation of molecular outflows (Cernicharo & Reipurth, 1996) and consequently if there is a unified model of the outflow formation?

Current estimates of the "typical" outflow properties may be far from accurate, since there is no large homogeneous sample of molecular outflows which have been mapped with good resolution and sensitivity (Richer et al., 2000). Consequently, our current understanding of the processes might be heavily subjective, and biased by a few frequently studied examples. This thesis work, is an effort in providing an excellent observational sample that can allow us to study molecular outflows in systematic, detailed approach. The combined optical/millimeter/submillimeter dataset provides insights into the mass ejection history of YSOs, kinematics of the molecular flow and the mechanisms by which HH flows entrain, accelerate and shock the ambient gas surrounding the forming star. It also provides important constraints to the future theoretical work.

In the next two sections we give a brief overview of the major observational characteristics of the outflows and recent developments in the theoretical works.

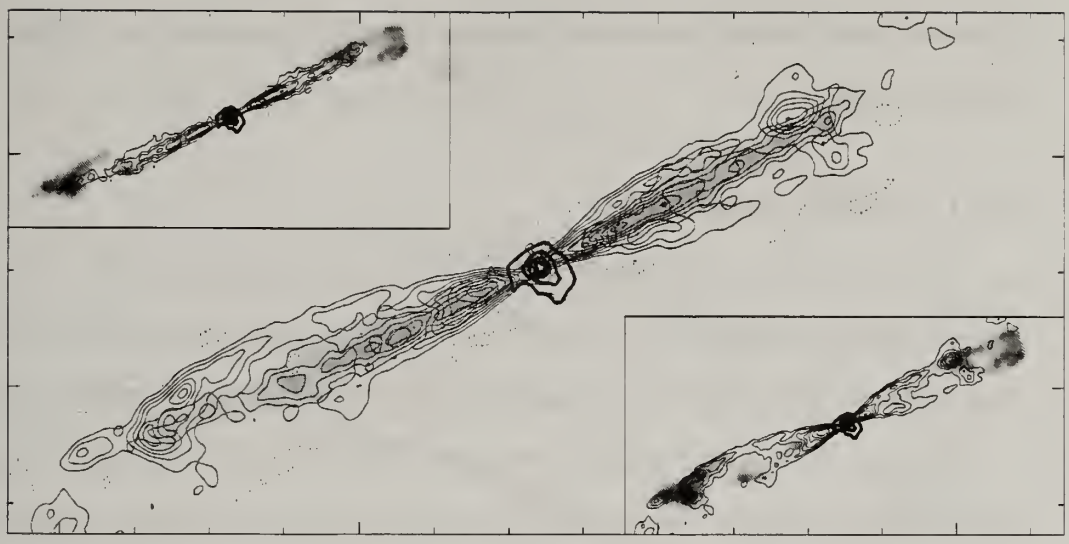

Figure 1.2 [Velocity Nesting and Correlation of High Velocity CO Gas With H_2 emission. The high resolution CO J=2→1 image of HH 211 molecular jet shows the morphological relation between high-velocity (gray scale) and low-velocity CO gas (contours) in the main panel. The driving source is surrounded with dust seen in 230 GHz continuum emission (thick contours). Relation between high(low) CO emission overlayed on H_2 shocked emission (gray scale) is shown in the upper left (lower right) box. The low-velocity CO delineates a pair of shells whose tips are associated with H_2 emission, while the high-velocity CO gas traces a narrower feature whose velocity increases linearly with distance from the star. Figure combines results of McCaughrean & Zinnecker (1996), and Gueth & Guilloteau (1999) and is adopted from Richer et al. (2000).

1.3 Observational Characteristics Of Molecular Outflows

The correlation of the outflow energetics with the bolometric luminosity L_{bol} over the entire observed luminosity range is established and confirmed by the sample of more then 390 molecular outflows, ranging over six decades in stellar luminosity (Wu et al., 2004). In addition, many flow properties, in particular the CO spatial and velocity structure, are broadly similar across the entire luminosity range (Richer et al., 2000) suggesting that similar mechanisms may be responsible for the production of molecular outflows from both low- and high-mass systems and that outflows from massive stars may be approximately modeled as scaled-up versions of lower mass outflows (Pudritz & Banerjee, 2005; Zhang et al., 2002; Beuther & Schilke, 2004).

Here we briefly review the major characteristics of the molecular outflows from low mass stars.

1.3.1 Outflow Morphology

Molecular outflows display a broad diversity of sizes and shapes. The length of typical molecular outflow is in the range of a fraction of a parsec to several parsecs. The collimation factor,i.e. the length-to-width ratio of the CO outflows, ranges from $\sim$ 3 to >20. It is worth noting that there is a clear trend of higher collimation at higher outflowing velocities. In addition, outflows from the CLASS 0 objects which are supposed to be in their main accretion phase, show the most collimated flows, where enhanced regions of molecular emission are often found related to shock emission tracers such as H_2 line or HH objects (HH 211 Gueth & Guilloteau, 1999; HH 212 Lee et al. 2000). One example is shown in Figure 1.2. Such morphological relations can be best explained if the CO gas is entrained along the jet in the turbulent cocoon (Stahler, 1994) or if the CO gas is entrained in the shocks that are propagating down the jet (so-called internal working surfaces Raga & Cabrit (1993)).

Sudden variations in the accretion rate onto the forming star or the interaction of the protostars in binary pairs can cause ejections to vary in velocity, mass and direction (Reipurth & Bally, 2001). Additionally the non-uniformity of the protostellar environment will contribute to the uniqueness of the lobe shape. Consequently the most common morphology of the outflows is not the simple jet-like, but the superposition of several shocked/outflowing gas structures, often resulting in differences of appearance of the redshifted and blueshifted lobes of the same outflow, clumpy or filamentary structure and generally much lower collimation factors. Such outflows are often associated with a combination of wide-angle wind and jet entrainment (Bachiller, 1996).

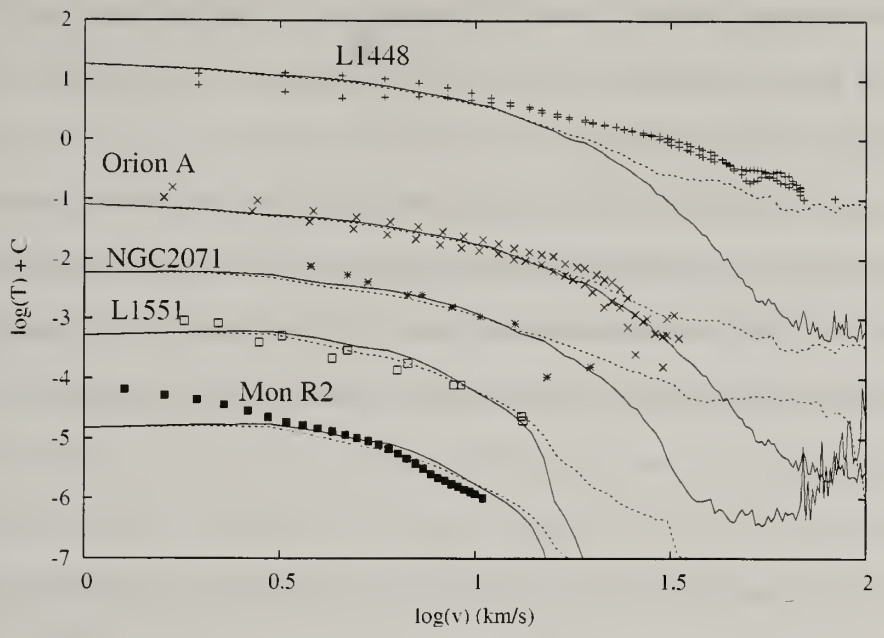

Figure 1.3 Mass-Velocity in Bow Shock Models. Plots of the observed intensity-velocity relations for L 1448, Orion A, NGC 2071, L 1551 and Mon R2 ("+" signs, crosses, stars, open boxes, and filled boxes respectively). Also shown are the simulated m(v) and $I_{CO}(v)$ based on bow shock model (dotted and solid lines, respectively, with arbitrary vertical offsets) for comparison. Figure taken from Downes & Cabrit (2003)

1.3.2 Mass-Velocity Relation

The CO spectral line shape, integrated over the entire molecular outflow can be used to trace the distribution of mass as a function of the line-of-sight velocity. A log-log plot of outflow mass as a function of velocity offset from the host cloud's mean velocity usually shows power-law mass-velocity (M-v) relations in which $dM(v)/dv \propto v^{-\gamma}$ (Arce et al., 2006), see Figure 1.3. The observed mass-velocity relations always imply more mass at low outflow velocities than at higher outflow velocities. Observations typically find the slope, γ, to range from 1 to 3, with median value of 2 (Richer et al., 2000). Sometimes a broken power law is observed with a steeper slope at higher velocities, with γ as large as 10 in some cases (Rodriguez et al., 1982; Lada & Fich, 1996). The velocity at which the slope changes is typically between 6 and 12 km s^{-1} although outflows can have CO break velocities as low as about 2 km s^{-1} and, in the youngest CO outflows, it can be high as 30 km s^{-1} (Richer et al. 2000,

and references therein). γ's at low velocities are similar in sources of all luminosity, which suggest common gas acceleration mechanism over six orders of magnitude in L_{bol} (Richer et al., 2000).

In the past, most observational outflow studies estimate outflow mass either by assuming that ^{12}CO emission is optically thin at all outflow velocities or by correcting for a constant (velocity-independent) ^{12}CO line opacity. However, the ^{12}CO line is often optically thick, and the exact value of opacity depends on velocity. Not correcting for the velocity-dependent opacity will, in most cases, underestimate the value of γ. A few recent outflow studies have explicitly taken the velocity-dependent opacity of the ^{12}CO line into account when estimating outflow mass, and these studies generally find that $\gamma > 2$ (Bally et al., 1999; Yu et al., 1999, 2000; Arce & Goodman, 2001a, 2002). With the availability of both isotopic tracers of CO molecule over the full extent of the molecular outflow, our observational sample is ideally suited to examine the value of γ applying velocity-dependent opacity correction.

1.3.3 Position-Velocity Relation

The other commonly observed property of molecular outflows is the Position-Velocity (PV) relation, believed to be one of the best kinematic diagnostics of outflows. A typical PV diagram is constructed by summing spectra in strips perpendicular to the assumed outflow axis and than contouring the line intensity as a function of position along the outflow axis and velocity. The simplest molecular outflow PV diagrams show maximum outflow velocity increasing approximately linearly as a function of distance from the source. This feature is commonly referred to as "Hubble law" of outflows. Clear examples of this kind of "Hubble-law" velocity distribution are seen in Monoceros R2 (Meyers-Rice & Lada, 1991) and NGC 2264G (Lada & Fich, 1996). However, PV relations are observed with more structured patterns, which can often be described as a series of "Hubble wedges" distributed at various distances from

the source, and not necessary symmetric with respect to the driving source (Arce & Goodman, 2001b).

Velocity nesting is the universal feature of the molecular outflows. The decrease in the velocity away from the outflow central axis, reflects the diminishing influence of the jet itself (see Figure 1.2). In addition, the "Hubble-law" velocity distribution, implies that outflows accelerate from the stars that generate them. The acceleration is the sign that cloud material is being continually pulled forward by the underlying jet.

1.4 Entrainment Models of Molecular Outflows

The relation between molecular outflows, and H_2 and HH jets has been extensively debated during the last two decades. In the past, most studies used analytical models to try to explain the outflow morphology and kinematics (e.g. Shu et al., 1991; Li & Shu, 1996; Zhang & Zheng, 1997; Matzner & McKee, 1999). In recent years progress has been made in modeling the dynamics and radiative signatures of the jets and winds using multidimensional hydrodynamical simulations which include molecular cooling and heating and their feedback onto the dynamics (e.g. Smith & Rosen, 2003; Keegan & Downes, 2005; Shang et al., 2006; Cunningham et al., 2005). Such synthetic flows can be directly compared to the observed flows in order to identify the driving agent responsible for outflow entrainment. However, it should be noted that simulations of the protostellar jets/winds are extremely challenging and the approaches adopted by different groups vary.

Most of these simulations are quite young, with the longest running time of t = 2300 yr (Keegan & Downes, 2005), which is an order of magnitude smaller compared to most of the molecular outflows lifetime, and even less compared to the lifetime of parsec-scale flows. Hence evolutionary effects on outflow properties may not be captured at all in the simulations.

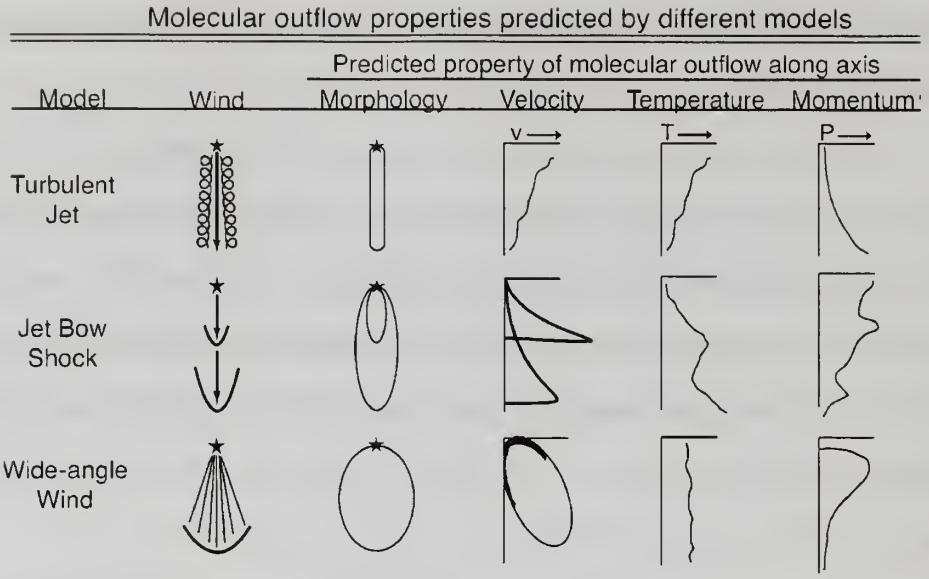

Figure 1.4 Outflow Entrainment Models. Observable molecular outflow properties predicted by the four leading broad classes of models: 1) turbulent jet 2) jet bow shock and 3) wide-angle wind. In the jet-driven bow shock model, an episodic variation in jet velocity produces an internal bow shock driving an internal shell, in addition to the terminal shock. This episodic variation can also be present in the other wind models, but in this figure the effects of an episodic wind are only shown for the jet bow shock model. This figure is based on Figure 2 of Arce et al. 2006

Currently there are three scenarios of the mechanism by which the jets/winds emerging from the embedded star/disk entrain and accelerate the surrounding molecular material. Here we briefly summarized their characteristics.

1. **The "wide-angle wind" models** in which a wide-angled magnetized wind expands like a bubble and sweeps up the stratified surrounding ambient medium in a momentum conserving manner into the thin shell at the wind-bubble ambient medium interface (Shu et al., 1991, 1995, 2000; Li & Shu, 1996; Matzner & McKee, 1999; Lee et al., 2000, 2001).

   Traditionally, this class of models is attractive to explain old outflows of large lateral extents and low collimation, but they are considered unable to account for the observational properties of young outflows. However, this view has been recently challenged by numerical simulation works of Shang et al. (2006); Cun-

ningham et al. (2005) and Gardiner et al. (2003). Numerical simulations allowed them to relax some of the simplifying assumptions made in the analytical models which yielded a better agreement of the modeled and observed outflows. Shang et al. (2006) concluded that the jet-driven and wind-blown scenarios are unified in the framework of Shu et al. (1991). All these studies produce satisfactory general outflow lobe appearance, however, no mass-velocity or position-velocity maps have been generated to compare with observations.

The wide-wind models yielded smaller values of γ over a narrower range, as compared to the jet models. For example in the models of Lee et al. (axisymmetric wind) γ has a value of 1.3 to 1.8, while Delamarter et al. (spherical wind) finds γ in the range of 1.3 to 1.5. In the analytical model of Matzner & McKee (1999) no other value but $\gamma \sim 2$ can be obtained. Jet models yield γ from 1.5 to 3.5. The position-velocity plots in these models show Hubble structure tilted with inclination that exhibits only a small velocity range at the tip, sometimes referred to it as the parabolic shape (Lee et al. 2000), see Figure 1.5. One of the biggest challenges to the wind models is to produce discrete bow-shock type features, since the wind impacts all locations on the shell (Lee et al. 2002)

2. **The "turbulent" jet entrainment models** in which ambient material is accelerated through a turbulent viscous mixing layer that surrounds the jet formed by Kelvin-Helmholtz instabilities Canto & Raga (1991); Stahler (1994); Lizano & Giovanardi (1995); Cantó et al. (2003). The radiatively cooled jet simulations reproduce the broken power law behavior of the observationally determined mass-velocity distribution, even though molecular chemistry or cooling is not included (Micono et al., 2000). However, these models produce decreasing molecular outflow momentum and velocity with distance from the powering source, opposite to that observed in most molecular outflows. In addition they can not match the less collimated outflows.

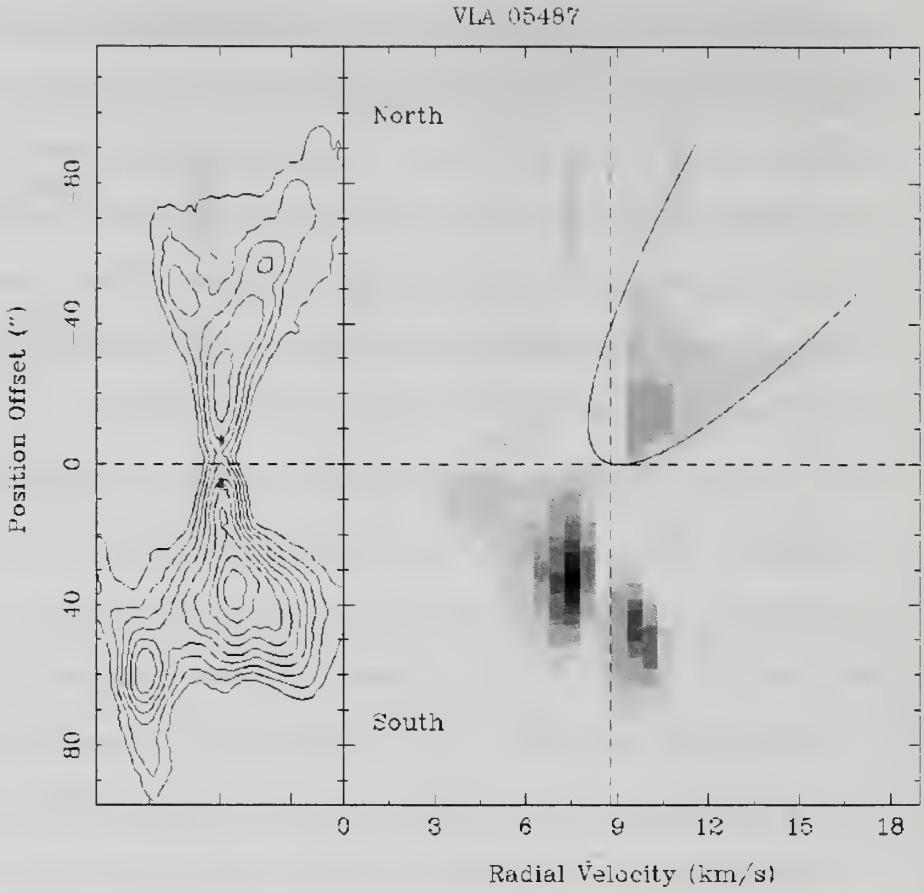

Figure 1.5 Parabolic Structure Of The PV Plot. CO emission, H_2 emission, and PV diagram of the VLA 05487 outflow, a good example of the wind driven outflow. Figure is taken from the Lee et al. (2001). On the left is the CO emission contours plotted over the gray-scale image of the H_2 emission. On the right is the PV diagram of the CO emission, showing a parabolic structure centered on driving source. The solid line plotted over the PV diagram is calculated with the X-wind model. The vertical dashed line indicates the ambient velocity around the outflow. The horizontal dashed line indicates the position of the driving source of the outflow.

3. **The "prompt" entrainment models** in which a highly collimated jet propagates into the surrounding ambient material, producing a thin outflow shell around the jet. The most violent action in a protostellar outflow occurs at the "terminal working surface" where the supersonic flow slams directly into the undisturbed ambient medium. The two-shock structure results, consisting of a "reverse shock," which decelerates the supersonic flow, and a "forward shock", which accelerates the material with which it collides (Hartigan, 1989). The for-

ward shock may take the form of a bow shock whose surface is normal to the flow direction on the axis, but which becomes increasingly oblique away from the axis in the swept-back wings. Such bow shock will drive material ahead and laterally to the axis of the flow and produce an outflow shell surrounding the jet (De Young, 1986; Raga & Cabrit, 1993; Stone & Norman, 1993a,b, 1994; Masson & Chernin, 1993; Suttner et al., 1997; Zhang & Zheng, 1997; Smith et al., 1997; Downes & Ray, 1999; Lee et al., 2001, 2002).

Somewhat milder collisions can occur within outflows whose ejection velocity varies with time. An "internal working surface" can form where faster-moving gas catches up with and "rear-ends" slower-moving material ejected earlier (Raga et al., 1990).

With respect to mass-V relation Keegan & Downes (2005) get $\gamma = 2$, while Smith & Rosen (2005) have a value near 1. Much of this difference can be attributed to the difference in jet-to-ambient density ratio adopted by two groups. The value of γ has been shown in these simulations to evolve over time, with steeper slopes associated with older flows. Given that the running time of these simulations is short, steeper slopes may be more realistic for the parsec-scale outflows. The analytical model of Zhang & Zheng (1997), finds turn down in the mass spectrum at high velocities, where $\gamma >> 2$. Downes & Ray (1999), with their numerical bow shock models, find that the slope of the power-law mass spectrum ranges between $\gamma = 1.58$ and 3.75 (depending on the parameters of the simulation).

The position-velocity diagrams have multiple Hubble wedges when outflow is entrained by episodic jet (Arce & Goodman, 2001b). Jet-driven bow shock models predict PV spur structure, see Figure 1.6, where the outflow velocity increases rapidly at the position of the internal and leading bow shocks (Lee et al. 2001). The PV diagrams in the jet-driven bow shock models are associated

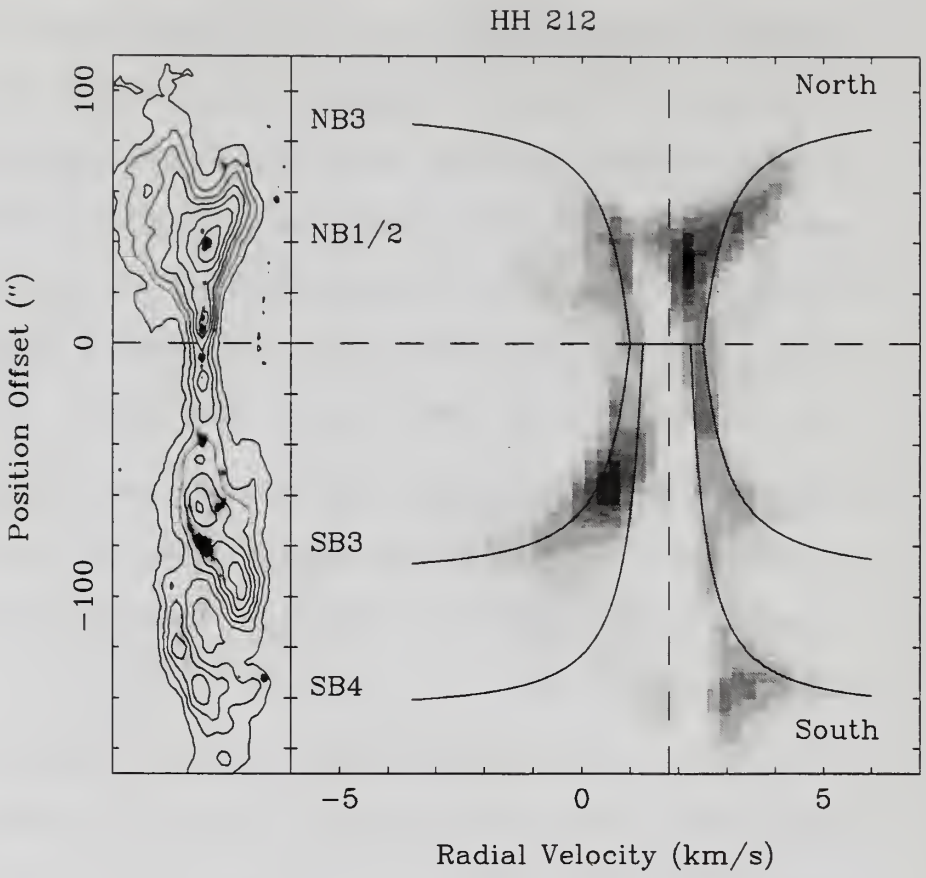

Figure 1.6 Spur Structure Of The PV Plot. CO emission, H_2 emission, and PV diagram of the HH 212 outflow, a good example of the jet driven outflow. Figure taken from Lee et al. (2001). On the left is the CO emission contours plotted over the gray-scale image of the H_2 emission. On the right is the PV diagram of the CO emission cut along the jet axis which shows a spur structure from the source toward the different H_2 shocks. The solid lines plotted over the H_2 image and PV diagram are calculated with the bow shock model. The vertical dashed line indicates the ambient velocity around the outflow. The horizontal dashed line indicates the position of the driving source of the outflow.

with the broad range of velocities near the bow tip, while there is a small almost constant velocity in the bow wing (Lee et al. 2000).

MHD simulations (Gardiner et al., 2003; Stone & Hardee, 2000; Cerqueira & de Gouveia dal Pino, 1999; Cerqueira & de Gouveia Dal Pino, 2001; O'Sullivan & Ray, 2000) show significant differences compared to simulations of jets without magnetic fields, with the difference being less prominent in 3D (Cerqueira & de

Gouveia Dal Pino. 2001). Magnetic fields are capable of collimating the jets at larger scales.

Jet models are often challenged because they produce narrow molecular outflows and have problems of too little momentum. Some suggest that the width and momentum of the outflow can increase if jet is wandering (Smith & Rosen, 2005), while other dispute it (Raga et al., 2004).

1.5 Thesis Outline

This Thesis work was motivated by the discovery of the parsec-scale HH flows and the improvements in the millimeter wavelength observational capabilities. Over a period of three years we built a high-sensitivity, high signal-to-noise ratio (>20), sample of 15 parsec-scale flows in the J=1→0 transition of ^{12}CO and ^{13}CO over the full parsec-scale extent of the HH flows. Such a large study would have been impossible to accomplish in finite lengths of observing time just a few years ago. Through collaboration with John Bally, narrow-band H_α optical data for majority of sources were available. We examined the relation between parsec scale HH flows and molecular flows, and how their properties compare to the commonly found smaller scale outflows. The morphological relation between HH and CO outflows will address a question of their unified origin.

Dual IF capability at the FCRAO 14 m telescope allowed us for the first time to have two CO isotopes observed over the full extent of the molecular outflow. Only a handful of such studies has been available so far in the literature. Therefore, the Thesis observational sample is ideally suited to apply the technique of the velocity-dependent opacity and correct for it the outflow mass estimate. Not only that this will give a better outflow entrained mass estimate, but γ (the slope of the M-v relation) can be derived with higher certainty. This is essential for the comparison with the theoretical models of different entrainment models in order to discriminate among

them. A smaller subset of sources has been observed at HHT 10 m telescope in ^{12}CO J=3→2 line which allowed us to examine variations of T_{ex} in the outflows. Energetics of such big flows will be estimated and their impact on the evolution of the parent cloud and whether they can be a potential source to replenish the decaying turbulence in the cloud.

Since there have been a mounting number of new theoretical works including numerical simulations and analytical models the time was ripe for an observational study of this kind. A good observational sample can therefore provide an excellent constrain to the existing models and future theoretical work.

Using a multiwavelength, multitelescope observation of 15 parsec scale flows we interpret the improved observations in the light of new predictions of theories, with an ultimate goal of distinguishing relative importance of different models for the formation and evolution of the molecular outflows. We will use multiple lines of evidence: the morphological relation between optical and molecular outflows, carefully derived γ indices for the mass distribution in the outflows and PV plots. It is essential to distinguish between these models to not only understand the processes that govern the formation of molecular outflows, but also the nature of the jet/wind launching mechanism and the underlying accretion disk processes.

In Table 1.1, 15 flows targeted by this multi-wavelength study are listed. We select five sources for which we perform detailed analysis and discuss their entrainment models, mass and energy content. In the following two chapters we will show the examples of L 1551 and L 1228, two beautiful parsec-scale molecular outflows associated with parsec scale HH outflows. In two subsequent chapters we will present the case studies of Haro 6-10 and L 1617 outflows. These two sources have nicely defined parsec-scale optical flows, with L 1617 flow reaching nearly 8 pc, but are characterized with very poor CO emission and clumpy morphology. In our sample we identify two classes of sources: the first class consists of parsec-scale optical HH flows associated

Table 1.1. Parsec-Scale Outflows Source List

Source	RA (1950)	DEC (1950)	Associated HH Objects
L1228	20:55:52.8	77:20:44	HH199,200
L1165	22:06:01.6	58:57:11	HH 354
L1152	20:35:30.0	67:42:00.0	HH 376A,B
L1455	03:24:30.0	30:02:00.0	HH 278,279,280,317,318
L1551	04:28:39.9	18:01:39	HH28,29,30,153,262,454
B18w	04:22:21.7	24:16:32	HH300
Haro 6-10	04:26:21.9	24:26:29	HH184,412,414
T-Tauri	04:18:48.1	19:43:40	HH355,155
L1535	04:32:31.6	24:02:08.0	HH434-436 + 5 new
L1641	05:33:03.7	-06:28:53	HH34
L1641N	05:33:52.5	-06:23:59.2	HH296-316,403-406
L1617	05:49:07.2	02:47:02	HH111,110,311,113
L1589	05:15:00.7	07:12:39	HH114/115
L1634	05:17:13.5	-05:54:43	HH240/241
L1630	05:39:25.9	-01:15:01	HH90/91

with parsec scale molecular outflows, and the second class consists of parsec-scale HH flows associated with little or no CO emission. Sources like L 1551 and L 1228 belong to the first class, while L 1617 and Haro 6-10 belong to the second class. In Chapter 6 we describe results for NGC 2071, which does not have a parsec scale associated HH flow, although it does have a parsec-scale shock-excited H_2 emission. Therefore NGC 2071 fits to the category of sources with parsec-scale shocked emission and we detect molecular outflow emission over the full extent of parsec-scale shock emission. Finally we summarize our findings in Chapter 7.

CHAPTER 2

L1551 CASE STUDY

The bipolar molecular outflow associated with the L1551 small dark cloud in the Taurus molecular cloud complex, was the first recognized bipolar outflow from a young stellar object (SLP) and is considered one of the best examples of its kind. At a distance of 140 pc (Lynds, 1962; Kenyon et al., 1994), the L1551 dark cloud has been the site of many multi-wavelength studies that reveal the dynamical complexity of this low mass star formation region.

Optical images of the L1551 outflow region, show new distant HH object, HH 286 (Devine et al., 1999a), making the whole extent of the optical emission in the L1551 flow 1.3 pc. We made sensitive, large spatial extent, high spatial and velocity resolution maps at millimeter and submillimeter wavelengths. Large-spatial extent mapping performed on parsec-scale outflows, allows us to study in detail the entrainment mechanisms by which jets/winds drive the observed molecular flows. With the availability of both ^{12}CO and ^{13}CO data over the full spatial extent of the flow, we are able to take a *full* and proper accounting of the mass and hence energetics of the outflows in the L1551 system. Comparing optical and millimeter data, we are able to discriminate among entrainment models based on morphological grounds.

2.1 Observations

2.1.1 FCRAO CO J=1→0 observations

A full mapping of ^{12}CO and ^{13}CO in the J = 1 — 0 transition has been performed in several observing seasons over a three-year period with the SEQUOIA receiver at the Five College Radio Astronomy Observatory (FCRAO) 14 m telescope. SEQUOIA (Erickson et al., 1999) is a cryogenic focal plane array designed for the 85–115.6 GHz range, and was upgraded in spring 2002 from the original 16 to 32 pixels. The receiver is configured as a dual-polarized 4×4 array. The telescope's half-power beamwidths are 45″ and 47″ for ^{12}CO and ^{13}CO transitions respectively. The antenna temperatures were corrected for the main beam efficiencies of 0.45 for ^{12}CO and 0.5 for ^{13}CO.

The initial observations were taken in 2001 using raster mapping mode in only the ^{12}CO J=1→0 transition, with channel spacing of 0.21 km s^{-1} and velocity resolution of 0.25 km s^{-1}. The data were baselined and convolved to the 22.5″ Nyquist sample grid using CLASS. From 2002, observations were taken using On-The-Fly mapping technique (OTF) and a dual channel correlator (DCC), which allows user to observe 2 frequencies simultaneously with all 32 pixels at SEQUOA, generating 64 spectra for each read of the DCC. The orthogonal polarizations of the SEQUOIA array are averaged to produce spectra with better signal-to-noise ratio (S/N). The OTF data were reduced with the "OTFTOOL" software. OTFTOOL is a suite of tools to inspect, edit, regrid the raw otf data and transform the result into a CLASS or FITS form, developed by M. H. Heyer, G. Narayanan and M. Brewer and available for public usage. Using OTFTOOL, data were examined, channel maps as well as individual spectra were checked for any scanning artifacts, baselined and regridded to the 22.5″ sampled grid. RMS noise weighting was used to combine the data. Regridding takes all of the redundant measurements of the OTF map and constructs the end product - convolved spectra on a regular grid written into a CLASS file. For both ^{12}CO J=1→0

and ^{13}CO J=1—0 transitions. the 50 MHz spectrometer bandwidth setting was used resulting in 50 kHz channel spacing.

Within CLASS, OTF data were smoothed and resampled to the channel spacing of the 2001 ^{12}CO data. The datasets were combined and FITS format files were generated. The resulting velocity spacing is 0.21 km s^{-1}and pixel spacing is 22.5″.

The system temperatures (T_{sys}) in our observations range from 400 – 700 K for ^{12}CO and between 200 – 500 K for ^{13}CO. Regions mapped with the higher noise level were repeated, combined and averaged in order to get a constant lower noise level over the whole extent of the map, with resulting mean rms per velocity channel of 0.19 K for ^{12}CO and 0.12 K for ^{13}CO. Antenna pointing and focus were checked every few hours and corrected using SiO masers.

The analysis were done both in the CLASS and IDL software of Research Systems Inc. Detailed studies of the physical parameters characterizing the outflows were performed using IDL.

2.1.2 HHT CO J=3—2 observations

Submillimeter ^{12}CO and ^{13}CO observations in the J=3—2 transition were carried in December of 2001 and January of 2004 at the 10m Heinrich Hertz Telescope (HHT). HHT's half-power beamwidths are 22″ and 23″ for ^{12}CO, ^{13}CO transitions respectively. Main beam efficiency is 0.5 and forward scatter efficiency of 0.9. As a front-end, the SIS-345GHz receiver was used in single channel mode to achieve the highest sensitivity in that channel. We used the availability of the OTF mapping procedure and mapped 5′×5′ maps with row spacing along declination axis of 6″ and 8″ along RA (scanning rate 10″/sec). L1551 has been mapped in ^{12}CO J=3—2 along the major outflow axis. Single ^{13}CO spectra towards the central YSO and selected lines of sight were also taken. As a back-end configuration, we used all three available AOS's: AOS A, AOS B and AOS C, filter banks and Chirp spectrometer. The two 1 GHz bandwidth

AOS's have mean resolutions of 934 kHz for AOSA and 913 kHz for AOSB. The 250 MHz bandwidth of the AOSC has mean resolution of 385 kHz. The AOS's use 2048 element linear CCD's and thus over sample the spectra by about a factor 2 for AOSA and AOSB and a factor 3 for AOSC. The filter bank spectrometer has 3 bandwidth modes: 256 channels of 1 MHz, 256 channels of 250 KHz, and 128 channels of 62.5 KHz resolution, respectively. The final data set is made using only AOSA and AOSB, since AOSC and filter banks experienced noise problems. Spectral resolution is 0.9 km s^{-1}. With T_{sys} around 900 K, several repeats resulted in mean rms of ~ 0.1 K for the data presented here.

2.2 Morphology and Kinematics of L1551 Outflows

2.2.1 Overview of the L1551 Region

Following the discovery of the Herbig-Haro objects, HH 28 and HH 29 (Herbig, 1974), and an embedded source, IRS 5 (Strom et al., 1976), in the L1551 dark molecular cloud (Lynds, 1962), SLP found a large bipolar outflow centered on IRS 5. Multiwavelength observations of L1551 cloud conducted through the last 25 years show that the region hosts several young stellar objects in different evolutionary stages and multiple overlapping outflows. What was thought to be a beautiful example of a single bipolar flow turns out to have at least three outflows (Moriarty-Schieven & Wannier, 1991; Pound & Bally, 1991; Torrelles et al., 1987). Figure 2.1 shows the blueshifted and redshifted integrated intensity map of our ^{12}CO J=1$\rightarrow$0 data overlayed on the Hα image, previously published by Devine et al. (1999a).

2.2.1.1 Young Stellar Objects

There are a number of star-formation sites within the L1551 cloud, some of the most studied are: IRS 5, L1551 NE and the HL Tau region. IRS 5 is a deeply embedded class I source (Strom et al., 1976), with bolometric luminosity of 38 $L_{\odot}$

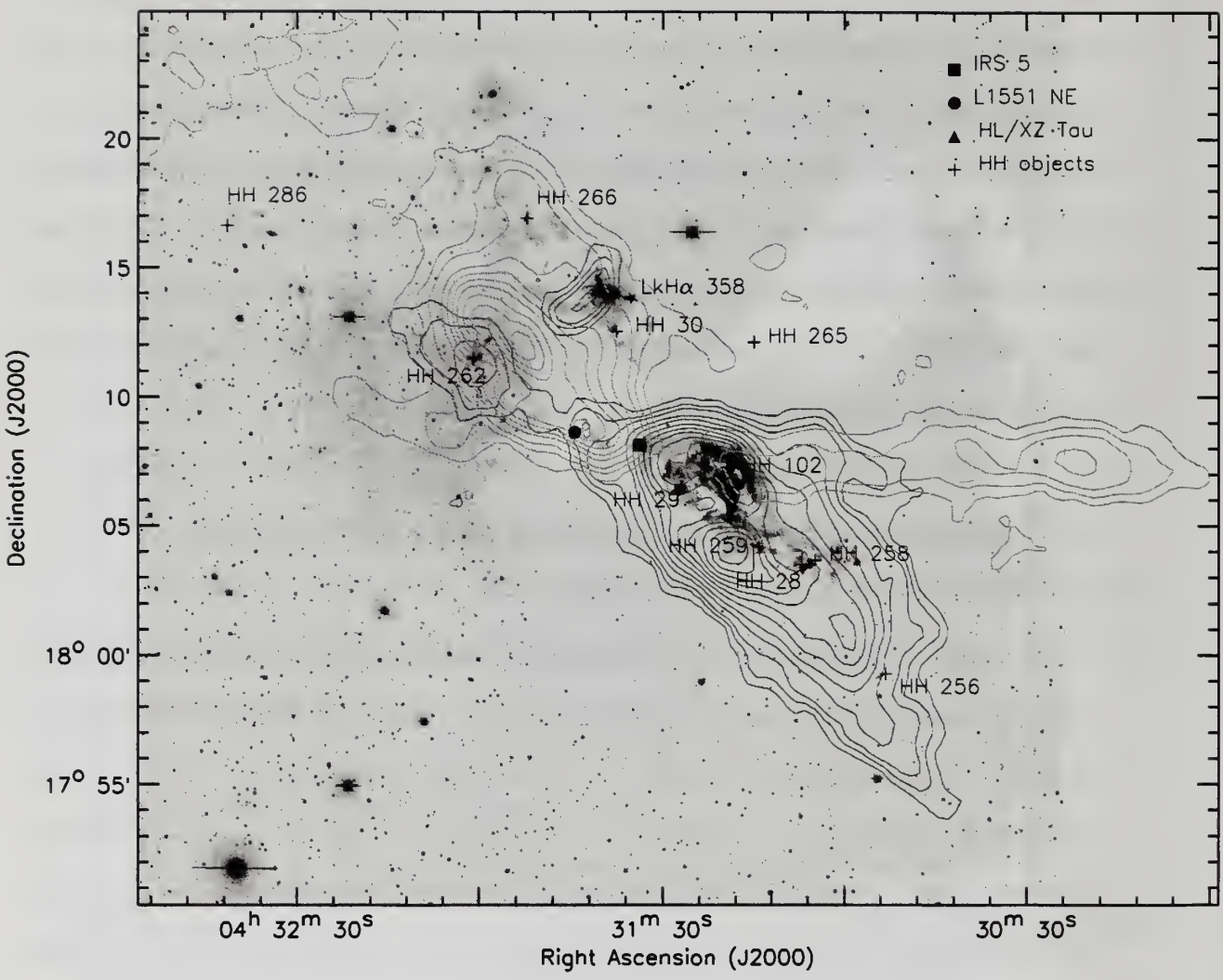

Figure 2.1 Molecular Outflow in L1551 overlayed on optical Hα data. Integrated intensity ^{12}CO J=1—0 emission in L1551 overlayed on optical Hα data Blueshifted gas is integrated in velocity range of -20 to 5 km s^{-1}. Contours start at 3σ and are 1.5, 3, 4.5, 6, 9, 12, 16, 20, 24, 28, 32, 36, 40, 44 K km s^{-1}, plotted in blue. Redshifted emission is integrated in velocity range of 8 to 20 km s^{-1}. Contours start at 4.5σ level and are 1.5, 3, 5, 9, 12, 15, 18, 22, 26, 30, 34, 38, 42, 46 K km s^{-1}, plotted in red. Symbols for different driving sources are introduced: filled square for L1551 IRS 5, filled circle for L1551 NE, filled triangle for HL/XZ Tau system and cross for various HH objects. Notation will be kept on following figures. CO mapping was performed well beyond the borders of the optical image, reaching a degree squared centered on IRS 5 source. Dark spots in the optical image are shock-excited gas, usually associated with various HH objects.

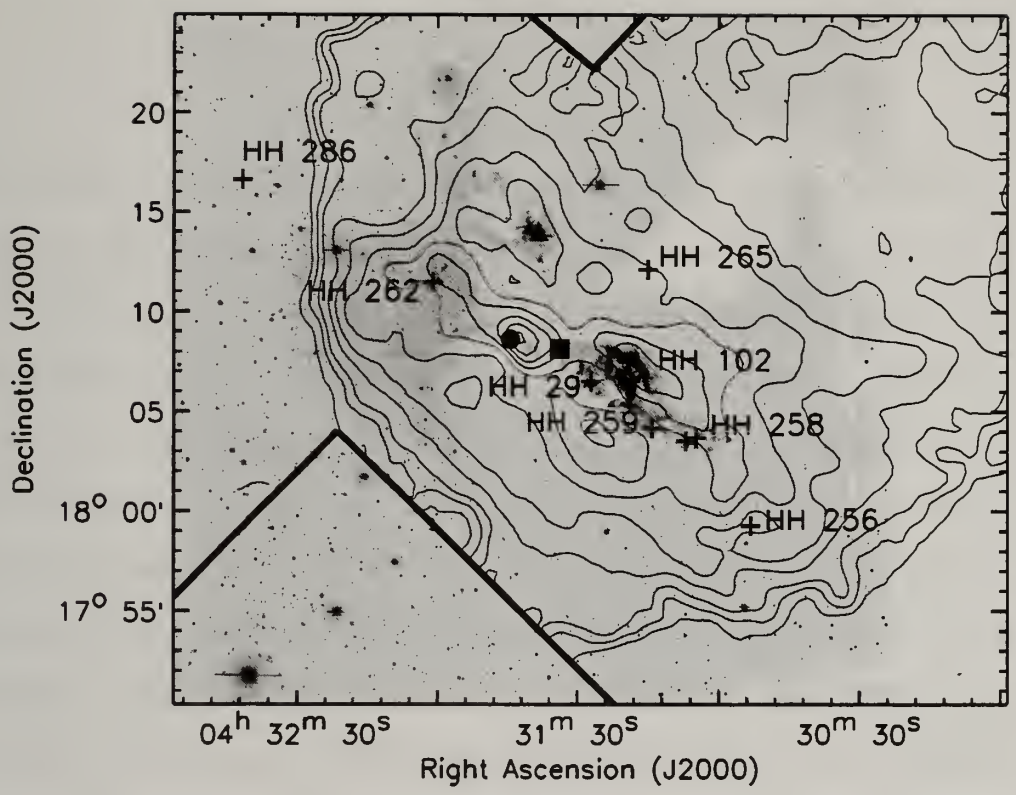

Figure 2.2 ^{12}CO J=1→0 line core emission overlayed on Hα data. Integrated intensity of the ^{12}CO J=1→0 line within core velocities from 5 to 8 km s^{-1} and overlayed on Hα data. Contours are 1.5, 3, 4.5, 6, 9, 12, 16, 20, 24, 28, 32, 36, 40, 44, 48, 52, 56, 60 K km s^{-1}, where 1σ level corresponds to $\sim$ 0.2 K km s^{-1}. ^{12}CO J=1→0 map in line core velocities shows the distribution of the molecular gas in the L1551 cloud. The straight thick lines in the figure outlines the borders of observed CO map.

(Emerson et al., 1984), hidden from the direct view by up to 150 magnitudes of visual extinction (Stocke et al., 1988). It is a close binary system (Rodriguez et al., 1986, 1998; Campbell et al., 1988; Bieging & Cohen, 1985) with components separated by $\sim$ 0.″35 (Looney et al., 1997). Located 149″ east-northeast from the IRS 5 is L1551 NE (Emerson et al., 1984), a Class 0 source with bolometric luminosity of 4.5 $L_{\odot}$. Radio continuum observations at 3.5 cm suggested (Rodriguez et al., 1995) and later confirmed (Reipurth et al., 2002) that L1551 NE is binary source with 0″.5 separation. Approximately 6′ to the north from IRS 5, lies the HL Tau region, with two well-

studied T-Tauri stars, HL and XZ Tau. In addition HH 30* and LkHα 358 embedded stars are found in the same HL Tau region.

2.2.1.2 Jets

Numerous jets have been reported emerging from these three embedded systems. IRS 5 which is believed to be the powering source for the large bipolar molecular outflow has two clearly defined jets (Fridlund & Liseau, 1998; Itoh et al., 2000; Rodríguez et al., 2003). The measured position angles are PA=247° ± 3° for the Northern IRS 5 jet and PA=235° ± 1° for the Southern IRS 5 jet, using 3.5 cm VLA observations with resolution of 0.″1 (Rodríguez et al., 2003). Surprisingly, the position angle of either jet powered by IRS 5 is not aligned with the PA=50° morphology of the molecular CO outflow. However, the Northern IRS 5 jet orientation points to two regions along the edges of the bipolar flow where unusually bright and warm "high-velocity" CS emission has been seen (Plambeck & Snell, 1995; Yokogawa et al., 2003). These regions are 4′ west, near HH 102, and 2′ east from IRS 5, at L1551 NE position, and have been hypothesized as working surfaces of the Northern IRS 5 jet. It has been speculated that the formation of L1551 NE was induced by the IRS 5 outflow impact (Emerson et al., 1984; Plambeck & Snell, 1995; Yokogawa et al., 2003).

The L1551 NE binary system is observed to drive a jet delineated by [Fe II] emission (Reipurth et al., 2000). The bright [S II] emission HH 454 knots lie within the 2° of the [Fe II] jet. The HH 454 - [Fe II] jet axis has PA ∼243°, and we refer to this axis as L1551 NE jet. Proper motion study of the HH 454 knots, show that blueshifted knots are extending toward the southwest and redshifted knots are found toward the northeast from L1551 NE (Devine et al., 1999a). This means that if L1551 NE is capable of entraining CO gas in the region, it would be in the same general orientation as the IRS 5 outflow.

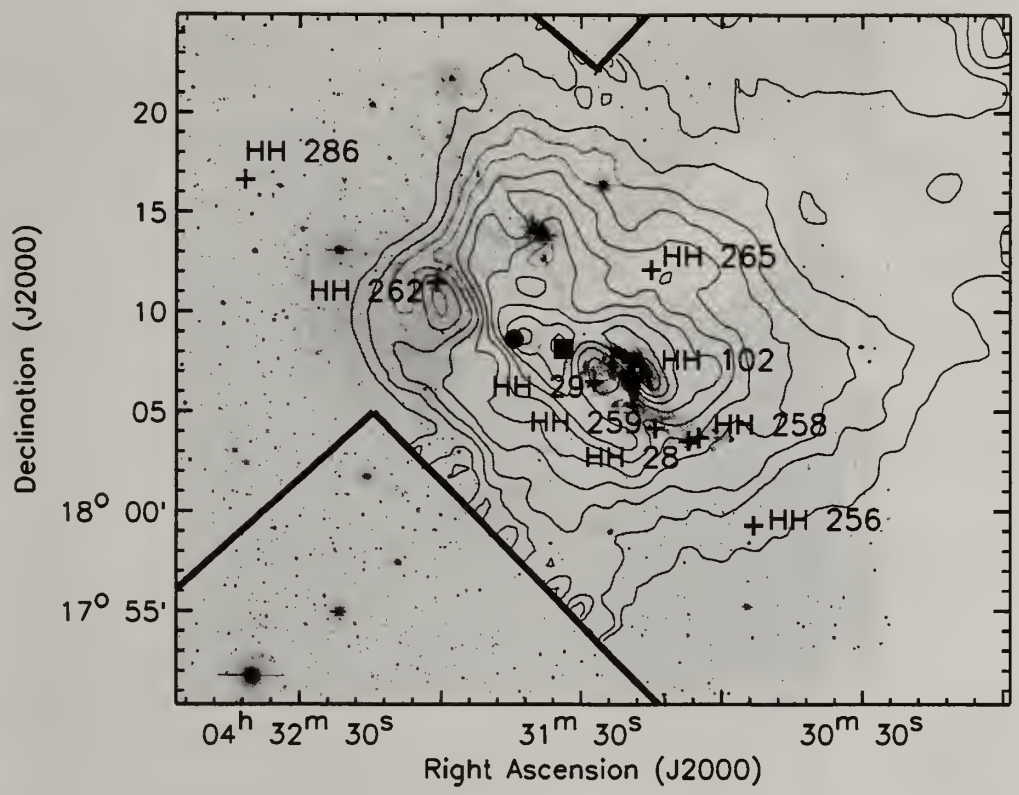

Figure 2.3 ^{13}CO J=1→0 line core emission overlayed on Hα data. Integrated intensity of the ^{13}CO J=1→0 emission overlayed on optical Hα data. Gas is integrated in line core velocity range of 5 to 8 km s^{-1} and the lowest contour is at 1 K km s^{-1} increasing in steps of 1 K km s^{-1}. 1σ level corresponds to 0.1 K km s^{-1}. ^{13}CO J=1→0 probes the higher column density regions within the cloud. The edges of the OTF map are shown here in straight thick lines.

In the HL Tau region several optically identified jets of high velocity gas are reported (Mundt et al., 1988). In the CCD images of Devine et al. (1999a), at least four flows emerge at different angles from four sources. HL Tau drives a jet at PA $\sim$ 50°, while XZ Tau drives a poorly collimated wind, traced by a set of expanding bubbles imaged by HST towards PA $\sim$ 20° (Krist et al., 1999). The HH 30* source is located 1′.5 south of HL Tau and its optical jet, stretches several arcmin from the source at PA $\sim$ 35/215°. LkHα 358 also appears to drive a flow, probably toward PA $\sim$ 70/250° and is a likely candidate for the origin of HH 265 object (Moriarty-Schieven et al., 2006).

2.2.1.3 CO and Herbig-Haro Outflows

Figure 2.1 is dominated by the well known bipolar structure which we will call the main outflow. The main outflow's blueshifted emission lies along PA ~230° and extends 20′ southwest from IRS 5. The main outflow redshifted emission extends 16′ north-east of IRS 5 along PA ~50°. Weak redshifted emission is detected in the far north-east corner of the map and may be related to a further extension of the outflow. In addition to the bipolar outflow symmetric about IRS 5, there are a number of other

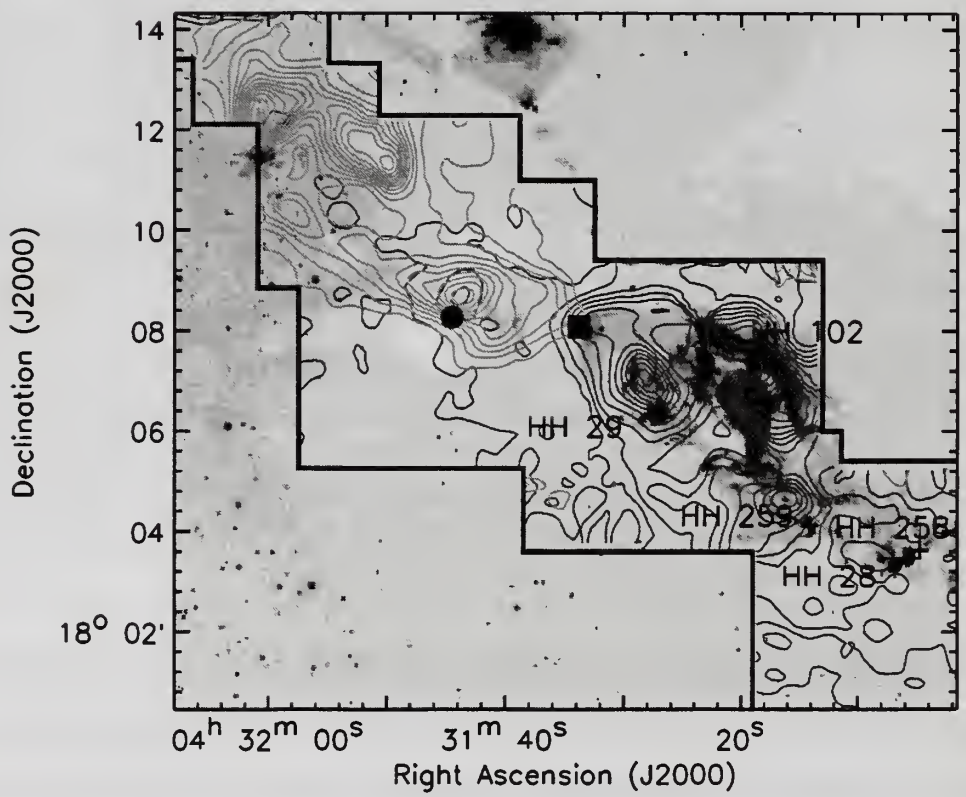

Figure 2.4 ^{12}CO J=3→2 molecular outflow emission overlayed on Hα data. Integrated intensity ^{12}CO J=3→2 emission in L1551 shown in dotted line for blueshifted lobe and in solid line for red shifted emission overlayed on optical Hα data. Blueshifted gas is integrated in velocity range of −20 to 4 km s^{-1} and the lowest contour is 5 K km s^{-1} (~10σ level) increasing in steps of 7 K km s^{-1}. Redshifted emission is integrated in velocity range of 8 to 20 km s^{-1}. Lowest contour is at 5 K km s^{-1} (15σ level) increasing in steps of 5 K km s^{-1}. Symbols for different driving sources and jets are kept as on Figure 2.1.

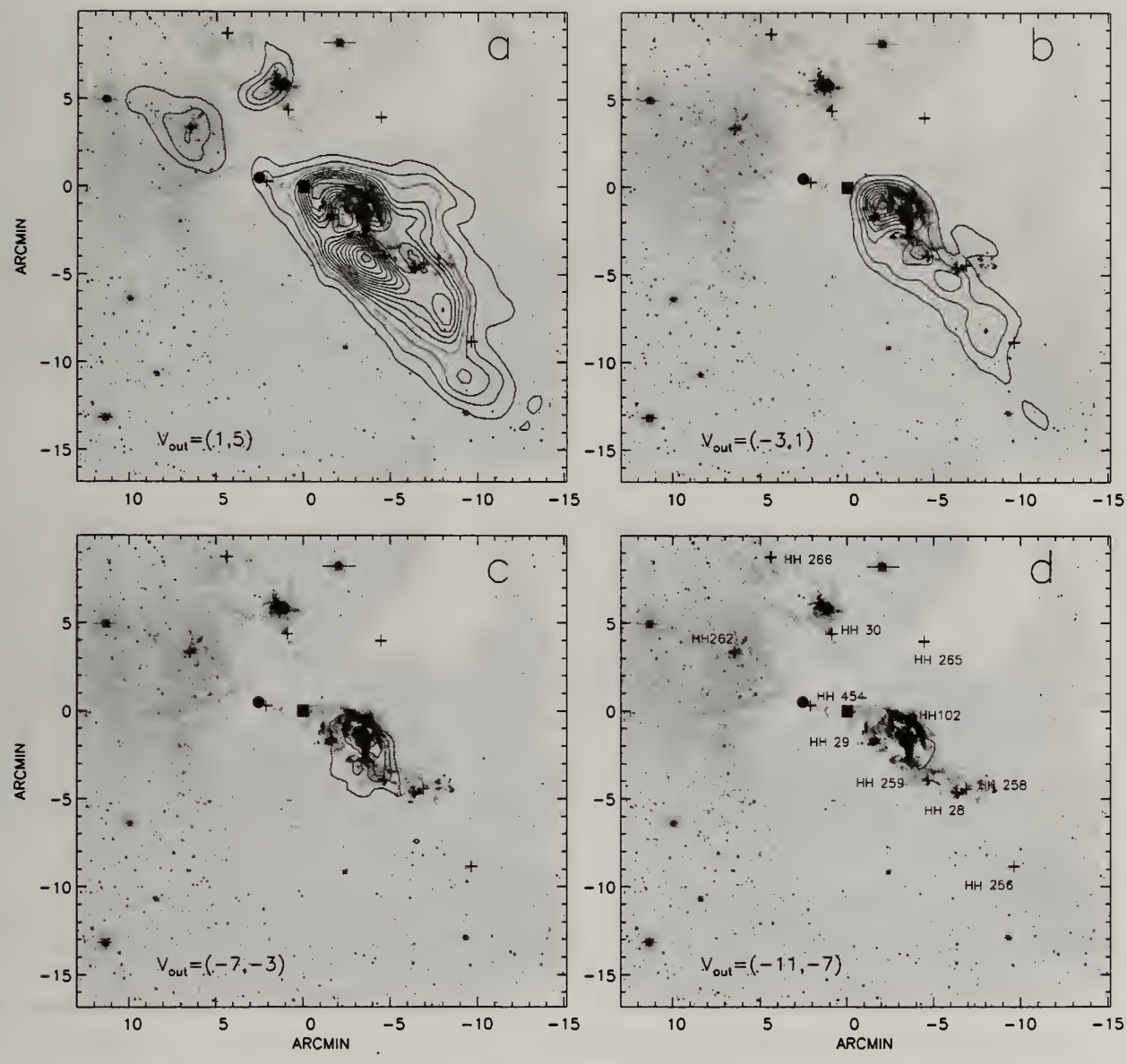

Figure 2.5 Channel-maps of the ^{12}CO J=1→0 blueshifted emission. The CO line is integrated within 4 km s^{-1} velocity bin, starting from 5 km s^{-1}. The velocity range used for the integration is given in each panel. The contours start at 2 K km s^{-1} (10 σ) and go in steps of 2 K km s^{-1} in panels "a" and "b". In the lower panels the step is changed to 1 K km s^{-1}. In each panel, embedded stars are noted with square (IRS 5 at (0.0) position), circle (L1551 NE) and triangle (HL/XZ Tau) and crosses are for HH objects. In the "d" panel we assign each cross to the corresponding HH object. The same holds for the next figure.

features that complicate the outflow. First, blueshifted emission is detected near the HL Tau region, well within the red lobe of L1551 flow, and presumably related to outflow activity in the HL Tau region (Moriarty-Schieven & Wannier, 1991; Pound

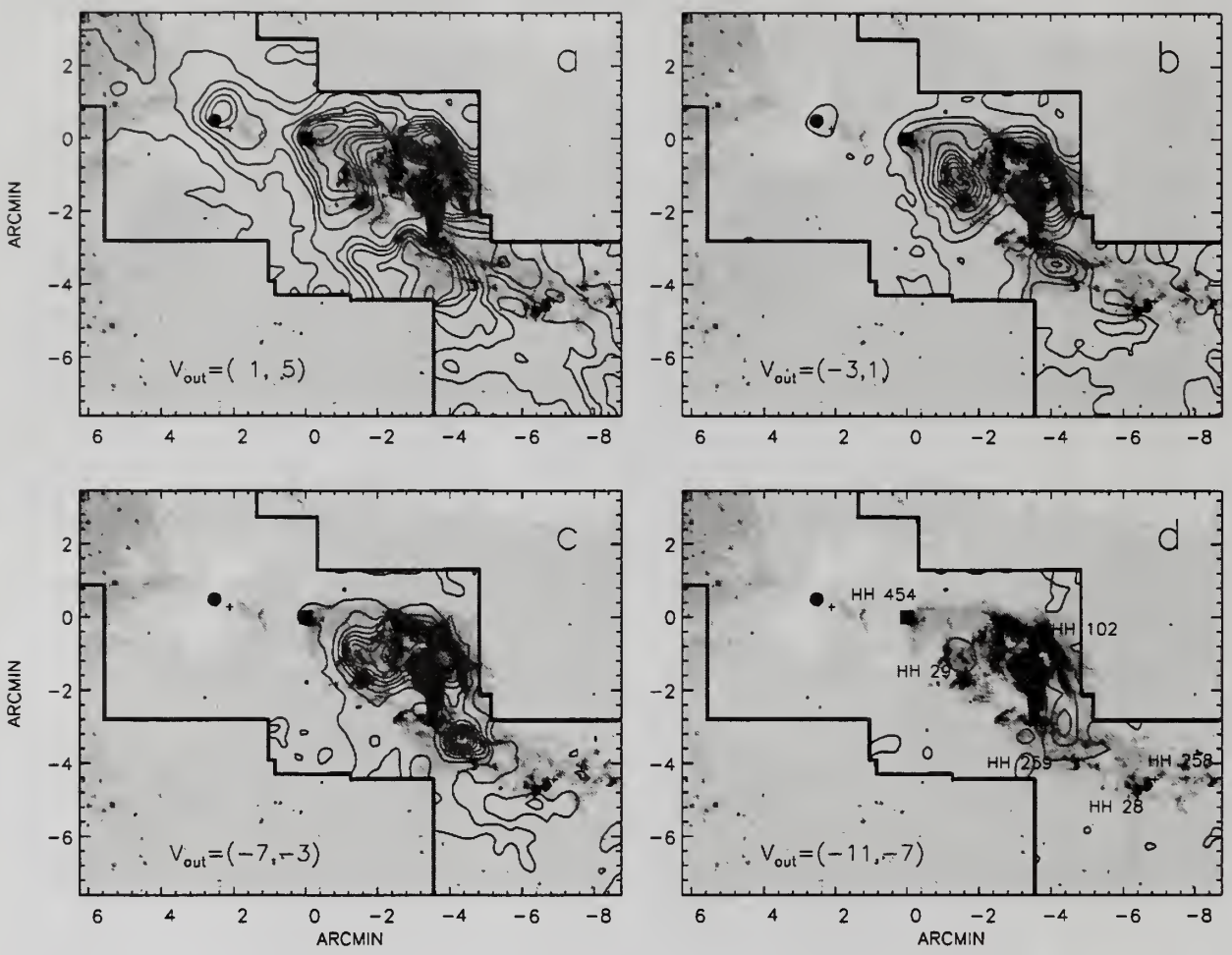

Figure 2.6 Channel-maps of the ^{12}CO J=3→2 blueshifted emission. The CO line is integrated within 4 km s^{-1} velocity bin, starting from 5 km s^{-1}. The velocity range used for the integration is given in each panel. The contours start at 2 K km s^{-1} (10 σ) and go in steps of 5 K km s^{-1} in the panels "a" and "b" and in the other two panels step is changed to 2.5 K km s^{-1}.

& Bally, 1991; Torrelles et al., 1987). The most striking feature is the previously discovered redshifted component oriented east-west (EW flow) that lies north of the blueshifted main outflow (Moriarty-Schieven & Wannier, 1991; Pound & Bally, 1991). Finally, a blueshifted feature, can be seen extending into the main redshifted outflow lobe to the north-east beyond HH 262 (Moriarty-Schieven & Wannier, 1991) and may be connected to the EW flow; an idea that will be discussed in more detail later in the paper.

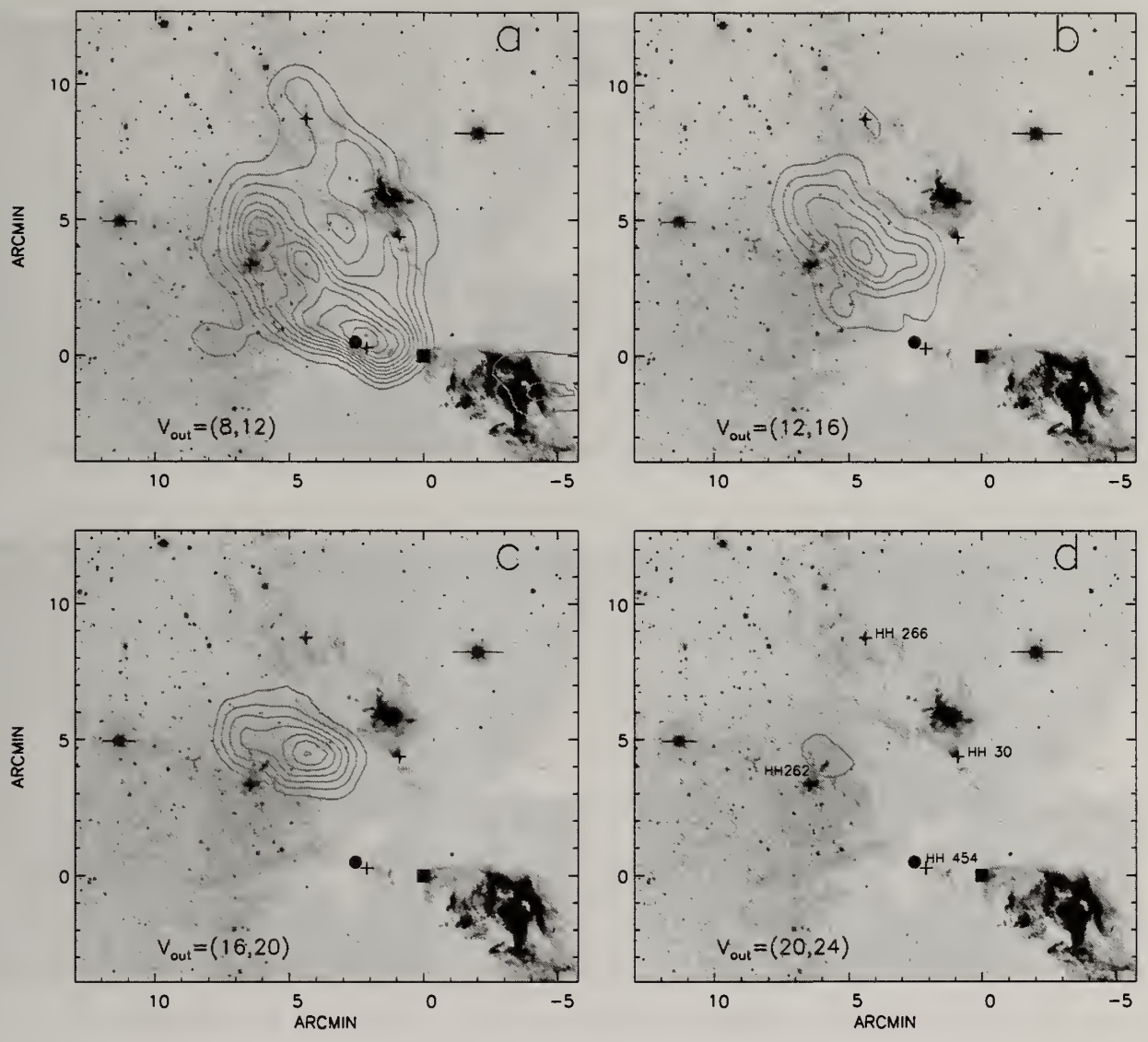

Figure 2.7 Channel-maps of the ^{12}CO J=1→0 redshifted emission. The line is integrated within 4 km s^{-1} velocity bins of the redshifted emission in the main flow's red lobe and the HL Tau region. The velocity range is given in each panel. The contours in each panel start at 1 K km s^{-1} (5 σ) and go in steps of 2 K km s^{-1} in panels "a" and "b" and in other two panels the step is changed to 1 K km s^{-1}. The (0.0) is at the IRS 5 location.

Devine et al. (1999a) reported the discovery of HH 286, making the whole extent of the optical flow 1.3 pc between HH 286 and HH 256. The molecular outflow extends slightly beyond HH 256 in the south-west, however the outflow terminates short of HH 286. The full extent of the CO outflow is approximately 32′ which corresponds to 1.3 pc at the distance of L1551 cloud. Therefore the spatial extents of the optical and

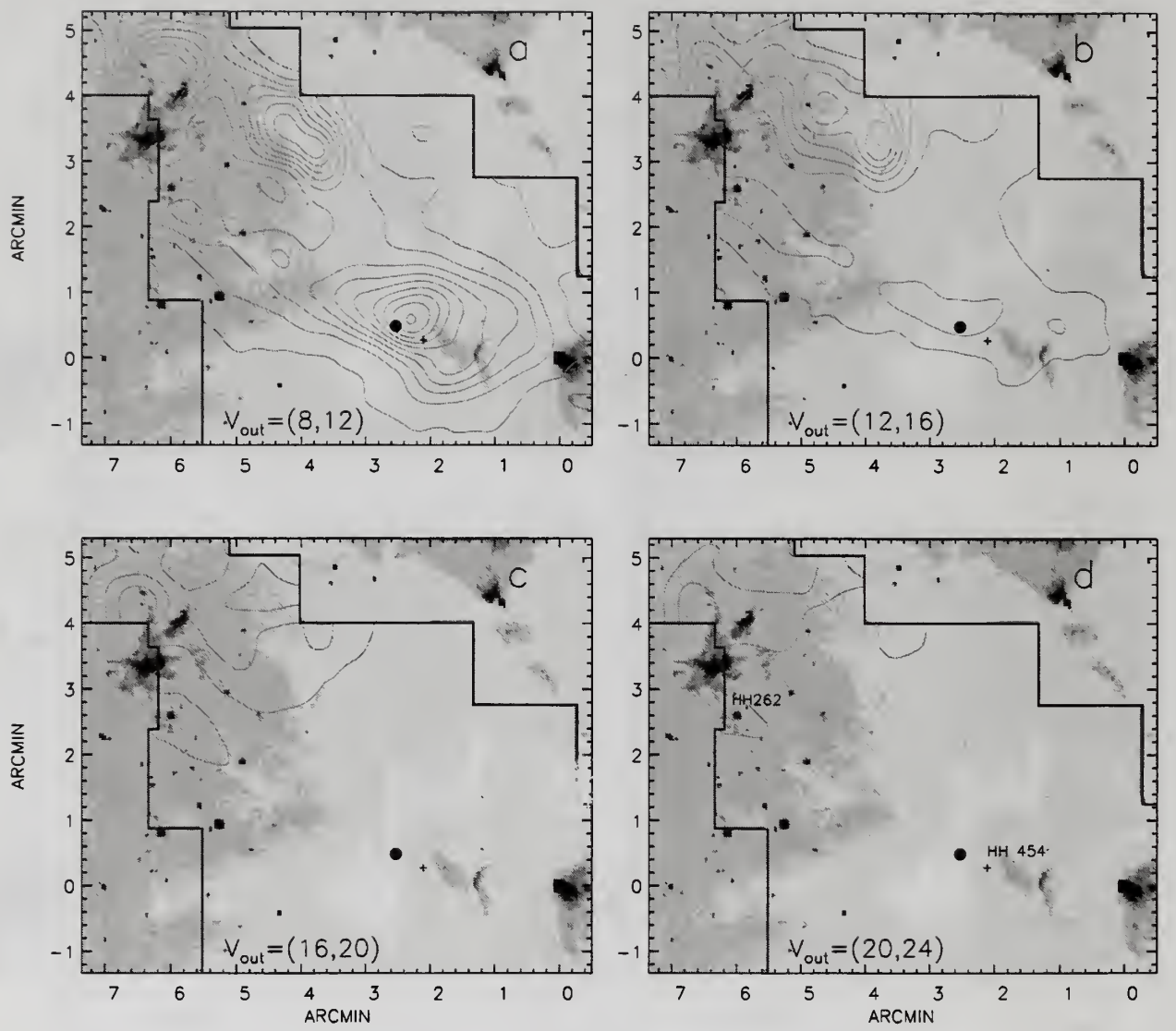

Figure 2.8 Channel-maps of the ^{12}CO J=3→2 redshifted emission. The line is integrated within 4 km s^{-1} velocity bins of the redshifted emission in the main flow's red lobe and the HL Tau region. The velocity range is given in each panel. The contours in panels "a" and "b" start at 2 K km s^{-1} (10 σ) and go in steps of 5 K km s^{-1}. In the panels "c" and "d" the contour step is 2.5 K km s^{-1}. The (0.0) is at the IRS 5 position.

CO outflows. are the same although displaced. Our CO maps extend well beyond HH 286 and in Figure 2.2 and Figure 2.3 we show the integrated intensity maps of the ^{12}CO and ^{13}CO J=1→0 emission within the velocity range of the line core. The ^{13}CO J=1→0 map of the line core emission provides our best measure of the distribution

of ambient velocity gas. Both figures clearly illustrate that there is no molecular gas at the position of the HH 286. Thus, the molecular outflow ends short of HH 286 because there is no molecular material to be entrained in the outflow.

2.2.2 Velocity Structure of the Outflows

In Figures 2.1 and 2.4 we show the integrated intensity maps of the redshifted and blueshifted outflowing gas in the ^{12}CO J=1→0 and J=3→2 transitions overlayed on an image of Hα emission. The spatial extent of the J=3→2 map is considerably smaller than that of the J=1→0 transition. Although the outflow appears more collimated in the J=3→2 map, this is largely due to the restricted angular extent of the map, which did not cover either the HL Tau or EW outflow regions. The J=3—2 data is primarily useful in probing the inner regions of the main flow at higher angular resolution.

In the following three sections, we will discuss in detail the velocity field associated with the molecular gas within the different flows in L1551. We will discuss the main, HL Tau, and EW outflows.

2.2.2.1 Main Flow

In Figures 2.5a and 2.6a the lowest velocity blueshifted emission is shown. In the larger J=1→0 map (see Figure 2.5a) one can identify the blue lobe associated with the main outflow, a bow-shaped emission feature associated with HL Tau, and a feature extending north-east from the main flow toward HH 262. The blue lobe of the main flow has a parabolic shell structure that originates at IRS 5, with IRS 5 embedded within it. This parabolic shell encompasses most of the Hα emission and is best delineated in the higher angular resolution image of the J=3→2 transition of CO seen in Figure 2.6.

At higher blueshifted velocities the emission becomes more collimated and is confined closer to the outflow axis. The nested velocity structure for the blue lobe of this

outflow is very well known. The emission (see Figure 2.6b,c) predominantly arises in three clumps associated with HH 29, HH 259 and HH 102. For the clumps associated with HH 29 and HH 259, the strongest CO J=3→2 emission lags behind the optically defined shock regions. At the highest blueshifted velocities, (see Figures 2.5d and 2.6d), the emission is confined to a region located toward the end of the outflow cavity defined by the optical emission, near HH 259.

The alignment of the HH 454a, HH 29, HH 259, HH 28 with L1551 NE jet axis and the proper motion studies of HH 28 and HH 29 have been used to suggest that they share a common origin in L1551 NE (Devine et al., 1999a). If indeed this is the case, it is possible that some of the blue emission we see in the main flow may originate in material entrained by L1551 NE outflow.

In Figures 2.7 and 2.8, we show mosaics of integrated intensity channel maps of the redshifted ^{12}CO emission. Besides the main flow, at the lowest redshifted velocities in the larger J=1→0 map, the beginning of the EW flow can be seen. The velocity structure in the redshifted gas of the main flow shows some similarities to that of the blue lobe. Again, there is evidence for a nested velocity structure, however the exact interpretation is complicated by the presence of HL Tau. In Figure 2.7a one can see an extension of redshifted emission from IRS 5 to the north towards HL Tau. This emission could either be part of a parabolic shell morphology of the main red lobe, or emission associated with the HL Tau outflow. As in the blue lobe, the higher velocity emission is offset from IRS 5 and confined closer to the outflow axis and the highest velocity emission is located near the end of the outflow near HH 262.

Maybe the most tantalizing evidence of molecular emission associated with L1551 NE jet is seen in Figure 2.8a,b where there is a linear emission feature that arises close to NE and extends for approximately 5′ to the north-east, close to the HH 262. The position angle of this linear feature is $\sim 60^\circ$ similar to the orientation of the [Fe II] jet driven by L1551 NE (Reipurth et al., 2000). A similar suggestion was made

by Moriarty-Schieven et al. (2006). However, the feature could instead be just part of the parabolic shell associated with the main flow from IRS 5. The radial velocity of HH 262 indicates that it is redshifted (López et al., 1998) and that it may be either related to L1551 NE or the outflow associated with IRS 5. Unfortunately, our submillimeter map is not complete in the region surrounding HH 262.

To better show the complex velocity structure within the L1551 outflows, we construct position-velocity (p-V) diagrams by averaging the spectra perpendicular to the p-V axis over a finite width. In Figure 2.9 we show a p-V diagram constructed from the J=1→0 data with a width of 2′.25. The p-V diagram is aligned along the main outflow axis (at a position angle of 50°) and passes through IRS 5 (at zero offset). Figure 2.10 shows the p-V diagram constructed from the J=3—2 data along the the same axis with a width of 1′.1.

In the red lobe of the main flow, the velocity structure is relatively simple, with velocity increasing approximately linearly with distance from IRS 5 (Figure 2.9). Such velocity structure is often dubbed as "Hubble" flow and corresponding feature in the p-V diagram a Hubble wedge. The velocity field within the Hubble wedge shows a systematic acceleration, with both the terminal flow velocity as well as the mean velocity both increasing within the wedge. The terminal velocity in the redshifted lobe is reached near HH 262 at an offset of approximately +11′ from IRS 5, where outflow terminates at all velocities, although cloud emission continues.

The velocity field in the blue lobe of the main flow is more structured than in the red lobe. The inner region of the outflow is shown in the p-V plot of the J=3—2 transition of CO, Figure 2.10. In this higher resolution p-V diagram, IRS 5 is clearly the symmetry point between the redshifted and blueshifted outflow lobes. In the blue lobe, Hubble wedges associated with HH 29 and HH 259 can be distinguished. The more extended, but lower resolution p-V diagram, constructed from CO J=1→0 transition, shows possible additional Hubble wedge features near HH 29, HH 259, HH

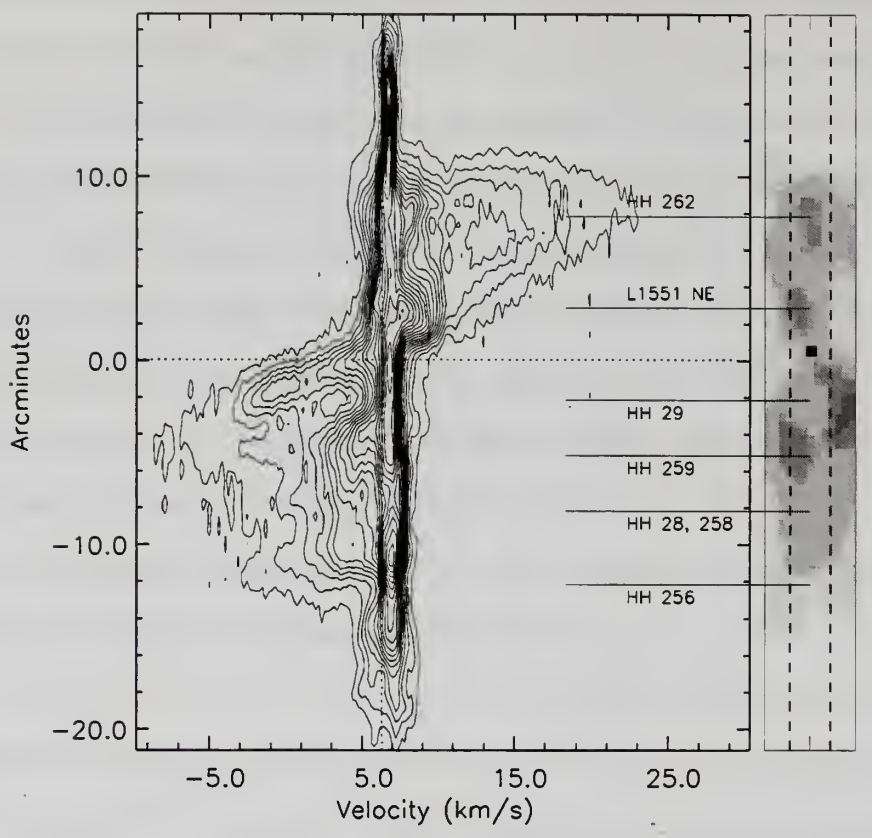

Figure 2.9 Position-velocity plot for L1551 IRS 5 in CO J=1→0. The left side of the plot shows the p-V plot, made along the 50° axis going through IRS 5. The width of the cut is 6 pixels or 2′.25. On the right side, is the integrated intensity image of the L1551 outflow in J=1→0 , rotated 50°. The dotted vertical lines outline the width of the p-V swath. The position of the driving source IRS 5, corresponds to the zero value on the y axis. The positions of the different HH objects are marked.

28 and HH 256. The presence of multiple Hubble wedges has been interpreted as due to either episodic or multiple outflow events (Arce & Goodman, 2001b). Low velocity outflow emission is detected out to an offset position of -18′, near the edge of the molecular cloud. Thus, the blue flow may be escaping the cloud, while the red flow is stopped within the molecular cloud. The different velocity structure of the red and blue lobes may reflect the differences in the underlying ambient gas distribution.

We also made p-V plots (not shown here) along the L1551 NE jet axis, and these plots are very similar to those shown in Figures 2.9 and 2.10. However, in these plots

the location of L1551 NE is clearly offset relatively to the symmetry point of the inner redshifted and blueshifted Hubble wedges.

2.2.2.2 HL Tau Flow

The most prominent feature associated with the HL Tau flow is the clam-shell morphology of the blueshifted CO emission seen in Figure 2.5a. This feature is centered on the HL Tau jet axis (PA $\sim$ 50°, Mundt et al. (1990)) and opens toward HH 266. It is likely that this feature reflects the collective impact of several flows on surrounding gas. As mentioned earlier, it is problematic to define the redshifted emission associated with the HL Tau flow since it overlaps main flow's redshifted emission. Figure 2.7b shows a linear feature extending north-east from the HL Tau region and well aligned with the direction of the HH 30 jet (PA $\sim$ 31°, Mundt et al. (1990)). The resolution of our J=1$\rightarrow$0 data does not allow us to study the details of the HL Tau flow and the J=3—2 map did not extend to this region.

2.2.2.3 EW flow

In Figure 2.11 we show a mosaic of integrated intensity maps within successive 4 km s^{-1} wide redshifted velocity intervals for the EW flow. We have not overlaid the Hα optical image on the EW flow, because the EW flow extends well beyond the coverage of the optical image. The portion of the EW outflow covered by the optical image, with exception of HH 102, shows no bright optical features associated with the flow. The EW flow has a length of approximately 21′ (corresponding to 0.85 pc at 140 pc distance) and has a relatively large velocity extent ranging from about 8 km s^{-1} to 20 km s^{-1}. This flow is highly collimated at all velocities. The EW flow appears to originate near HH 102 and at successive higher velocities the emission is further offset from the origin. The Hubble flow character to the velocity structure of EW flow is also shown in the p-V plot constructed from the J=1$\rightarrow$0 CO data, Figure 2.12. The p-V plot passes through HH 102 (the zero offset position) and is at position angle

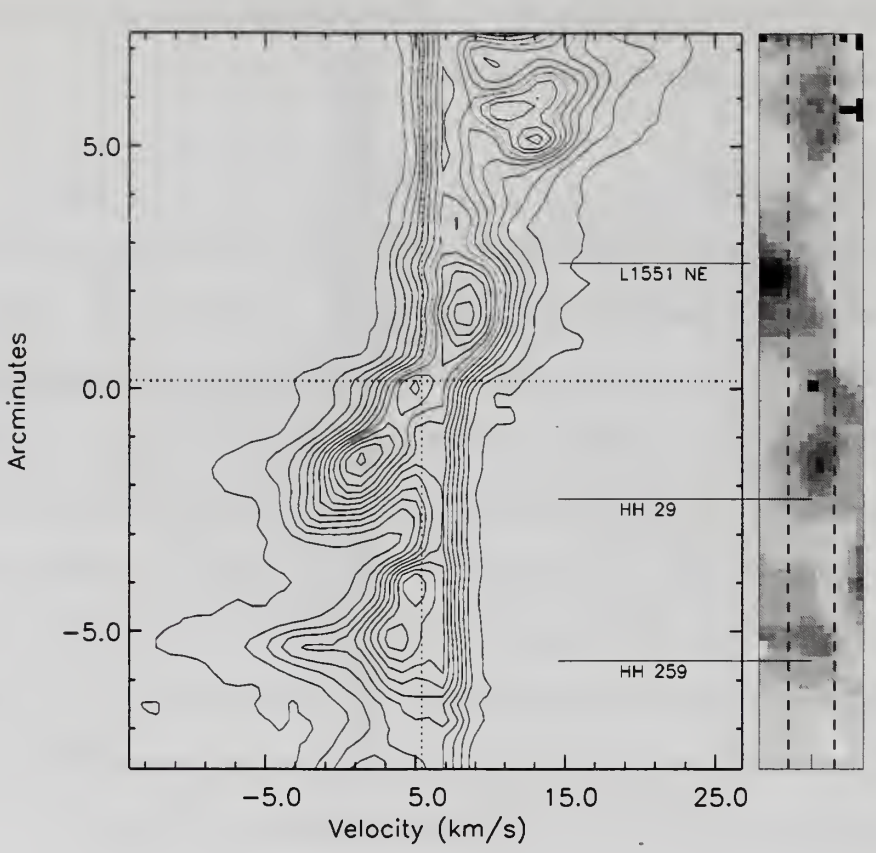

Figure 2.10 Position-velocity plot for L1551 IRS 5 in CO J=3—2. The J=3—2 integrated intensity image on the right side is rotated 50°. The width displayed in the integrated intensity image is 2′.2, while the width of the p-V cut is 1′.1 centered on IRS 5 (dotted vertical) lines.

270°. The outflow emission in the EW flow is much weaker than in the main flow, so the p-V plot is much noisier. However, there is evidence for a Hubble flow feature that terminates at a V_{LSR} of +16 km s^{-1} at an offset position of approximately 16′.

We speculate that the blueshifted counterpart to the EW red flow is the feature seen in Figure 2.7a extending into the red lobe of the main outflow. If this feature is related to the EW flow, the redshifted and blueshifted flows are not co-linear and would require that the blueshifted portion of the flow curves northward. The corresponding blueshifted feature that we tentatively identified with EW outflow is not seen in the p-V diagram since it curves north and does not lie along the east-west

axis. Figure 2.1, however, provides a good overview of the possible connection of these two velocity features.

It is intriguing that the high velocity dense gas clumps detected in CS by Plambeck & Snell (1995) are located near L1551 NE and HH 102. Based on the interferometer results, Plambeck & Snell (1995) and Yokogawa et al. (2003) suggested that NE was formed in a swept-up shell of gas produced by the IRS 5 outflow. The spatial and velocity structure of the CS emission toward HH 102 is similar to that near NE. We speculate, that like NE, the outflow from IRS 5 may have triggered another star formation event within the dense shell of swept-up gas near HH 102. Additional evidence for the interaction of the IRS 5 jet with material in this region is provided by the optical spectroscopy of HH 264, presented by Hartigan et al. (2000). In fact, recently, Moriarty-Schieven et al. (2006) detected relatively strong far-infrared dust emission at 850 μm toward HH 102. Due to insufficient spatial resolution they were not able to conclude if there is any point source within the extended structure. Thus, a newly formed star in this region may be responsible for producing the EW flow and its blueshifted counterpart.

2.3 Mass and Energetics

The L1551 cloud contains over a dozen young stellar objects concentrated in a region less than 1 pc in diameter and many have associated HH objects or molecular outflow activity, all of which attest to the overall complexity of the L1551 region. We define four areas of interest to study the molecular outflow activity and these are shown in Figure 2.13. Since the mass distribution along the outflow can be a good indicator of the entrainment mechanism, the idea is to isolate the various outflow components as much as possible. Regions A1 and A2 mark the blue and redshifted lobes of the main outflow. We also separately analyze the blueshifted emission in region A2, which may be associated with the EW outflow. Region A3 delineates the

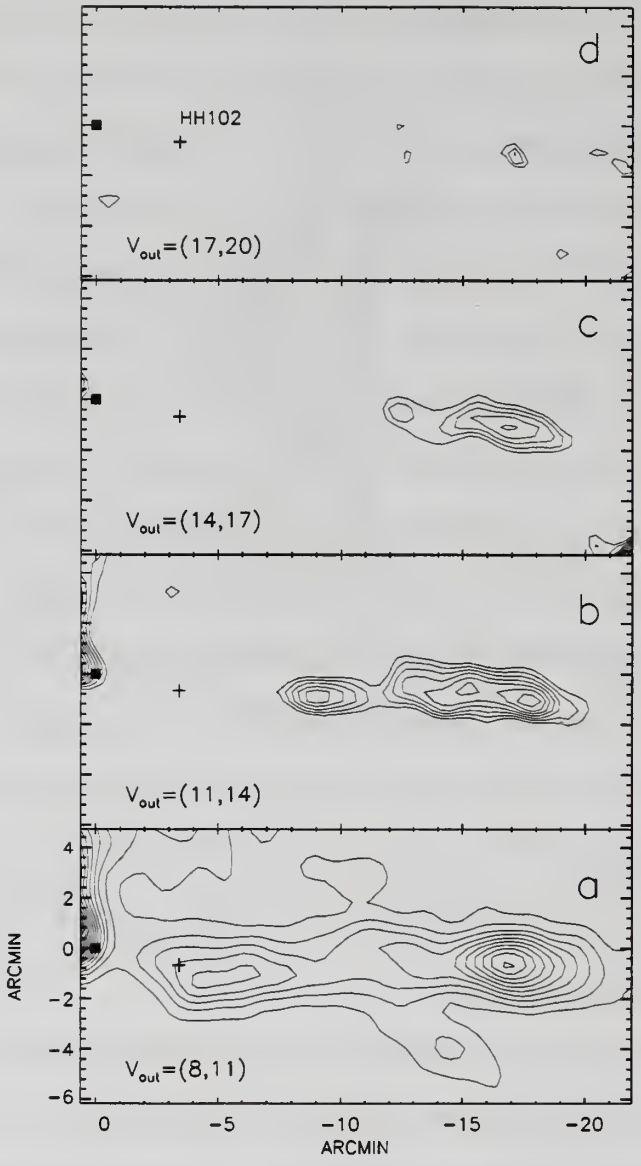

Figure 2.11 Channel-maps of the ^{12}CO J=1—0 EW redshifted emission. ^{12}CO redshifted integrated intensity emission in the EW direction within 2 km s^{-1} velocity bins. The square at (0.0) position marks the IRS 5 and the cross marks HH 102 position. The contours in panel "a" start at 0.75 K km s^{-1} (6 σ) and go in steps of 0.75 K km s^{-1}. In panel "b" the step is changed to 0.125 K km s^{-1}, and the lowest contour level is 0.5 K km s^{-1}. In the top two panels, the step is 0.125 K km s^{-1}and the lowest contour is 0.25 K km s^{-1}.

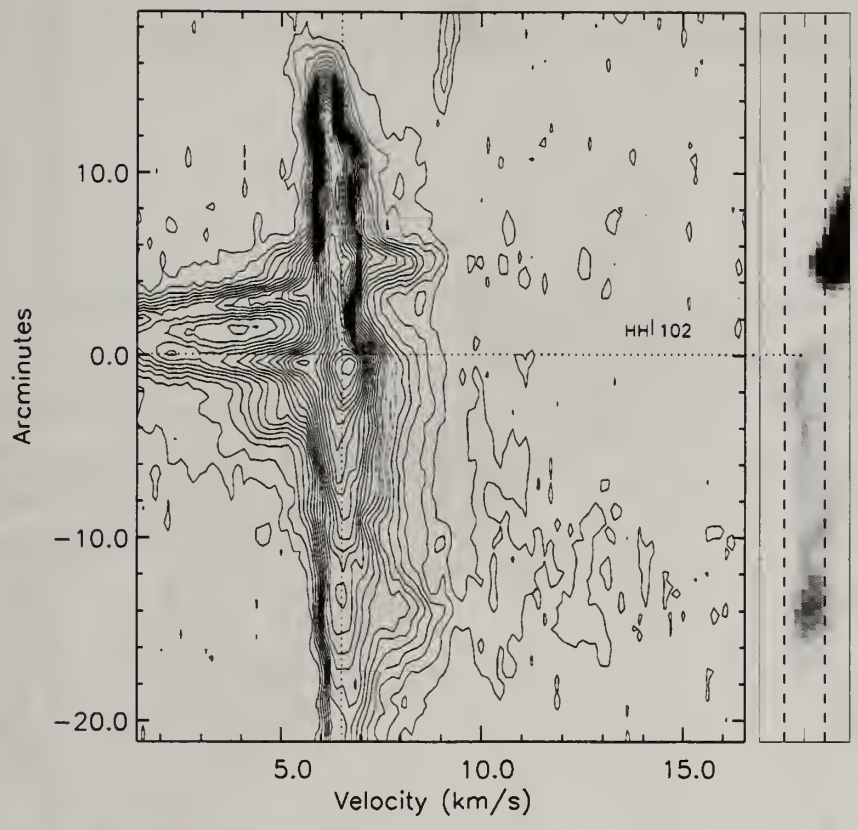

Figure 2.12 Position-velocity plot for EW flow in CO J=1→0. The cut is made along the 270° axis emerging from HH 102 (zero on the y axis). The cut is 90′ wide. and on the right side. the integrated intensity image made over redshifted velocities. and rotated 270° is shown.

redshifted and blueshifted emission likely associated with HL Tau outflow and region A4 the redshifted emission associated with the EW outflow.

2.3.1 Excitation Temperature

The excitation temperature (T_{ex}) of the high velocity gas can be estimated from the ratio of ^{12}CO J=3—2 to ^{12}CO J=1—0 line, both available over a significant part of areas A1 and A2. The ^{12}CO J=3→2 data have been spatially convolved to match the spatial resolution of the ^{12}CO J=1—0 data, and ^{12}CO J=1—0 data have been spectrally smoothed to match the 0.9 km s^{-1} velocity resolution of the ^{12}CO J=3→2

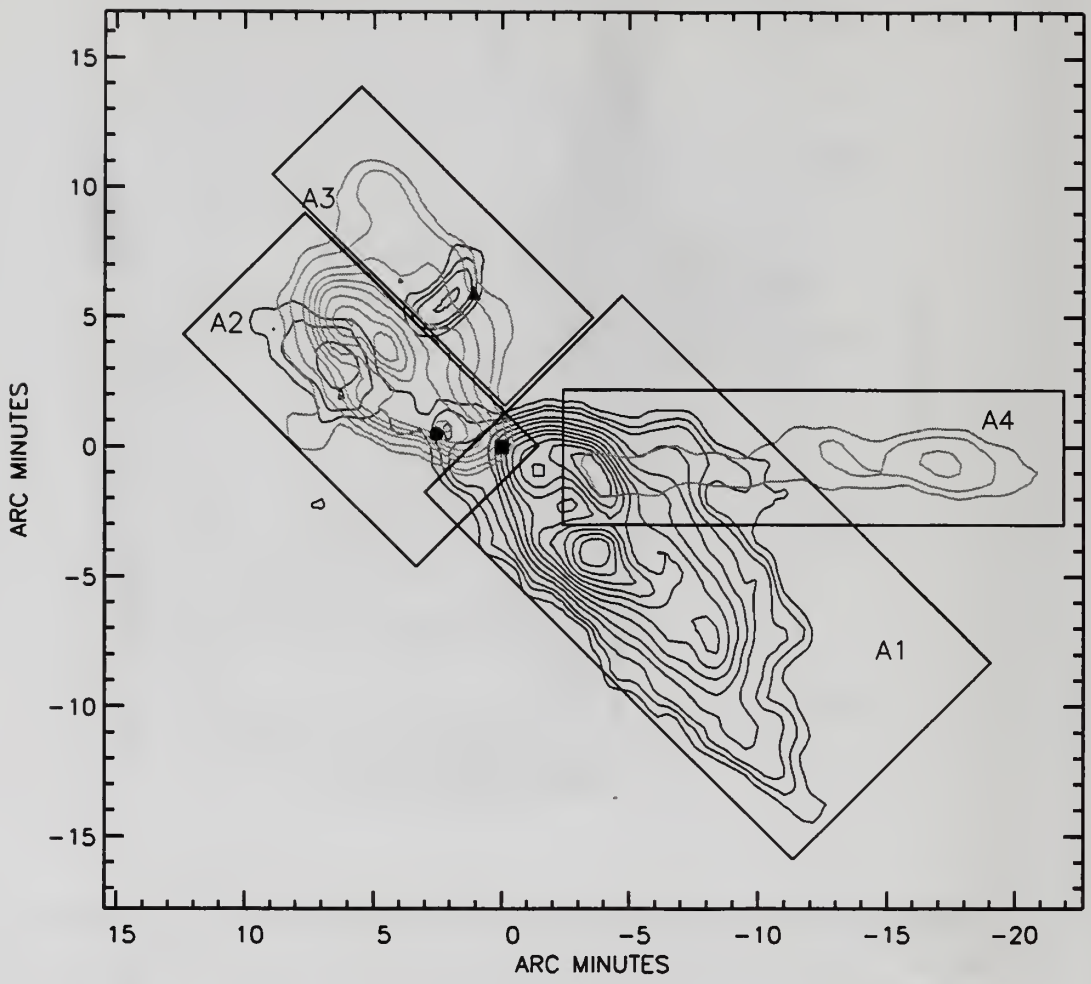

Figure 2.13 Subregions for the mass-velocity calculation. Four different areas A1, A2, A3 and A4 are identified along the L1551 flow (see text for more).

data. Using positions where both J=1→0 and J=3→2 data exist and where there is a significant outflow emission, we compute an average spectrum for regions A1 and A2; these spectra and their ratio are shown in Figure 2.14. At the velocity of the ambient cloud emission the ratio, R = T(J=3→2)/T(J=1→0), has a minimum value close to the ratio of R= 0.58 predicted for optically thick, thermalized gas at temperature of 10 K.

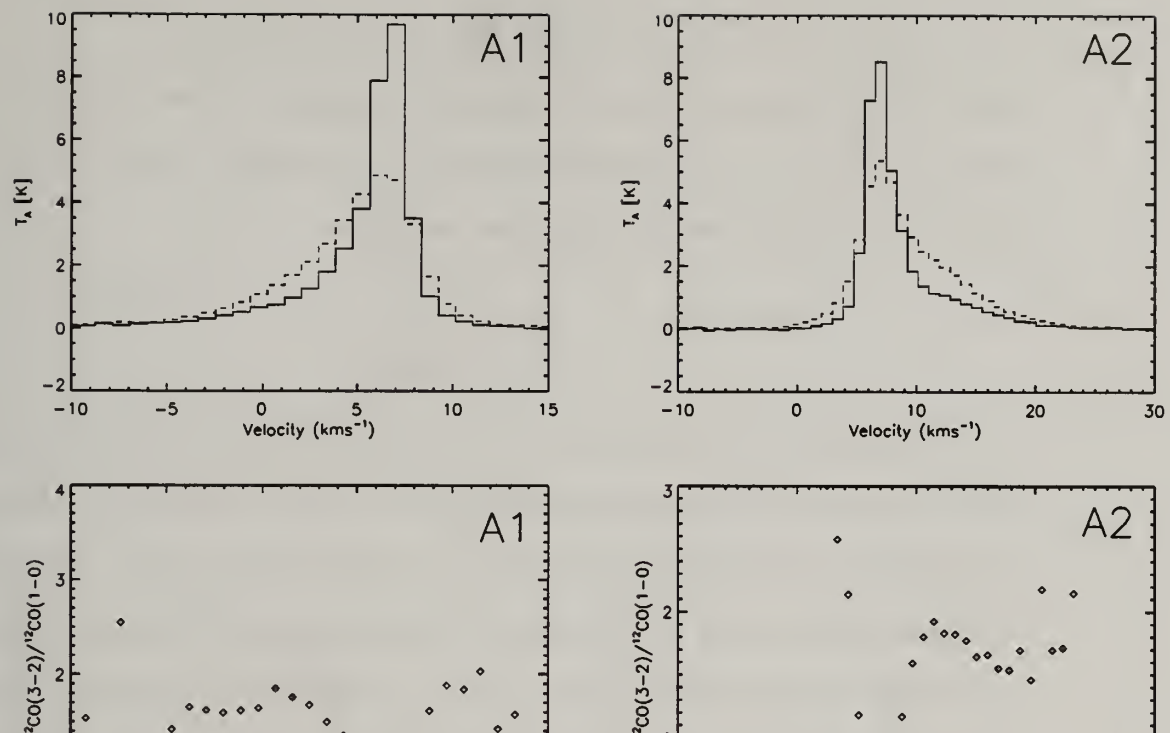

Figure 2.14 T_{ex} calculation : Average ^{12}CO J=1→0 and ^{12}CO J=3→2 spectra and their ratio. Upper panels show averaged ^{12}CO J=1→0 (solid line) and ^{12}CO J=3→2 (dotted line) spectra for A1 (left panel) and A2 (right panel) regions. ^{12}CO J=1→0 data are smoothed to the 0.9 km s^{-1} velocity resolution of ^{12}CO J=3→2 . In the lower panels, the ratios of the averaged ^{12}CO J=3→2 and ^{12}CO J=1→0 spectra are displayed. The weighted mean ratio in each region is computed using only filled points, i.e. in the line wings where lines are less optically thick.

With the increasing velocity, ratio R increases and becomes relatively constant at outflow velocities. The weighted mean ratio in region A1 from V_{LSR} of 2 to -9 km s^{-1} (blueshifted) is R= 1.69±0.16, and in region A1 from V_{LSR} 10 to 23 km s^{-1} (redshifted) is R= 1.71 ± 0.15. If we assume that the line wing emission is optically thin, and ignore the CMB background term in the radiation equation, the line ratio R between any two transitions, can be related to the T_{ex} as follows:

$$R = \frac{\nu_{J_2}^2}{\nu_{J_1}^2} exp(-\frac{h}{2kT_{ex}}[\nu_{J_2}(J_2+1) - \nu_{J_1}(J_1+1)]) \quad (2.1)$$

where J_2 and J_1 are the upper state quantum numbers of the two transitions, respectively: ν_{J_2} and ν_{J_1} are the frequencies for the two transitions. In the case of the ratio R of the J=3→2 and J=1→0 transitions, we derive:

$$T_{ex} = \frac{-27.7}{ln(R/9)} \quad (2.2)$$

If the emission were optically thin, then the excitation temperature for both regions A1 and A2 would be approximately T_{ex} = 16.5 K. However, if the gas is not optically thin, then this ratio provides only a lower bound to T_{ex}. For example, if the optical depth of the J=3→2 line of CO is of order 2, then the observed ratio would imply an excitation temperature of T_{ex} = 25 K instead of 16.5 K. In the next section we will show that over the most of the outflow velocity extent, the CO J=1→0 line has moderate optical depths (τ = 1–2), larger in the near line wings and slowly decreasing to higher outflow velocities. It is surprising that the ratio R is relatively unchanged as a function of velocity since the optical depth of the gas decreases at higher outflow velocities. Therefore if there is any change of T_{ex} with velocity, it must decrease from lower to higher outflow velocities. Although the ratio R provides only a lower limit to the excitation temperature, the optical depth is relatively small, so the excitation temperature is unlikely to be grossly underestimated.

2.3.2 Outflow Mass and Energy

Ideally, the mass of outflowing molecular gas should be determined using an optically thin line such as ^{13}CO or C^{18}O. However the emission in the rarer isotopic lines of CO is weak, and thus the spatial and velocity extent to which the outflow could be traced would be extremely limited. In early studies of outflows, the mass was often derived from ^{12}CO without corrections for optical depth. Even after it was recognized that the ^{12}CO emission in the outflowing gas was not optically thin, a single correction

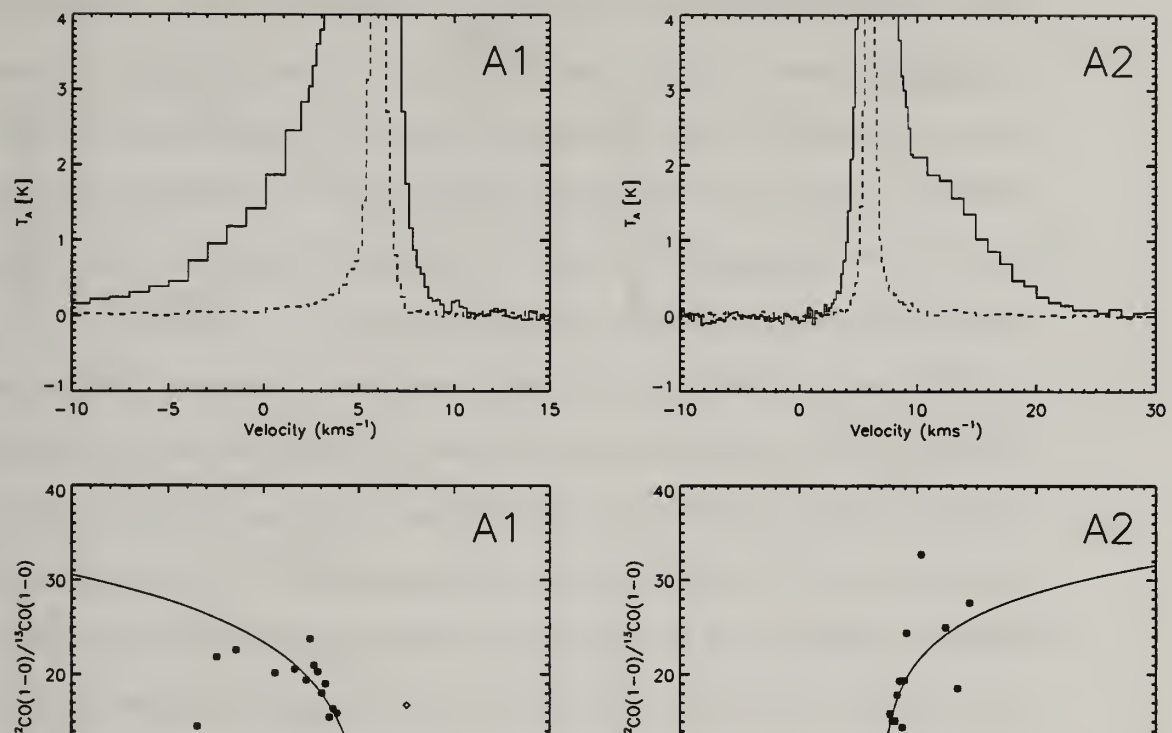

Figure 2.15 Optical depth estimates : Average ^{12}CO and ^{13}CO spectra and the fit to their ratio. The averaged ^{12}CO (solid line) and ^{13}CO (dotted line) spectra in A1 and A2 areas are shown in the upper panels. In region A1, for velocities larger then 2 km s^{-1}, we show spectra in full resolution, and for lower velocities, data are binned in 1 km s^{-1} bins. Similarly, in region A2, for velocities larger then 10 km s^{-1} data are binned in 1 km s^{-1} bins. The lower panels show the logarithmic fit to the ratio in the A1 and A2 regions respectively.

for optical depth was used at all velocities. More recently, Bally et al. (1999) and Yu et al. (1999) introduced a velocity dependent opacity-corrected column density approach, that has been used with modifications in many recent observational studies such as Arce & Goodman (2001a). This type of correction is essential for evaluating the outflow mass as a function of velocity.

Since an individual ^{13}CO spectrum does not have the signal to noise to detect the outflowing gas, we need to average over large regions of the outflow. This is the

same procedure as employed by Bally et al. (1999) and Yu et al. (1999). In each of the regions previously defined (see Figure 2.13), we average over the extent of the outflow emission and form an average ^{12}CO and ^{13}CO spectrum. For areas A1 and A2 these average spectra are shown in Figure 2.15. At velocities where both ^{12}CO and ^{13}CO are detected with at least 3σ certainty, we form the ratio (Figure 2.15). Similar results are obtained for A3 and A4 regions.

In Bally et al. (1999), Yu et al. (1999) and Arce & Goodman (2001a), they fit the ratio points with a parabolic function in order to extrapolate the optical depth beyond the velocity extent of detectable ^{13}CO emission. Examination of the ratio trends for regions A1 and A2 show that they would not be well fit by a parabolic function. The ratio remains flat in the high velocity wings, implying that the moderate optical depths persist to relatively large velocities. The largest measured ratios are $\sim$ 30, considerable smaller than the expected value of isotopic ratio of approximately 62 for optically thin lines (Langer & Penzias, 1993). Instead of a parabolic function, we have fit the ratio with a logarithmic function of the form: $R_{12/13}(v) = A\ln|B - v| + C$, where A, B and C are fitted parameters, and v is the velocity. This functional form fits reasonably well the variations in the observed ratio from the line core to the line wing velocities. Figure 2.15. We use the logarithmic fits to correct for the optical depth in ^{12}CO line.

We derive the column density of the gas in the outflow by a two step process. Assuming that ^{12}CO emission is optically thin we use the following equation, at each position:

$$N_{12}^{thin}(v) = 1.15 \times 10^{14} \frac{(0.36T_{ex} + 0.33) \int T^{12} dv}{e^{-T_0/T_{ex}}(1 - 0.15(e^{T_0/T_{ex}} - 1))} \qquad (2.3)$$

where T_0 is the value for $h\nu/k$, equal to 5.53 K for the ^{12}CO J=1$\rightarrow$0 line, and the velocity is in km s^{-1}. The derived optically thin column densities can then be

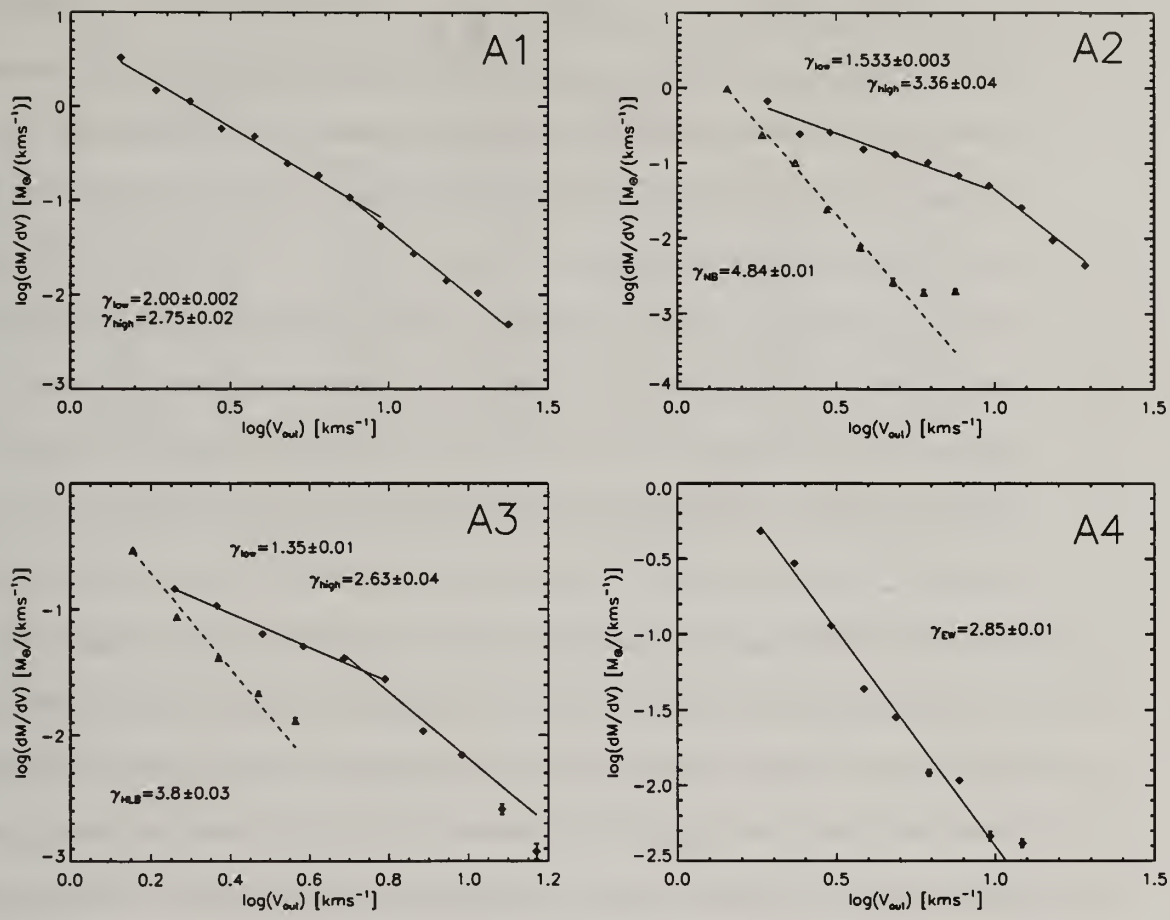

Figure 2.16 The mass-velocity distribution. For the outflows within each area A1-A4 in L1551. The $M(\mathrm{v})$ distribution is plotted as $\log(dM/d\mathrm{v})$ vs. $\log(\mathrm{v_{out}})$ where $\mathrm{v_{out}}$ is outflow velocity $\mathrm{v_{out}} = \mathrm{v} - \mathrm{v_{LSR}}$. The mass points are in velocity bins thet are uniformly spaced in log velocity (see text for more). For regions A2 and A3, we present data for both the blueshifted outflow (triangle points) and the redshifted outflow (diamond points) within these regions. The slopes of the linear fits (the power law index, γ) are indicated in the figure.

corrected for optical depth effects using the following expression:

$$N_{12}^{thick}(\mathrm{v}) = \mathrm{N_{12}^{thin}}(\mathrm{v})\frac{62}{\mathrm{R_{12/13}}(\mathrm{v})}. \tag{2.4}$$

where $\mathrm{R_{12/13}}$ is determine from the logarithmic fits as a function of velocity, and we assume an isotopic abundance ratio of 62.

The outflow mass as a function of velocity in each pixel is then computed from $M(v) = 2\mu m_H A N_{H_2}(v)$, where $\mu = 1.36$ is the mean hydrogen mass accounting for He and other molecular constituents, m_H is the mass of the hydrogen atom and A is the physical area of one pixel at the distance of the source. N_{H_2} is the molecular hydrogen column density obtained using the relation $N_{H_2} = 1.1 \times 10^4 N_{12}$ by Frerking et al. (1982) for the Taurus cloud; this result is consistent with more recent determinations, summarized by Harjunpää et al. (2004), for other nearby dark clouds. Table 4.1 summarizes our results for the mass of the outflowing gas in the various regions previously defined, tabulated for both $T_{ex} = 16.5$ K and $T_{ex} = 25$ K. Gas at velocities ≤ 5 km s^{-1} and ≥ 8 km s^{-1} is considered blueshifted and redshifted respectively. The total outflow mass in each area A1-A4, is obtained by summing up calculated mass over all outflow velocities. The total outflow mass in blueshifted and redshifted emission are denoted as BT and RT in the Table 4.1. The redshifted emission in A2, A3 and A4 do not overlap, so RT is simply the sum of all redshifted mass, momentum and energy of A2 R, A3 R and A4 R. However, there is some overlap of blueshifted emission in A1 B and A2 B (see Figure 2.13), which we have accounted for in our mass estimate labeled BT.

In Table 4.1, we also give estimates for total momentum $P = MV_{out}$, and kinetic energy, $E_K = 0.5MV_{out}^2$ in the molecular outflows. We have made no attempt to correct for the inclination of the outflow, so these are only lower limits to the true values of momentum and kinetic energy. Not correcting for the inclination of the outflow, will not affect the mass estimate, since accounting for the tangential velocity will only rescale the velocity axis. The highest uncertainty in the mass estimates, factor of 2, comes from the uncertainty in the N_{H_2} to N_{12} ratio (Frerking et al., 1982). In addition, the outflow mass at the lowest velocities, may have a contribution by the ambient cloud mass. The ambient cloud contamination will decrease with the outflowing velocity. We consider the outflow to start at $\sim$1.5 km s^{-1} from the host

Table 2.1. L 1551 Outflow Mass, Momentum and Energy Estimates

T_{ex}	25 K			16.5 K		
Lobe	Mass $M_\odot$	Momentum $M_\odot$ km s^{-1}	Energy $\times 10^{43}$ (ergs)	Mass $M_\odot$	Momentum $M_\odot$ km s^{-1}	Energy $\times 10^{43}$ (ergs)
A1 B	4.25	15.65	111.5	3.28	12.09	88.33
A2 R	1.40	7.46	60.7	1.08	5.76	46.80
A2 B	0.53	1.52	6.2	0.41	1.17	4.75
A3 R	0.34	1.46	8.6	0.26	1.13	6.63
A3 B	0.23	1.06	15.6	0.18	0.82	12.02
A4 R	0.59	1.92	9.82	0.46	1.48	7.57
BT	4.54	15.66	116.7	3.50	12.08	90.01
RT	2.33	10.84	79.12	1.80	8.37	61.00
Total	6.87	26.50	195.19	5.30	20.45	151.01
AC[a]	110		85			

[a]Ambient Cloud. Mass of the ambient cloud is estimated using T_{ex} determined in each spatial point from the ^{12}CO line thick condition. See text for more.

cloud's mean velocity both for the blueshifted and redshifted velocities. Therefore the effect of the cloud contamination to the low velocity outflow mass is minimal. The choice of the polynomial fit function, is a result of arbitrary choice, and although logarithmic function mimics the behavior of ^{12}CO to ^{13}CO emission ratio better than the parabolic function at the intermediate outflow velocities, it never reaches the thin limit and if ^{12}CO emission becomes optically thin we will overestimate mass at these highest velocities.

2.3.3 Mass-Velocity Power Law Dependence

It is well established that mass distribution within the molecular outflow has a power-law dependence on velocity, such that $M_{CO}(v) \propto v^{-\gamma}$ (see for e.g. Richer et al., 2000). Observationally the relation is typically obtained by calculating mass per velocity bin and plotting $\log(dM/dv)$ as a function of velocity offset $\log(v_{out})$ relative to the host cloud's mean velocity v_0 ($v_{out} = v - v_0$). In a log-log plot, the slope of the linear fit determines the γ index. The value of γ is an important test for proposed mechanisms of molecular outflow entrainment.

The mass spectra and derived power law indices for regions A1 through A4 are shown in Figure 2.16. We bin the data in velocity bins uniformly spaced in log scale. The velocity width for each point varies from 0.25 km s^{-1} on the left side of the plot to $\sim$ 5 km s^{-1} on the right side. This has the beneficial effect of increasing the signal-to-noise at high velocities, where the mass is decreasing. Propagation of error is carried out as mass points are binned together, and the error bars for each point are also plotted in the figure. The error bars represent the statistical uncertainty in the mass estimates that comes primarily from the rms noise in each measured spectra and uncertainty in the logarithmic fit parameters. There are also systematic errors such as the uncertainties in the excitation temperature, the functional form of the logarithmic fits to optical depths (Figure 2.15), and the uncertainty in the N_{H_2} to N_{13} (this latter uncertainty does not affect the slope of the $M(v)$ law). For low velocities, the errors are small enough that the error bars are not visible in Figure 2.16. Because the statistical errors are very small, but systematic errors could be large, we chose to fit the data to a straight line, assuming uniform weights for all points (Figure 2.16). If we used the statistical errors in the fit, the uncertainties at low velocities are much lower than at higher velocities, resulting in γ values with formally low uncertainties (typically $\lesssim 0.05$), but with large chi-square values in the fits.

In regions A1 and A2 (the blueshifted and redshifted lobes of the main flow), the dependence of $M(v)$ are best fit with two power-law relations (Figure 2.16). The break in the power law occurs at $v_{out} \sim 8$ km s^{-1} in A1 one and at $v_{out} \sim 10$ km s^{-1} in A2. The redshifted and blueshifted emission in the HL Tau region (A3) have slightly different $M(v)$ distributions. While the redshifted emission has a broken power law, the blueshifted emission extends to much smaller velocities, and shows a single, steep power-law dependence. The redshifted lobe of the EW flow (see region A4 in Figure 2.16), and its possible blueshifted counterpart (see the dashed line in region A2 of Figure 2.16) both show a single, steep power-law dependence. When

there is a broken power-law, the average slopes for the low-velocity and high-velocity portions of all outflows in the L1551 region are 1.63 and 2.92 respectively. These values are significantly lower than γ values reported towards other outflows in several recent papers (see §2.4.3 for a more detailed discussion on this point).

2.3.4 Cloud Mass and Energy

We determine the cloud mass by using the ^{13}CO map. The line center optical depth at each point in the map is derived from the ^{13}CO peak temperature. The excitation temperature is obtained at each position by solving the radiative transfer equation for the excitation temperature, assuming ^{12}CO line to be optically thick. The column density for the ^{13}CO J=1→0 transitions is calculated at each map point in the velocity range of 5 to 8 km s^{-1} . We find, the total mass of the cloud using this method to be 110 $M_{\odot}$, and is reported in Table 4.1 in the AC (ambient cloud) row. The newly estimated cloud mass is larger than the previous estimate of Moriarty-Schieven & Snell (1988) and in agreement with Sandqvist & Bernes (1980). The kinetic energy of the cloud is assumed to be the turbulent energy of the cloud, and is estimated using $E_{turb} = 3/(16ln2)M_{cloud}\Delta v^2$. Mean turbulent velocity of the ambient gas, Δv = 1.2 km s^{-1} is determined from several ^{13}CO line profiles in the cloud, as the full line width at the half maximum. We find that kinetic energy of the L1551 cloud is $\sim 8.5 \times 10^{44}$ ergs.

2.4 Discussion

2.4.1 Entrainment Mechanism for CO Outflows in L1551

The combination of optical Hα, millimeter and submillimeter CO data provides a more complete picture of the structure and kinematics of the molecular outflows in the L1551 region, allowing us to better investigate the driving mechanism of molecular outflows. Currently the two most promising models of entrainment of outflows are

the jet-driven bow-shock model and the wind-driven shell model. Numerous hydrodynamic and analytical models have treated both types of entrainment mechanisms and predict distinct morphologies for the appearance of the integrated intensity maps, position-velocity maps, and the mass-velocity power law indices (for examples see Smith et al., 1997; Zhang & Zheng, 1997; Lee et al., 2000, 2001; Ostriker et al., 2001).

One of the most distinctive observational characteristics of molecular outflows is the power-law dependence of flow mass with velocity, $M_{CO}(v) \propto v^{-\gamma}$. Usually, log(dM/dv) versus log(v) has a linear dependence, with a single power law index γ ranging from about 0.5 to 3.5, with the majority of observations indicating $\gamma \sim 2$ (Richer et al., 2000). At velocities larger than 10 km s^{-1} from the ambient cloud velocity, many outflows show a break in the power-law with higher velocities showing a steeper slope. The break at higher velocities might indicate that there are two distinct outflow components, perhaps corresponding to a recently accelerated component, and a slower-moving swept-up component. It also appears that the low-velocity power-law index of ~ 2 is the same for low-mass as well as high-mass objects, indicating that some common acceleration mechanism operates over several decades of stellar luminosity (Richer et al., 2000). There is also some indication, especially for high-mass objects that the slope, γ steepens with age (Richer et al., 2000). Thus, observations of γ and the occurrence of breaks in the power law could thus be used to constrain the driving mechanism in a given outflow. In turn, the trends seen in the mass versus velocity ($M(v)$) power laws of observed outflows can be used to refine the theoretical models of outflow entrainment. Accurate determination of the value of γ is thus quite important.

Numerical simulation of both jet- and wind-driven models (Lee et al., 2001) show that the power law index in $M(v)$ plots for jet-driven bow-shock systems ranges from 1.5 to 3.5, while the wind models yield smaller value of γ in the range of 1.3 to 1.8. In the jet-driven models, γ is a strong function of inclination, with lower values of

γ obtained when the outflow has larger angles of inclination to the plane of the sky. Zhang & Zheng (1997) show that power-law with break is produced for the jet-driven entrained gas.

Jet-driven bow-shock models show Hubble-law like features in the position-velocity plots with the highest velocities at the "hot spots" (head of the jet) and decreasing velocity trend toward the source (wings of the bow shock). The p-V structure is associated with the broad range of velocity near the bow tip while there is a small and almost constant velocity in the bow wings, often producing a convex spur structure along the jet axis at the highest velocities (Lee et al., 2000, 2001). Figure 20 in Lee et al. (2000) shows a strong dependence on inclination angle for the p-V diagram structure in bow shock model. In the case where several bow shocks are driven because of the presence of a pulsed jet, several spur structures can be seen in the p-V diagram. (see Fig. 7. Lee et al., 2000, HH 212). On the other hand, wind-driven entrainment mechanism do not show any evidence for spur features in the p-V plots; the p-V plots are typically parabolic in shape with the vertex of the parabola coincident with the location of the source. The morphology of the shape is somewhat inclination dependent, but the p-V plots are quite distinctive in appearance from that produced by jet-driven models.

In § 2.3.3, we report our results for the mass-velocity power laws. Our main result is that when there is a break in the power law, the power law slope for low velocities is shallow, $\gamma \lesssim 2$. The power law index for high velocities is $\gtrsim 3$ (see Figure 2.16).

The main CO outflow oriented at 50° from IRS 5 shows mostly jet-driven bow-shock features, but also shows some morphological features seen in wind-driven flows. The $M(v)$ plots for the blue and redshifted lobes (regions A1 and A2) of the main IRS 5 outflow show a power-law break as predicted by a jet-driven flow (see Figure 2.16). The millimeter and submillimeter p-V plots for IRS 5 (Figures 2.9 and 2.10) show multiple Hubble-law wedges, with spur-like features at the highest velocities (see

especially the submillimeter data in Figure 2.10). The blueshifted side of the CO J=1→0 p-V plot (Figure 2.9) might be interpreted as a parabolic feature, or it may be two Hubble like wedges adjacent to each other. But the redshifted side shows no evidence for any parabolic structure. A single convex spur-like feature is seen in the p-V plot on the redshifted side. The channel maps in Figures 2.5 through 2.8 show a morphology where the highest velocity emission is the most collimated, and is along the projected jet axis, and is often seen in the vicinity of HH objects, probably highlighting the interaction regions of shocks at the heads of the bow-shock interfaces of the underlying jet with the swept-up molecular material. The overall spatial morphology of the low-velocity gas in blue and redshifted lobes is roughly parabolic (see Figures 2.5 through 2.8), with the slower swept-up gas manifesting itself as limb-brightened shell-like features. It has been proposed that the entrainment mechanism itself may evolve in outflows, with the early stages being a collimated jet-driven flow, which in later stages evolves into very wide-angle wind (Velusamy & Langer, 1998; Richer et al., 2000). If so, the characteristics of both jet-like and wind-driven entrainment for the IRS 5 flow might be indicative of its relatively evolved stage as an outflow.

The EW flow on the other hand shows only jet-like features. The flow is highly collimated (see Figure 2.11), the $M(v)$ plots for both the redshifted western component and the possible blueshifted component (in the redshifted lobe of IRS 5 flow) show single sloped power law with steep power-law indices (γ = 3.1 and 4.5 respectively) indicative of jet-driven bow-shock entrainment. The p-V diagram for the EW flow (Figure 2.12) shows no parabolic features, but a low-intensity Hubble-like wedge ending in a broad spur at the tip. It is noteworthy that the $M(v)$ plot (see Figure 2.16) for the EW flow is quite distinct from that of the IRS 5 flow. As suggested earlier, it is possible that the EW flow is dynamically younger flow, driven from an hitherto undetected source close to the location of HH 102 at about the location of

the 850 μm peak emission seen by Moriarty-Schieven et al. (2006). Unlike the IRS 5 flow, no optical counterpart HH objects have yet been detected along the EW jet axis.

2.4.2 Sequential Star Formation in L1551?

The L1551 molecular core is an active star-forming region which harbors at least 2 small clusters of protostars, one centered in the IRS 5 and L1551 NE region, and another in the HL Tau region. These two mini-clusters are clearly undergoing active star-formation characterized by HH objects, optical and near-infrared jets. In addition, multi-wavelength surveys in mid infrared (Gålfalk et al., 2004), X-ray (Favata et al., 2003), optical and near-IR (Briceño et al., 1998), optical spectra (Gomez et al., 1992), and in Hα (Garnavich et al., 1992) have shown that the whole L1551 molecular core is surrounded by a halo of young stars in the Class II stage or older, indicating that star-formation activity has been ongoing in this region for at least a few million years. Here, we explore the possibility that the current epoch of star-formation activity in L1551 may be the result of sequential star-formation induced by the effects of the multiple outflows in the system.

The protobinary system in IRS 5 has two active jets. The current direction of either of these jets is not aligned with the $\sim 50^{\circ}$ oriented main CO outflow in this region, the latter being driven by the source(s) at IRS 5. At least at some point in the past, the predominant direction of the jets from the IRS 5 system was probably aligned with the bulk molecular outflow direction in L1551. It has been suggested that L1551 NE was formed in the swept-up shell of gas produced by the IRS 5 outflow (Plambeck & Snell, 1995; Yokogawa et al., 2003). L1551 NE is itself a multiple stellar system, and possesses optical jets, and is thought to power a large-scale HH flow including HH 454, HH 28 and HH 29 (Devine et al., 1999a; Hartigan et al., 2000). The evidence for a CO outflow from L1551 NE is not as clear-cut despite many observational attempts to

delineate the outflow, mostly because of its similar alignment and close proximity to the main flow from IRS 5. The high angular resolution interferometric observations of Plambeck & Snell (1995) and Yokogawa et al. (2003) show two symmetric CS structures, one eastward from IRS 5 near L1551 NE, and thought to be responsible for the formation of L1551 NE, and another near HH 102. As discussed before, with the presence of a 850 μm dust-continuum clump near HH 102 (Moriarty-Schieven et al., 2006), it is tempting to suggest that a similar triggering mechanism can be attributed to the EW outflow. It is possible that the same bipolar jet streaming eastward started the star-formation process in L1551 NE, and streaming westward, started the star-formation process in the clump near HH 102. This new driving source near HH 102 is maybe responsible for the EW flow. This new protostar is obscured in the HH 102 region, and the highly collimated CO outflow, and the jet-like characteristics of the EW flow are indeed consistent with a relatively young protostellar system. Follow-up high angular resolution observations of the HH 102 region would allow us to probe the possibility that there is a new embedded source near HH 102.

The evidence for sequential star-formation activity is further strengthened by some recent observations of the L1551 region. A new pre-protostellar clump, dubbed L1551-MC has been discovered near HH 265 Swift et al. (2005) using NH_3 observations, and later confirmed (Moriarty-Schieven et al., 2006) by 850 μm continuum observations. L1551-MC is located at the edge of HH 265, which may be a HH object at the end of a jet arising from a driving source within the HL Tau complex (see Figure 17 of Moriarty-Schieven et al. (2006)). It is possible that the next generation of star-formation in the L1551 molecular cloud could occur at the L1551-MC region.

2.4.3 Systematic Effects on Mass Spectra Slopes

The power law indices at both low and high velocities that we derive for L1551 are not as steep as some recent determinations of γ in other outflows. For example,

other groups have found $\gamma > 3.5$ (single power-law) for Circinus (Bally et al., 1999) and Barnard 5 (Yu et al., 1999), broken power-law with $\gamma \sim 2$ (low velocities) and $\gamma \gtrsim 5$ (high velocities) in OMC-2/3 (Yu et al., 2000), broken-power law with $\gamma \gtrsim 3$ (low velocities) and $\gamma > 6$ (high velocities) for HH 300 (Arce & Goodman, 2001a), broken power-law with $\gamma \sim 2.2$ (low velocities) and $\gamma \gtrsim 3.5$ (high velocities) for PV Cep (Arce & Goodman, 2002). These recent studies have reported systematically steeper power law indices than reported before, and when accompanied with a break in the power law, much steeper slopes at higher velocities. One common feature of these recent results with larger values of γ was that they employed a velocity-dependent opacity correction. In this work, we have employed a similar velocity-dependent opacity correction approach, but we derive smaller values of γ. Our results here seem to counter this trend towards larger values of γ. Does this indicate that L1551 is a different kind of outflow system than these other outflows? There are several systematic effects in the derivation of mass-velocity spectra that if not properly accounted for, can result in errors in the determination of γ. Below we consider these systematic effects to explain the difference in γ derived in this paper compared to some recent determinations of this quantity.

(1) The overall mass estimate at all velocities can be affected by the size of the outflow mapped. If high velocity portions of the outflow are missed in the mapping, the derived γ would be an over-estimate. Our study as well as the studies of Bally et al. (1999); Yu et al. (1999, 2000); Arce & Goodman (2001a, 2002) have mapped a larger area of the outflow lobes than most previous studies (primarily due to the higher sensitivities of receivers and the advent of OTF mapping). The size of the mapped region is probably not the cause of difference in derived value of γ.

(2) The exact form for the functional fit to the velocity dependent opacity correction can affect the slopes of the mass spectra. In the studies of Bally et al. (1999); Yu et al. (1999, 2000); Arce & Goodman (2001a, 2002), parabolic fits were used to

extrapolate the value of the ratio ($^{12}CO/^{13}CO$) beyond values where the ratio is well determined. We use a logarithmic function (see Figure 2.15) instead. The logarithmic function is a better fit to the variation of the ratio seen in our data, but it tends to be a more slowly varying function with velocity than the parabolic fits. This makes for larger corrections (more mass) for the higher velocity points, which in turn makes the mass spectral slopes shallower. It should be noted that, compared to earlier studies, our data have higher sensitivity even at higher velocities from the systemic velocity, and this leads to a better constraint of the $^{12}CO/^{13}CO$ ratio to much higher velocities. The variation of optical depth of CO in molecular outflows with velocity has not been well determined to high velocities. However, when high signal-to-noise ratio spectral data have been obtained towards high velocity molecular outflows, the ratio of $^{12}CO/^{13}CO$ seems to be slowly varying with velocity (Snell et al., 1984), as is seen in our study. As another example, in Figures 7(c) and 7(d) of Arce & Goodman (2002), it is seen that the ratio of $^{12}CO/^{13}CO$ seems to be actually flat, however, the authors use a parabolic fit. A parabolic fit is a much faster extrapolation function in velocity and predicts that the gas gets to the optically thin limit at lower velocity offsets from the systemic velocity.

(3) Previous studies of mass spectra apply a method of only using data which exceeds a specified threshold in rms value of T_A^*. For example, Arce & Goodman (2001a) used a 2σ threshold, while Bally et al. (1999) used a 1σ threshold. Figure 2.17 shows the effect of using a rms threshold in the determination of the mass spectra. The rms thresholding method preferentially rejects points at higher velocity channels, since those points have the lowest signal to noise, and hence do not meet the rms threshold. Because of this, mass is under-estimated preferentially at higher velocities, thereby artificially steepening the mass-spectral slopes.

The velocity-dependent optical depth correction used in Bally et al. (1999); Yu et al. (1999, 2000); Arce & Goodman (2001a, 2002) as also in this work does result in

more accurate mass determinations. In particular, not using the correction results in an under-estimation of the mass at especially lower velocities, artificially giving low mass-spectra slopes. On the other hand, care must be taken with the functional form of the fit of optical depth with velocity. Figure 2.17 shows the importance of using all the data or at least being aware of the effect that posing a specified threshold in rms value will have on mass spectrum.

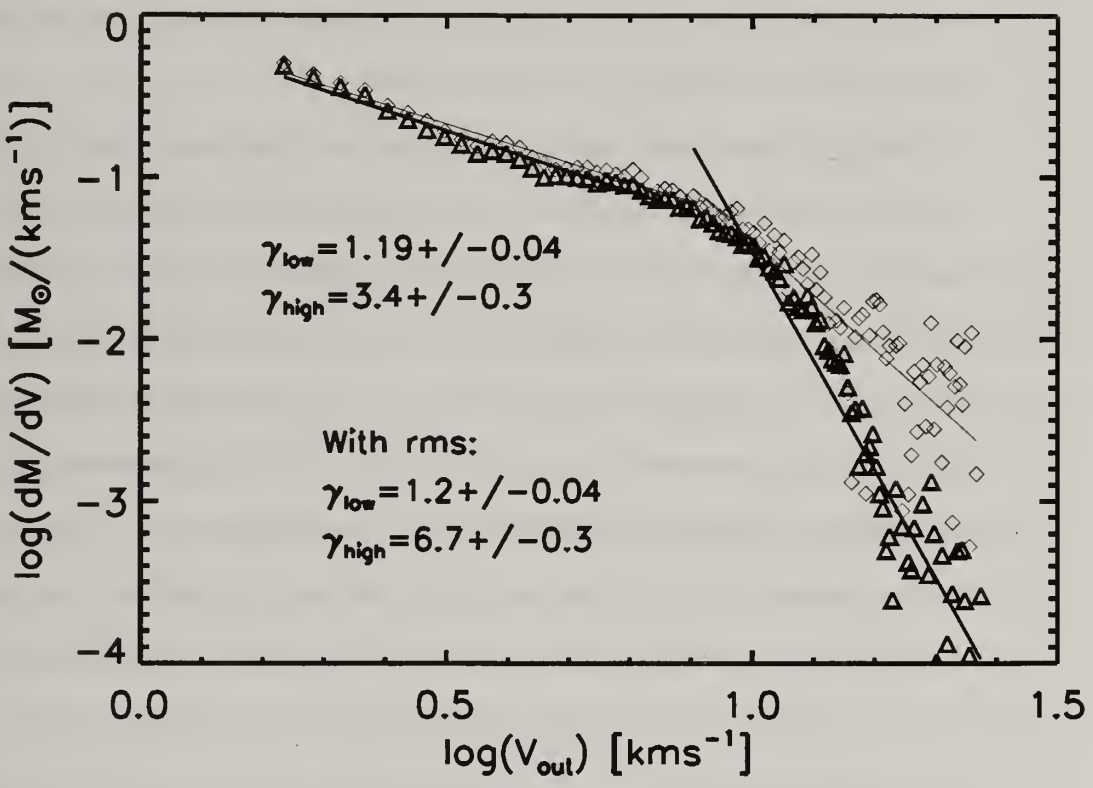

Figure 2.17 Mass-velocity slope dependance on rms threshold. The $M(v)$ relation derived for region A2 redshifted gas by using all the data without an rms threshold (diamonds), and by setting a threshold of 3σ for the ^{12}CO emission (triangles). We show fits to both $M(v)$ relations with broken power laws.

2.4.4 Combined Effect of the Outflows on the Cloud

The mass for the L1551 cloud estimated from the fully sample ^{13}CO map at line core velocities of 5 to 8 km s^{-1} is ~ 110 $M_\odot$. Outside of the line core velocities, the

total mass estimated in the outflow is $\sim$ 5.3 $M_\odot$ for T_{ex} = 16.5 K or $\sim$ 6.7 $M_\odot$ for T_{ex} = 25 K. Therefore the mass in the outflow is approximately 5-6.5% of the mass of surrounding cloud, depending on the adopted value for the T_{ex}. The total momentum and energy carried by the outflow, estimated from only the line of sight (radial) velocity, is 20 $M_\odot$km s^{-1}and 1.5×10^{45} ergs, respectively. It it usually assumed that the L1551 outflows have small inclination angles relatively to the plane of the sky, so there is a large inclination correction to the momentum and energy determinations. However, since the inclination angle is extremely uncertain, we will use the values quoted above as lower limits to the true values.

Many authors suggest that outflows provide a mechanism to regulate star formation by removal of the gas from star-forming regions, especially in the regions that lack massive stars (eg. Matzner & McKee (2000), and references therein). For the outflow entrained gas, to escape from the cloud, it must be moving at least at the escape velocity. Using a mass of 110 $M_\odot$ and $\sim$ 1 pc radius for the cloud, the escape velocity is calculated to be $\sim$ 1 km s^{-1}. If all of the momentum of the outflowing molecular gas was transferred to the cloud uniformly, then the gas would not escape. However, since outflows are highly collimated, momentum is transferred non-uniformly and much of the present outflowing molecular gas is likely to escape, unless it is slowed down by encounters with ambient gas. Our observations suggest that in fact the main blue lobe has broken out of the cloud near HH 256, and that their is insufficient column density of gas to slow the gas as it escapes. However, in the main red lobe, the molecular outflow is still well within the boundaries of the cloud and it remains to be determined if there is sufficient column density of gas to halt the outflow. Thus, the outflows are unlikely to disperse the entire cloud, but in local regions will be a major agent for disruption.

The total binding energy of the cloud is given by $\sim GM_{cloud}^2/R$. Using a cloud mass of 110 $M_\odot$ and $\sim$ 0.5 pc for the cloud radius, we find the binding energy to be

2×10^{45} ergs. Thus, the energy of the outflow 1.5-2×10^{45} ergs, is comparable to the binding energy of the cloud, even if no correction for the inclination angle is made. It has been suggested that parsec-scale outflows can be a source of energy to replace the energy dissipated in turbulence and thus provide the power to maintain the magnetohydrodynamic (MHD) turbulence (Li & Nakamura, 2006). The rate of turbulent energy dissipation can be estimated from equation (7) in Mac Low (1999). Assuming a cloud mass of 110 $M_\odot$ and a mean turbulent velocity dispersion of 0.45 km s^{-1} (estimated from the ^{13}CO line width), we find that the energy dissipation rate of turbulence in L1551 cloud is 0.003 $L_\odot$. Thus, if even a small fraction of the outflow energy could be coupled into cloud turbulence, the outflow could sustain the turbulence for over a million years, much greater than the lifetimes of molecular outflows.

We have shown that the molecular outflows contain substantial kinetic energy. However, the effect outflows have on their parent clouds depends on the efficiency in which momentum and energy can be transferred from the outflowing molecular gas to the surrounding cloud material. Currently, the observations are insufficient to answer this question, and there are no good theoretical models that address the effect outflows have on disruption of the cloud or on their role in replenishing the reservoir of turbulence energy in clouds. However, our work and several recent studies of parsec scale outflows, suggest that young stars, through the combined effect of their outflows, may have an important impact on the dispersal of their parent molecular cloud and to power turbulent motions.

2.5 L1551 Summary And Conclusions

All L1551 molecular outflows have been mapped at high sensitivities in the ^{12}CO and ^{13}CO J=1$\rightarrow$0 transitions. Follow-up submillimeter observations in ^{12}CO J=3$\rightarrow$2 emission towards a good fraction of the L1551 outflow system were carried out as well. The millimeter and submillimeter data are combined with large-scale, narrow band,

optical Hα images in order to perform a detailed study of the outflows in L1551. The main conclusions of the paper are summarized below.

1. The full extent of the main CO outflow is 32′ (1.3 pc), and is oriented at $\sim 50°$ position angle. The molecular outflow extent is similar to the optical extent of the flow seen by Devine et al. (1999a). Outflowing molecular material extends well beyond the last known HH object, HH 256 in the south-west, but stops short of HH 286 in the north-east. Our molecular line maps indicate that HH 286 has completely exited the L1551 cloud.

2. Most of the CO molecular outflow appears to be driven by source(s) in the IRS 5 region. Some features, especially in the redshifted lobe of the outflow may be attributed to outflows originating in L1551 NE and the HL Tau region.

3. Our maps cover a much larger extent of the collimated redshifted EW flow. The EW flow is ~ 0.82 pc in length, and is ~ 0.15 pc in width. In contrast to earlier studies, the sensitivity in our data reveals that the EW flow extends to high velocities (6.5 km s^{-1} to 20 km s^{-1}). It is suggested that a smaller extent blueshifted component seen in the main northwestern redshifted lobe is the blueshifted counterpart of the EW flow, and that the driving source for the EW flow is close to the location of HH 102.

4. We refine the procedure of velocity-dependent opacity correction adopted by recent authors to obtain a more accurate determination of outflow mass with velocity. The resultant mass-spectral power law indices are lower (less steep) than recently obtained indices towards other outflows. We attribute this systematic difference in power-law index to the better quality of our data, and the more careful approach we use in calculating mass. The resulting mass of the L1551 molecular cloud core is $\sim 110\ M_\odot$ and the combined mass of the outflows in L1551 is $\sim 7.2\ M_\odot$.

5. Even for no inclination angle correction, and lower T_{ex} assumption, the kinetic energy of the outflow is comparable to the binding energy of the cloud and there seems to be enough outflow energy to maintain turbulence in the cloud. Therefore the parsec scale outflow in L1551 has a potential of making a strong impact on the cloud's evolution and fate.

6. Multiple lines of evidence from $M(v)$ spectral indices, position velocity plots, and morphological appearance of our multi-wavelength data indicate that the EW molecular outflow is a good example of jet-driven bow shock entrainment. The main molecular outflow in L1551 shows evidence for entrainment from both jet-driven and wind-driven mechanisms.

7. We suggest that new stars are being triggered to form in the L1551 system as a result of the effects of the multiple outflows in the region.

CHAPTER 3

MOLECULAR OUTFLOWS IN L 1228 REGION

3.1 Introduction

The Lynds 1228 is a high galactic latitude dark cloud located in the Cepheus Flare molecular cloud complex. Although isolated, L 1228 is an active site of clustered low-mass star-formation (Bally et al., 1995). Extinction studies of field stars show that the Cepheus Flare has clouds at a variety of distances from 200 to 450 pc. Most previous studies of L 1228 have used a 300 pc distance to the cloud based on measurements of Grenier et al. (1989), however more recent study by Kun (1998) found a distance of 200 pc which we will adopt. The molecular outflow associated with L 1228 cloud, was discovered by Haikala & Laureijs (1989), and studied thereafter by Bally et al. (1995); Tafalla & Myers (1997); Arce & Sargent (2004). This outflow is parsec-scale, bipolar, with a well collimated blueshifted lobe and wide-angled redshifted lobe.

At least two embedded young stellar objects drive two separate HH outflows, a molecular hydrogen jet and a molecular CO outflow (Bally et al., 1995). One source is IRAS 20582+7724 (hereafter IRAS 20582) a low-luminosity (3-4 $L_{\odot}$), CLASS I protostar. IRAS 20582 drives the optical HH 199 flow whose full extent is nearly 1.2 pc (Bally et al., 1995), assuming a distance of 200 pc, oriented at a position angle of 60°. The blue HH 199 knots lie along an almost perfect line which coincides with the symmetry axis of blueshifted CO lobe, and based on that fact, Bally et al. (1995) postulated that IRAS 20582 drives both the HH 199 and the molecular outflow. High-

resolution interferometer observations show clearly that IRAS 20582 is the originating point for both blueshifted and redshifted molecular outflow (Arce & Sargent, 2004). In addition to HH 199, IRAS 20582 drives a second small flow detected in H_2 emission and oriented at a position angle of 100° (Bally et al., 1995; Hodapp, 1994). Correlation of density tracers, such as the CS J=2→1 line, with outflow geometry shows that the dense gas around IRAS 20582 is strongly perturbed by the bipolar flow and that outflow should significantly disperse the dense gas in the core by the time the outflow phase ends (Tafalla & Myers, 1997).

An optically visible star lies 1.5′ northwest from IRAS 20582 and drives the HH 200 flow which has an extent of $\sim$ 1 pc and is oriented at position angle 50°. Although knots of the HH 200 jet are found within the redshifted CO lobe, the orientation, location and kinematics of the HH 200 jet indicate that it is not part of the molecular outflow centered on IRAS 20582. Bally et al. (1995) measured the radial velocities of these HH 200 knots and found them to be in the range of -100 to -50 km s^{-1}. HH 199 and HH 200 both contain multiple HH knots. Spectroscopy was not obtained for all HH knots but Bally et al. (1995) distinguished on morphological grounds, three knots within the redshifted molecular outflow lobe that belong to the redshifted HH 199 flow.

The relation between the HH 199 and the H_2 emission flow, suggests that IRAS 20582 is possibly an unresolved binary, with each star driving its own outflow. Rodríguez & Reipurth (1996) searched for the binary companions and found two 3.6 cm sources. One VLA source was associated with IRAS 20582, while the other had no known counterpart but was located in the direction of the high extinction part of the L 1228 cloud. They could not conclude, whether the second VLA source (which had elongated emission along the H_2 flow axis) was due to a thermal jet or due to unresolved binary companions. More recently Arce & Sargent (2004) detected 2.7 mm dust

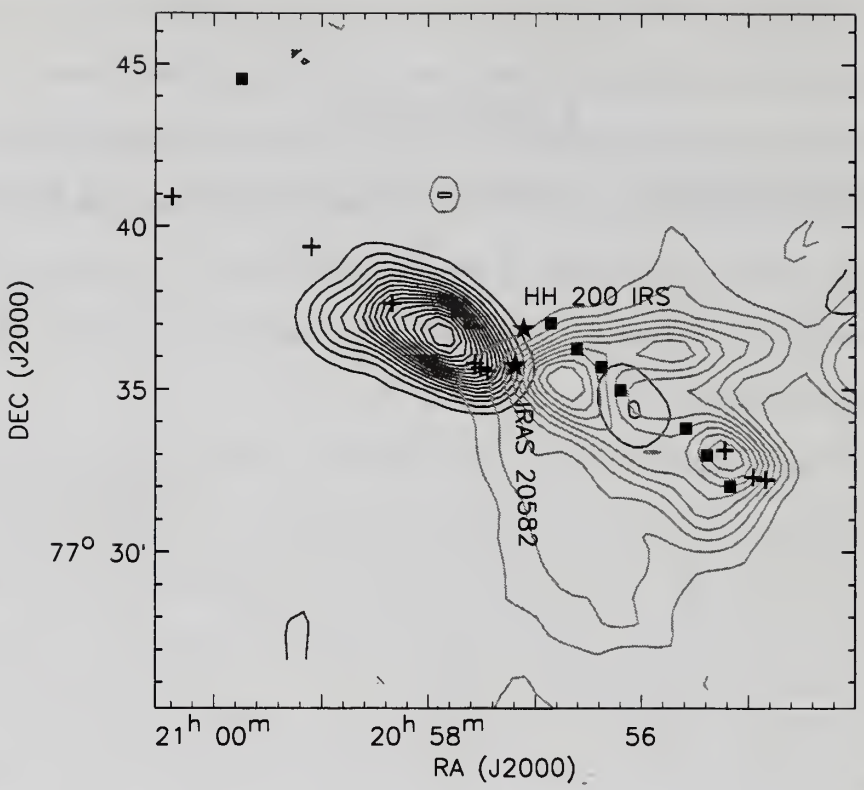

Figure 3.1 Molecular Outflow in L 1228. Integrated intensity ^{12}CO J=1—0 emission in L 1228. Blueshifted gas is integrated in velocity range of -16 to -9.5 km s^{-1}. Contours start at 2σ (1 Kkm s^{-1}) and go in steps of 3σ. Redshifted emission is integrated in velocity range of -6 to -2 km s^{-1}. Contours start at 2σ and increase in the same step (0.9 Kkm s^{-1}). Two stars represent two driving sources : IRAS 20582 and HH 200 IRS. Crosses are optically visible knots of the HH 199 object, driven by IRAS 20582, while filled squares are optically visible knots of HH 200 object, driven by HH 200 IRS. Labels will be kept on following two figures.

continuum peak about 5″ northwest from IRAS 20582 and associated with the dust envelope of binary companion.

3.2 Observations

As is the case of L 1551, a full mapping of ^{12}CO and ^{13}CO in the J = 1 → 0 transition has been performed in several observing seasons from 2001 till the end of 2002 year, with the SEQUOIA receiver at FCRAO 14 m telescope. The initial

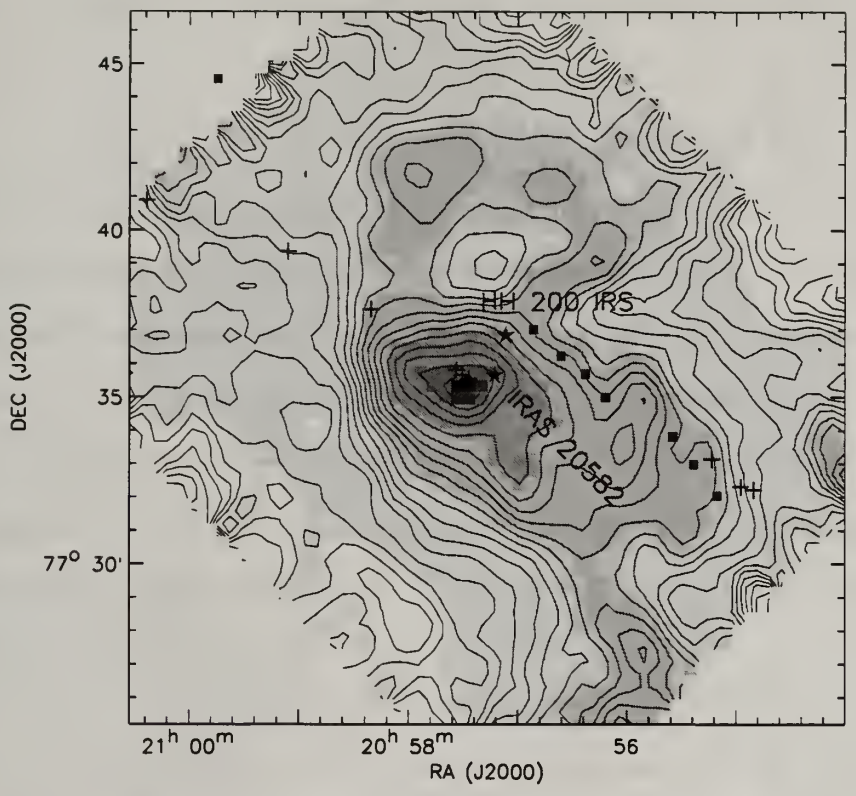

Figure 3.2 Molecular Core in L 1228. Integrated intensity ^{13}CO J=1→0 emission in L 1228 in -11 to -6 km s^{-1} velocity range. Contours start at 2σ (0.5 Kkm s^{-1}) and go in the same step.

observations were taken in 2001 using raster mapping mode in only the ^{12}CO J=1→0 transition, with channel spacing of 0.2 km s^{-1} and velocity resolution of 0.25 km s^{-1}. The later data were obtained in the on-the-fly (OTF) mapping mode using a dual channel correlator which permitted simultaneous observations of the ^{12}CO and ^{13}CO lines. Spectra obtained by OTF were checked for any scanning artifacts, baselined and resampled on to a grid spaced by the 22.5″, the spacing of the 2001 data. Spectrally the data were smoothed and resampled to the 0.2 km s^{-1} channel spacing of the 2001 ^{12}CO data. Antenna temperatures were corrected for the main beam efficiencies of 0.45 for ^{12}CO and 0.5 for ^{13}CO. The resulting mean rms per velocity channel is

0.49 K for ^{12}CO and 0.17 K for ^{13}CO. The antenna pointing and focus were checked and corrected every few hours using SiO masers.

3.3 CO Emission Morphology

The L 1228 molecular outflow emission with accompanying HH flows is plotted in Figure 3.1. This figure provides a good overview of the region, and we will go into more details of CO emission in the following two subsections. The total extent of the molecular outflow in the L 1228 cloud is 1 pc (see Figure 3.1). The outflow terminates short of the furthest HH knots on the blueshifted side. Two groups of HH knots are marked in Figure 3.1, the filled squares belonging to HH 200 flow and crosses for the HH 199. Also two stars are noted. The labels will be kept in the following figures.

3.3.1 Ambient Cloud Structure Traced by ^{13}CO

From the Gaussian fit to the mean ^{13}CO spectrum obtain by averaging data in 5′ area centered on IRAS 20582, we find that the ambient cloud rest velocity is -8.1 km s^{-1}. Figure 3.2 shows the integrated ^{13}CO line emission in the velocity range from -11 km s^{-1}to -6 km s^{-1}. For most of its spatial and velocity extent, ^{13}CO emission is thin and represents an excellent tracer of the column density in the cloud. In L 1228, column density peaks near IRAS 20582 and is elongated toward the blueshifted and redshifted molecular outflow lobes.

In Figure 3.3 we show in a series of maps in adjacent velocity intervals, the ^{13}CO emission associated with the L 1228 cloud. Due to enhanced sensitivity compared to previously published data by Tafalla & Myers (1997) we can better map the outflow traced by ^{13}CO molecule. At the highest blueshifted velocities shown, ^{13}CO emission is found in the blueshifted lobe of CO outflow, elongated along the axis of the HH 199 flow.

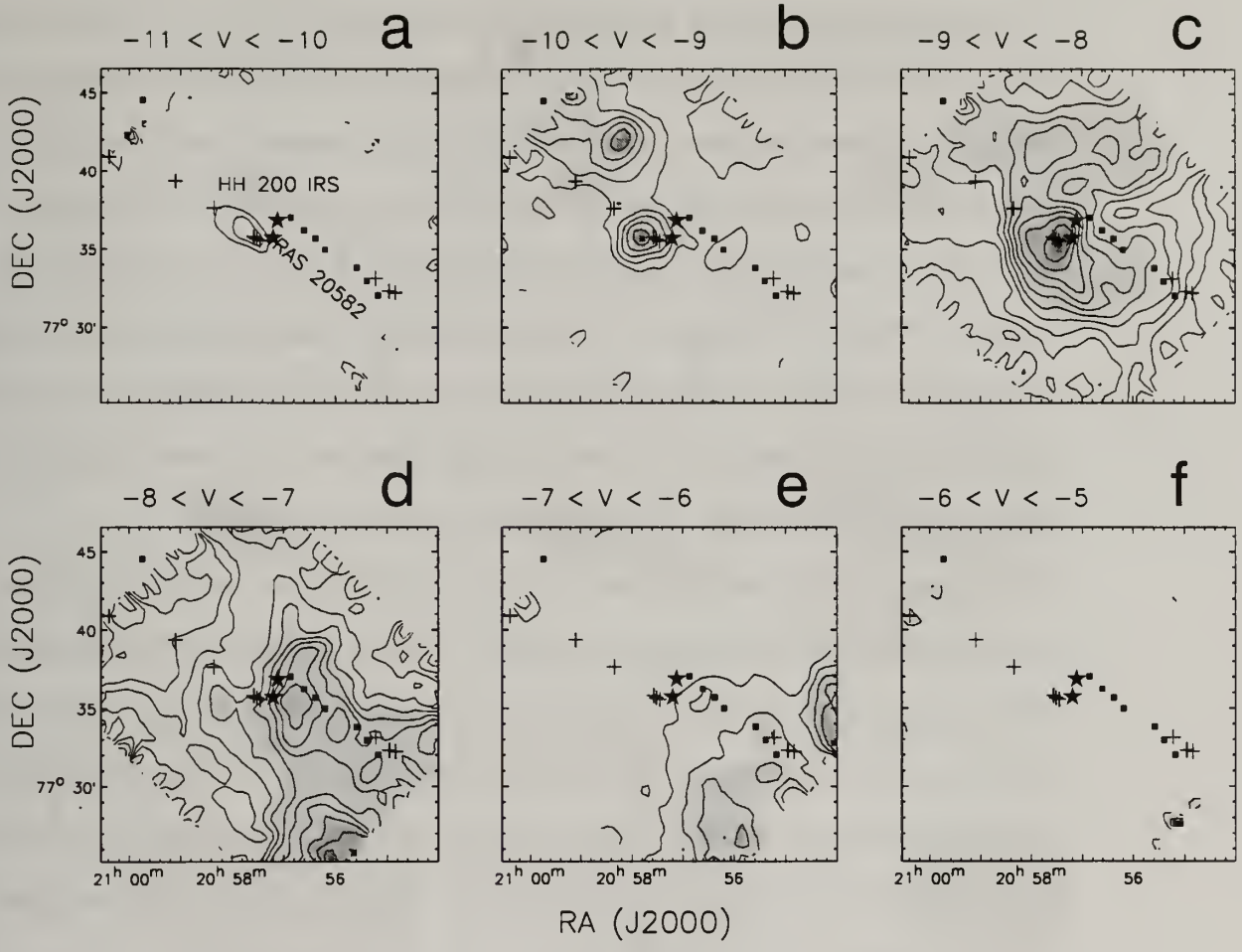

Figure 3.3 L 1228 Cloud Emission in ^{13}CO. Channel maps of ^{13}CO J=1→0 emission in L 1228. At panel *a* contours start at 0.15 Kkm s^{-1}, and go in the same step (2σ). In all other panels the lowest contour is 0.2 Kkm s^{-1}, and they go in 0.5 Kkm s^{-1} (*c*), and 0.35 Kkm s^{-1} (*b.d.e*).

In the velocity range from -9 to -10 km s^{-1}. Figure 3.3b. two strong column density peaks are detected. One column density peak slightly offsets from IRAS 20582, with the strongest emission coinciding with two HH 199 knots within blueshifted lobe of the outflow. The other ^{13}CO emission peak is located about 6′ north. Two CS density peaks identified by Tafalla & Myers (1997), spatially coincide with these two column density peaks, although there is a slight velocity offset for the northern peak. In addition a weaker emission component is found along the knots of HH 200 jet.

In the next two velocity intervals, Figures 3.3*c,d*, we trace the emission symmetrically distributed with respect to the ambient cloud velocity. The ^{13}CO emission in both velocity intervals peaks close to IRAS 20582. However, the bulk of the emission in each velocity interval reflects the sense of the outflow shown in Figure 3.1. In -9 to -8 km s^{-1}velocity range the emission is enhanced toward blueshifted lobe, while in -8 to -7 km s^{-1} emission is enhanced along the redshifted lobe of the outflow.

In Figure 3.4*e*, the ^{13}CO emission is extended and fan shaped, very different from the emission seen in the corresponding blueshifted velocities (Figure 3.4*b*), but mimicking the morphology of the redshifted outflow emission.

It is very rare to see ^{13}CO emission with such a strong outflow component as in this case. Bipolarity of the gas as traced by ^{13}CO has been reported and interpreted as the consequence of the outflow impact on the cloud core gas (Tafalla & Myers, 1997). The disruption of the core traced by ^{13}CO shows that not only the core gas is moving in the same sense as the outflow, but that corresponding blueshifted and redshifted ^{13}CO outflow lobes have the same collimation as the blueshifted and redshifted lobes of ^{12}CO emission.

3.3.2 Outflow Morphology Traced by ^{12}CO

In a series of panels shown in Figure 3.4, we plot the integrated ^{12}CO emission in different velocity intervals. The lowest contour in each panel is set at 2σ. In Figures 3.4*a,b,c*, the blueshifted lobe is very collimated, well aligned with the knots of the parsec scale HH 199 flow. IRAS 20582 lies near its edge. As mentioned in the introduction, the alignment of the HH 199 optical features and the molecular outflow supports the assumption that both are driven by the same source. It is also interesting to note that the HH 199 outflow axis of the blue lobe does not pass through IRAS 20582, but it has 30″ offset from the source toward south. The same is evident in the interferometric map of Arce & Sargent (2004), although the extent of their map

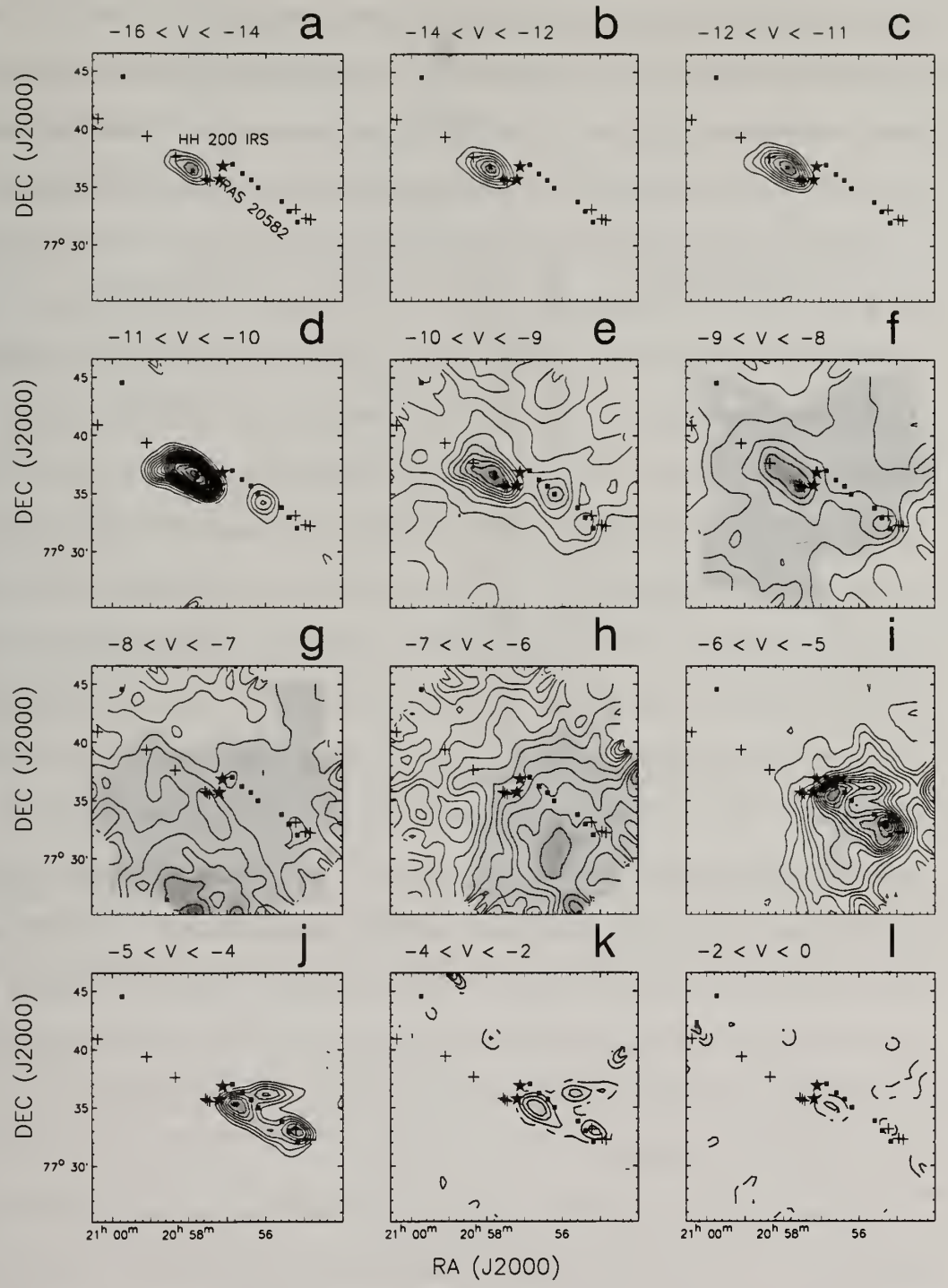

Figure 3.4 L 1228 Cloud Emission in ^{12}CO. Channel maps of ^{12}CO J=1→0 emission in L 1228. In each image contours start at 2σ (0.4 Kkm s^{-1} in unit velocity interval. and 0.6 Kkm s^{-1} in 2 km s^{-1}interval) and go in steps of 5σ in *e-f* and in steps of 2σ in all other panels.

covers only the first blueshifted HH knot (closest to the IRAS 20582). In their map this HH knots coincides with the peak of CO emission and is located within parabolic shell-like feature centered on IRAS 20582. In all panels where blueshifted emission is seen the molecular emission does not extent as far as the optical HH flow.

In Figure 3.4*d*. a second blueshifted emission peak appears in the redshifted lobe along the HH 200 jet axis or alternatively. as Tafalla & Myers (1997) noted. approximately half way between two knots of the HH 199 chain and IRAS 20582. Bally et al. (1995). associate this CO blueshifted feature with the flow from the HH 200 IRS because the HH knots of this flow are all blueshifted. Tafalla & Myers (1997) disagreed. and suggest that the second blueshifted CO emission peak is associated with the red outflow lobe rather than the blue HH 200 jet. They argued that the second blue feature is more extended and branches toward southwest and west. matching the distribution of the red lobe. In Figure 3.4*d* this western blue feature appears at the same location of HH 200 knots. where ^{13}CO enhanced emission was detected in Figure 3.3*b*. The southwest end of the HH 200 jet is its brightest Hα point. where a bright bow shock is seen (Bally et al.. 1995). In Figure 3.4*e* additional weaker ^{12}CO peak appears at the terminating point of HH 200 jet. where two HH 200 knots are found. In the next velocity interval. Figure 3.4*f*. only weaker CO peak at Hα bow shock remains of western blueshifted emission and is connected via CO weak feature with IRAS 20582 and HH 200 IRS. The emission in this velocity interval is confused with strong cloud emission.

Our maps clearly show that this second blueshifted feature is quite collimated and coincides with the HH knots of blueshifted HH 200 flow over their full extent. We do not see flaring of the blueshifted emission as discussed by Tafalla & Myers (1997). Consequently on purely morphological grounds it seems that the second CO blueshifted emission is entrained by the blueshifted jet of HH 200 IRS. If indeed. the blueshifted gas is a CO counterpart to HH 200 optical emission. there does not seem

to be an indication of a redshifted CO flow in our data. In the optical image a faint HH object, 9′ to the northeast of the driving source of HH 200, directly opposite the HH 200B6, has been detected (Bally et al., 1995) and assigned to the HH 200 redshifted jet counterpart terminating point.

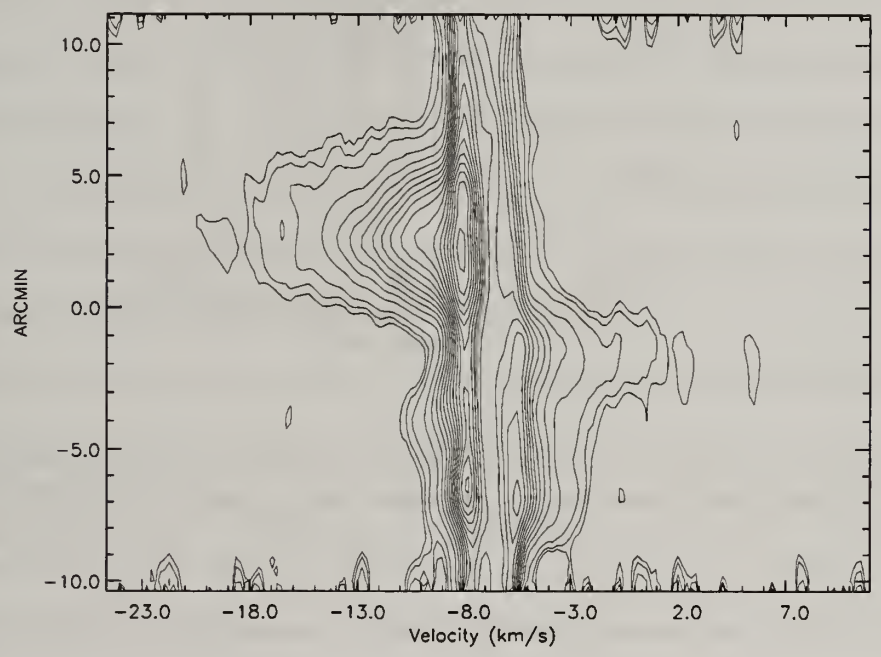

Figure 3.5 L 1228 ^{12}CO PV cut. Position velocity cut in ^{12}CO, with IRAS 20582 at the 0.0 position. The cut is along the position angle of 60° (HH 199 axis). The width of the cut is 4 pixels. Contours are 0.2,0.3,0.5,1,1.5,2.2.5,3.3.5,4,4.5,5. 5.5,6,6.5,7,7.5,8,8.5,9

At velocities between −8 and −6 km s^{-1}, the CO emission is dominated by the very extended ambient cloud emission, which is strongly self-absorbed over a large area (see Haikala & Laureijs (1989)). For this reason, little structure is seen in Figure 3.4*g,h* but there is a general trend for the ^{12}CO emission to move from the northeast to the southwest as the velocity increases, reflecting the influence of the bipolar outflow even at velocities close to the line center.

The low velocity redshifted emission in Figure 3.4*i* has a broad fan shape and is not as collimated as the low velocity blueshifted emission. The strongest emission forms two arms that diverge from IRAS 20582, one along position angle of 240° and

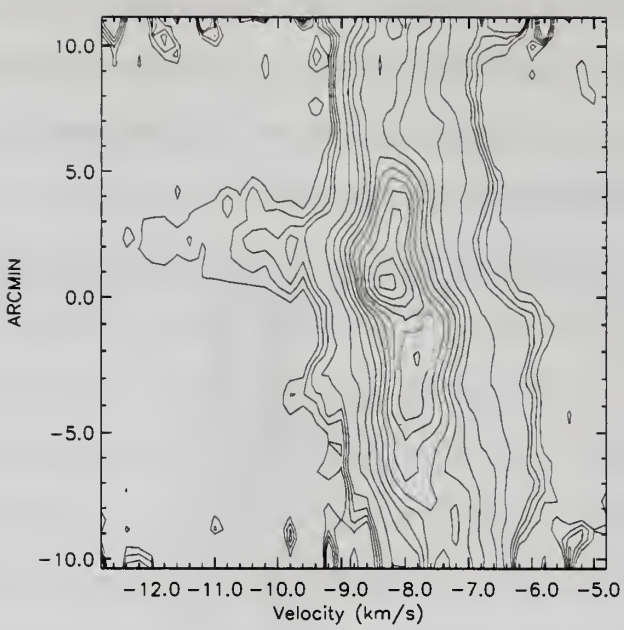

Figure 3.6 L 1228 ^{13}CO PV cut. Position velocity cut in ^{13}CO with IRAS 20582 at the 0.0 position. The cut is along the position angle of 60° (HH 199 axis). The width of the cut is 4 pixels. Contours are 0.2,0.3,0.4,0.5,1.1,5,2,2.5,3,3.5,4,4.5,5, 5.5,6

the other at position angle of 280°. The arm at position angle 280° is oriented close to the position angle of the H_2 jet detected from IRAS 20582. The other arm at position angle 240° is along the same axis as the collimated blueshifted lobe. It is interesting to note that western blue feature would partially fit between the two arms. At these velocities there appears to be an extension toward west of redshifted emission along the 280° arm that although strong feature is at the map edge Figure 3.4*i*. We checked for this feature in the larger map of Cepheus Cloud Complex (Chris Brunt private communication) and such a strong emission is not present in their data. Therefore we believe that the edge feature is not real, but an artifact introduced by our contouring routine.

At higher velocities (Figures 3.4*j*,*k*) the emission is restricted to the two arms. The highest velocity emission is found closest to the IRAS 20582 in the Figure 3.4*l*. Overall, compared to the blueshifted lobe redshifted lobe is poorly collimated, lower

velocity, and its emission drops quickly in intensity. Such a striking morphological difference between two lobes of the outflow may be best understood as the consequence of the differences in the ambient gas distribution in each lobe.

In Figures 3.5 and 3.6 we show PV cut along optical flow axis at position angle 60° with IRAS 20582 at 0.0 position in ^{12}CO and ^{13}CO respectively. The S-symmetry for the gas in Figure 3.6 shows that the bulk of the gas has a small acceleration. In addition, a fraction of the ambient gas is accelerated to larger outflow blueshifted velocities. The ambient component in the ^{12}CO PV cut is significantly enhanced over the whole extent of the outflow, reaching 5 km s^{-1} width compare to the 2 km s^{-1} observed toward the L 1551 redshifted lobe.

In Figure 3.5 substantial overlap between redshifted and blueshifted emission is present suggesting that the flow is inclined to the plane of the sky. The same can be seen in Figure 3.1 and Figure 3.4*i*. Although both blueshifted and redshifted lobes have velocity field showing Hubble-like structure (i.e. increasing velocity with increasing distance) the blue- and redshifted flows have distinct PV features. First velocity increase is steep, and there seem to be constant velocity present along the major part of the outflow extent. The maximum velocity in the blueshifted lobe is observed over 5′ spatial scale and it is reached at several arcmin from the IRAS 20582. The highest redshifted emission is detected close to the IRAS 20582 source, with intermediate outflow velocities observed along the whole spatial extent of the outflow. Similar PV diagrams have been observed in the velocity gradient sensitive tracer C_3H_2, which showed no significant velocity change along the lobes of the outflow, but sudden transition in velocity around IRAS 20582, much larger that the velocity gradient for typical core (Tafalla & Myers, 1997).

In the ^{12}CO PV cut the presence of the blueshifted outflow from HH 200 is noted around -4′ from the IRAS 20582. The gas in HH 200 flow is accelerated to smaller velocities compared to the IRAS 20582 blueshifted gas.

3.4 Mass and Energetics Analysis

The IRAS 20582 outflow is detected in both ^{12}CO and ^{13}CO lines. Although the ^{13}CO emission is optically thin and therefore is a good tracer of the outflow mass, the spatial and velocity extent to which the outflow can be traced are somewhat limited. Since more abundant ^{12}CO isotope is usually optically thick, we need to correct for the optical depth in the thick tracer in order to use it as a mass tracer. As discussed in the L 1551 case, the best approach to estimate mass along the outflow is to use both lines. The first step is to estimate the optical depth from the ratio of two lines in each velocity bin. Then estimate outflow mass from the stronger, more extended and more optically thick tracer. Finally, correct the estimated mass, using the line ratio.

Since an individual ^{13}CO spectrum does not have the signal to noise to detect the outflowing gas, we need to average over large regions of the outflow. We constructed an average blueshifted and redshifted spectra making the following assumptions. For the blueshifted gas we found the integrated intensity in each spatial point of the ^{12}CO map in the velocity range from -16 to -10 km s^{-1}. We then select, in both ^{12}CO and ^{13}CO data cubes, only spectra at the location where integrated ^{12}CO intensity in the given velocity range is at least one third of the maximum integrated intensity. For the redshifted gas we applied the same approach using the velocity interval -6 to -2 km s^{-1}. The idea behind this approach is to select spatial locations that most contribute to the CO outflow emission. To increase the signal to noise ratio in the line wings, we smooth the data in 1 km s^{-1} wide velocity intervals, at velocities more negative than -12 km s^{-1} and at velocities larger than -4.5 km s^{-1}. The resulting spectra are shown in Figure 3.7.

The ratio of ^{12}CO^{13}CO emission in the average spectra, $R_{12/13}(v)$, is plotted in Figure 3.8. The variation of the ratio with velocity is quite different in the blueshifted and redshifted lobes. The ^{13}CO emission is stronger in the blue lobe and the ratio

can be traced to higher outflow velocity. As in the case of L 1551 the best fit to this distribution is logarithmic fit of the $R_{12/13}(v) = A\ln|B - v| + C$ form. where A, B and C are fitted parameters, and v is the velocity. We use this logarithmic fit to correct for the optical depth in ^{12}CO line in the blue lobe. The logarithmic function will not reach the thin limit over the velocity extent of the outflow. To check if this is consistent with the data we find the ratio of ^{12}CO to ^{13}CO integrated intensity beyond the last detected ratio point (at -13.5 km s^{-1}. Figure 3.7). The ratio of integrated intensities in the -14.5 to -13.5 km s^{-1} velocity range is 64 $\pm$ 51. In the larger velocity interval, from -19 to -13.5 km s^{-1}, the ratio is 85 $\pm$ 85. With such results for the ratios, we are uncertain if the logarithmic correction for the optical depth is the best approximation in the outer wings of ^{12}CO line.

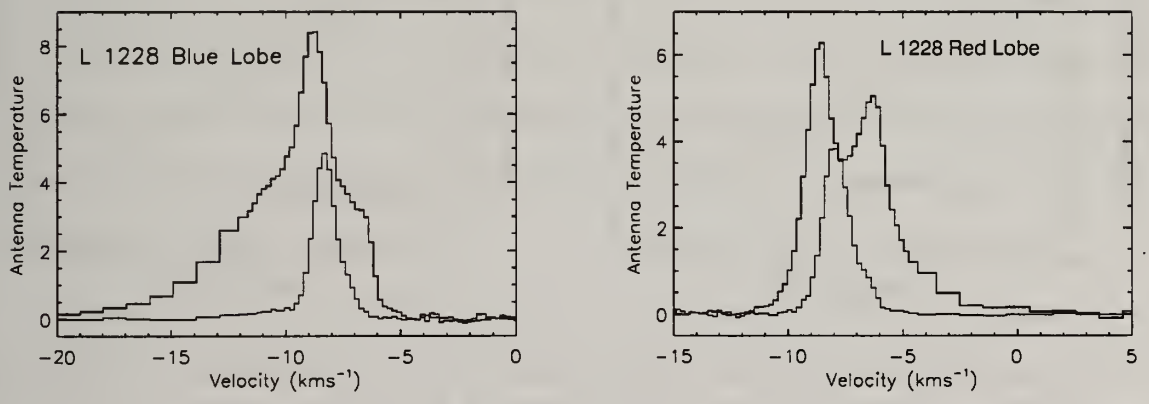

Figure 3.7 L 1228 Blue and Red lobe Averaged Spectra. Spatially averaged ^{12}CO and ^{13}CO spectra in the blueshifted and redshifted lobe of the L 1228 cloud. Spectra are shown in their full velocity resolution in -12 to -4.5 km s^{-1}, and with binned to 1 km s^{-1}velocity been at smaller (larger) velocities in the blueshifted (redshifted) lobe.

In the case of redshifted lobe, there are only few ratio points in the line wing and they all have a similar value. The averaged ^{12}CO spectrum in the red lobe is dominated by self-absorption feature with peak emission around -6 km s^{-1}, while ^{13}CO shows very little of wing extent. All five line wing ratio points are near the self-absorption peak. Therefore we fit this data distribution with the parabolic func-

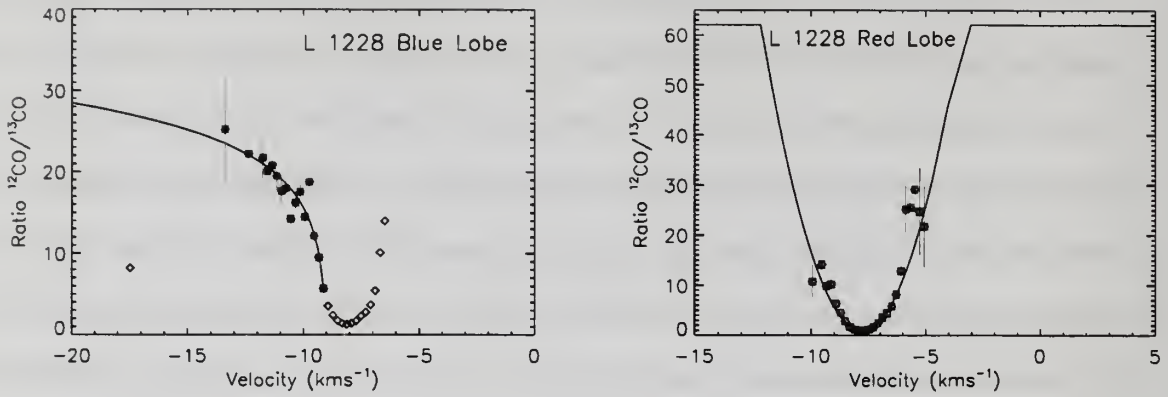

Figure 3.8 L 1228 Blue and Red Ratio Fit and MV. Logarithmic and parabolic fit to the line ratio of ^{12}CO to ^{13}CO averaged spectra in blueshifted and redshifted lobes respectively

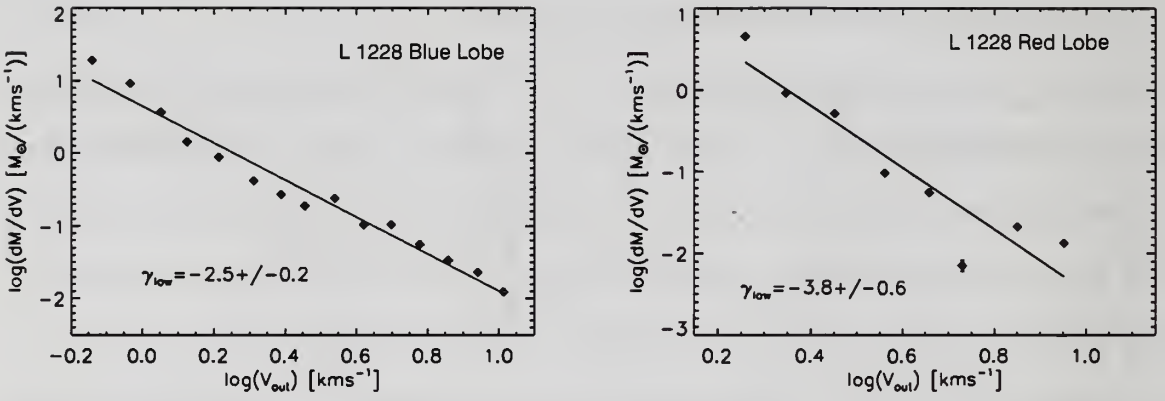

Figure 3.9 L 1228 Blue and Red MV. Mass velocity relation over the velocity range traced as outflow emission in ^{12}CO tracer for blueshifted lobe and combining ^{12}CO and ^{13}CO to determine mass in redshifted lobe (Table 3.1).

tion. This function will reach thin limit (isotopic ratio = 62) very quickly. To check the validity of such approach, we made estimates of the optical depth in a broader velocities interval. We find the ratio of ^{12}CO to ^{13}CO in the -5 to -4 km s^{-1} range to be 56 $\pm$ 33. This means that ^{12}CO really approaches thin limit at velocities higher then -4 km s^{-1}and parabolic fit extrapolation at higher velocities is in agreement with the data.

To derive the column density of the gas in the outflow we follow the process outlined in the L 1551 case: assuming that ^{12}CO emission is optically thin we estimate

thin mass. We then multiply the thin mass by $\frac{62}{R_{12,13}(v)}$ to correct for the optical depth. We use the same assumptions for the relative molecular abundance ratio of CO/H_2 as in the case of L 1551.

In addition, to reduce the underestimate of the redshifted outflow mass by completely ignoring inner wing velocities, we estimated mass in the in the -10 to -9 and -7 to -6 km s^{-1} velocity range using ^{13}CO line and assuming that its emission is thin at these velocities. In the redshifted lobe this is additionally motivated by the presence of heavily self-absorbed ^{12}CO line profile in this velocity range, which if used would greatly underestimate the mass.

The resulting mass is calculated for the excitation temperature of 10 and 25 K and presented in Table 3.1. In the same Table we present the results for the momentum and energy in the outflow assuming 25 K excitation temperature and accounting only for the line of sight velocity component. Although the resulting outflow mass varies greatly with the velocity range adopted for the calculation, the energy and momentum are less affected since the bulk contribution to the total momentum and energy comes from gas at higher velocities.

Mass distribution within the molecular outflow has a power-law dependence on velocity, such that $M_{CO}(v) \propto v^{-\gamma}$ (Richer et al., 2000). In a log-log plot, the slope of the linear fit determines the γ index. We find $\gamma = 2.5 \pm 0.2$ for the blueshifted gas, and $\gamma = 3.8 \pm 0.6$ in the redshifted lobe, Figure 3.9. As an additional exercise, we split red lobe into two subregions along two arms diverging from IRAS 20582, but no qualitative difference has been observed in mass distribution neither between two regions nor comparing each of them to the combined redshifted m-V law presented here.

3.4.1 Cloud Mass

We determine the cloud mass by using the ^{13}CO map. Figure 3.3d. The line center optical depth at each point in the map is derived from the ^{12}CO and ^{13}CO peak temperatures. The excitation temperature is obtained at each position assuming ^{12}CO is optically thick and using the peak intensity. We find, the total mass of the cloud using this method to be $\sim$ 108 $M_{\odot}$. The cloud mass estimate is free from the second core contamination identified in Figure 3.3*b* contamination. since we only searched for peak CO emission in the narrow velocity range around VLSR. Since ^{12}CO line is heavily self-absorbed. as seen in Figure 3.7*b* and extensively discussed by Haikala & Laureijs (1989), the cloud mass estimate is most likely the lower limit of the true mass.

3.5 Discussion

3.5.1 Multiple Outflows In L 1228

We discussed in §3.2 the presence of the blueshifted emission within the redshifted lobe of the IRAS 20582. Using morphological arguments, we suggested that this latter blueshifted emission is not related to the IRAS 20582 flow. but instead related to the HH 200 flow. If this suggestion is correct. then the molecular outflow associated with HH 200 is one-sided as there is no evidence for the redshifted counterpart.

It has been argued that there may be more then one outflow associated with IRAS 20582 source due to precession of its jet caused by the interaction with its binary companion Bally et al. (1995). One primary reason for conjecturing precession is the misalignment of the H_2 jet knots with the HH flow axis and the alignment of H_2 jet with the northern arm of the redshifted CO emission. Arce & Sargent (2004) show 2.7 mm continuum peak at about 5″ northwest of IRAS 20582. which they associate with a binary component. However, they argue that there is no indication that the binary companion drives its own flow and that the interactions in the binary pair are

not on a required timescale to produce jet orientation variations to account for the observed morphologies.

Our CO maps. show the fan-shaped morphology of the redshifted lobe and quite collimated blueshifted lobe. Although they differ from each other. the morphologies of both lobes are not inconsistent with a single driving source. Therefore we have assumed that IRAS 20582 outflow is a single outflow driven by the single protostellar source and that is how we analyzed our mass-velocity and position-velocity data in previous sections.

3.5.2 Entrainment Mechanism Of IRAS 20582 Outflow

The results of Arce & Sargent (2004) give us an opportunity to connect our parsec-scale data of the outflows to the arcsecond environment around the IRAS 20582 traced by the high-resolution interferometric observations. see Figure 3.10. On this small scale blueshifted and redhifted lobes are quite similar. symmetric with respect to IRAS 20582 and both have a wide-angle morphology with limb-brightened shells around outflow cavities. The interferometric map also shows evidence for the higher velocity gas along the axis defined by BC1 and RC1 knots in Figure 3.10, which are within CO cavities. along the symmetry axis of the limb-brightened shells. The mass probed by this interferometric data is very small compared to the total mass of the outflow and accounts for less than 1% of the outflow mass. Most H_2 knots superimposed on the interferometric map are within the CO parabolic shell structure and both H_2 and CO morphologies on the arcsecond scale are fully consistent with the common entrainment by both wide-angle wind and jet component emerging from the IRAS 20582.

On the parsec scale however, the blueshifted and redshifted lobes of the IRAS 20582 outflow differ with respect to their morphological appearance (Figures 3.1. 3.3. 3.4).

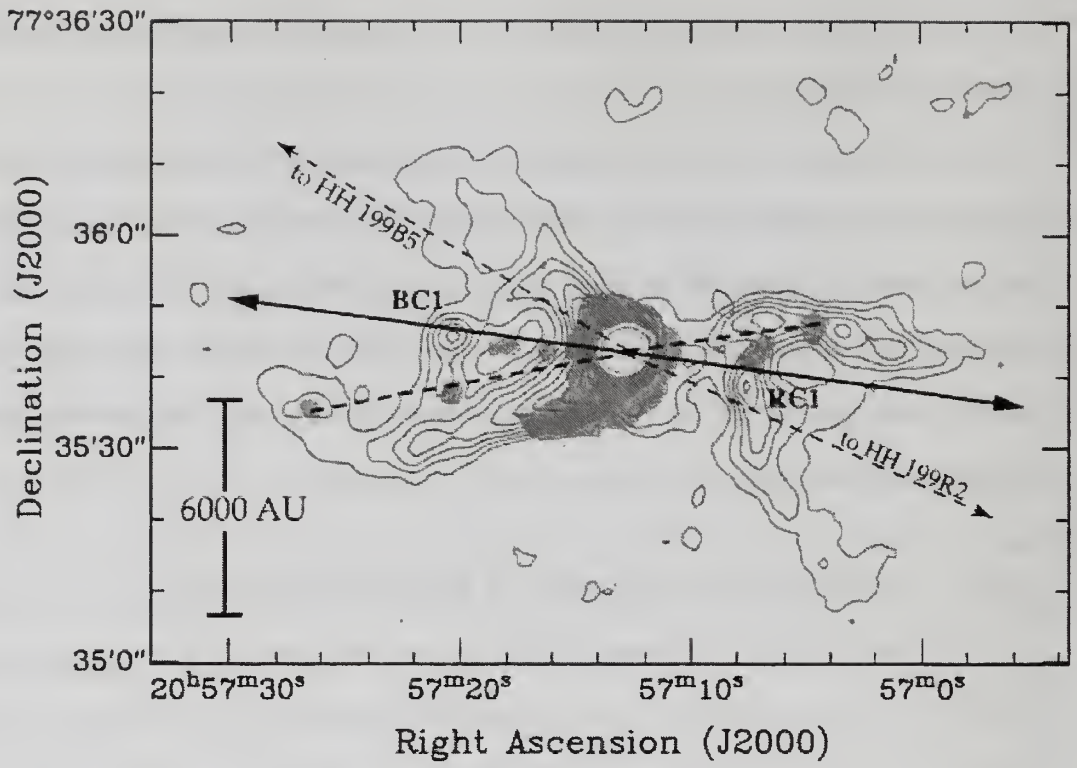

Figure 3.10 Interferometric Map of IRAS 20582 outflow. Figure 2 from Arce & Sargent 2004, which shows the outflow in L 1228 using high-resolution interferometric data. Blue (red) contours represent the blueshifted (redshifted) emission. White contours show the 2.7 mm continuum emission surrounding the protostar IRAS 20582. The H_2 S (1) 2.122 μ m emission in the region (from Bally et al. (1995)) is shown in gray. The dark solid arrow represents the axis of the observed molecular outflow. The dashed lines show the direction (from the source) to the emission knots (optical or near-IR) of the L 1228 flow with the most extreme angles. The dashed lines (with no arrows) connect the position of the source to the southernmost (in the blue lobe) and the northernmost (in red lobe) H2 knots. The dashed arrows show the direction toward the northernmost HH knot in the blue lobe (HH 199B5) and the direction toward the southernmost HH knot in the red lobe (HH 199R2). The outflow clumps BC1 and RC1 are identified.

kinematics traced by PV cut (Figure 3.5) and mass distribution of the swept up gas traced by the γ slopes of M-v relation (Figure 3.9).

The redshifted CO emission on the parsec scale has fan shaped morphology at the lowest velocities, and splits into two arms that diverge from IRAS 20582 at slightly higher velocities (see Figure 3.1). Overall its morphology is similar to the one observed on the arc-second scale. On the contrary, the parsec scale map of blueshifted

CO outflow shows a collimated quasi-elliptical lobe morphology. The originally east directed blueshifted lobe of the outflow is redirected toward the northeast near the first HH 199 blue knot. The axis that connects all the knots of blueshifted HH 199 has an offset from IRAS 20582 and from the H_2 jet axis. It is also different from the position angle of the axis connecting IRAS 20582 with two knots of redshifted HH 199. The opening angle of the blueshifted lobe on the arcsec scale is 80° compared to much smaller opening angle of the large scale CO outflow (see Figure 3.1).

The column density in the L 1228 core is distributed in such way that it peaks in the blueshifted lobe near IRAS 20582, Figure 3.2. At this point two HH 199 knots are found (HH 199B1 and HH 199B2), and this is where the blueshifted lobe redirects toward the north-east. However, in the blueshifted lobe after HH 199B3, a rapid decrease in the column density is noted along the outflow axis and laterally. In the redshifted lobe substantial column density is present over the larger lateral extent of the core. Therefore there may be just more gas in the redshifted lobe to entrain laterally and that would explain its wider morphology at the lower velocities compared to the blueshifted lobe. In addition, the steeper column density gradient in the blueshifted lobe close to the IRAS 20582 may play a role in collimating the originally wider flow into a more collimated flow on the larger scale. It is likely for the outflow driving wind to change its direction when interacting with the ambient medium and this might explain the resulting morphology of the blueshifted lobe.

Examining the channel maps of L 1228 region, we see that the highest velocity ^{12}CO gas is very collimated and extends between HH 199B1 and HH 199B3, suggesting that the CO emission is entrained through the same mechanism as the different knots of the HH 199 (see Figure 3.4*a.b.c*). Although, redshifted lobe has a fan shaped, low-collimated morphology at the low-velocities, comparing the symmetric higher velocity intervals with respect to the ambient cloud rest velocity, Figures 3.4*d.j.* we see that the major entrainment in the redshifted lobe takes place along the same position

angle as in the blueshifted lobe. The channel maps of the ^{12}CO emission show the highest velocity in both lobes along the jet axis delineated by the HH 199 knots. In addition, a falloff in the speed away from the jet axis is present.

The PV diagram for the blueshifted and redshifted outflow lobes of the IRAS 20582 source, show somewhat different appearances, Figure 3.5. While both of them show increase in the velocity further from the IRAS 20582, the maximum velocity in the red lobe is reached quickly, almost at the location of the IRAS 20582, while the blueshifted maximum velocity is detected at the 2-3′ distance from the IRAS 20582. The Hubble-like definition for the PV diagram requires that the highest velocity in the lobe is reached at the greatest distance from the source and the PV kinematics in the redshifted lobe violate this criterion. The velocity field within the blueshifted lobe of the IRAS 20582 outflow is similar to the L 1551 PV redshifted features, with the distinction that the maximum velocity of IRAS 20582 outflow is observed over a larger spatial extent (between HH 199B1 and HH 199B3), and not localized around single HH object as in the case of redshifted L 1551, where maximum velocity is observed near HH 262. Similarly in the IRAS 20582 redshifted lobe, a substantial emission is found at the highest velocities and even large emission fraction is moving at some intermediate velocity with respect to maximum and ambient cloud velocity.

We used velocity dependent opacity correction to estimate the mass of the outflow and derive γ slopes for the mass-V relation. The value of γ is an important test for proposed mechanisms of molecular outflow entrainment. In the case of L 1551, the resulting mass spectral indices from our analysis, were systematically lower (less steep) than the power law indices obtained towards other outflows in several recent studies that use a similar opacity correction method. We showed that systematic errors and biases in the analysis procedures for deriving mass spectra could result in errors in the determination of the power-law indices. We repeat these careful analysis for the IRAS 20582 outflow. The γ slopes for the M-v relations in the both lobes are best fit

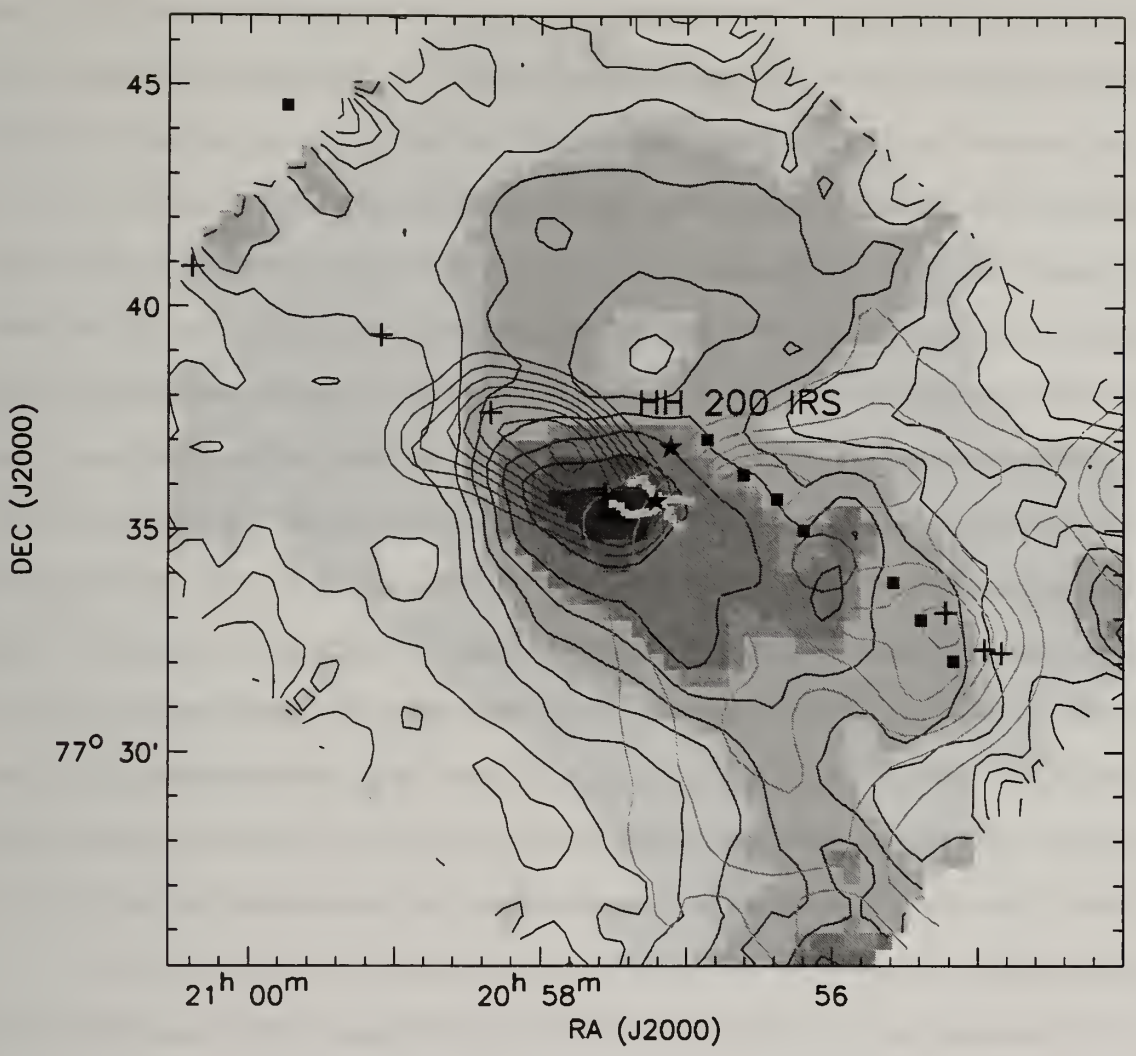

Figure 3.11 Superposition of different tracers in L 1228. We overlay the ^{13}CO emission of Figure 3.2 (gray scale and black contours) with IRAS 20582 outflow emission integrated in the velocity range as in Figure 3.1 (blue and red contours for blue- and redshifted gas respectively). We plot the interferometric limb-brightened shells observed by Arce & Sargent (2004) in green.

with the single slope and both show steep mass distribution. compared to the median value $\gamma = 2$ found by observations (Arce et al.. 2006). We derived $\gamma = 2.5$ for the blueshifted lobe and $\gamma = 3.8$ for the redshifted lobe.

The mass spectral indices. the morphological appearance of the PV plots and integrated intensity emission maps of the molecular data. compared with the optical, can

be all used to constrain the entrainment mechanism for the outflows in L 1228. Our PV results are somewhat inconclusive with respect to the entrainment model since the observed velocity field does not resemble neither spur, nor parabolic structure predicted by jet and wind models of Lee et al. 2000, respectively. However, there is an indication that the entrainment in the IRAS 20582 is jet dominated on the larger scale. This is best supported by channel maps which show highly collimated gas along the HH 199 axis at the highest velocities and steep M-v slopes in both outflow lobes. The wide-angle wind models yield smaller value of γ over a narrower range compared to the jet model. Most of the wind models find γ to be between 1.3 and 1.8, while jet models produce γ in the range from 1.5 to 3.5. Both slopes, $\gamma = 2.5$ for the blueshifted lobe and $\gamma = 3.8$ for the redshifted lobe of the IRAS 20582 outflow are outside of the range predicted by the wind-models. In the case of L 1551, broken power law in the both lobes of the main outflow was a clear indicator of the jet-entrainment. Our data do not show indication for the possible broken power law in either of the IRAS 20582 lobes, but observed steep γ slopes would suggest jet entrainment for both lobes of the outflow.

We have already point out the key role the ambient gas distribution around IRAS 20582 must play in producing the observed morphological differences on the parsec scale, from the initially symmetric outflow on the arcsec scale. The similarity of two lobes on the arcsecond scale, translates directly to the symmetry in the underlying wind emerging from the protostar. As ambient gas distribution determines the morphology of the lobes it will also make interpretation of the M-v and PV plots difficult. PV and M-v relations used to discriminate between entrainment mechanisms may not reflect completely the nature of the driving agent but be a combined product of the wind and ambient gas distributions. To what level the slope of the M-v relation is uniquely determined by the driving agent and to what level it depends on the ambient gas properties is hard to distinguish. Given that the outflow is symmetric on the

arcsecond scale, can the difference in the observed r slope and PV in these two lobes be solely the result of the different ambient mass distribution the primary wind/jet is encountering?

Arce & Sargent (2004) suggested that the best scenario for the outflow entrainment even at the arcsecond scale in L 1228 is the combination of both wide-angle wind and jet component emerging from the IRAS 20582. A two-component wind is required to explain observational properties of many outflows such as outflows in B5-IRS1 (Yu et al., 1999), PV Cep (Arce & Goodman, 2002), L 1551 (Stojimirović et al., 2006). (Shang et al., 2006) performed Zeus2D simulations using the original framework for the wide angle wind model of Shu et al. (1991). Traditionally, this model is attractive to explain old outflows of large lateral extents and low collimation, but they are considered unable to account for the observational properties of collimated outflows. Numerical simulations allowed (Shang et al., 2006) to relax some of the simplifying assumptions made in the analytical models. In the simulations, the apparent two-component density structure is present: a dense axial jet, which is part of the primary wind and a dense, closed shell which surrounds the jet. Between the jet and the shell lies the wide-angle wind. Shang et al. (2006) noted that jet is responsible for the length of the flow while the wide-angle components determines the width. They concluded that the jet-driven and wind-blown scenarios are thus unified in the framework of Shu et al. (1991). Numerical simulations of Shang et al. (2006) produce satisfactory general outflow lobe appearance, however, no m-V or PV have been generated to compare with observations.

3.5.3 Energetics

The mass for the L 1228 cloud estimated from the fully sampled ^{13}CO map at line center assuming optically thin emission is ~ 108 $M_\odot$. The total mass estimated in the outflow is ~ 7.8 $M_\odot$ for $T_{ex} = 10$ K or ~ 12.5 $M_\odot$ for $T_{ex} = 25$ K. Therefore

the mass in the outflow is approximately 7.5-11.5% of the mass of surrounding cloud, depending on the adopted value for the T_{ex}. The higher density tracer ^{13}CO line, shows strong bipolar structure around IRAS 20582 and it has been found that other density tracers show strong spatial correlation with molecular outflow. This has been interpreted as a strong impact outflow has on the parent core and that the outflow is setting the whole core into motion. By choosing -9.5 to -6 km s^{-1} as a line core range, we are probably underestimating significant fraction of the outflowing gas at lower velocities since we ignore all the outflow mass at these velocities. Therefore the total mass of the outflow is highly sensitive to the adopted cut off velocities where we distinguish outflow from the ambient gas.

The total momentum and energy carried by the outflow, estimated from only the line of sight (radial) velocity, are 15 $M_{\odot}$km s^{-1}and 4.5×10^{44} ergs, respectively. Accounting for an inclination angle correction to the momentum and energy determinations would be proportional to $\sin(\alpha)^{-1}$ and $\sin(\alpha)^{-2}$. For the inclination angle of 45° this is 1.4 and 2.25 times respectively. There may be more energy in the outflow than reported here, since the whole core is moving. However the underestimate of the momentum and energy is less than that of the outflow mass, since the highest contribution to the energy and momentum comes from the mass at higher outflow velocities and these are not affected by the adopted cut off velocity for outflow/ambient cloud. The total binding energy of the cloud is given by $\sim GM^2_{\rm cloud}/R$. Using a cloud mass of 108 $M_{\odot}$ and $\sim$ 0.3 pc for the cloud radius, we find the binding energy to be 2×10^{45} ergs. Thus, the energy of the outflow is comparable to the binding energy of the cloud, even if no correction for the inclination angle is made. Tafalla & Myers (1997) argued that the kinetic energy deposited by the outflow to the core is enough to explain the large perturbation observed in the core.

It has been suggested that parsec-scale outflows can be a source of energy to replace the energy dissipated in turbulence and thus provide the power to maintain

the magnetohydrodynamic (MHD) turbulence (Li & Nakamura, 2006). Energy dissipation rate of turbulence in L 1228 is estimated to be ~ 0.003 $L_\odot$, using equation (7) from Mac Low (1999). Thus, outflow again as in the case of L 1551 has enough energy that even if the small fraction of it could be coupled into cloud turbulence, the outflow could sustain the turbulence for over a million years, much greater than the lifetimes of molecular outflows. However, Tafalla & Myers (1997) used narrow line, C_3H_2, sensitive to velocity gradient and noted that it exhibits a shift of the full line profile in the direction of the outflow. Thus acceleration occurs without appreciable line width enhancement, suggesting that outflow has not increased substantially the turbulence of the gas.

Following on the argument from the L 1551 section that outflows may provide a mechanism to regulate star formation by removal of the gas from star-forming regions, high-resolution observations of Arce & Sargent (2004) indicate that wide-angle outflow from IRAS 20582 has excavated large cavities in the circumstellar envelope and has limited the infalling region, and thus has an important effect on the mass assembling process in protostar. The ^{13}CO PV cut (see Figure 3.6) reveals that most of the gas in the L 1228 region is set into motion, while ^{12}CO PV cuts show much larger ambient cloud velocity width compared to what is observed in for example L 1551. Therefore outflow must have a strong dynamical impact on the cloud gas distribution and major role in the cloud disruption.

3.6 Conclusions

Molecular outflows in L 1228 have been mapped at high sensitivities in the ^{12}CO and ^{13}CO J=1—0 transitions. We summarize the main conclusions below.

1. The IRAS 20582 outflow has an extent of 1 pc along $\sim 60^\circ$ position angle. We argue that the single source is entraining the outflow and that the ambient gas distribution must play a key role in producing the observed differences

Table 3.1. L 1228 Outflow Mass and Energy Estimates

CO Line	Lobe	Velocity Interval km s^{-1}	T_{ex} = 10 K Mass $M_\odot$	T_{ex} = 25 K Mass $M_\odot$
^{13}CO	Red	-7 to -6	3.2	5.1
^{12}CO	Red	-6 to 5	0.47	0.74
^{12}CO	Blue	-9 to -10	3.7	5.8
^{12}CO	Blue	-10 to -20	0.56	0.87
Total	Red Mass		3.5	5.8
Total	Blue Mass		4.3	6.7
Total	Red Momentum			10.4 $M_\odot$ km s^{-1}
Total	Red Energy			24.5 $\times$ 10^{43} ergs
Total	Blue Momentum			4.2 $M_\odot$ km s^{-1}
Total	Blue Energy			19 $\times$ 10^{43} ergs

in appearances of redshifted and blueshifted outflows. Due to the unknown ambient properties it is not trivial to translate the observed outflow morphology and kinematics to the physical properties of the driving wind.

2. We argue that the blueshifted emission superimposed on the redshifted IRAS 20582 molecular outflow lobe is unrelated to the parsec scale outflow emerging from IRAS 20582. Correlation of this CO blueshifted emission with the blueshifted HH knots of HH 200 flow. suggests that they are entrained by the same jet. No evidence for the CO redshifted counterpart is seen.

3. We applied a slightly-refined procedure of velocity-dependent opacity correction adopted by recent authors. with more careful approach to obtain a total mass in the outflow and more accurate determination of outflow mass with velocity. The mass of the L 1228 molecular cloud is $\sim$ 108 $M_\odot$ and the total mass of the outflow in L 1228 is at least $\sim$ 7.8 $M_\odot$. The mass determination is strongly underestimated since the whole core is moving and we ignored all the mass in the velocity range from -9.5 to -6 km s^{-1}.

4. The resultant mass-spectral power law indices are steep, γ = 2.5 for the blueshifted lobe and γ = 3.8 for the redshifted lobe of the IRAS 20582. Channel maps

show highly collimated gas along the HH 199 jet axis at the highest velocities. Unfortunately our PV results are somewhat inconclusive with respect to the entrainment model. Combining our results with the interferometric images of Arce & Sargent (2004) we conclude that the morphology and kinematics are consistent with the entrainment of the gas by an underlying wind that has both a wide-angle and a collimated component. In the future outflow entrainment studies could greatly benefit from high resolution interferometric observation of a larger area around driving source which can probe how and where collimation of the initially wide-angled flows takes place.

5. The kinetic energy of the L 1228 outflow is comparable to the binding energy of the cloud and multiple line of evidence demonstrate the disruption of the cloud core by the outflow activity. Although outflow has big enough energy reservoir to contribute to the turbulent motions in the cloud, the spectral studies of Tafalla & Myers (1997) showed that gas acceleration occurs without appreciable line width enhancement, suggesting that outflow has not increased substantially the turbulence of the gas. This may imply extremely inefficient coupling of the outflow momentum and cloud kinematics.

CHAPTER 4

DISCOVERY OF THE MOLECULAR OUTFLOW IN HARO 6-10

We present high sensitivity ^{12}CO and ^{13}CO J=1—0 molecular line maps covering the full extent of the parsec scale Haro 6-10 Herbig-Haro (HH) flow. We report the discovery of the molecular CO outflow. along the axis of parsec-scale HH flow. Previous molecular studies missed the identification of the outflow probably due to their smaller mapping area and confusing spectral features present towards the object. Our detailed molecular line study of the full 1.6 pc extent of the optical flow shows evidence for both blueshifted and redshifted gas set in motion by Haro 6-10 activity. The molecular outflow is centered at Haro 6-10. with redshifted gas being clumpy and directed towards the north-east. while blueshifted gas is in the south-western direction. The molecular gas terminates well within the cloud. short of the most distant HH objects of the optical flow. Contamination from an unrelated cloud along the same line of sight prevents a thorough study of the blueshifted outflow lobe and its mass distribution at the lowest velocities in both lobes. The cloud core in which Haro 6-10 is embedded is filamentary and flattened in the eastwest direction. The total cloud mass of the cloud core is calculated to be $\sim 200\ M_{\odot}$. The mass associated with the outflow is $\sim 0.1\ M_{\odot}$.

4.1 Introduction

In the last ten years, wide-field CCD camera observations have shown that it is quite common for outflows traced by Herbig-Haro (HH) objects to attain parsec scale dimensions, at least an order of magnitude larger than previously thought (Reipurth et al., 1997). It is now becoming clear that optical HH objects (which are lit up from the cooling behind shock fronts within the flows), near-infrared H_2 jets (tracing shocked regions), and the swept-up CO bipolar molecular outflows are intimately linked to one another (see for e.g. Bachiller et al., 1995). With the development of large-format heterodyne arrays at millimeter wavelengths and the availability of "on-the-fly" (OTF) mapping capabilities, millimeter mapping of the full extent of some of the known parsec-scale HH flows is possible with increased data sensitivity. This allows a more thorough study of the observational properties of the outflows and provides better constraints on the theoretical models of molecular outflow entrainment mechanism.

Devine et al. (1999b) discovered a giant 1.6 pc long HH flow, centered on Haro 6-10 at a position angle of 220° delineated by HH 410 and HH 411 at its edges, and HH 184 and HH 412 along the HH flow axis. Haro 6-10 is located in the L 1524 cloud within the B18 region of the Taurus Molecular Cloud Complex. It is a binary system composed of an optically visible southern component (Haro 6-10S), and its infrared companion (Haro 6-10N). High-resolution 3.6 cm VLA map (Reipurth et al., 2004) strongly suggests that the optical component, Haro 6-10S, is driving the current outflow activity. The same set of data suggests that there might be an additional stellar companion to Haro 6-10S, more closely bound to it than Haro 6-10N.

There has been other evidence for the outflow activity from the Haro 6-10 system such as 2.12 μm molecular hydrogen emission, observed at the position of the northern companion (Carr, 1990; Herbst et al., 1995). Movsessian & Magakian (1999) found a small HH jet associated with Haro 6-10 itself at a position angle of 195° with

blueshifted radial velocities. Reipurth et al. (2004) reported a VLA jet along the same angle. These latter jet angles are significantly different from the 220° angle of the parsec scale HH flow. The difference in these position angles have led some authors to suggest that the outflow from Haro 6-10 has undergone precession (Reipurth et al., 2004; Devine et al., 1999b).

In the past, a few attempts have been made to detect molecular CO outflow from the Haro 6-10 source. Small maps, only a couple of arcminutes wide, have been made toward Haro 6-10 which presented the evidence of weak non-Gaussian CO wings emission in the direction of the optical object (Edwards & Snell, 1984; Levreault, 1988; Hogerheijde et al., 1997, 1998; Chandler et al., 1998). Hitherto, Haro 6-10 has been considered to be devoid of molecular outflow (Devine et al., 1999b).

We made large, sensitive, ^{12}CO J=1→0 and ^{13}CO J=1→0 maps of the Haro 6-10 region, over the full extent of the optical parsec-scale HH flow. Here we show the evidence for the redshifted high velocity CO gas along the outflow axis defined by the HH parsec scale flow. Due to "contamination" by emission from another molecular cloud along the same line of sight, a thorough study of the blueshifted outflow lobe is limited.

4.2 Observations

A full mapping of ^{12}CO and ^{13}CO in the J=1→0 transitions has been performed with the SEQUOIA receiver at the Five College Radio Astronomy Observatory (FCRAO) 14 m telescope. The receiver is configured as a dual-polarized 4×4 array. The orthogonal polarizations of the SEQUOIA array are averaged to produce spectra with higher signal-to-noise ratio (S/N). The telescope's half-power beam widths are 45″ and 47″ for ^{12}CO and ^{13}CO transitions respectively. Channel maps as well as individual spectra were checked for any scanning artifacts, baselined and regridded to the 22.5″ sampled grid. RMS noise weighting was used to combine the data. For all

calculations, the antenna temperatures were corrected for the main beam efficiencies of 0.45 for ^{12}CO and 0.5 for ^{13}CO.

Both ^{12}CO and ^{13}CO spectra are smoothed to 0.13 km s^{-1} channel spacing. The system temperatures (T_{sys}) in our observations range from 400 – 700 K for ^{12}CO and between 200 – 500 K for ^{13}CO. Regions mapped with the higher noise level were repeated, combined and averaged in order to get a constant lower noise level over the whole extent of the map. The resulting mean rms per velocity channel is 0.2 K for ^{12}CO and 0.1 K for ^{13}CO. Antenna pointing and focus were checked every few hours and corrected using SiO masers.

The analysis were done both using the Gildas software package and IDL software of Research Systems Inc. Detailed studies of the physical parameters characterizing the outflows were performed using IDL.

4.3 Morphology of The CO gas

4.3.1 Two component emission in B18 cloud

In Figure 4.1 we show ^{12}CO and ^{13}CO spectra averaged over the 15′ area, centered on Haro 6-10. In both lines, the averaged spectra consists of two Gaussian-like components: a stronger component centered at 6.4 km s^{-1} and a weaker component at $\sim$ 4 km s^{-1}. A similar double peak profile has been observed by Arce & Goodman (2001a, hereafter AG) by studying the parsec scale outflow from IRAS 04239+2426 in the adjacent B 18w cloud. They named the component at lower velocity "cloud A", and surmised that is was produced by another cloud in Taurus along the same line of sight.

The stronger Gaussian component is associated with the Haro 6-10 host cloud, L 1524. This is in agreement with the ammonia core identified at LSR velocity of 6.4 km s^{-1}(Codella et al., 1997) towards L 1524. Haro 6-10 is located at the edge of the compact ammonia core (see Figure 3 (Codella et al., 1997)). Our spatially averaged

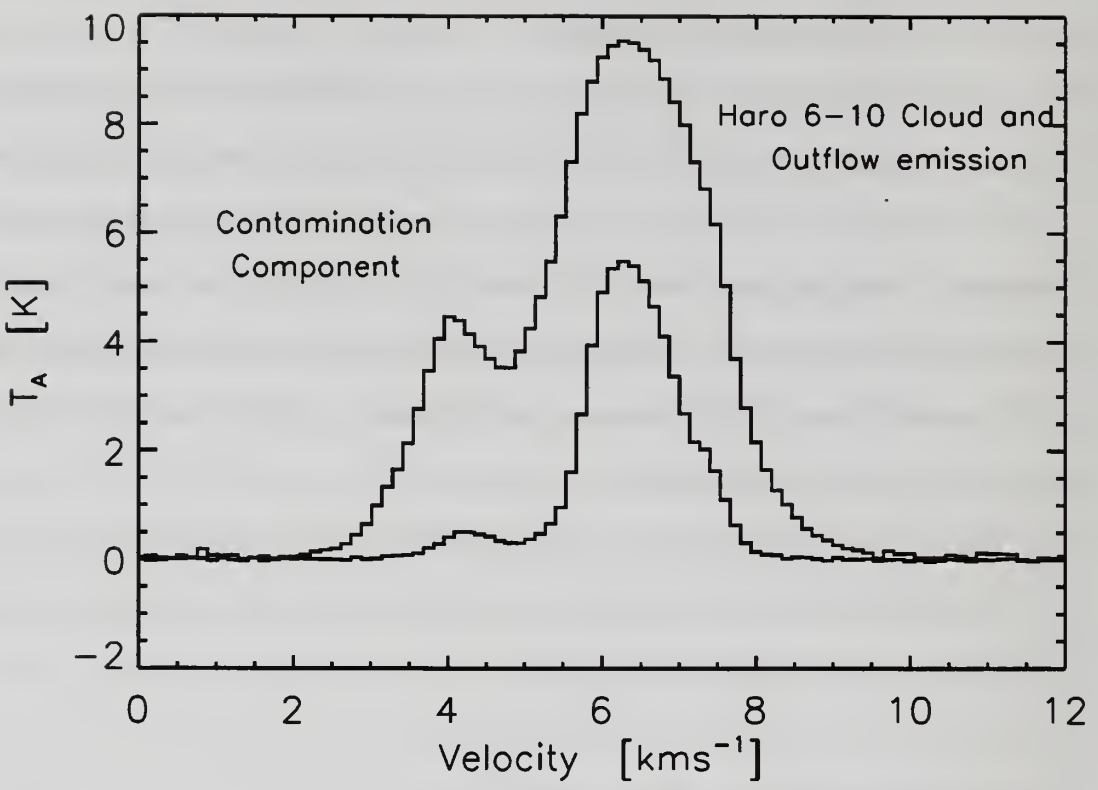

Figure 4.1 Haro 6-10: L 1524 Cloud and Contamination Related Emission. The ^{12}CO and ^{13}CO spectra averaged in 12′ area centered on Haro 6-10. Foreground contamination from another cloud in Taurus gives rise to the blueshifted emission peaking at $\sim$ 4.5 km s^{-1}.

spectra towards the L 1524 cloud show some evidence for linewing emission at both blueshifted and redshifted velocities, although the contaminating cloud component at $\sim$ 4 km s^{-1} obscures much of the wing emission at blueshifted velocities. Even with our higher sensitivity data, we do not see evidence for high velocity molecular gas as is seen in other prototypical outflows. Since the outflow is composed mainly of gas with slow radial velocities, emission from outflowing gas at the slowest velocities might be hidden under the ambient cloud emission.

In order to examine this contaminating emission at 4 km s^{-1}, we used a 2° by 2° portion of the much larger FCRAO Taurus Molecular Cloud Survey in both ^{12}CO and ^{13}CO J=1→0 (Narayanan et al., 2007). In Figure 4.2, we plot for each line,

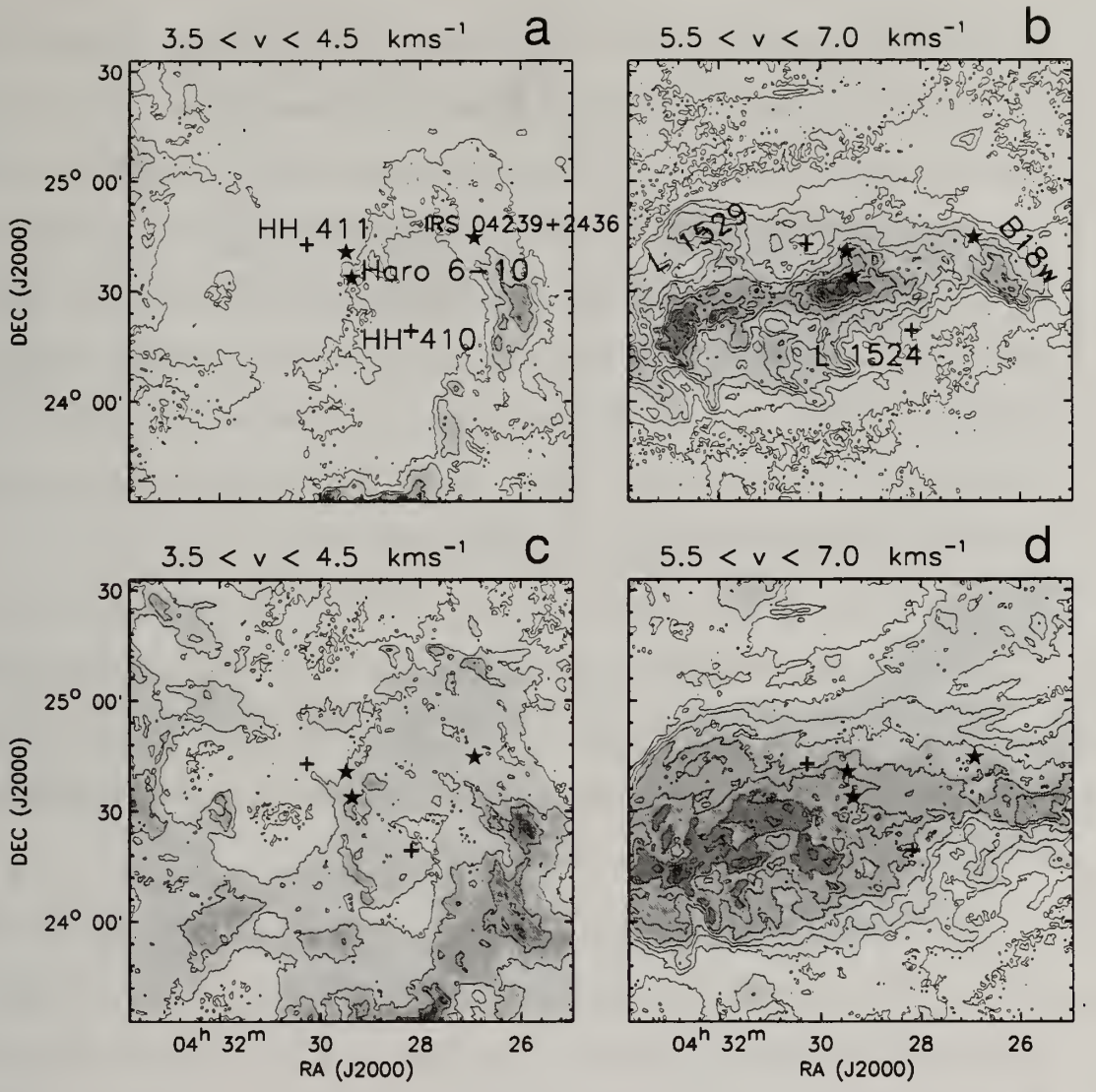

Figure 4.2 Two velocity components of B18 cloud in Taurus complex. Overview of the Haro 6-10 Region. A zoomed view into the B18 region derived from a much larger-scale map from the Taurus molecular cloud survey (Narayanan et al., 2007) in ^{13}CO J=1→0 (a,b) and ^{12}CO J=1→0 (c,d). These images demonstrate the presence of two emission components at different velocities, along the same line of sight. Panels a and c show emission unrelated to the B 18 cloud, while panels b and d trace the B 18 cloud sub-structure. In panel b we identify three clouds found in B 18: L 1529, L 1524, B18w, from east to west). Several YSOs and T-Tauri stars are embedded in the L 1529 region. L 1524 hosts Haro 6-10 star and nearby HH 414 IRS (filled stars). B 18w at the western most point, hosts IRAS 04239+2436 source which drives parsec scale HH 300 flow. In the panel a we label Haro 6-10 binary system, the driving source of parsec-scale HH flow with terminating points at HH 410 toward SW and HH 411 toward NE. Contours at each panel start at 2σ level and go in steps of 4σ.

the integrated intensity emission in two narrow velocity intervals. The first velocity interval preferentially selects the contaminating emission in the 3.5 to 4.5 km s^{-1} velocity range. (Figure 4.2*a.c*). This contaminating cloud component is traced by ^{13}CO molecule as an arc like filament. stretching from south of Haro 6-10 to north and appearing to bend toward IRS 04239+2436 in B18w cloud and south from it again. (see Figure 4.2*a*). The maximum intensity of this emission is south from IRS 04239+2436 source in the B 18w cloud. while at the location of Haro 6-10. the contaminating emission is quite clumpy. The ^{12}CO tracer shows similar morphology of the emitting gas in the region (see Figure 4.2*c*).

In the other velocity interval. from 5.5 to 7.0 km s^{-1} we preferentially select the CO emission associated with the B 18 clouds. which have LSR velocities around 6.4 km s^{-1}. In ^{13}CO (see Figure 4.2*b*). the B 18 cloud is revealed as a flattened. elongated structure in the east-west direction. In the same panel we identify L 1529. L 1524 and B 18w clouds within the B 18 region.

The dramatic change in the morphology for each isotope at only a slightly different velocity offset indicates quite clearly that we are looking at two spatially distinct and possibly unrelated cloud features. From Figure 4.2. it can be seen that towards Haro 6-10. the intensity of the contaminating emission is not as high as the intensity of the L 1524 cloud. However, towards B 18w. it is seen that the emission in both velocity bins seem to be of comparable intensity. The same was evident in the average spectra of the region presented by AG. In this study by AG. it was thus a clear cut in the case of IRAS 04239+2426 to concentrate only on the redshifted emission in the outflow. From the large-scale CO maps derived from the Taurus survey. it appears that while the blueshifted component in the Haro 6-10 spectra at 4.5 km s^{-1} is part of the contaminating emission seen towards B 18w. the contamination is not nearly as severe as in the case of B 18w. Some of the emission towards Haro 6-10 at 4.5 km s^{-1} might be part of the outflow system from that object.

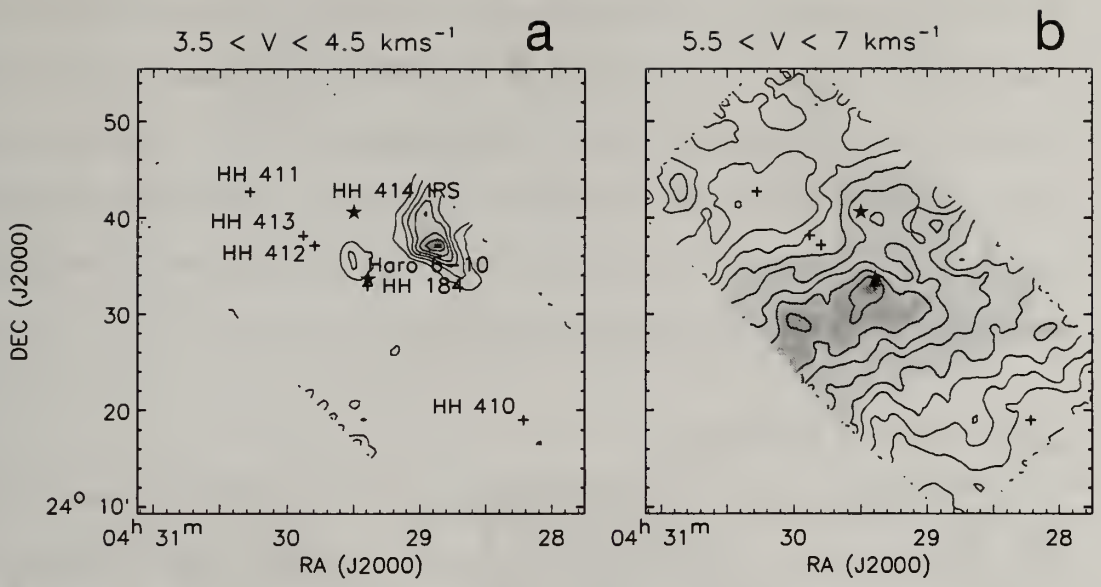

Figure 4.3 L 1524 cloud in ^{13}CO J=1→0. L 1524 cloud emission using our high sensitivity ^{13}CO J=1→0 data integrated in two velocity bins, representing two distinct component in L 1524 cloud. Contours at each panel start at 5σ level and go in steps of 10 σ in panel a (0.4 Kkm s^{-1}) and in steps of 20σ (0.9 Kkm s^{-1}) in panel b.

4.3.2 The Haro 6-10 cloud core

In the following sections, we will examine in more detail the behavior of the ambient, blueshifted and redshifted gas using our new ^{12}CO and ^{13}CO J=1→0 data of Haro 6-10 outflow, which are of smaller scale compared to the Taurus survey, but have better sensitivity. For the rest of this paper, the Taurus Survey data are not used for any analysis. As already discussed, in the velocity range between 3.5 and 4.5 km s^{-1}, the emission is dominated by the contaminating cloud component. Figure 5.1 shows the ^{13}CO in two different velocity bins. Here, the contamination is clearly detected as strong feature at the northwest edge of the map (see Figure 5.1*a*). In addition, a small clump of emission centered at Haro 6-10 is present, which is elongated and extended toward north, at the $\sim 30^{\circ}$ angle with respect to the axis defined by the HH flow (crosses in Figures 5.1a). In the next panel, ^{13}CO emission traces the column density distribution within the L 1524 cloud. The flattened structure of the L 1524 cloud seen in the larger-scale map of Figure 4.2 is also visible here, and Haro 6-10

lies close to the peak of integrated intensity emission. This peak traces the same core identified in ammonia by Codella et al. (1997). The elongated L 1524 cloud is perpendicular to the HH outflow axis. From Haro 6-10, along the HH flow axis, the integrated intensity decreases, and HH 411 and HH 410 are found in the regions of very low ^{13}CO integrated intensity. The ridge of ^{13}CO emission is seen to extend northward from Haro 6-10 towards HH 414 IRS.

4.3.3 Outflow Emission

In Figure 4.4, we show integrated intensity emission of ^{12}CO in several different velocity bins. In the panels *a,f* and *g* we show the distribution of emission at the highest blueshifted and redshifted velocities. We believe that at these velocities we are selecting almost exclusively emission that arises from the outflow associated with Haro 6-10. Figure 4.4 *a* shows that the blueshifted emission in the velocity range from 0 to 2 km s^{-1}is spatially restricted and centered on Haro 6-10. In Figure 4.4 *f,g* the redshifted emission is shown and this emission consists of two emission regions centered on Haro 6-10 and HH 412 respectively. The clump centered at Haro 6-10 has extended emission toward southeast, similar to the highest velocity blueshifted gas identified in Figure 4.4 *a*. The redshifted emission seen toward HH 412, located about 7′ northeast of Haro 6-10, is detected to velocities as high as 14 km s^{-1}, nearly 8 km s^{-1} from the ambient cloud line center. The emission is slightly extended along the HH flow axis. In the optical images (Devine et al., 1999b), HH 412 appears as a 1′ long fairly diffuse emission feature, also elongated along the flow axis. Therefore, morphologies of the CO and optical emissions are quite similar around HH 412.

In Figure 4.5 we show the optical Hα image of the Haro 6-10 region (Devine et al., 1999b), overlayed with the ^{12}CO J=1→0 integrated emission in 9 to 14 km s^{-1} velocity range for the redshifted gas and 0 to 2 km s^{-1} for the blueshifted gas. In the optical image, HH 410 and HH 411, lie at the extremes of the HH flow, and are seen against

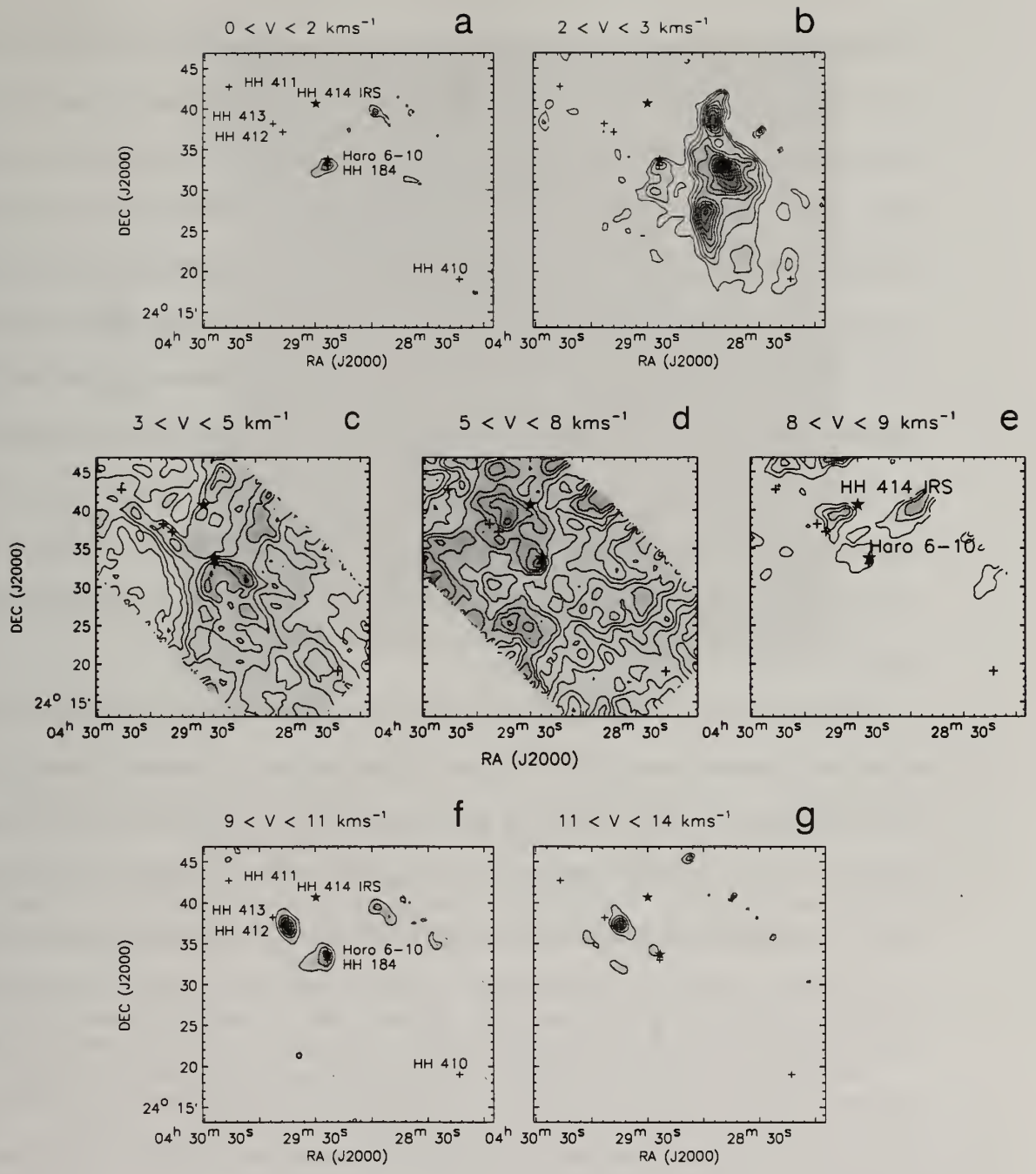

Figure 4.4 Haro 6-10 ^{12}CO J=1→0 channel emission. ^{12}CO line integrated in different velocity range. Upper row: Blueshifted gas. In panel a contours start and increase with 2σ certainty (2 Kkm s^{-1}). while on panel b they start and increase in 3σ steps (2.1 Kkm s^{-1}). Middle row: line core velocity range. Contours in a and b panels start at 10σ and go in step of 10 σ (1 Kkm s^{-1} at panel a and 1.2 Kkm s^{-1} at panel b) In panel c contours start at 8σ level (0.56 Kkm s^{-1}) and increase in the same step. Lower row: Redshifted velocity range. At both panel contours start and increase with 2σ certainty, which is 0.2 Kkm s^{-1} in panel a and 0.32 Kkm s^{-1} in panel b.

a background with many galaxies, demonstrating that the flow has burst out of the L 1524 cloud in both direction and is now moving through the gas and dust with greatly reduced column density. Our ^{13}CO maps confirms this result. The expanded image of the CO outflow in Figure 4.5 shows that even toward Haro 6-10 that the redshifted and blueshifted outflowing gas is slightly offset, suggesting that the outflow is bipolar with the redshifted emission to the northeast and blueshifted emission to the southwest. Devine et al. (1999b) speculated, based on morphology and brightness, that the large HH flow has the same bipolar orientation. Additional information is provided by the radial velocity measurement of the small HH jet oriented at position angle 195° that shows that it is blueshifted (Movsessian & Magakian, 1999), and thus has the same velocity sense at the CO outflow, although the jet is oriented about 30° from the large HH flow.

The distribution of CO emission in the near outflow wings, 2 to 3 km s^{-1} for the blueshifted gas and 8 to 9 km s^{-1} for the redshifted gas, is shown in Figure 4.4 *b,e*. On the blueshifted side, emission is seen toward Haro 6-10 along with the extended emission to the southwest that lies along the HH flow axis. However, in addition, bright emission is seen to the north of the HH flow that presumably has nothing to do with the CO outflow. Therefore the emission in the 2 to 3 km s^{-1} range may be a mix of emission from the contaminating gas component as well as from an extended outflow. Likewise in the 8 to 9 km s^{-1} range there is emission that appears to be related to the CO outflow and an additional feature near HH 414 IRS. Again the emission in this velocity range is likely a mix of emission from the outflow and from the ambient gas. It is interesting that the emission near HH 412 is clearly offset from that seen at higher velocities and closer to the position of HH 414. HH 414 is a small bipolar jet which coincides with the IRAS 04264+2433 source. Devine et al. (1999b) found that this jet points toward HH 413 and that the morphology of the HH 413

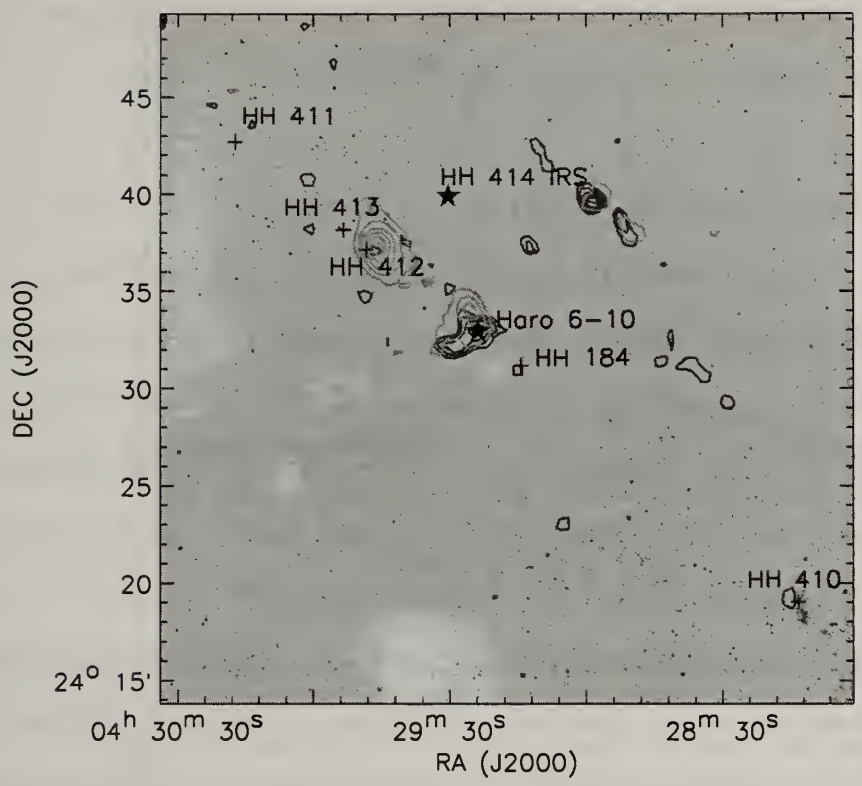

Figure 4.5 Haro 6-10 Outflow in H_α and ^{12}CO. Best case scenario for the outflow in the Haro 6-10 region: blueshifted emission is integrated in the velocity interval from 0 to 2 km s^{-1} and contours start at 0.3 Kkm s^{-1} and go in steps of 0.1 Kkm s^{-1}; redshifted emission is integrated in velocity interval from 9 to 14 km s^{-1} and contours start at 0.5 Kkm s^{-1} and go in steps of 0.5 Kkm s^{-1}. Molecular gas is overlayed on the optical image of the Haro 6-10 region (Devine et al., 1999b).

knots resembles bow shocks caused by the flow coming from HH 414 direction. It is uncertain whether this emission might be related to this second HH flow.

Finally it is interesting to note the structure in the 3 to 5 km s^{-1} interval. Figure 4.4*c*. This velocity interval would be expected to include the outflow emission from Haro 6-10, since it lies a few km s^{-1} from the line center of the L1524 cloud emission, however the second cloud contaminates the emission. It is intriguing that there a finger-like emission from Haro 6-10 toward the northeast, and a bow shaped feature centered on Haro 6-10, and opening toward HH 410 in the southwest. These two features line up with the HH flow direction. The relevance of this structure to the outflow is unclear. In the following velocity bin (5 to 8 km s^{-1}), the ^{12}CO emission is

dominated by L 1524 ambient cloud emission and no clear structure can be identified, although there is a maximum of emission towards Haro 6-10.

4.4 Mass and Energetics

The emission from ^{13}CO is usually optically thin and therefore a good tracer of the gas column density. However, the emission can also be very weak, limiting the spatial and velocity extent to which outflows can be traced. While ^{12}CO is more readily detected, it is often optically thick, even in the high velocity emission of outflows. To derive accurate gas column densities we may need to correct for the optical depth of this line. Several recent studies have combined ^{12}CO and ^{13}CO J=1→0 data to estimate the mass of the outflow, using a velocity-dependent opacity correction (Bally et al., 1999; Yu et al., 1999; Arce & Goodman, 2001a; Stojimirović et al., 2006). This approach usually requires construction of spatially averaged spectra, since ^{13}CO emission is usually not detectable in most mapping positions. The application of this method in Haro 6-10 has some limitations due to the weak emission in the line wings.

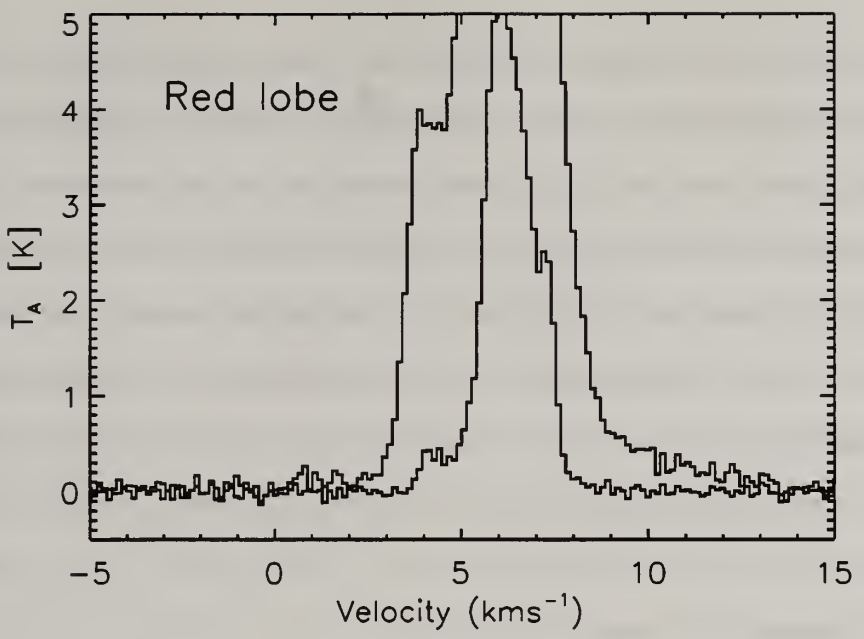

Figure 4.6 Average ^{12}CO and ^{13}CO Spectra in The Redshifted Outflow.

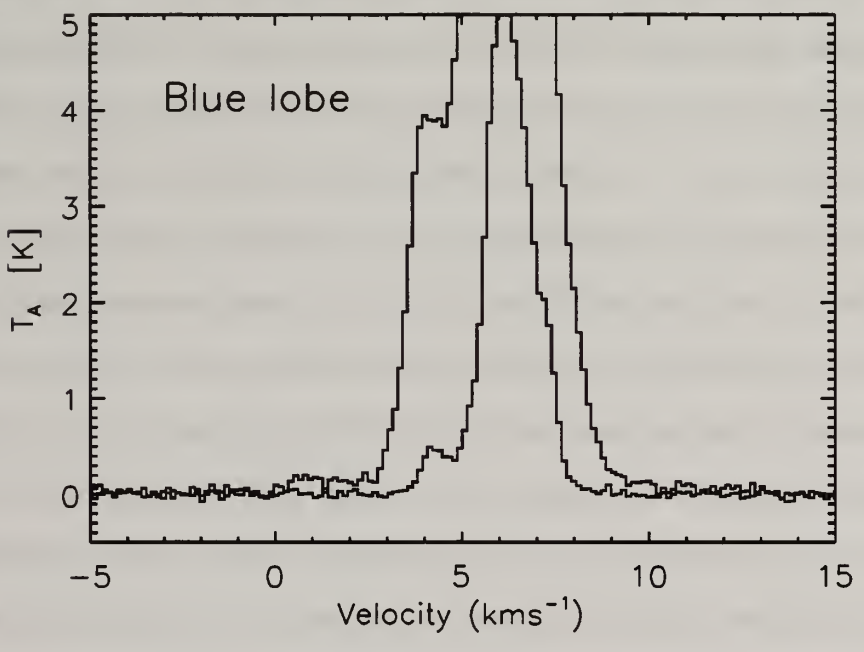

Figure 4.7 Average ^{12}CO and ^{13}CO Spectra in The Blueshifted Outflow.

4.4.1 Outflow Mass

In Figures 4.6 and 4.7 we show the spatially averaged ^{12}CO and ^{13}CO spectra in the redshifted and blueshifted gas respectively. These spectra were constructed using

the following proceedure to isolate the strongest outflow emission. For the blueshifted gas we found the integrated intensity at each location in our ^{12}CO map in the velocity range from 0 to 2 km s^{-1}. We then averaged the spectra at every location where the integrated intensity of ^{12}CO was at least one-third of the peak integrated intensity. The ^{13}CO spectrum was obtained by averaging the same spatial locations as was used to form the ^{12}CO spectrum. For the redshifted gas we applied the same approach integrating over the velocity range of 9 to 12 km s^{-1}. The resulting spectra differ from the average spectrum shown in Figure 4.1 in having both a weaker contaminating component and enhanced outflow wings. The outflow in ^{12}CO can be traced over a full velocity range from 0 to 14 km s^{-1}.

Despite this averaging approach, the ^{13}CO emission outside the line cores, has low signal to noise. Examining both Figures 4.6 and 4.7 we see that at the full spectral resolution, the ^{13}CO emission is lost in noise at velocities below than 2 km s^{-1} and greater than 9 km s^{-1}. The ^{13}CO outflow emission is too weak to use velocity-dependent opacity correction. We have instead integrated the emission in four velocity intervals. In the near-wings of the redshifted outflow emission (between 8 and 9 km s^{-1}) the ratio of ^{12}CO to ^{13}CO is 112 $\pm$ 20, consistent with the ^{12}CO emission being optically thin. At higher outflow velocities (between 9 and 12 km s^{-1}), ^{13}CO emission is not detected, and the 1σ limit on this ratio is > 47. The ^{13}CO emission in the blueshifted gas is even weaker, and only limits on the ratio can be obtained. In the near blueshifted outflow (2 to 3 km s^{-1}) the 1 σ lower limit is 45 and at higher blueshifted velocities (0 to 2 km s^{-1}) the lower limit is 20. Thus, where ^{13}CO emission is detected it is consistent with optically thin ^{12}CO emission and everywhere else we can only determine an upper limit to the ^{12}CO optical depth. Therefore to estimate the gas column density and outflow mass, we will assume that ^{12}CO emission is optically thin (equation 3 from Stojimirović et al. (2006)), and we will apply no correction for the optical depth.

The outflow mass as a function of velocity and position is then computed from $M(v) = 2\mu m_H A N_{H_2}(v)$, where $\mu = 1.36$ is the mean atomic weight including He and other constituents, m_H is the mass of the hydrogen atom and A is the physical area of one pixel at the distance of the source. N_{H_2} is the molecular hydrogen column density obtained using the relation $N_{H_2} = 1.1 \times 10^4 N_{12}$ by Frerking et al. (1982) for the Taurus cloud; this result is consistent with more recent determinations, summarized by Harjunpää et al. (2004), for other nearby dark clouds. The greatest uncertainty in our mass estimates comes from the uncertainty in the N_{H_2} to N_{12} ratio (Frerking et al., 1982).

The gas column density derived assuming that CO is in LTE depends on the gas temperature. For a gas temperature of 10 K we find 0.02 $M_\odot$ in the velocity range from 9 to 14 km s^{-1}, while the mass in the velocity range from 0 to 2 km s^{-1} is found to be 0.01 $M_\odot$. For a gas temperature of 25 K, in the same velocity ranges, the redshifted gas has mass of 0.04 $M_\odot$ and blueshifted of 0.02 $M_\odot$. We believe that these velocity ranges are dominated by outflow emission.

The cutoff velocities of 9 and 2 km s^{-1} respectively for the start of the redshifted and blueshifted components of the outflow correspond to velocity offsets from the systemic velocity of the cloud of 2.5 and 4.5 km s^{-1} respectively. There may be slower-moving components of outflowing gas at lower redshifted and blueshifted velocities. Within the blueshifted velocities, the presence of the contaminating emission at 4.5 km s^{-1} clearly makes it problematic to separate this low-velocity outflow component. In an effort to include any lower-velocity outflow component, we have repeated the mass calculation for the redshifted velocity range of of 8 to 9 km s^{-1} and derive a mass of 0.15 $M_\odot$, and for the lower-velocity blueshifted gas between 2 to 3 km s^{-1} we derive a mass of 0.04 $M_\odot$, both assuming a gas temperature of 25 K. Are mass estimates for the outflow are summarized in Table 4.1.

Table 4.1. Haro 6-10 Outflow Mass Estimates

Velocity Interval	T_{ex} = 10 K Mass $M_\odot$	T_{ex} = 25 K Mass $M_\odot$
Red 8 to 9 km s^{-1}	0.1	0.15
Red 9 to 14 km s^{-1}	0.02	0.03
Blue 0 to 2 km s^{-1}	0.01	0.02
Blue 2 to 3 km s^{-1}	0.02	0.04
Red Total	0.12	0.18
Blue Total	0.03	0.06

The mass distribution with velocity for molecular outflow has been shown to have a power-law dependence, such that $M_{CO}(v) \propto v^{-\gamma}$ (Richer et al., 2000). We have derived the mass-velocity relation for Haro 6-10 using the ^{12}CO emission and assuming it is optically thin as we assumed earlier. We computed the mass in each velocity channel within the outflow and plotted this versus the velocity offset from the host cloud's mean velocity. The velocity range over which outflow gas is detected in Haro 6-10 is very limited, making the determination of this relation very uncertain. In a log-log plot, the slope of the linear fit determines the γ index. The value of γ for the blueshifted gas is 6 $\pm$ 0.6 and for the redshifted gas is 5.5 $\pm$ 0.6.

4.4.2 Cloud Mass and Energy

We determine the cloud mass by using the ^{13}CO map, Figure 5.1*b*. The line center optical depth at each point in the map is derived from the ^{13}CO peak temperature. The excitation temperature is obtained at each position by solving the radiative transfer equation for the excitation temperature, assuming ^{12}CO line to be optically thick. We find, the total mass of the cloud using this method to be $\sim$ 200 $M_\odot$. The cloud mass estimate is mostly free from the foreground contamination, since we only searched for peak ^{13}CO emission in the narrow velocity range around line center.

The kinetic energy of the cloud is dominated by the turbulent energy of the cloud, and is estimated using $E_{turb} = 3/(16ln2)M_{cloud}\Delta v^2$. The mean turbulent clumps,

each of which is readily apparent in position-position-velocity space. They each have masses of thevelocity of the ambient gas is determined from the ^{13}CO line profiles in the cloud. We find the full line width at the half maximum to be $\Delta v = 1.2$ km s^{-1}. We find that kinetic energy of the L 1524 cloud is $\sim 1.6 \times 10^{45}$ ergs.

4.5 Discussion

Although at the lowest outflow velocities, the blueshifted emission is strongly contaminated by the foreground cloud emission, we see signatures of the outflow from Haro 6-10 at the higher blueshifted velocities. There is significant overlap between blueshifted and redshifted emission at the position of Haro 6-10, which together with relatively low velocities observed in the line wings, suggests that the flow is in the plane of the sky. If the flow is in the plane of sky, slower radial velocities are hidden under the ambient cloud emission. In such a scenario, the clumps that we see defined in the redshifted gas (see for instance Figure 4.5) are probably the highest velocity components seen projected in the map.

The position-velocity cut made along the axis of the HH flow, shows clear acceleration at the position of HH 412, where the highest velocities are found (see Figure 5.6). Also at the position of Haro 6-10 we see broader line profiles, indicating possible acceleration in both redshifted and blueshifted components.

It can be seen from Figure 5.6 that at $+20'$ and $-10'$ offsets, the low-velocity gas (presumably associated with just the ambient gas) shows broadening specifically at redshifted and blueshifted velocities respectively. These velocity broadened components correspond to the right sense of the outflow direction - redshifted lobe for positive y offsets, and blueshifted lobe in negative y offsets of Figure 5.6. This further bolsters the argument that the Haro 6-10 molecular outflow is, at least in the current epoch, a low-velocity outflow that has slowed down close to ambient cloud velocities. If the outflow has slowed to ambient velocities, it may be possible to see the subtle

signature of the outflow at low velocities from constructing a centroid velocity map with velocities confined to the ambient cloud emission alone (velocity range from 2 to 9 km s^{-1}). When such centroid velocity mapping was performed, for instance in the Cepheus A outflow system (see Figure 4 of Narayanan & Walker, 1996), it was found that the outflow signature is clearly seen as a velocity gradient along the outflow direction. We have performed such centroid velocity mapping analysis (figure not shown) for Haro 6-10, but we do not see any such gradient present at ambient cloud velocities. This leads us to conclude that even if the outflow has slowed to ambient cloud velocities in Haro 6-10, the outflow has not imparted any significant velocity gradients over the normally present random velocities inherent in the ambient cloud.

Yet another puzzling feature of the Haro 6-10 outflow is, that it entrains very little gas. The morphology of the outflow is very clumpy and the total mass found in the outflow in only 0.25 $M_{\odot}$. In evolved sources, the previous outflow episodes may clear up the ambient gas and leave no gas to be entrained by later outflow episodes. In such a case, large ambient gas cavities are expected to be seen around source. Our ^{13}CO maps show that no such cavities are found around Haro 6-10 and that the overall L 1524 cloud is somewhat flattened and filamentary, with the column density decreasing from Haro 6-10 source toward HH 410 and HH 411 along the outflow axis. While the L 1524 cloud is flattened, there appears to be enough ambient gas in the direction of the outflow lobes to be entrained (see Figure 5.1).

The clumpy morphology and low total mass may be a consequence of the outflow viewing geometry. If the outflow is mostly in the plane of sky, much of the its mass would be missed since we have excluded ambient gas components from our calculations. It would be interesting to obtain proper motion study of the HH knots to determine the orientation of the flow with respect to the plane of the sky. If indeed Haro 6-10 is in the plane of the sky and the density gradient in the cloud is such that it does not allow lateral expansion, it would be very difficult to detect the outflow further

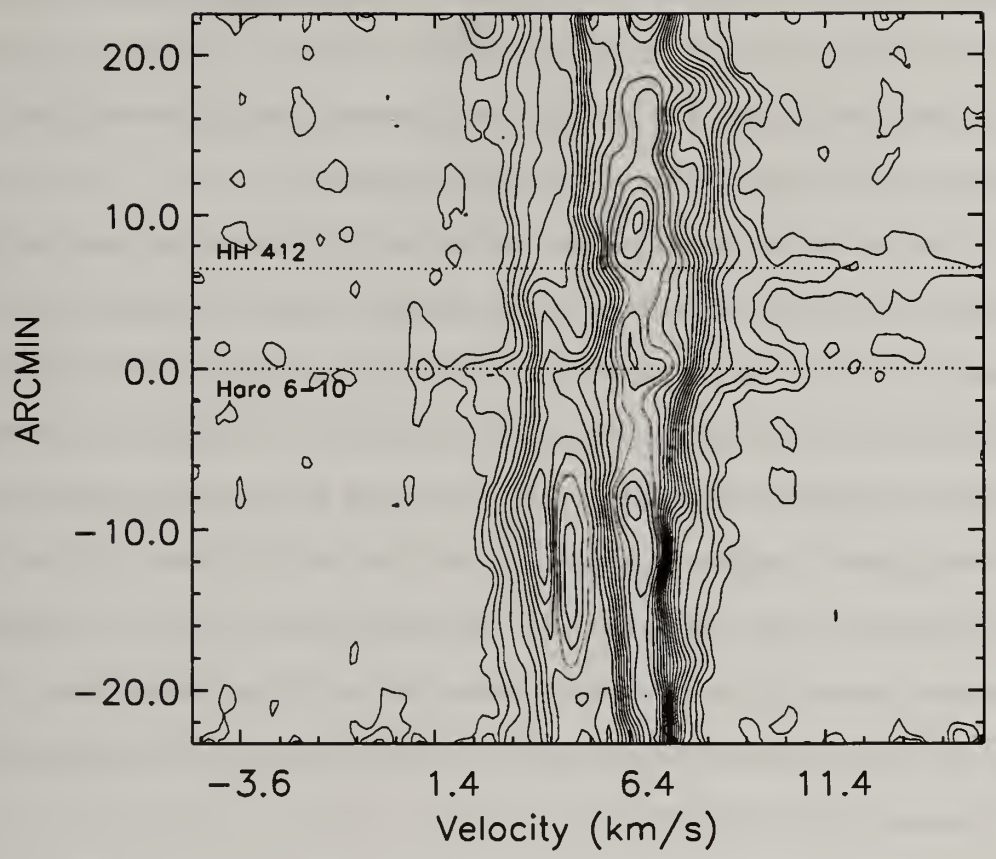

Figure 4.8 PV Cut Along The Haro 6-10 Outflow. PV cut is made along the axis defined by the parsec-scale HH flow, position angle 40°. Zero value on the y axis, is at the Haro 6-10 position. The cut is wide 5 pixels.

from the source. Haro 6-10 consists of a T-Tauri star and its IR companion. Since T-Tauri stars are past its main accretion phase, most of the ambient gas surrounding them is accreted, which allows outflow to laterally expand close to the star. Careful inspection of our maps shows that both blueshifted and redshifted gas overlap right at the star and they have also flattened morphology almost perpendicular at the outflow axis.

The next chunk of outflow gas detected is strictly confined to the HH 412 knot and it has the same elongated morphology as its optical counterpart. Therefore they seem to be created by the same mechanism. The HH knots are formed where the fast jet is interacting with the ambient gas. They can be found at the head of the jet or

along its body at the locations of internal working surfaces where the new ejecta is catching up with the previously ejected slow-down gas. The CO clump at HH 412 is detached from the Haro 6-10 source. It has small mass, and it is detected up to the projected velocities of 8 km s^{-1} from the line center.

Due to various contaminations, we had to use velocities far from the line core to study the mass distribution in the case of Haro 6-10. This could be another reason why there is so little mass recovered in the outflow. Observational studies show that outflows show a power law distribution of the mass with respect to the velocity offset from the cloud velocity. This distribution is such that most of the outflow mass is at low velocities. The first mass point that we account for, in Haro 6-10 outflow, is offset by 2.6 km s^{-1} from the line center. For the V_{LSR} of 6.4 km s^{-1} we calculated the outflow mass only for the points between 9-14 km s^{-1} and 0 to 2 km s^{-1}. Therefore we may be missing a significant fraction of the mass as it will be decreasing with the decreasing outflow velocity.

We find the slope γ in the mass-velocity distribution of the Haro 6-10 outflows to be around ~ 6. This value is much steeper than the average of $\gamma \sim 2$ reported for a collection of outflow sources (Richer et al., 2000). The steepening of the γ index is expected for the older outflows, where once accelerated ambient material will slow down leading to accumulation of slow material. Also, recent studies of the parsec-scale molecular outflows, show that many outflows show a so-called "broken power law", where mass at lower and higher outflow velocities have two different slopes. Usually when there is a broken power law in the mass-velocity relationship the slope at lower velocities is shallower than at higher velocities (see Stojimirović et al., 2006, for more details). In the case of Haro 6-10, we do not see a broken power-law, but a steep index which is as high as the high-velocity power-law index reported in other sources. It is possible that if we were able to disentangle the low-velocity component of the Haro 6-10 outflow from the ambient gas, it might have had a different, shallower

distribution. The broken power law is usually a good indicator of the jet entrainment model.

Lastly, we would like to compare Haro 6-10 outflow to the HH 300 parsec scale flow in the nearby B 18w cloud, studied by Arce & Goodman (2001a). Arce & Goodman (2001a) found that the HH 300 outflow has a very clumpy structure and they identified five ^{12}CO redshifted clumps with masses from 0.03 to 0.23 $M_{\odot}$ and radial velocities of about 3 km s^{-1} from the ambient cloud velocity. They also noted that the clumps have different position angles with respect to the driving source and concluded that the flow most likely precess with each clump corresponding to the different ejection event. The similarity of the HH 300 and Haro 6-10 outflow in terms of clumpy morphology and mass content is apparent. However while the redshifted clumps of HH 300 flow are found at different position angles with respect to the IRAS source the redshifted clump at HH 412 location in Haro 6-10 flow is found elongated along the jet (as is HH 412) axis defined by HH flow. The jet in the Haro 6-10 appears to have a stable orientation since all HH knots are found at 220° position angle. The HH 300 outflow exhibits larger impact on its host clout, with ^{13}CO line showing bipolar structure of the cloud gas at velocities close to the line center. Surprisingly, Haro 6-10 outflow does not seem to be affecting its host cloud's kinematics significantly.

4.6 Summary And Conclusions

We made large, sensitive, ^{12}CO J=1→0 and ^{13}CO J=1→0 maps of the Haro 6-10 region, over the full extent of the optical parsec-scale HH flow. Here we summarize our main conclusions:

1. The redshifted outflow component is clearly detected emerging from Haro 6-10 toward northeast, along the axis of optically defined parsec-scale HH flow.

2. Contamination from an unrelated foreground cloud along the same line of sight prevents a thorough study of the blueshifted outflow lobe, which we detect

centered on Haro 6-10 in the opposite direction from redshifted lobe, and in the velocity range from 0 to 2 km s^{-1}.

3. The mass and energies of the outflow are significantly smaller then those of the host molecular cloud. However, most of the mass might be missed due to an unrelated contamination at lower outflow velocities, along the same line of sight, and/or in the plane of the sky orientation of the outflow.

4. In the optical maps next to the HH 412, Haro 6-10 parsec scale flow is crossed by HH 414/413 flow. In CO data at the lowest redshifted velocities, there seem to be evidence of HH 414 IRS activity toward HH 413.

CHAPTER 5

L1617 OUTFLOW CASE STUDY

5.1 Introduction

The parsec scale Herbig-Haro flow located in the L 1617 molecular cloud in Orion B has a total extent of 7.7 pc and is one of the most impressive examples of its kind (Reipurth et al.. 1997). It consists of three HH objects: HH 111 lies close to the driving star IRAS 05491+0247 (hereafter IRAS 05491); HH 311 lies approximately 0.5° northwest of IRAS 05491; and HH 113 lies approximately 0.5 degrees southeast of IRAS 05491. All three HH objects are co-aligned and lie along a position angle of $\sim 15°$. HH 111 is associated with a highly collimated bipolar optical jet that extends for nearly 1 pc. This jet has been resolved into a series of small bow shocks by Hubble Space Telescope (Reipurth et al.. 1997b). The mosaic of optical and infrared data for the HH 111 jet has been shown in Figure 1.1. The combination of proper motion studies and velocity reveal that the jet is nearly in the plane of the sky with an estimated inclination of only 10° (Reipurth et al.. 1992). The knotty structure of the HH 111 jet has been also observed in H_2 (Gredel & Reipurth. 1994; Coppin et al.. 1998) and in centimeter radio continuum (Rodriguez & Reipurth. 1994).

A bipolar molecular outflow has also been detected associated with the HH 111 jet (Reipurth & Olberg. 1991). They found a short blueshifted outflow extending west of IRAS 05491 and a more extended redshifted outflow to the east. Higher angular resolution observations reveal that the blueshifted outflow is more collimated with a

collimation factor of 9 (Cernicharo & Reipurth, 1996). Interferometric observations of the blueshifted molecular outflow suggests that the emission forms a shell surrounding the HH jet (Nagar et al., 1997). Along the jet axis, but beyond the extent of the low-velocity bipolar outflow and optical HH 111 jet, several CO bullets have been detected up to distance of 300″ from IRAS 05491 and with space velocities as high as 500 km s^{-1} based on the small inclinations angle (Cernicharo & Reipurth, 1996; Hatchell et al., 1999). The extremely high-velocity CO emission may originate in jet gas that has cooled and become molecular (Hatchell et al., 1999).

The driving source IRAS 05491 is a CLASS I source with bolometric luminosity of 25 $L_\odot$ (Reipurth et al., 1993), embedded in the 30$M_\odot$ cloud core. Reipurth et al. (1999) studied the multiplicity of the HH 111 driving source and detected two 3.6 cm radio counterparts (VLA1 and VLA2) separated by 3″. They also detected an infrared jet that can be traced back to the VLA sources. VLA 1 has a quadrupolar structure which are interpreted as two radio continuum jets suggesting this may be a close binary. One of the radio jets is oriented with the HH 111 flow and the second is oriented at a large angle from the HH 111 flow and may be driven by the binary companion (Gredel & Reipurth, 1994). This second radio jet has both an optical counterpart (HH 121) and an associated bipolor molecular outflow (Cernicharo & Reipurth, 1996; Gredel & Reipurth, 1994). This second bipolar outflow has its blueshifted lobe northeast and its redshifted lobe southwest of VLA1. A molecular disk with an observed extent of $\sim$ 0.04 pc around the exciting source of HH 111 is identified from CS emission (Yang et al., 1997).

While the HH 111 flow represents the best example of jet-like HH flow with a well-defined jet head and bow-shock morphology (Reipurth et al., 1997b), the directional stability of the 7.7 parsec scale L1617 flow along that jet axis is unique. Numerous theoretical works examined the possible driving mechanism for such a system. The morphological characteristics of the HH 111 jet are best explained if variation in both

jet velocity and direction is assumed (Reipurth et al., 1997b; Raga et al., 2002). CO observations have been carried out in the past only covering the extent of the HH 111 jet flow (Reipurth & Olberg, 1991; Cernicharo & Reipurth, 1996; Nagar et al., 1997; Hatchell et al., 1999). We made sensitive, high spatial and velocity resolution maps at ^{12}CO and ^{13}CO J=1→0 wavelengths over the full 7.7 pc extent of the optical data. We find no signs of a comparable scale molecular outflow, but only the molecular outflow associated with the HH 111 flow that has been previously reported. We therefore study in detail only the properties of the molecular outflow associated with optical HH 111 flow.

5.2 Observations

L1617 was observed starting in October 2002 and continued over several observational seasons. Using On-The-Fly mapping technique (OTF) and a dual channel correlator (DCC) we obtained Nyquist sampled grids of both ^{12}CO and ^{13}CO J=1→0 transitions. By 2002, SEQUOIA had been updated from 16 to 32 pixels and the receiver was configured as a dual-polarized 4×4 array. The orthogonal polarizations were averaged to enhance the signal-to-noise ratio (S/N). The OTF data were reduced with the "OTFTOOL" software and data analyzed in IDL. The FCRAO 14 m telescope's half-power beamwidths are 45″ and 47″ for ^{12}CO and ^{13}CO transitions respectively. The antenna temperatures were corrected for the main beam efficiencies of 0.45 for ^{12}CO and 0.5 for ^{13}CO.

The channel spacing for the data presented here is 0.14 km s^{-1}and the mean rms is 0.55 K per channels for ^{12}CO and 0.31 K per channel for ^{13}CO.

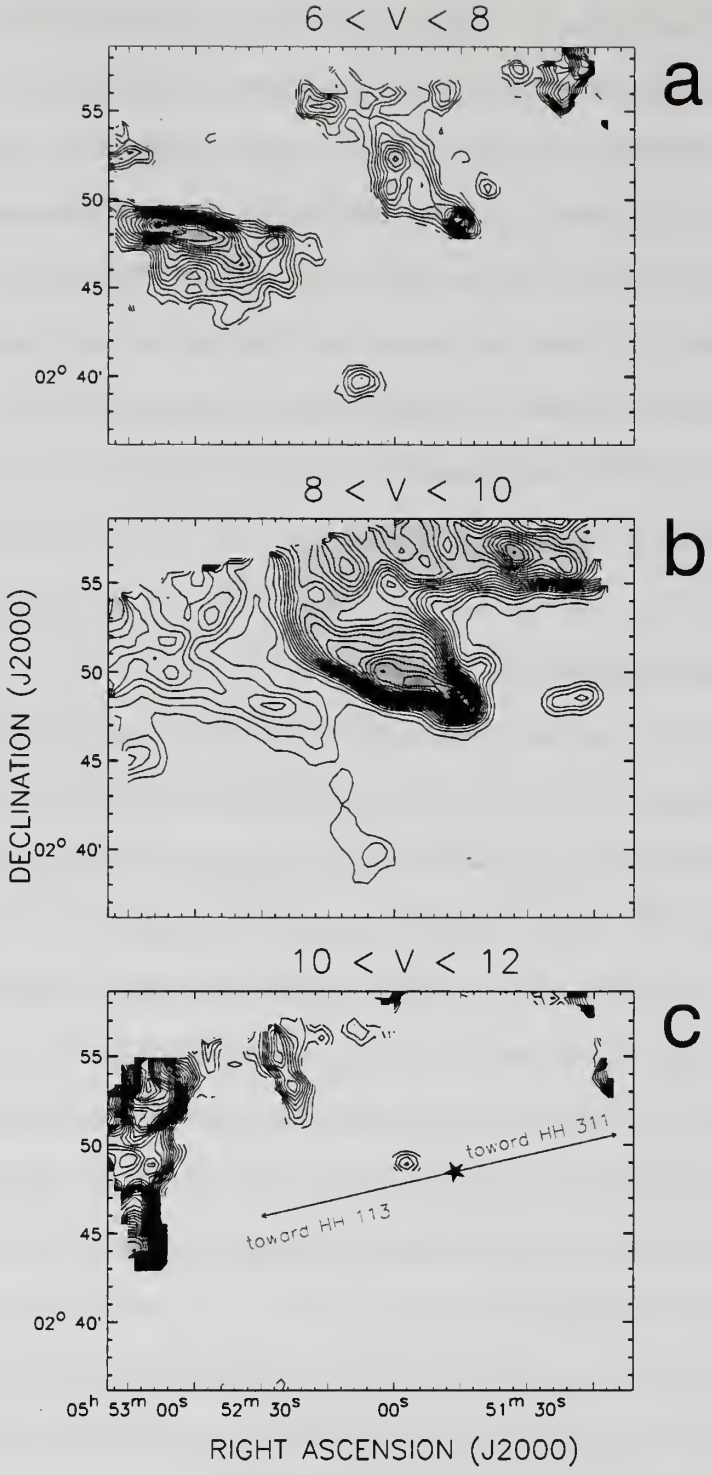

Figure 5.1 ^{13}CO J=1→0 channel emission on 7.7 pc scale in L 1617. The ^{13}CO emission is integrated in different velocity intervals. The star in the center of the map corresponds to the VLA 1 source, while HH 113 is found toward southeast and HH 311 toward northwest (crosses in the map)

5.3 Morphology Of The Cloud and Outflow Emission

5.3.1 Cloud Emission

A ^{13}CO map of the entire L 1617 complex covering an area of one square degree was made by (Bally et al., 1991). Their map revealed the clumpy, filamentary appearance of the L1617 cloud. In Figure 5.1 we show the part of the L 1617 cloud covered in our ^{13}CO observations. Figure 5.1*b* panel best shows the filamentary branches seen in the L 1617 cloud. The OB star association in Orion Ia is located southwest from the L 1617 cloud, and the cometary appearance of the cloud is likely a consequence of the strong influence of this association on the cloud. The HH 111 VLA source is found close to the cloud boundary in one of these long filaments. This filament has an abrupt edge in ^{13}CO emission, and appears cometary, with a "head" that points toward the southwest OB star association (see Figure 5.1*b*) The cloud is extended and lies mostly to the northeast of HH 111. However, the large-scale HH outflow is largely directed into region devoid of molecular emission.

5.3.2 Parsec Scale CO Morphology

In Figure 5.2 we show the ^{12}CO J=1—0 emission integrated in different velocity intervals. This figure shows the molecular emission over the *full* 7.7 pc extent of optical HH flow in L 1617 and beyond. The star in the center of the map corresponds to the VLA 1 source and HH 111, and at all velocities shown in Figure 5.2, we detect CO emission. The terminating points of the parsec scale optical outflow are HH 113 found toward the southeast and HH 311 found toward the northwest and these HH objects are marked with crosses in Figure 5.2. Along the outflow axis defined by HH 113, HH 111 and HH 311, we find little CO emission present at any velocity. Around HH 311 there is no CO emission at any velocity interval. We averaged the ^{12}CO spectra in the small area surrounding the HH 311, and even in the averaged spectrum no CO emission was detected. The optical data also indicated very low extinction

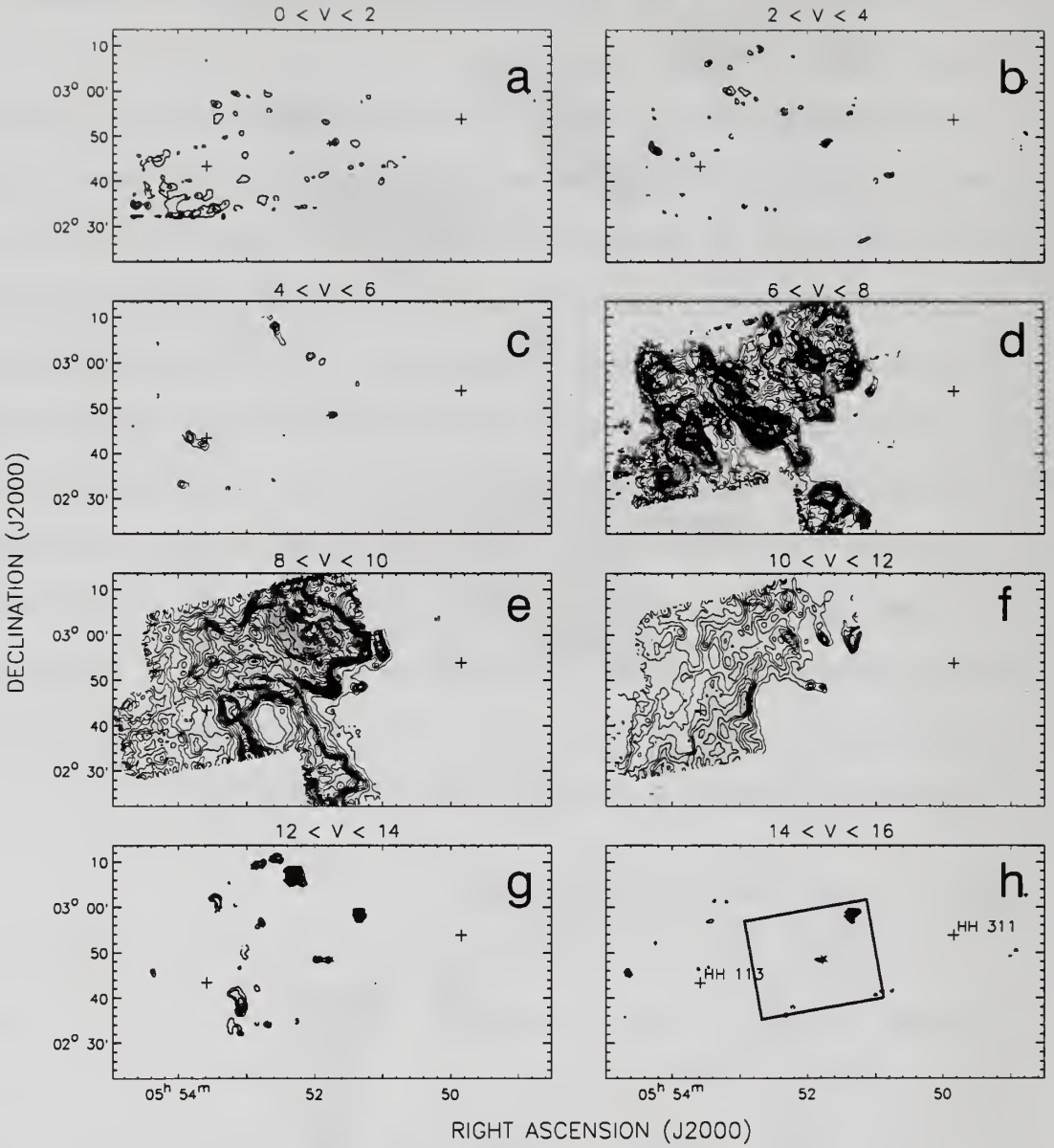

Figure 5.2 ^{12}CO J=1→0 channel emission on 7.7 pc scale in L 1617. The ^{12}CO emission is integrated in different velocity intervals associated with 7.7 pc extent of optical HH flow in L 1617. Star in the center of the map corresponds to the VLA 1 source, while HH 113 is found toward southeast and HH 311 toward northwest (crosses in the map). In the panel *h* the drawn box shows the sub-region mapped in ^{13}CO which was shown in the Figure 5.1

toward HH 311 as background stars are clearly visible. Therefore, it is clear that HH 311 lies entirely outside the L 1617 cloud, and hence, there is no molecular gas to be entrained by the flow.

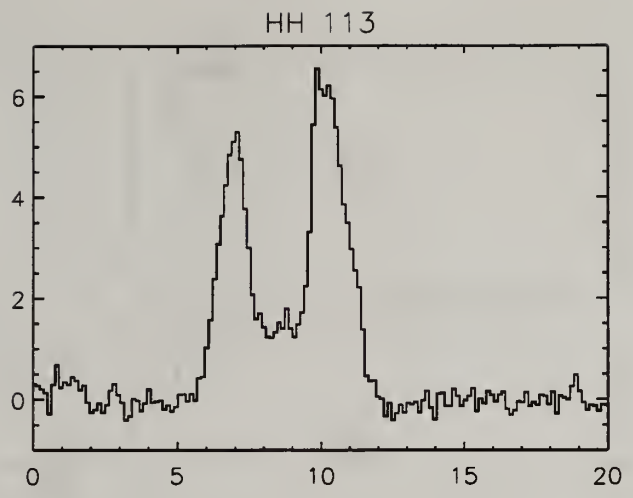

Figure 5.3 HH 133: ^{12}CO J=1→0 spatially averaged spectra. ^{12}CO J=1→0 spatially averaged spectra at the location of HH 113

Toward HH 113 the situation is more complex. Strong CO emission is seen over the velocity range of 6 to 12 km s^{-1} (see Figure 5.2*c*). Weak, higher velocity gas is found near HH 113 in the 4 to 6 km s^{-1} range. However since the optical knots comprising HH 113 are all redshifted (as would be expected for the overall bipolar geometry of the flow), it is unlikely this emission is a molecular counterpart to the HH object. This emission is part of more complex and extended emission that lies across the axis of the optical flow (see panels *d-f*). The spatially averaged ^{12}CO spectrum toward HH 113 is double peaked, with components at 7 and 10 km s^{-1} and is shown in Figure 5.3. The rest velocity of the L 1617 cloud is $\sim$ 8.8 km s^{-1}. Therefore both of these components have a slight offset from the L 1617 cloud velocity. In addition, the large 3 km s^{-1} velocity separation between the two peaks in Figure 5.3 indicates that it is less likely to be due to self-absorption within a single cloud, but rather traces unrelated multiple component CO emission along the same line of sight. If so, identifying any outflow component from the L 1617 towards HH 113 becomes extremely confused.

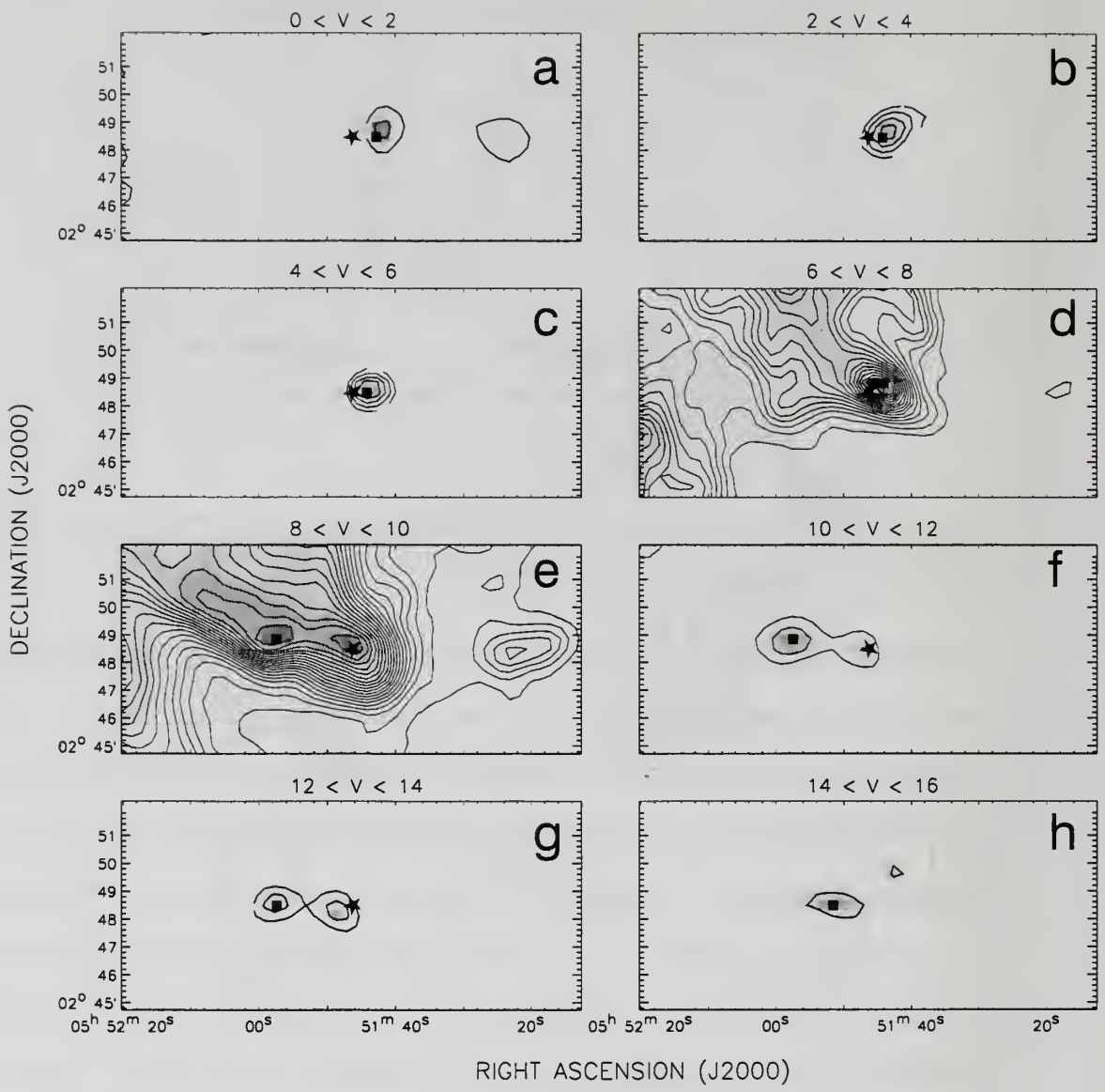

Figure 5.4 ^{12}CO J=1—0 channel emission on HH 111 scale in L 1617 emission. The integrated intensity ^{12}CO emission in different velocity intervals associated with the HH 111 flow in L 1617. The star in the center of the map corresponds to the VLA 1 source

Because of the lack of emission in the HH 311 region and confusion in the HH 113 region. we henceforth restrict our molecular flow study to the components of the flow in and around the HH 111 optical flow. We show the outflow in the inner 20×8 arcmin region around the driving star in Figure 5.4. The blueshifted outflow is

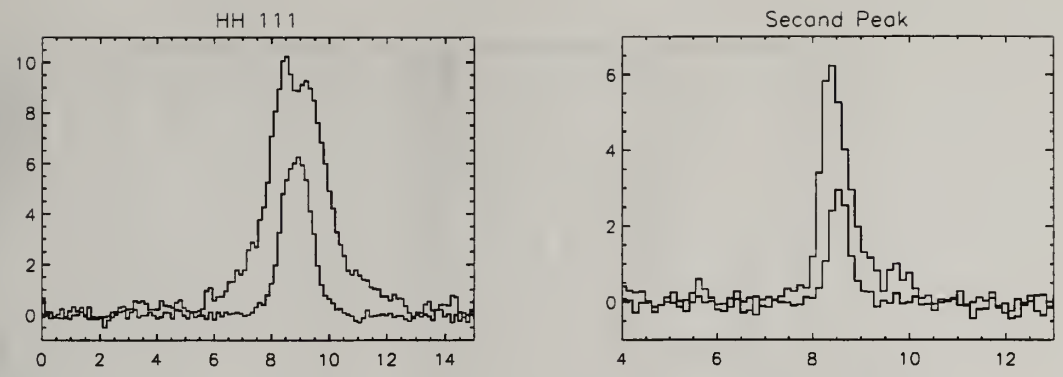

Figure 5.5 HH 111 and nearby ^{12}CO J=1→0 spatially averaged spectra. ^{12}CO J=1→0 spatially averaged spectra at the location of HH 111 and the location of the Second Emission Peak found near VLA 1 and prominent in Figure 5.4

found west of the VLA source (best seen in panels *a–c*). while the redshifted outflow is found east (see ipanels *f–g*). The redshifted lobe is more extended. reaching ∼ 0.8 pc. The redshifed lobe is entirely contained with the filament described earlier. On the contrary. the blueshifted lobe extends to the edge of the cloud as delineated by the ^{13}CO emission. and may explain its shorter extent compared to the redshifted lobe. The blueshifted CO emission has an extent of only ∼ 0.25 pc (2′). The other interesting feature of the molecular outflow is that the extended redshifted lobe has a slightly different position angle as the optical flow. While the optical flow has PA of ∼ 15° the redshifted flow is oriented nearly east-west.

The position velocity (PV) diagram along the HH 111 jet axis is shown in the Figure 5.6. The PV plot resembles that of Haro 6-10 in that it is rather featureless. The highest velocity emission is present immediately at the driving source in both the blueshifted and redshifted outflows. The short extent of the blueshifed lobe is also evident in PV diagram, since beyond 2′ in extent the outflow ends. Only a few arcminutes beyond the outflow. the cloud emission is also rapidly declining. The redshifted lobe is more extended. but shows little velocity structure. The maximum velocity is reached near the driving source and decreases slowly over the length of the outflow. In the Figure 5.7 we show the PV cut made along the axis of the 7.7 pc

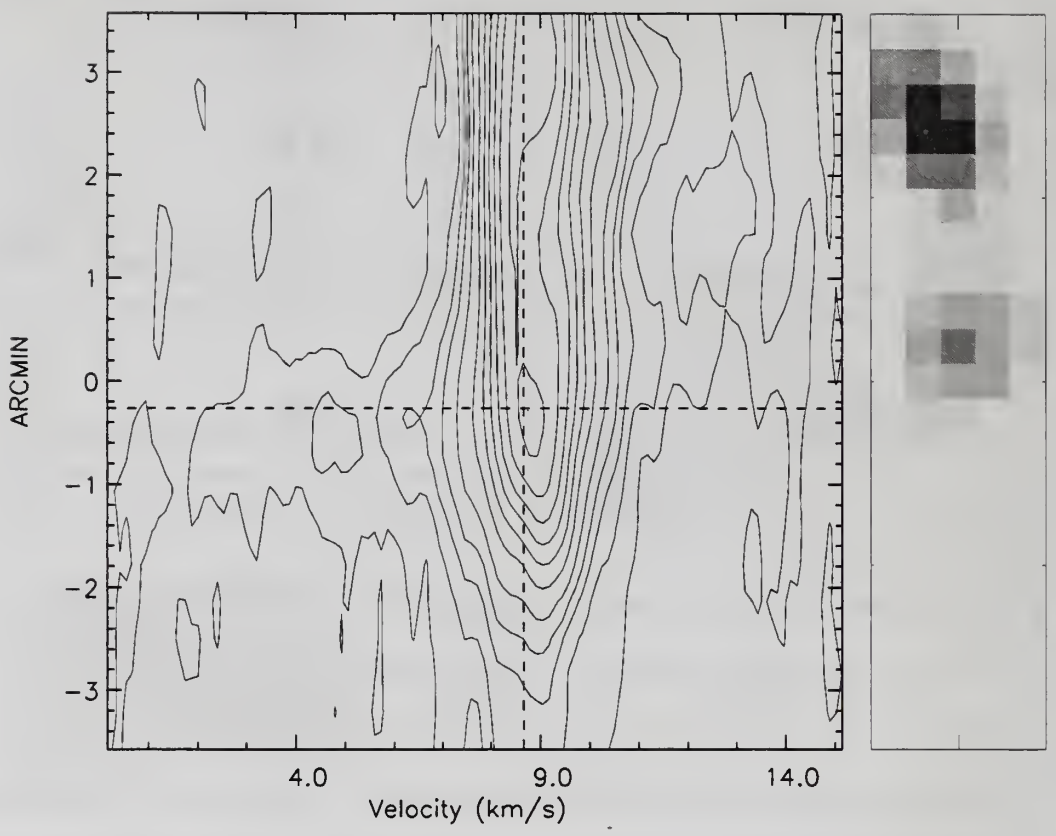

Figure 5.6 L 1617 position velocity. Position velocity cut along the HH 111 jet axis. Horizontal dashed line marks the location of HH 111 VLA source, while vertical dashed line is at V_{LSR} velocity. The integrated intensity image in 10 to 16 km s^{-1} is toward right. The image is rotated for 15° and displaced molecular outflow has north-south orientation

outflow with HH 311 and HH 113 at the edges of these plot (each has an offset of $\pm$ 26′ from HH 111 which is at the 0.0 position in the Figure 5.7). The ambient gas component in this PV plot, shows emission in the wider velocity range beyond the extent of the red lobe (positive y offsets), while toward blueshifted lobe the velocity component narrows and vanish when the cloud end is reached (negative y offsets).

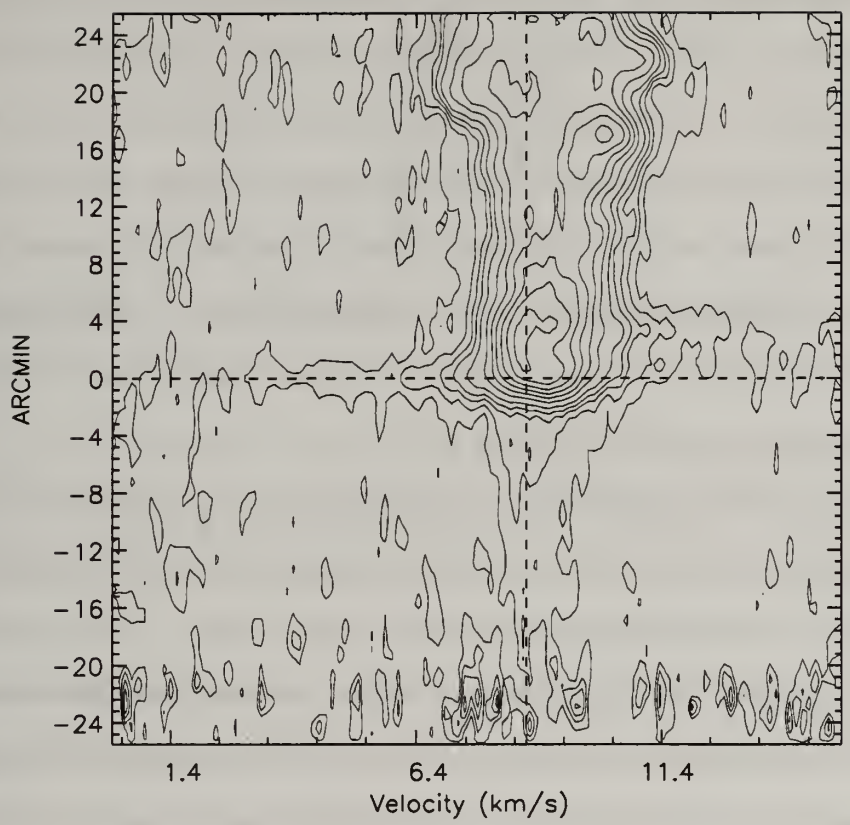

Figure 5.7 L 1617 position velocity. Position velocity cut along the 7.7pc scale HH outflow axis. Horizontal dashed line marks the location of HH 111 VLA source, while vertical dashed line is at V_{LSR} velocity. The HH 311 source is found at +26′ offset on the y axis, while HH 113 is at -26′ offset.

5.4 Mass and Energetics

As was discussed in the previous chapters of this dissertation, the availability of both CO tracers over the full extent of the outflow emission allows the implementation of the "velocity dependent opacity correction" method (Bally et al., 1999; Yu et al., 1999) in the outflow mass analysis. We compute the spatially averaged ^{12}CO and ^{13}CO spectra along the extent of the outflow. We make the following assumptions: for the blueshifted gas we find the ^{12}CO integrated intensity in the velocity range from 0 to +6 km s^{-1}, while in the redshifted lobe we use +10 to +16 km s^{-1} velocity range. These velocity intervals are not symmetric with respect to the V_{LSR}, but they

best represent the outflow emission in both lobes, as it can be seen in Figure 5.4. We then select, in both ^{12}CO and ^{13}CO data cubes, only spectra at the location where integrated ^{12}CO intensity in the given velocity range is at least one third of the maximum integrated intensity. The idea behind this approach is to select spatial locations that most contribute to the CO outflow emission. To increase the signal to noise ratio in the line wings, we smooth the data in 1 km s^{-1} wide velocity intervals, at velocities less than +5 km s^{-1} and at velocities larger than +10 km s^{-1}. The resulting spectra are shown in Figure 5.8.

The ^{13}CO outflow emission in the averaged specta is too weak to implement a velocity dependent correction. We have instead integrated over the redshifted emission (2 to 6 km s^{-1}) and the blueshifted emission (10 to 14 km s^{-1}) to estimate the global optical depth of the CO. ^{13}CO emission was not detected in either velocity intervals, so we can only determine a limit to the ^{12}CO to ^{13}CO ratio. In the redshifted gas we find that the ratio is > 84 and in the blueshifted gas the ratio is > 55, both are 3 sigma limits. However these, lower limits are somewhat suspect because of the ^{13}CO baselines in the averaged spectra are not flat. Based on these results, we will assume that the ^{12}CO outflow emission is optically thin.

To derive the column density of the gas in the outflow we follow the process outlined in the previous chapters, but assuming that the ^{12}CO emission is optically thin. As before, from the column densities we can derive the outflow mass. For the blueshifted lobe we estimate the mass in the velocity range 0 to 7 km s^{-1} and for the redshifted lobe we estimate the mass in the 10 to 16 km s^{-1} velocity range. The resulting mass, calculated for an assumed 25 K excitation temperature, is ~ 0.08 M$_\odot$ in the blueshifted lobe and ~ 0.15 M$_\odot$ in the redshifted lobe. In the redshifted velocity range, only seven position had positive integrated intensities.

We have also determined the mass as a function of outflow velocity to estimate the slope, γ, in the log-log M-v plot. Due to the small range in velocity where there

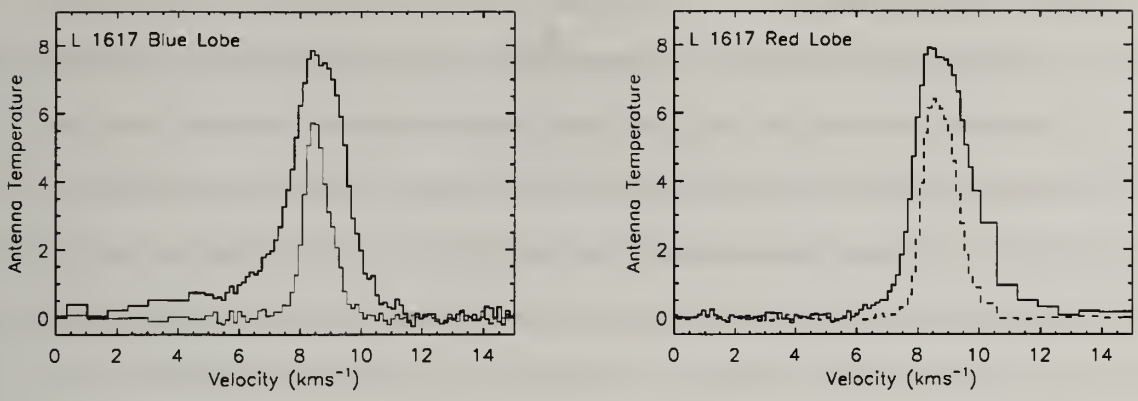

Figure 5.8 L 1617 Blue and Red lobe Averaged Spectra. Spatially averaged ^{12}CO and ^{13}CO spectra in the blueshifted and redshifted lobe of the L 1617 cloud. Spectra are shown in their full velocity resolution in 5 to 10 km s^{-1}. and with binned to 1 km s^{-1}velocity been at smaller (larger) velocities in the blueshifted (redshifted) lobe.

is detected outflow emission, we do not perform any binning in the log velocity space but we fit the data at their full velocity resolution. In the blueshifted lobe we fit only first eight points and find steep slope $\gamma = 4.5 \pm 0.4$. The rest of the points follow the general distribution captured in the averaged spectra (see Figure 5.8). i.e fluctuate around zero value and therefore depart in non uniform manner from the line fit in the log-log plot. For the redshifted gas mass has a broken power law distribution with $\gamma_{low} = 2.4 \pm 0.3$ and $\gamma_{high} = 5.4 \pm 0.4$. Both M-v plots are shown in Figure 5.9.

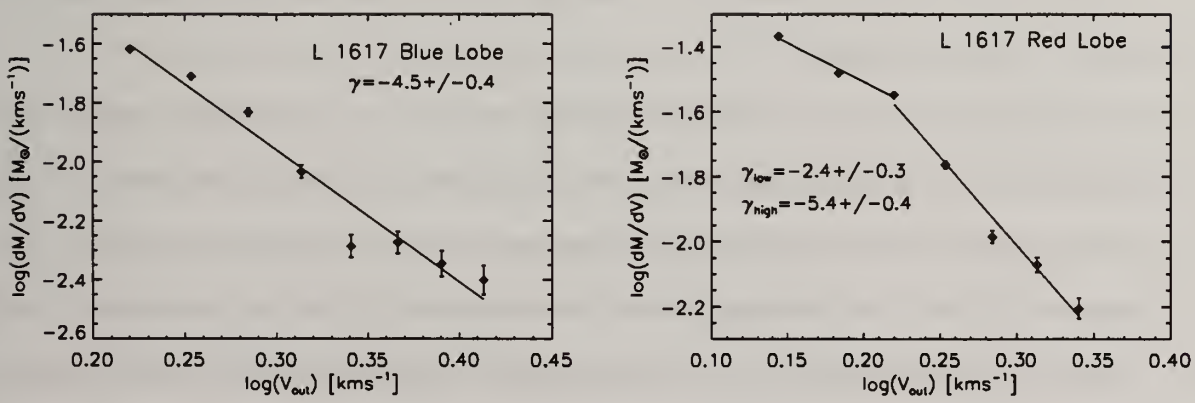

Figure 5.9 L 1617 Blue and Red MV. Mass velocity relation for the blueshifted and redshifted lobes in HH 111 outflow.

5.5 Discussion

In the previous chapters we have seen that by obtaining large, sensitive maps we were able to find new and/or report larger extents to outflows in regions where previous observations failed or missed the full extent. With the same goal, we pursued the study of the outflow entrained by the HH 111 - HH 113- HH 311 jet. While the optical flow has 7.7 pc extent and amazing directional stability, the molecular outflow is of a smaller extent and mostly related to the optically revealed HH 111 jet. Our ^{13}CO map indicates that the driving source of the HH 111 jet is found toward the edge of the L1617 cloud and that the blueshifted outflow to the northwest is launched into a region largely devoid of molecular cloud material. The terminating point at HH 311 of the optical many parsec-sized flow to the north-west has no CO emission present and is a regions of low extinction. This HH source is located well beyond the boundaries of the molecular cloud. At the opposite end of the parsec-scale flow at HH 113, more complex CO emission is found. The emission in the vicinity of HH 113 has two velocity components, neither we believe are related to the flow. At HH 113 we should see redshifted entrained molecular gas, however no evidence for such gas is found. Therefore we conclude that molecular outflow is associated with only the inner part of the 7.7 pc optical flow around the HH 111 jet. We restricted our outflows studies to the emission associated with HH 111 and have analyzed the propertis of this $\sim$1 pc scale outflow.

Blueshifted lobe of the HH 111 molecular outflow is quite short with its full length equivalent to only three beam sizes of the FCRAO telescope at CO frequencies. Therefore its shell structure seen in the interferometric maps of CO is not resolved in our data set. Such a morphology has been best modeled by the jet entrainment mechanism. The steep slope (γ $\sim$4.5) of the mass distribution in the mass-V relation, supports such jet entrainment. The structure of the position-velocity plot also suffers from the low spatial resolution of our data, but there seems to be some indication in

the blueshifted lobe that jets play an important role in the gas entrainment. Namely, the large range of velocities is present around the area where maximum velocity in the lobe is detected, which is in agreement with the jet bow shock models.

Although of a larger spatial extent, the emission within redshifted lobe of HH 111 outflow has slightly lower velocity and the CO emission is weaker. Two CO peaks in the velocity integrated line maps are also identified as the highest velocity sites in the PV plot. Multiple acceleration regions are best explained by the bow shock models where velocity is variable. In addition steep and broken power law in the mass-V relation (γ_{low} ~2.4 and γ_{high} ~5.4) supports jet entrainment for the red lobe as well.

The total mass entrained in the outflow is relatively small compared to the total mass of the cloud, found to be 110 $M_{\odot}$. We find that blueshifted lobe contains only 0.08 $M_{\odot}$ while redshidted lobe has 0.15 $M_{\odot}$. Relatively small mass amount can be a consequence of no optical depth correction at low outflow velocity (inner line wings) where most of the mass is found. Based on our previous experience, when application of the velocity dependent opacity correction method was possible, the most massive, lowest outflow velocity points, have been corrected the most, i.e. sometimes the corrected mass was as an order of magnitude larger. Since this gas is launched toward the edges of the cloud and beyond cloud extent, most of its momentum and energy is dissipated in the interstellar medium.

Through study of physical characteristics of the molecular outflow via their CO morphological maps, mass-V and PV distributions we have been able to constrain the entrainment mechanisms responsible for outflow generation in the previous chapters. Although many sources show signature of both wind and jet entrainment, the molecular outflow in L1617 shows clearly only jet signatures. From its tight morphological relation to the optical jet flow, through steep mass velocity slopes in both lobes. Once again PV plot turned out to be harder to relate to theoretical models since no clear

spur or parabolic structure has been identified. However the velocity field within the both lobes is most consistent with jet entrainment.

CHAPTER 6

MOLECULAR OUTFLOWS IN NGC 2071

6.1 Introduction

NGC 2071 is a reflection nebula located in the Lynds 1630 (Orion B) molecular cloud at a distance of 390 pc (Anthony-Twarog, 1982). Approximately 4′ north of the NGC 2071 reflection nebula lies the ∼0.5′ diameter infrared cluster NGC 2071IR (Persson et al., 1981) that has been the target of numerous studies. The infrared cluster has been resolved into eight distinct near-infrared sources (Walther et al., 1993) with a total luminosity of 520 $L_\odot$ (Butner et al., 1990) suggestive of intermediate-mass young stars.

Centered on the infrared cluster is a powerful bipolar molecular outflow first detected by Bally (1982). This outflow has been extensively studied in CO emission (Snell et al., 1984; Scoville et al., 1986; Moriarty-Schieven et al., 1989; Kitamura et al., 1990) and it is one of the most energetic bipolar outflows known, exhibiting full velocity extent in CO emission of over 100 km s^{-1} (Chernin & Masson, 1992; Chernin & Welch, 1995). The outflow reaches ∼ 5′ in length (∼ 0.6 pc) along the northeast-southwest direction (Snell et al., 1984). In contrast, the extremely high velocity CO emission is confined within 1.′5 of the center. The observations of Moriarty-Schieven et al. (1989) and Kitamura et al. (1990) reveal a shell-like morphology and it was suggested that the outflow may be wind-driven. Although this outflow does not belong to the class of parcsec scale HH flows, it is associated with shocked molecular

hydrogen emission at 2.12 μm (Lane & Bally, 1986; Burton et al., 1989; Garden et al., 1990). The molecular hydrogen emission has a broad velocity width (Persson et al., 1981) and has a similar bipolar morphology as the molecular outflow (Aspin et al., 1992). More extensive imaging of the H_2 emission (Eislöffel, 2000) reveal complex emission with multiple filaments and bow-shaped knots extending for more than a parsec in length. Eislöffel (2000) find evidence for the presence of multiple outflows. A single HH knot, HH 437, has been reported close to the center of the molecular outflow (Zhao et al., 1999). The absence of many HH objects may be due to the large visual extinction to this star forming region.

Three radio continuum counterparts to the IR sources were reported by Snell & Bally (1986) and these were surrounded by weak, extended radio emission. Further radio continuum observations and observations of H_2O masers (Smith & Beck, 1994; Torrelles et al., 1998) suggest that both IRS 1 and IRS 3 have strong winds and are surrounded by rotating circumstellar disks. The IRS 1 source has been suggested to be the outflow powering source of the observed bipolar molecular outflow because its dominates the luminosity in the region (Persson et al., 1981) and is located at the center of the bipolar H_2 outflow (Aspin et al., 1992). The outflow activity around IRS 3 was also suggested by Fabry-Perot images of the H_2 emission (Aspin et al., 1992). While IRS 1 dominates the luminosity at near-infrared wavelengths, IRS 3 is a significant contributor at longer wavelengths (Snell & Bally, 1986; Kawabe et al., 1989; Torrelles et al., 1998), which implies that the IRS 3 is a relatively less evolved object than IRS 1.

Although numerous molecular studies have been published on the NGC 2071 outflow, they were of a much smaller spatial extent. We have obtained a large, high sensitivity ^{12}CO J=1$\rightarrow$0 and ^{13}CO J=1$\rightarrow$0 maps of the NGC 2071 region and we report the detection of a new molecular outflows. The new bipolar outflow is located north of NGC 2071 is associated with one of the H_2 outflows detected by Eislöffel

(2000). In addition. we detect redshifted outflow emission south-east of the infrared cluster and may be a third outflow in the region. Our large-scale and sensitive images of the main molecular outflow show that it extends beyond the parsec-scale at its lowest velocities. We study the entrainment mechanism for all the outflows in the light of new theories and models and compare the results of this intermediate mass stars driven outflow with the results of the low-mass powered outflows.

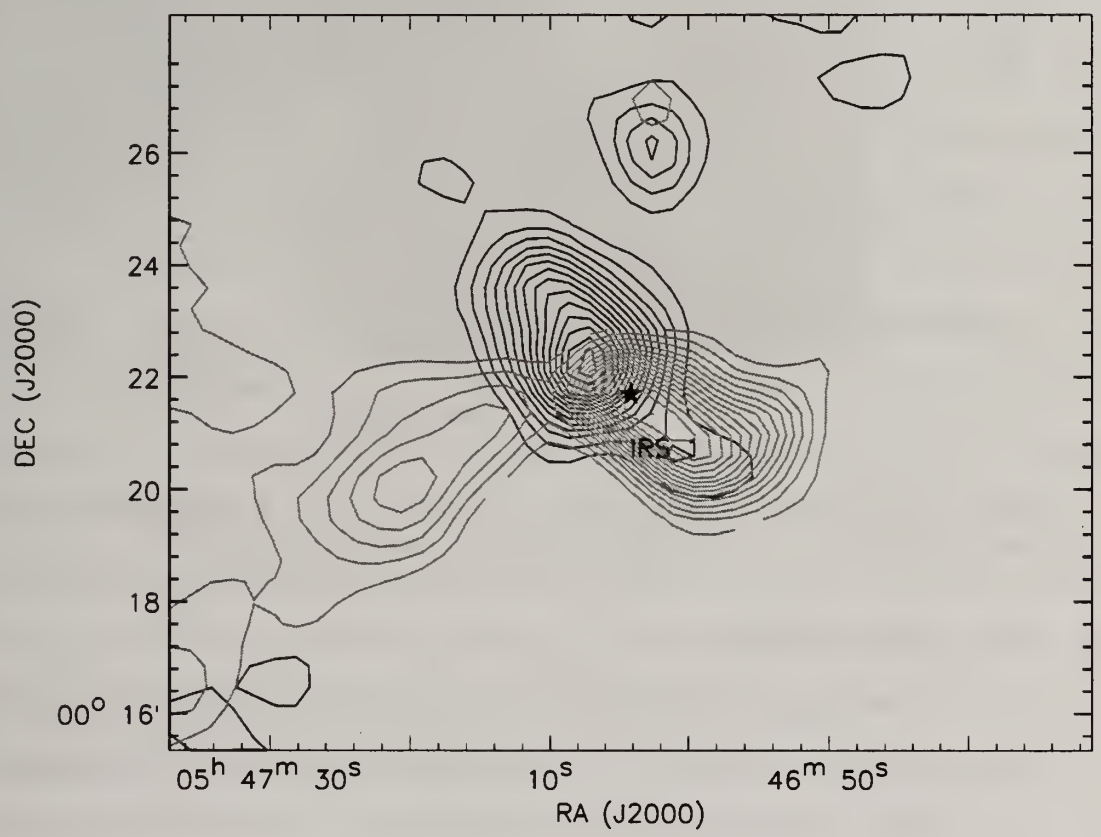

Figure 6.1 NGC 2071 Outflow. Outflow in NGC 2071 traced by ^{12}CO J=1→0. Blueshifted lobe is integrated in the velocity range 0 to 7 km s^{-1} and redshifted lobe in 12 to 20 km s^{-1}. Contours start at 20σ and go in steps of 10σ. The star marks the location of IRS 1 source which belongs to the NGC 2071 IR cluster. The notation will be kept on all following figures.

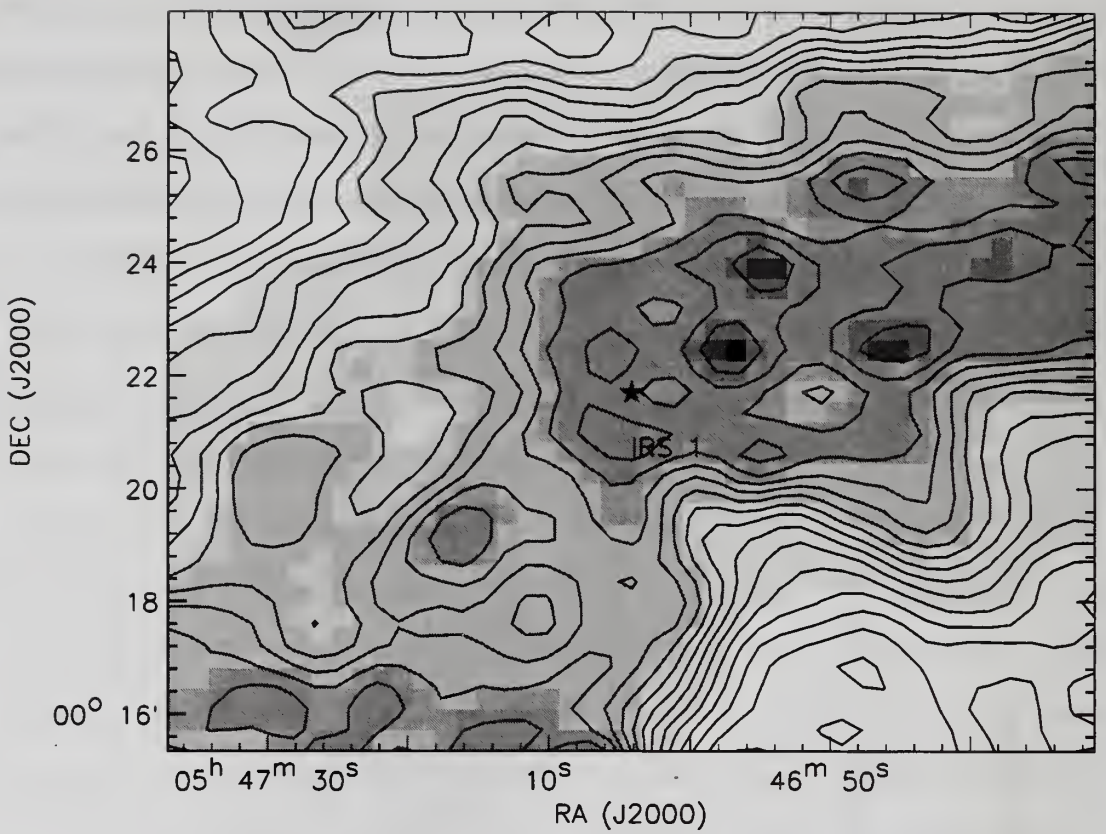

Figure 6.2 NGC 2071 Cloud Core. ^{13}CO J=1→0 line is integrated in the velocity range 6 to 12 km s^{-1}. Contours start at 10σ and go in steps of 5σ.

6.2 Observations

A full mapping of ^{12}CO and ^{13}CO in the J=1→0 transitions has been performed with the SEQUOIA receiver at the Five College Radio Astronomy Observatory (FCRAO) 14 m telescope using the on-the-fly mapping mode. The receiver is configured as a dual-polarized 4×4 array. The orthogonal polarizations of the SEQUOIA array are averaged to produce spectra with higher signal-to-noise ratio (S/N). The telescope's half-power beam widths are 45″ and 47″ for ^{12}CO and ^{13}CO transitions respectively. Channel maps as well as individual spectra were checked for any scanning artifacts, baselined and regridded to the 22.5″ sampled grid. RMS noise weighting was used to

combine the data. For all calculations. the antenna temperatures were corrected for the main beam efficiencies of 0.45 for ^{12}CO and 0.5 for ^{13}CO.

Both ^{12}CO and ^{13}CO spectra are smoothed to 0.13 km s^{-1} channel spacing. The resulting mean rms per velocity channel is 0.55 K for ^{12}CO and 0.31 K for ^{13}CO. Antenna pointing and focus were checked every few hours and corrected using SiO masers.

6.3 CO Results

In the following sections. we will examine in more detail the behavior of the ambient. blueshifted and redshifted gas using ^{12}CO and ^{13}CO J=1—0 data of NGC 2071. but first we present two overviewing figures of the region. In Figure 6.1 we show the ^{12}CO data integrated in the blueshifted and redshifted velocity range. This figure shows the well-known northeast-southwest bipolar outflow associated with IRS 1 (the main outflow. hereafter). An extension of the redshifted emission toward south-east is detected (the south-east outflow hereafter). This feature can be seen in the earlier results of Moriarty-Schieven et al. (1989). but was not fully mapped. In addition. a newly discovered smaller bipolar outflow located $\sim 4'$ north of the main outflow is reported (the north outflow. hereafter). Figure 6.2 shows the integrated ^{13}CO intensity in the region. and reveals an elongated cloud with peak near the infrared cluster.

6.3.1 Multiple Molecular Outflows

In the Figure 6.3 we show the ^{12}CO line emission in different velocity intervals. The mean velocity for the ambient cloud in NGC 2071 is found to be 9.2 km s^{-1} based on a Gaussian fit to the ^{13}CO averaged spectrum in the 2 $'$ area around IRS 1. Figures 6.3*a* through Figures 6.3*c* show the blueshifted emission while Figures 6.3*g* through Figures 6.3*i* show the redshifted outflow.

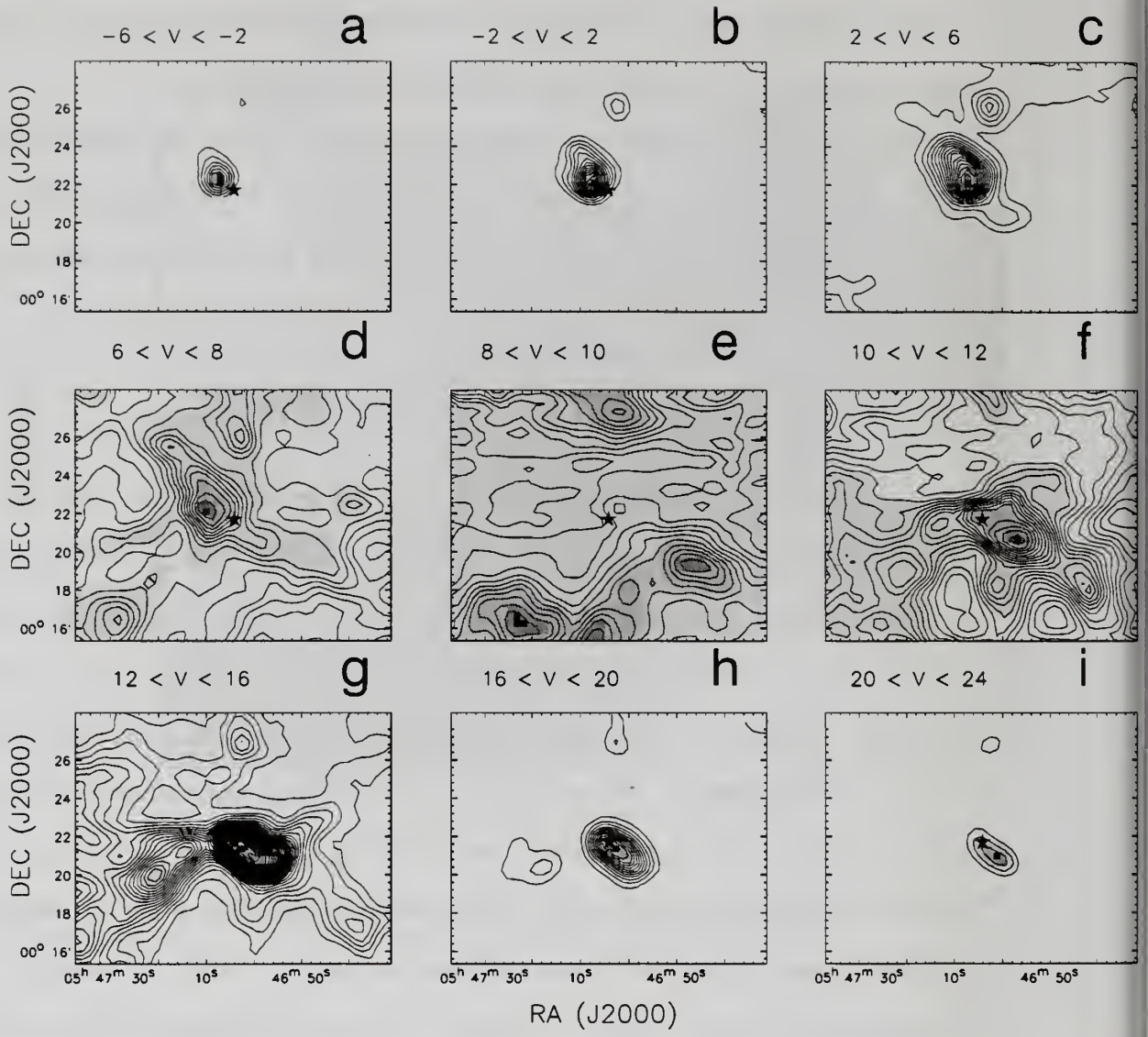

Figure 6.3 NGC 2071 Cloud Emission in ^{12}CO. Channel maps of ^{12}CO J=1→0 emission in NGC 2071. In each image contours start at 2σ and go in steps of 7σ in c-g and in steps of 5σ in all other panels.

What sets NGC 2071 outflow apart from the outflows presented so far is that the highest velocity emission is found very close to the IRS 1 location. At the highest blueshifted velocities the outflow emission is nearly unresolved. see Figure 6.3*a*. and at progressively less blueshifted velocities. the emission has larger extent and extends away from IRS 1. see Figure 6.3*c*. The highest velocity redshifted emission of the main outflow is found elongated in the south-west direction from the IRS 1. see Figure 6.3*i*.

The main redshifted lobe becomes more extended at lower outflow velocities and in Figure 6.3*g* the redshifted outflow has an extend of nearly 8′ from the IRS 1. Both the redshifted and blueshifted outflow emission show the largest spatial extent at the lowest outflow velocities. At very low velocities. see Figure 6.3*d* and Figure 6.3*f*. the outflow extent is over 15′ along northeast-southwest direction. which corresponds to 1.6 pc at the cloud distance. At these velocities there is some confusion with the ambient cloud emission (best identified in the Figure 6.3*e*). but outflow emission is clearly seen on top of the cloud emission.

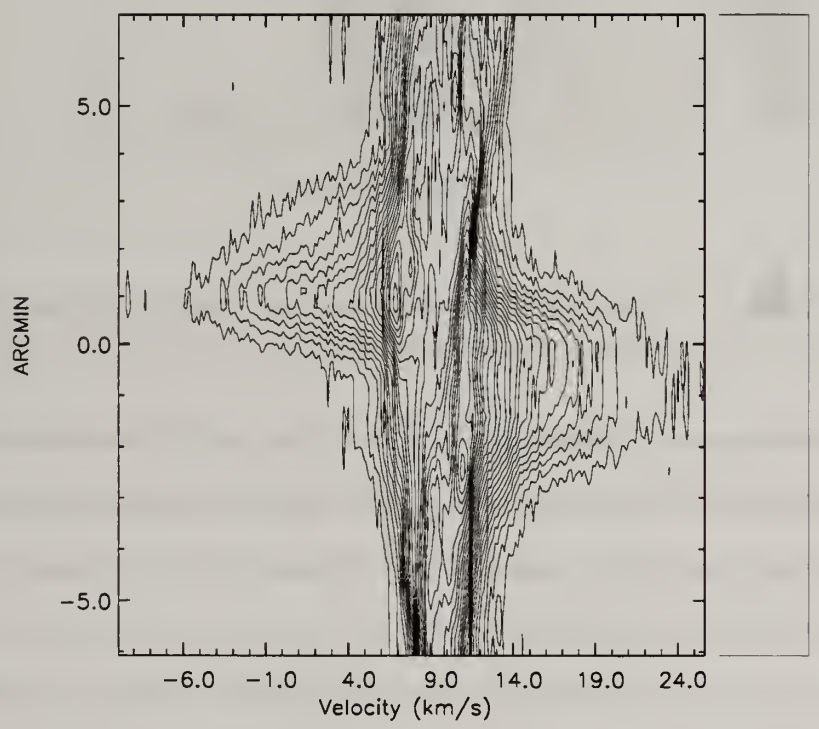

Figure 6.4 NGC 2071 PV. PV cut along 45° using ^{12}CO data. IRS source is in 0.0 position. The width of the cut is 4 pixels. The right panel is ^{12}CO integrated intensity. Two emission peaks correspond to the main and north outflows. respectively.

Over the full range of velocities where the main outflow is detected the north bipolar outflow is present. located at $\sim$ 4′ north from the main outflow. Although this outflow is of a smaller spatial extent and emission intensity. the velocity extent is

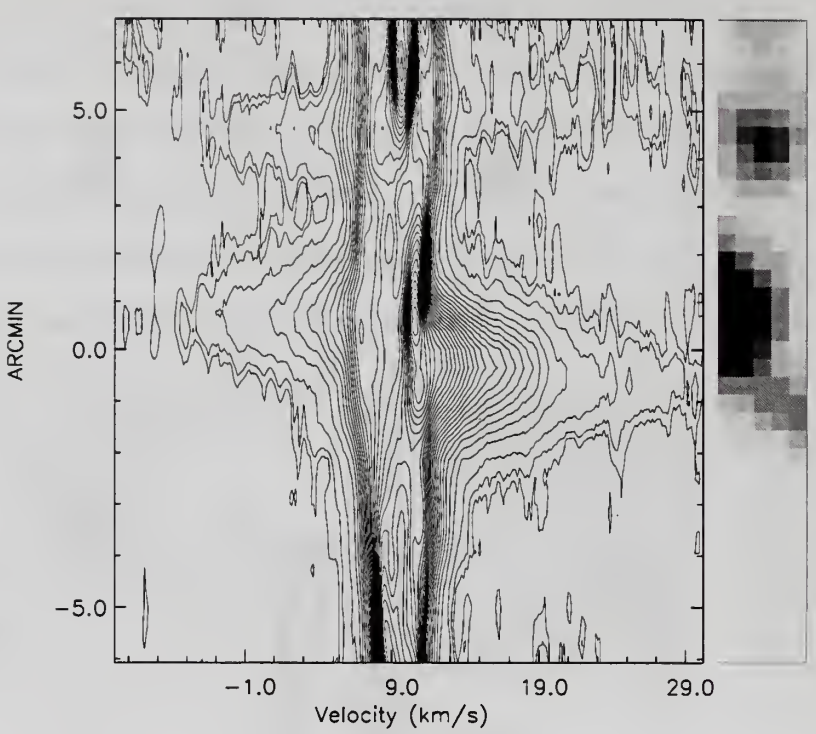

Figure 6.5 North Outflow PV. PV cut along 90° using ^{12}CO data. IRS source is in 0.0 position. The width of the cut is 4 pixels

nearly the same as of the main flow. And while it seems that our map fully covers the blueshifted lobe of the north outflow, the redshifted emission extends to the northern edge of our map. The second outflow is aligned with the 4′ long knotty H_2 XI flow reported by Eislöffel (2000). The peak of the CO emission for this second outflow is coincident with the originating point of the Eisloffel's H_2 XI jet, which is identified as a near-IR continuum source (Eislöffel, 2000). Recent SCUBA submillimeter dust observations (Mitchell et al., 2001) revealed the discrete continuum peak at the exact location of the second outflow (α(J2000) = $05^h47^m01^s.2$, δ(J2000) = 00°26′20″), which they identified as peak 1 (OriBsmm 1). Therefore, the north outflow is likely driven by a separate young star not belonging to the infrared cluster. We show in the Figure 6.15 a blow-up view of the north outflow together with the location of SCUBA source.

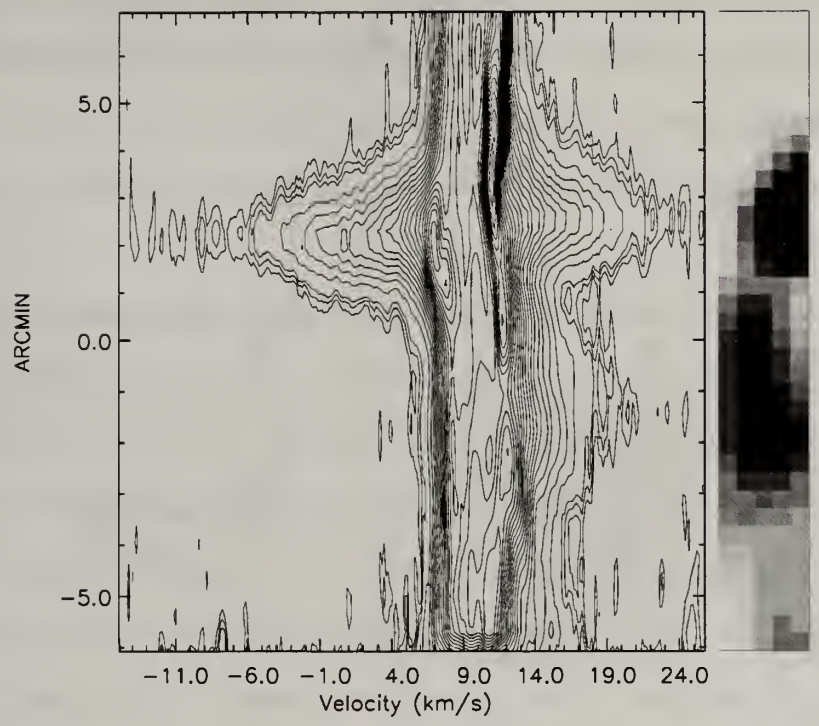

Figure 6.6 South-East PV cut. PV cut along 60° using ^{12}CO data. IRS 1 source is in 0.0 position. The width of the cut is 4 pixels

The south-east redshifted outflow, the third outflow in the region, is detected in the Figures 6.3*f.g.h* toward south-east from the main outflow. At lower velocities, Figure 6.3*g*, the south-east redshifted outflow and main redshifted outflow are connected via lower level contours. There is no obvious blueshifted counterpart present in the corresponding blueshifted velocity intervals. We examined the spectra at the location of the CO peak emission of this south-east redshifted outflow and the enhanced wing emission is found (look at the Figure 6.14 for the averaged spectra in the region). The signature of the south-east redshifted flow close to the IRS 1 has been present in previous maps (see for example Moriarty-Schieven et al. (1989)), but it has never been mapped along its full extent before. Compared to the Eislöffel (2000) H_2 map, the south-east outflow extents from H_2 VI knots toward H_2 VII and IX knots and beyond the extent of H_2 map. Mitchell et al. (2001) SCUBA submillimeter dust observations

identified the discrete continuum peak identified as OriBsmm 14, located at the head of the south-east outflow. The convenient location of the OriBsmm 14 makes it an attractive candidate for a potential driving source of the south-east outflow. We show a blow-up image of the south-east flow and mark the location of OriBsmm 14, see Figure 6.16.

The position-velocity cut through IRS 1 along the position angle 45°, is shows in the Figure 6.4 and reveals the bipolar outflow with very symmetric velocity fields in the blue- and redshifted outflow lobes. In both of these lobes the maximum velocity is reached very close to the IRS 1 source and it slowly decreases further from the IRS 1 source. Significant overlap of blueshifted and redshifted emission is present at IRS 1 location. The position-velocity cut through the second outflow, which alsoincludes the part of the main outflow, is shown in Figure 6.5. This figure shows clearly the bipolar nature of the north outflow and that its velocity extent is comparable to the main outflow. A region free of outflow emission is clearly present between the two outflows. The PV cut through south-east redshifted feature, see Figure 6.6 shows gas at velocities larger then ambient, present over 4′ of spatial extent. The maximum velocity of these gas is detected in the middle of the redshifted outflow lobe.

6.3.2 Cloud Core Emission

As ^{13}CO line is more optically thin than the ^{12}CO line, its photons come out from the deeper regions of the molecular cloud, and carry more information about the cloud core gas distribution. In the Figure 6.7 we show the ^{13}CO line emission in different velocity intervals. We see the main outflow in ^{13}CO is similar to the one in ^{12}CO. Surprisingly, at low velocities (Figure 6.7*d* and Figure 6.7*f*) we do not see the strong outflow features as seen in the same velocity intervals traced by ^{12}CO (see Figure 6.3*d* and Figure 6.3*f*). This is rather puzzling.

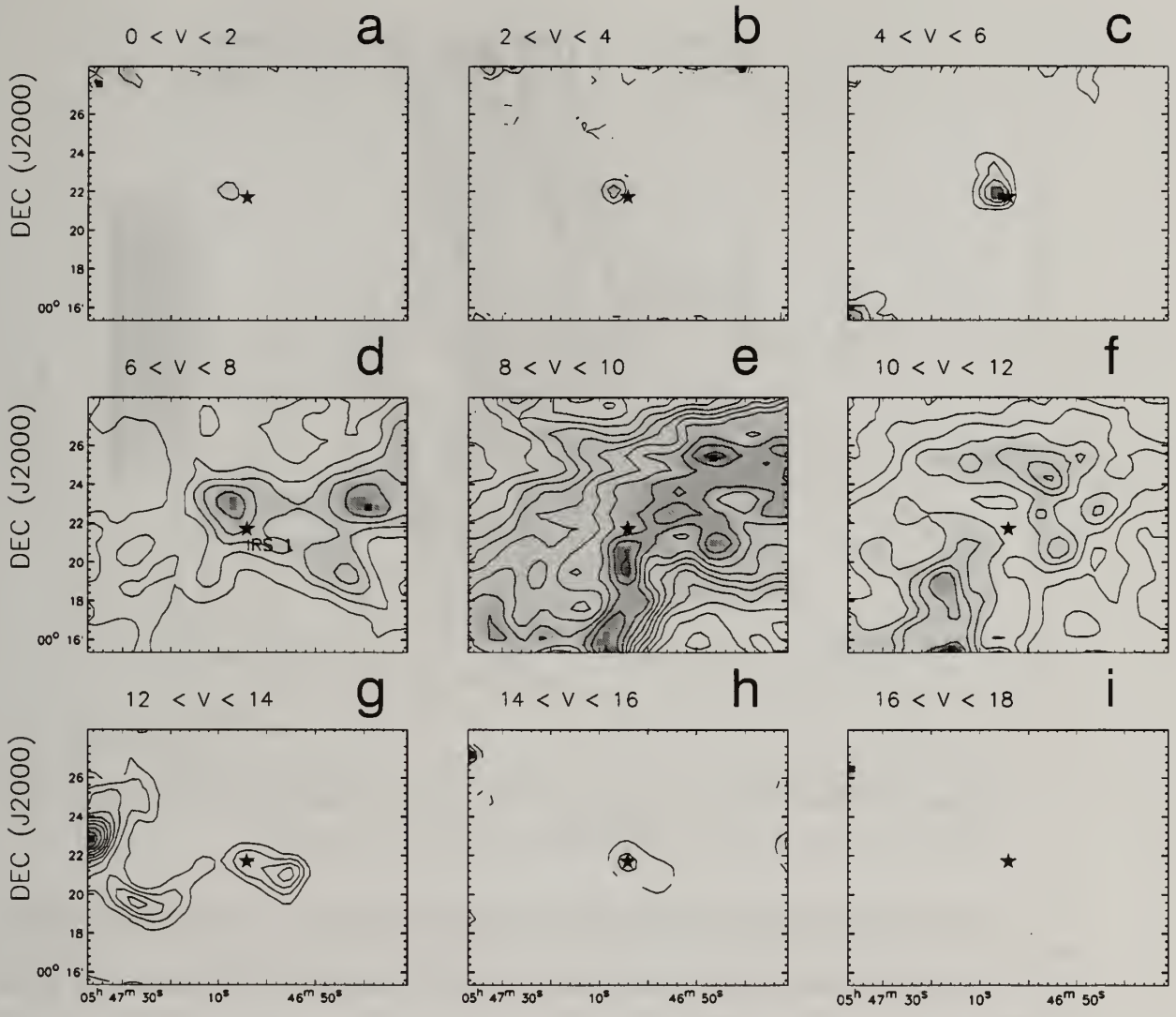

Figure 6.7 NGC 2071 Cloud Emission in ^{13}CO. Channel maps of ^{13}CO J=1→0 emission in NGC 2071. In each image contours start at 2σ (0.4 Kkm s^{-1} in unit velocity bin. wand 0.6 Kkm s^{-1} in 2 km s^{-1}bin) and go in steps of 5σ in e-f and in steps of 2σ in all other panels.

The outflow imprint to the gas kinematics is also evident in the position-velocity cut along the 45° axis that passes through IRS 1. see Figure 6.8. It also shows that the ^{13}CO maximum velocity is found right at the IRS 1 location. as in the case of the ^{12}CO emission.

Two additional column density peaks are detected in the Figure 6.7*g*: the first along the extent of the south-east redshifted outflow and the second, stronger peak

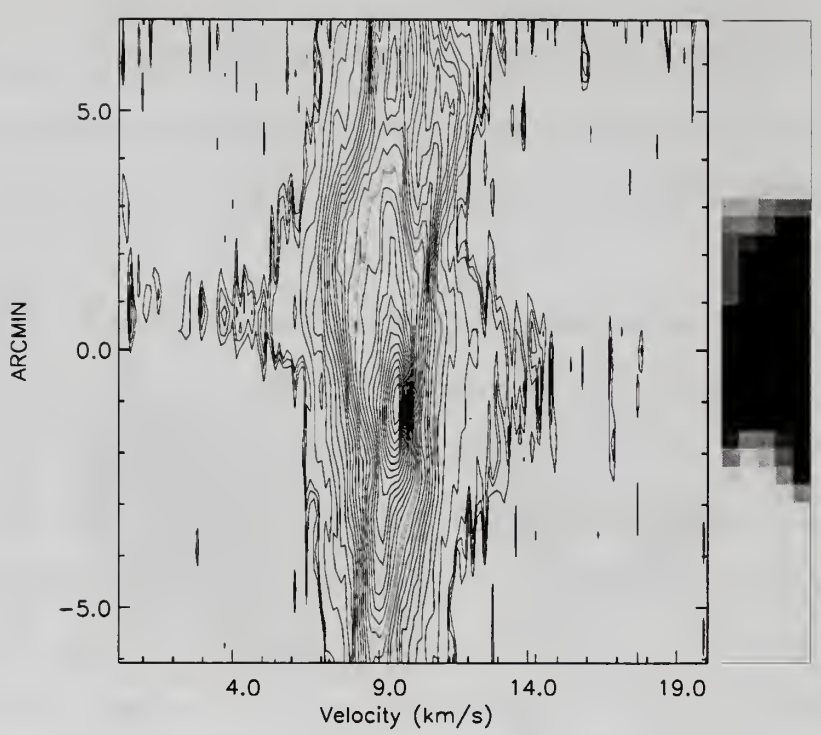

Figure 6.8 NGC 2071 PV Cut In ^{13}CO. PV cut along 45° using ^{13}CO data. IRS source is in 0.0 position. The width of the cut is 4 pixels

toward the east edge of the map. We examine spectra at the second peak position and conclude that the strong emission is not the real feature but rather an artifact due to the edge effects in contour routine. The Gaussian fit to the data in the south-east outflow area gives mean cloud velocity of 9.3 km s^{-1}. similar to the 9.2 km s^{-1} found in the area centered on IRS 1. No column density enhancement is detected in any velocity interval of Figure 6.7. near the position of the second bipolar outflow north from IRS 1. and the Gaussian fit to the ^{13}CO spectra at the peak ^{12}CO location gives 9.5 km s^{-1}.

6.4 Mass and Energetics

In addition to the known main outflow of the NGC 2071 region. we have identified 2 new outflows in the region: the north outflow and south-east outflow. Since the

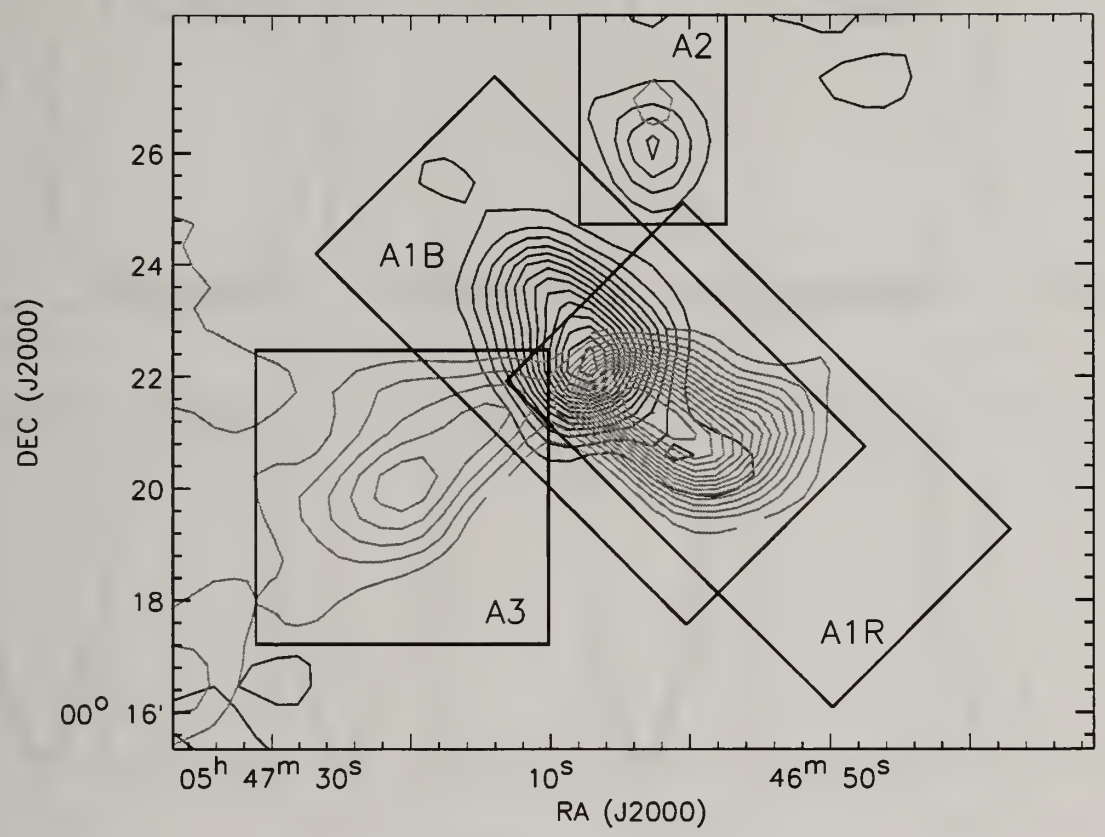

Figure 6.9 NGC 2071 Mass Calculation Regions. We identify four sub-regions in the outflow area mapped. A1B and A2R correspond to the areas of the main outflow blue- and redshifted outflows. A2 area covers the north outflow, while A3 captures the gas in the south-east outflow. In each of these regions we find averaged spectra, fit to their ratio and derive γ slope for its mass distribution.

mass distribution with velocity along the outflow can be a good indicator of the entrainment mechanism we isolate the various outflow components into smaller sub-regions. In the Figure 6.9 we identify the main outflow (both red and blueshifted components), the north outflow and southeast redshifted flow and we study the mass distribution with velocity in each of them separately.

The best approach to estimate the total mass in the outflow and its distribution with respect to the velocity is to use a tracer with the greatest velocity extent, i.e. the ^{12}CO line. However, this tracer suffers the effects of optical depth and to obtain accu-

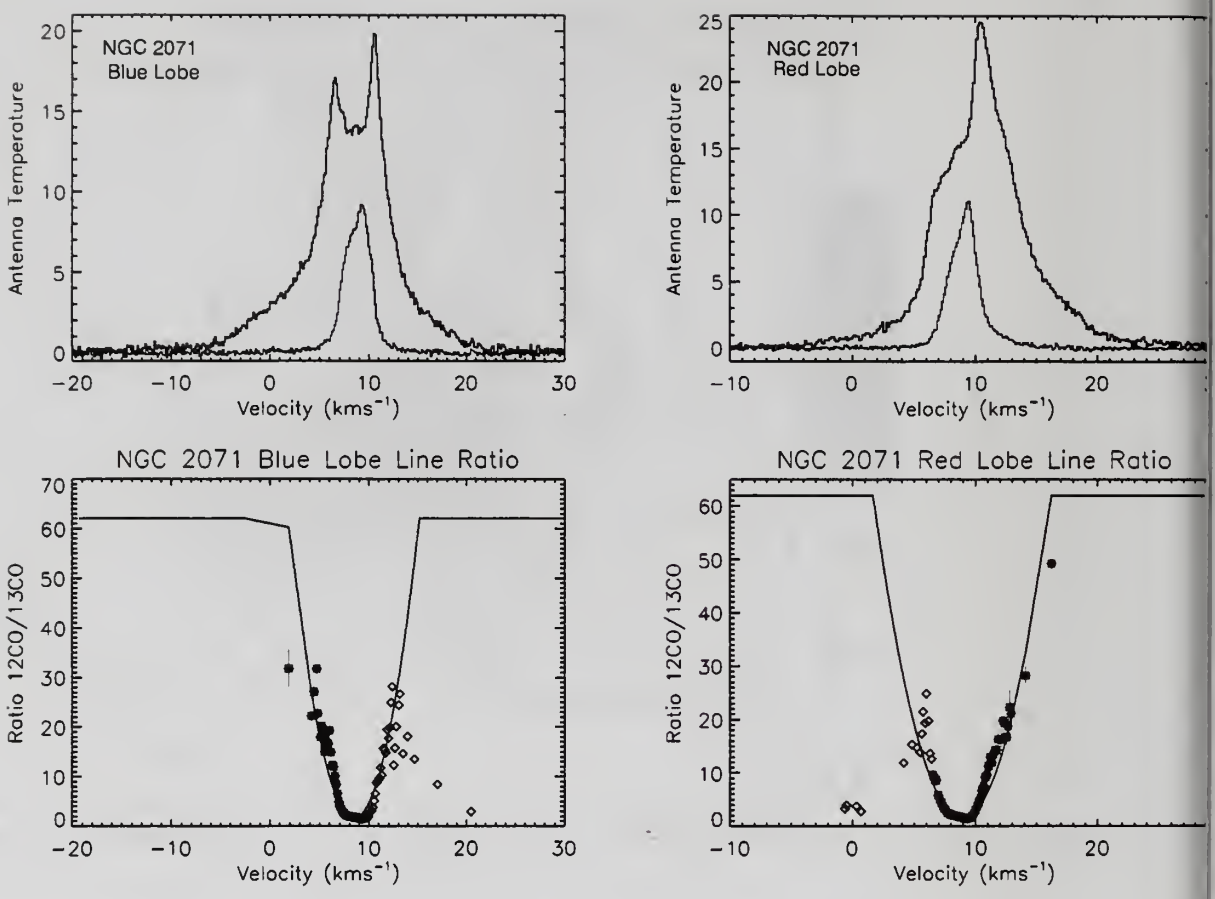

Figure 6.10 NGC 2071 Mass-V: Averaged Spectra. Averaged spectra in blueshifted and redshifted lobes of main NGC 2071 outflow respectively. Data are binned in 4 km s^{-1} wide intervals at velocities lower than 6 km s^{-1}, and in 2 km s^{-1} wide intervals at velocities greater than 13 km s^{-1}.

rate mass estimates, we need to take into account the opacity variations at different velocities. Since ^{13}CO line is available over the full extent of all three outflows we use the ratio of ^{12}CO -to- ^{13}CO line emission to estimate the optical depth as a function of velocity and correct for it. Several recent studies have combined ^{12}CO and ^{13}CO J=1—0 data to estimate the mass of the outflow, using a velocity-dependent opacity correction (Bally et al., 1999; Yu et al., 1999; Arce & Goodman, 2001a; Stojimirović et al., 2006). The application of this technique in NGC 2071 is successful.

The emission from ^{13}CO is usually optically thin and can also be very weak. Consequently ^{13}CO is not detectable in most mapping positions and to get good

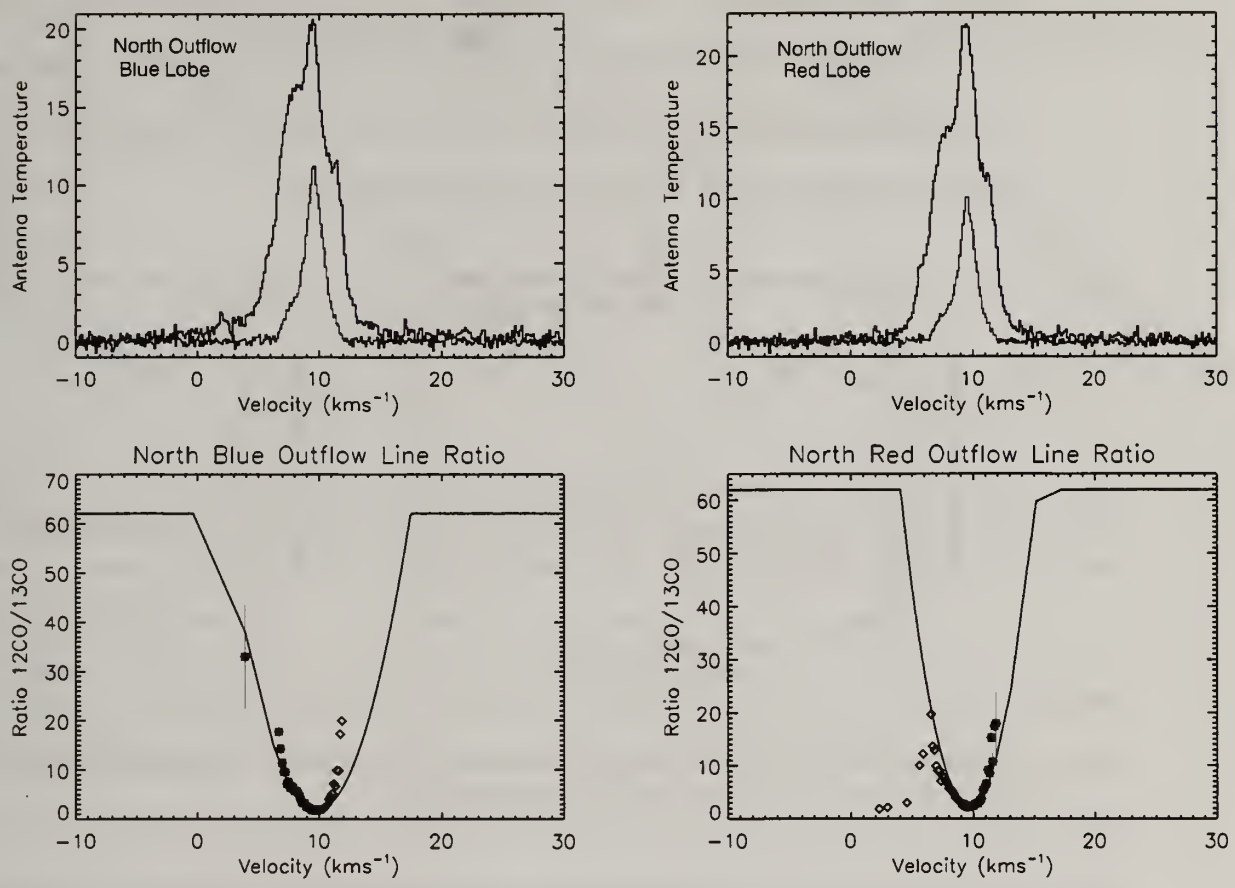

Figure 6.11 North Outflow Mass-V: Averaged Spectra. Averaged spectra in the second outflow north from NGC 2071. Data are binned in 4 km s^{-1} wide intervals at velocities lower than 4 km s^{-1}, and in 2 km s^{-1} wide intervals at velocities greater than 12 km s^{-1}.

signal-to-noise ^{13}CO spectra we need to average data over a large regions of the outflow. We construct the spatially averaged spectra. in each outflow lobe identified in Figure 6.9, making the following assumptions. For the blueshifted gas we find the integrated intensity in each spatial point of the ^{12}CO map in the velocity range from -2 to 6 km s^{-1}. We then select, in both ^{12}CO and ^{13}CO data cubes, only spectra at the location where integrated ^{12}CO intensity in the given velocity range is at least one third of the maximum integrated intensity. For the redshifted gas in the main and southeast outflows we applied the same approach using the velocity interval 12 to 20 km s^{-1} and 11 to 16 km s^{-1} in the second outflow redshifted lobe. The idea

behind this approach is to select spatial locations that most contribute to the CO outflow emission. In the upper panels of Figure 6.10 we show averaged spectra for main blue- and redshifted outflows. In the Figure 6.11 and Figure 6.14 we show the averaged spectra in the second and south-east outflow.

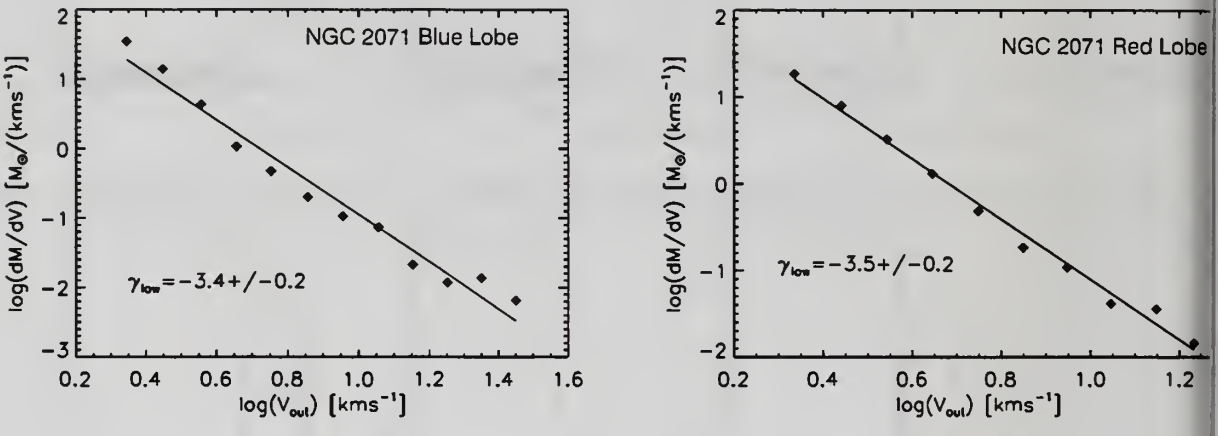

Figure 6.12 NGC 2071 Mass-V Relation. The mass-V for the blueshifted and redshifted lobes of the main outflow respectively

While the ^{12}CO line shows strong outflow emission, in ^{13}CO the outflow emission is very weak. In order to enhance the signal in ^{13}CO spectra we smooth the data at velocities less than 6 km s^{-1} and at velocities greater than 13 km s^{-1}. At velocities where both ^{12}CO and ^{13}CO averaged spectra are detected with at least 3σ certainty, we find their ratio $R_{12/13}(v)$ and plot it in the lower panels of Figure 6.10 and Figure 6.11. In both figures all ratio points are found within the inner line wings, close to the line core. In order to extrapolate the optical depth beyond the velocity extent of detectable ^{13}CO emission we fit the ratio distributions with parabolic function.

We derive the mass of the gas in the outflow assuming that ^{12}CO emission is optically thin and we correct for optical depth by multiplying the thin mass by $62/R_{12/13}(v)$ at each velocity channel (see Stojimirović et al. 2006 for more details). Table 6.1 summarizes our results for the mass of the outflowing gas in the main, north and south-east outflows, assuming $T_{ex} = 20$ K. Emission at velocities ≤ 6 km s^{-1} and

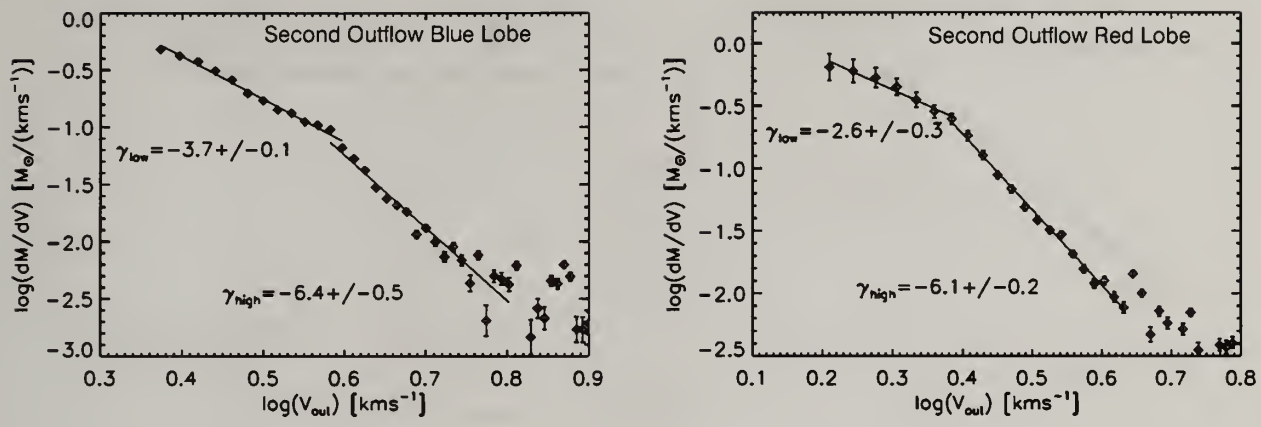

Figure 6.13 North Outflow Mass-V Relation. The mass-V for the blueshifted and redshifted lobes of the second outflow respectively. These date are not binned in the same log intervals because the outflow is detected over a smaller velocity extent (see text for more).

$\geq$ 12 km s^{-1} is dominated by the outflows. Using these velocity limits, we find mass in the north outflow to be 0.8 M$_\odot$ and 0.6 M$_\odot$ in the blue- and redshifted lobes respectively. The mass in the main outflow is 6.4 M$_\odot$ and 8.4 M$_\odot$ in the blue- and redshifted lobes respectively, while the southeast redshifted lobe has comparable mass of 7.6 M$_\odot$. Since the defined areas do not overlap in position and velocity, the total mass in the outflow in the NGC 2071 is the sum of the mass in each area and we find it to be $\sim$24 M$_\odot$ assuming 20 K excitation temperature. At low velocities there may be much more outflow emission (see Figure 6.3*d* and Figure 6.3*f*), and in an effort to estimate mass at lower outflow velocities we also calculate mass at velocities 6 $\leq$ v $\leq$ 7 for the blueshifted outflows and at 11 $\geq$ v $\geq$ 12 for the redshifted outflows using ^{13}CO line and assuming emission is thin (see Table 6.1). These estimates give an upper limit to the outflow mass, because we have seen that the strong ambient gas component is also present at these velocities. Accounting for the low velocity outflow gas, the upper limit on the total mass in all outflows is found to be $\sim$69 M$_\odot$. The mass estimate is very sensitive to the adopted velocity range chosen for the mass calculation. Moving 1 km s^{-1} further from the line core, i.e. velocities $\leq$ 6 km s^{-1}

Table 6.1. NGC 2071 Outflow Mass Estimate For T_{ex}=20 K

Lobe	Velocity Range km s^{-1}	Mass [a] $M_\odot$
Main B	$v < 6$	6.4
Main B	$6 \leq v \leq 7$	9.7
Main R	$11 \geq v \geq 12$	13
Main R	$v > 12$	8.4
North B	$v < 6$	0.8
North B	$6 \leq v \leq 7$	1.2
North R	$11 \geq v \geq 12$	2.3
North R	$v > 12$	0.6
SouthEast R	$11 \geq v \geq 12$	20.5
SouthEast R	$v > 12$	7.6

[a]For velocities $v \leq 6$ km s^{-1} and $v \geq 12$ km s^{-1} the mass is estimated from the ^{12}CO line correcting for the opacity using line ratio, while for $6 \leq v \leq 7$ and $11 \geq v \geq 12$ we used ^{13}CO line with no optical depth correction

and ≥ 12 km s^{-1} for blueshifted and redshifted gas respectively, reduces the outflow mass substantially.

6.4.1 Cloud Mass

We determine the cloud mass by using the ^{13}CO map, shown in Figure 6.2. The line center optical depth at each point in the map is derived from the ^{12}CO and ^{13}CO peak temperature. The excitation temperature is obtained at each position by solving the radiative transfer equation for the excitation temperature, assuming ^{12}CO emission is optically thick. We find, the total mass of the cloud using this method to be $\sim$2000 $M_\odot$.

6.4.2 Mass-Velocity Distribution

The mass distribution within a molecular outflow has a power-law dependence on velocity, such that $M_{CO}(v) \propto v^{-\gamma}$ (Richer et al., 2000). In a log-log plot, the slope of the linear fit determines the γ index. The value of γ is an important test for proposed mechanisms of molecular outflow entrainment. In the main outflow, we find $\gamma = 3.4 \pm 0.2$ for the blueshifted gas, and $\gamma = 3.5 \pm 0.2$ for the redshifted lobe. Figure 6.12.

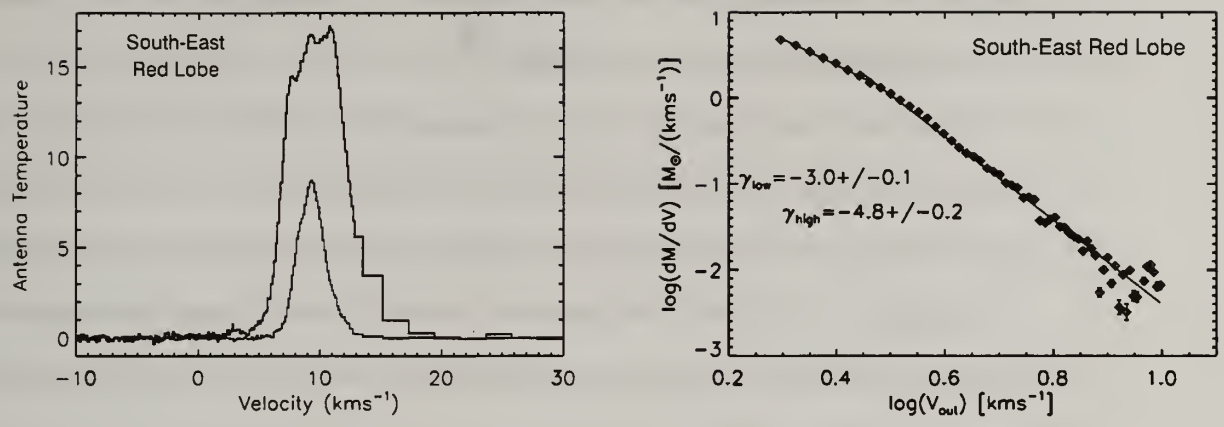

Figure 6.14 South-East Outflow Averaged Spectra and Mass-V Relation. Data are binned in in 2 km s^{-1} wide intervals at velocities greater than 13 km s^{-1}. The mass-V shows broken power law.

For the blueshifted and redshifted lobes of the north outflow we decided not to perform binning because. velocity range over which mass distribution is detected with good signal to noise is limited. Binning data in 0.1 wide log bins tends to erase the information by smoothing out the data. The unbinned data show broken power law in both lobes, with slopes $\gamma = 3.7 \pm 0.1$ at low velocities and $\gamma = 6.4 \pm 0.5$ at higher velocities for the blueshifted gas and $\gamma = 2.6 \pm 0.3$ at low velocities and $\gamma = 6.0 \pm 0.2$ at higher velocities for the redshifted gas. We also exclude all mass points at velocities lower than 3 km s^{-1} from the fit and at velocities greater than 14 km s^{-1}, since they depart from the straight line and have much larger errors associated with them (Figure 6.13). The south-east outflow has a slight break in the mass distribution and we fit the data with $\gamma = 3.0 \pm 0.1$ at low velocities and $\gamma = 4.8 \pm 0.2$ at higher velocities. see Figure 6.14.

6.5 Discussion

6.5.1 Multiple Outflows in the NGC 2071 Region

The large scale mapping that has been undertaken enables us to obtain a more complete picture of these star-forming regions. The observations of the NGC 2071

region, revealed multiple outflows present in the region, which we named the main, the north and the south-east outflow.

The main molecular outflow is associated with NGC 2071IR cluster and has a parsec-scale extent at its lowest outflow velocities, reaching a size of nearly 1.6 pc. Surprisingly only single HH knot is found along its extend, very close to the cluster itself (Zhao et al., 1999). On the other hand, strong H_2 emission is detected over a parsec scale length suggestive of the strong outflow activity in the region (Eislöffel, 2000).

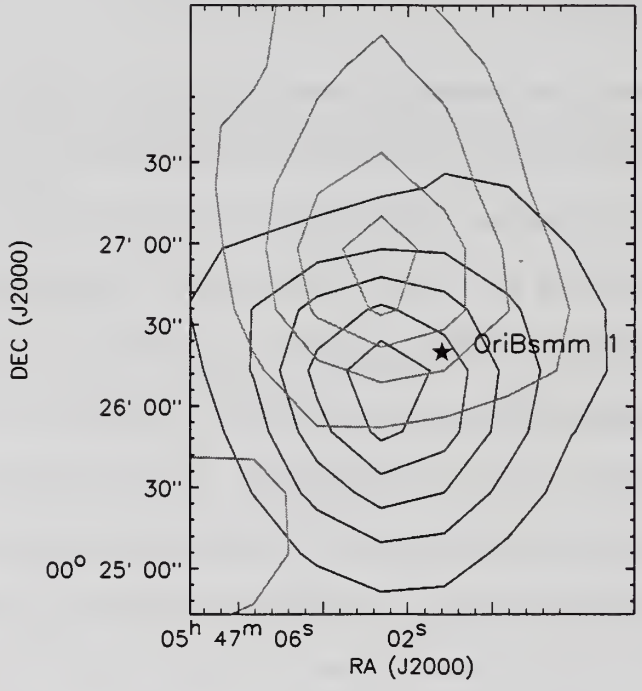

Figure 6.15 Second Outflow and SCUBA source. We zoom into the A2 region identified in the Figure 6.9 and show the closer look to the north outflow and location of its likely driving source.

The north outflow is also associated with the H_2 emission, and the CO bipolar outflow is well aligned with the H_2 emission jet (Eislöffel, 2000). This outflow may be driven by a star identified as a continuum source in the near-infrared (Eislöffel, 2000) and also detected SCUBA dust continuum source, OriBsmm 1 (Mitchell et al.,

2001). This source is well removed from the NGC2071 cluster. No corresponding 2MASS source has been identified to OriBsmm 1. Eislöffel (2000) classified the star as a CLASS 0 source and called the outflow NGC 2071 XI. In our channel maps the main and the north outflows are clearly separated (see Figure 6.3) as they are in the PV cut (see Figure 6.5). The main outflow is nearly ten times more massive than the north outflow. The north outflow may be driven by a much lower mass star.

The origin of the south-east outflow is more puzzling. The SCUBA maps identify a dust continuum source OriBsmm 14 at the very tip of this outflow, near the NGC 2071IR cluster, and we speculate that OriBsmm 14 could be a driving source for the outflow. As it has been discussed in §3.1, the H_2 emission is observed at the spatial position of the south-east outflow toward the NGC 2071 reflection nebula. However, there is no H_2 emission connecting this region with the IR cluster's H_2 emission, as if there was another star in this region entraining gas. The large mass found in the south-east outflow is comparable to the main outflow redshifted lobe is yet another surprise. The emission in the south-east outflow is present over a large velocity range ($\sim$10 km s^{-1}) and is very spatially extended at intermediate outflow velocities (see Figure 6.3*g*). The south-east redshifted outflow seems to originate near the region where the main outflow's redshifted emission is launched and there seems to be no blueshifted counterpart to this redshifted outflow.

6.5.2 The Entrainment Mechanism For The Outflows in NGC 2071

The main bipolar outflow driven by IRS 1 is amazingly symmetric in entrained mass, mass-velocity relation and kinematics between the redshifted and blueshifted lobes. This is very unlike the outflow studied for example in the L 1228 cloud, where we have seen completely different characteristics in the blue- and redshifted lobes of the outflow. Using higher-resolution study, 20″ images of CS Kitamura et al. (1990) have argued that the main outflow is wind-driven because it consists of two

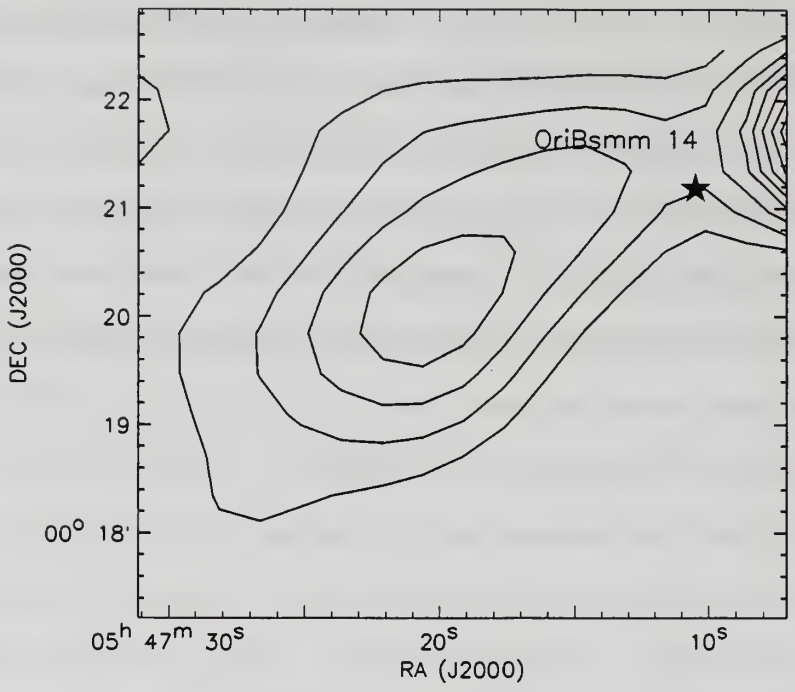

Figure 6.16 South-East Outflow and SCUBA source. We zoom into the A3 region identified in the Figure 6.9 and show the closer look to the south-east redshifted outflow and location of the OriBsmm 14 source, a possible driving source for this outflow.

expanding clumpy dense bubbles. This was also supported by the CO studies of Moriarty-Schieven et al. (1989).

Although at the highest blueshifted velocities we do not resolve the structure of the outflow, at lower outflow velocities both main blue- and redshifted outflows are very collimated along the outflow axis. In addition, multiple H_2 emission features (Eislöffel, 2000) are seen along the full extent of the highest velocity ^{12}CO emission identified in Figure 6.3*a* and Figure 6.3*i*. The parsec-scale H_2 shocked emission features, have been interpreted as a precessing jet, with the precession period longer than the observed part of the flow (Eislöffel, 2000). Many of the main outflow characteristics we studied are in agreement with the jet entrained outflows. For example, we find that the γ in the main blueshifted lobe is 3.4 ± 0.2 and in the main redshifted lobe 3.5 ± 0.2. The steep mass distribution is reproduced in the prompt entrainment models, where

ambient gas is swept up into molecular outflows via the jet driven bow shocks. The PV plots are somewhat inconclusive with respect to the entrainment model. The highest velocity is reached very close to the source and after it reaches maximum, the velocity steadily decreases for the rest of the outflow extent. This is not typical of either jet entrained outflows or wind driven outflows.

The north outflow has completely different features than its southern neighbor, i.e. the main outflow. First the mass distribution in the both lobes of the outflow well defined broken power law with a steep γ even at low velocities. We find at low velocities $\gamma = 3.7 \pm 0.1$ in the blue lobe an $\gamma = 2.6 \pm 0.3$ in the red lobe of the north outflow. These steep slopes together with the break at higher velocities are common in the jet entrainment models. Indeed, the jet model of Zhang & Zheng (1997) is the only one that can produce break in the outflow mass distribution. Second the north molecular outflow is associated with very collimated H_2 emission XI outflow, whose total extent is ~ 0.3 pc and symmetric with respect to its driving continuum source. The underlying jet traced by H_2 emission and molecular outflow are well aligned. In the PV plot through north outflow (see Figure 6.5), it is not obvious whether this outflow has a Hubble flow. Emission associated with north outflow is weak and it is difficult to define its morphology.

Finally, based on the steep and broken power law identified in the south-east redshifted outflow, the jet entrainment may play a major role in driving this outflow. However, without a certain driving source for this outflow its origin and driving mechanism remains puzzling.

6.6 NGC 2071 Summary And Conclusions

We performed high sensitivity ^{12}CO and ^{13}CO J=1$\rightarrow$0 large scale mapping observations and present results for the known NGC 2071 outflow, which we called main

outflow. Also we report the discovery of two new outflows and study their properties. Here we summarize our main conclusions.

1. The main outflow has a full extent of 1.6 pc at its lowest velocities. The main blue- and redshifted outflows have nearly the same γ slopes, similar mass content and symmetric velocity fields with respect to the driving IRS 1 source.

2. The main outflow is morphologically very well correlated with the H_2 shocked emission (Eislöffel, 2000), and multiple lines of evidence, such as steep γ slopes and spatial correlation of the highest velocity CO gas and H_2 features imply that jet must play a role in gas entrainment.

3. Approximately $\sim 4'$ north of the main outflow we report the discovery of a new bipolar outflow, which we call the north outflow. The north outflow may be driven by OriBsmm 1, a source identified by Mitchell et al. (2001). The redshifted lobe of this outflow may extend beyond the edge of our map.

4. The features of the north outflow such as a steep broken power law and spatial correlation of CO emission with H_2 XI jet emission are consistent with the jet entrainment. The mass content of the outflow is much smaller than in the main outflow.

5. The second, newly discovered outflow, lies south-east of the main outflow and consist only of redshifted emission. The source of the south-east outflow can not be clearly identified although we speculate that OriBsmm 14 (Mitchell et al., 2001) may be a potential candidate. Mass content of this outflow is similar to the redshifted main outflow and broken power law points toward jet entrainment.

CHAPTER 7

SUMMARY AND CONCLUSIONS

In the previous five chapters we have presented results of the study of molecular outflows in five star-forming regions associated with parsec-scale HH outflows. Two of these outflows, L1551 and L1228 have parsec scale molecular outflows associated with parsec scale HH flows, while Haro 6-10 and L1617 have spatially much smaller molecular outflows associated with parsec-scale HH flows. The last source NGC 2071 has multiple molecular outflows, one of which has a parsec-scale extent, associated with only one HH object, but H_2 shocked emission is present over parsec-scale lengths. In addition, what sets this source apart from the other four presented here is that it is driven by a intermediate mass cluster of stars and not a low mass star.

In the mid-90s, improvements in optical observational capabilities allowed the discovery of parsec scale HH flows (Bally & Devine, 1994; Reipurth et al., 1997). Improvements at millimeter wavelengths in the form of large heterodyne arrays, like the SEQUOIA 32 pixel array and OTF mapping capabilities at FCRAO 14 m telescope, provided faster, more sensitive mapping of the parsec scale regions. This allowed surveys, like one presented here, to be done in reasonable observational time. In addition, dual IF capability at the FCRAO 14 m telescope allowed to have two CO isotopes observed over the full extent of the molecular outflow. We have demonstrated in the previous chapters that the combination of ^{12}CO and ^{13}CO is essential for the determination of the optical depth in more abundant tracer and therefore accurate mass derivation. To our knowledge, only PV Cep (Arce & Goodman, 2002) and HH 300

(Arce & Goodman, 2001a) outflows have been studied so far in the similar manner as the five sources presented here, i.e. from the Nyquist sampled maps in two isotopic transition along the full extent of the outflow.

Below we summarize and discuss the major findings of this work.

7.1 New Outflows Revealed By Large Area Sensitive Mapping

Maybe one of the most obvious benefits of this work is that by obtaining large, sensitive maps we were able to report new outflows in the regions where previous observations failed to detect one. In the case of Haro 6-10 by extending our map from the central source along the axis of the parsec scale HH flow we detected the associated molecular outflow emission. Previous molecular studies missed the identification of the outflow probably due to their smaller mapping area and confusing spectral features present towards the object. Towards NGC 2071 we observed the larger region around the known main outflow in order to study outflow interaction with the ambient cloud and we reported the presence of two new outflows in the vicinity of the main outflow. Using published SCUBA survey data of the NGC 2071 area, we identify two potential driving sources for these two new outflows.

However, we were not always successful in finding new or larger extent molecular outflows than previously reported for all sources surveyed. For example, in L1617 a long 7.7 pc HH outflow has been detected (Reipurth et al., 1997). Millimeter line mapping showed that the outflow is only observed very close to the driving source, only over a fraction of the HH flow extent. The majority of the parsec scale HH outflows from our sample show clumpy CO outflow emission as in the example of Haro 6-10 flow where weak and low velocity outflow emission was detected. The blueshifted and redshifted emission overlaps at the location of Haro 6-10, and the only other outflow emission is a region of redshifted emission toward HH 412.

In Table 1.1, we introduced 15 parsec-scale HH flows targeted by this multi-wavelength study. Five sources have been studied in detail and results presented in the previous chapters. The data for all other sources have been fully reduced and we examined the integrated intensity maps in order to check for the existence and the extent of the outflow emission. We find that only the L1152 source does not have the outflow emission associated with parsec scale HH flows. From the remaining nine sources, six (L1165, B18 (HH300), L1589, L1535, L1630, RNO 43) have clumpy outflow emission similar to Haro 6-10 outflow morphology. L1455 and L1641N have complex morphology with multiple overlapping flows, while T-Tauri shows small bipolar outflow right on top of the driving star. In Table 7.1 we summarized our findings in terms of outflow extent and morphology in the observed sample.

The absence of much outflowing molecular gas in many parsec-scale HH flows. (see Table 7.1) may be a consequence of an evolutionary scenario in which young stars through prolonged outflow activity lose their surrounding gas progressively, weakening the CO outflow emission, while on the other hand, making optical jets traced by HH flows more detectable. In Table 7.1, we associate each outflow with the evolutionary stage of its driving star. The classification from CLASS 0 to CLASS III (Andre 1994) assumes evolution from the most embedded, youngest stars (CLASS 0) to the more evolved, less embedded T-Tauri stars (CLASS III). CLASS 0 also represents the main accretion and outflow phase with the duration of 10^4 years. CLASS I is a late accretion phase, when much of the surrounding envelope material have been either accreted or ejected and the protostar is $\sim 10^5$ years old. Most of our sources are driven by the protostars in the late accretion phase. Table 7.1. This implies less ambient material around them available for entrainment and at the same time the presence of the CO cavities around protostars are expected, as seen in L1551 outflow.

On the other hand, the very nature of being able to detect parsec scale optical flows, may bias our selection of star-forming regions to those at the edges of the

molecular clouds where extinction at optical wavelengths is small and where there is less CO gas available to entrain. Examining the optical images of L1617 region, we see HH 311 at the west terminating point of the HH flow, against the background stars. Our molecular line data at the location of HH 311, show no CO emission. This implies that this source has bursted out of the cloud and is freely moving through the ISM, where there is no CO gas to be entrained. Many HH objects in parsec-scale flows are detected beyond the edges of their molecular clouds (Reipurth et al., 1997). This holds for some of the HH knots in all of the sources presented in the previous chapters except for the NGC 2071 which had a single HH knot on top of the driving star. L1152 the targeted source where no outflow emission was found, is associated with parsec-scale HH 376 flow which has broken out from the surrounding molecular cloud into a region of low extinction which gives optically visible shocks faint appearance (Reipurth et al., 1997) and hints why no CO outflow emission is detected. However, some of the targeted regions are high-extinction regions and abundant in CO emission at least toward the driving sources, and yet they have poor CO outflows: for example, Haro 6-10 and B18w. Haro 6-10 remains puzzling since there is a strong cloud emission component with no CO cavities around the driving IRAS source, still very little gas has been entrained in the molecular outflow.

7.2 Velocity Dependent Opacity Correction Method

For each of the sources studied here, we presented high sensitivity ^{12}CO and ^{13}CO J=1$\rightarrow$0 molecular line maps covering the full extent of the parsec scale outflow. We used velocity dependent opacity correction to estimate the mass and the energy of the outflow. This technique has been applied only to few other sources so far (Arce & Goodman, 2001a, 2002; Yu et al., 1999). In the past, mass in the outflow has been estimated by assuming either constant opacity in ^{12}CO line or assuming that ^{12}CO line emission is thin. Accurate mass determination is important for the estimate of

Table 7.1. Outflow Detection In Parsec-Scale HH Outflows

Source	Parsec-Scale CO Y/N?	Driving Star class	Morphology of CO[a] Outflow
L1228	Y	CLASS I	bipolar
L1165	Y	CLASS I	clumpy (bipolar?)
L1152	N	CLASS I	no outflow
L1455	Y	?	bipolar (complex)
L1551	Y	CLASS 0/I	bipolar
B18w (HH300)	Y	CLASS I	clumpy
Haro 6-10	N	CLASS I/II	clumpy
T-Tauri	N	CLASS II	bipolar, small
L1535	N	?	no outflow
RNO 43	Y	CLASS 0/I	clumpy (bipolar)
L1641N	Y	CLASS I	?
L1617	Y	CLASS I	bipolar, small
L1589	?	CLASS I	clumpy
NGC 2071	Y	IR cluster	bipolar
L1630	N	CLASS I	no outflow

[a] *Bipolar* morphology refers to outflows like L1551; *clumpy* means similar to Haro 6-10; where ? left, more careful analysis remain to be done; *complex* morphology refers to multiple flows from multiple stars and more detailed analysis to follow.

the total mass entrained in the outflow, but even more importantly for the accurate determination of the power-law index γ in the M-V relation. Observationally derived γ can be directly compared to the predictions of different theoretical models. In turn, the trends seen in the γs of observed outflows can be used to refine the theoretical models of outflow entrainment.

Observations typically find the slope γ to range from 1 to 3, with median value of 2 (Richer et al., 2000). This result is derived from the observations that did not use velocity dependent opacity correction but rather constant correction or no opacity correction at all for mass calculation. Richer et al. (2000) noted that observational studies suffer from the lack of large homogeneous sample of molecular outflows mapped with good resolution and sensitivity in order to better constrain the typical properties of the molecular outflows. Recent works (Arce & Goodman, 2001a, 2002; Yu et al., 1999) find steeper γ than compiled by Richer et al. (2000). One common feature of these recent results is that they employed a velocity-dependent opacity correction. In the L1551 chapter we have discussed that systematic errors and bi-

ases in the analysis procedures for deriving mass spectra could result in errors in the determination of γ. We have demonstrated that by only using data which exceed a specified threshold in rms value of T_A^*, γ will increase.

In the L1551 case the resulting γ indices from our analysis, are systematically lower than the power law indices obtained towards other outflows in several recent studies that use a similar opacity correction method. However, repeating the same careful approach outlined in the L1551 chapter to other sources presented here, we find that some outflows have indeed steep γ indices and often show break in the mass distribution. In the case of Haro 6-10 we find that both blue- and redshifted outflows have $\gamma \sim 6$, while outflow in L1228, and main and north outflow in NGC 2071 have γ at low velocities in the range from 2.6 to 3.7, with the mean $\gamma \sim 2.5$ at low velocities. The north outflow in NGC 2071 shows break with $\gamma \sim 6$ at higher velocities. Therefore steep γ slopes seem to be commonly associated with molecular outflows and theoretical models should be able to account for them. In addition, sensitive line mapping reveals an increasing number of breaks in M-V distributions. We find that L1551 main outflow, HL Tau flow, NGC 2071 north and south-east outflows all have two distinct distributions of mass at low and high velocities. In the L1551 chapter we stated our main result in case of the broken power law was a shallow slope at low velocities, $\gamma \leq 2$, and $\gamma \geq 3$ at higher velocities. However, this does not seem to be a general case, since north NGC 2071 outflow shows broken power law with much steeper slope at low velocity: $\gamma = 3.7$ in blueshifted lobe and $\gamma = 2.6$ in redshifted lobe.

How different are these new results compared to the previous studies of the same outflows that did not use the velocity dependent opacity correction? We were surprised to find that well studied L1551 outflow has not been observed so far in its full extent in ^{13}CO emission. Therefore M-V relation was derived using ^{12}CO line and correcting mass for the constant optical depth. The correction for the optical depth

has been estimated from the ratio of ^{12}CO -to- ^{13}CO spectra at the single position within the outflow (Moriarty-Schieven & Snell. 1988). The M-V slope for both blue- and redshifted outflows in the L1551 has been reported as a single slope with $\gamma \sim 1.8$. We reported for the blueshifted main flow the broken power law with $\gamma = 2$ at low velocities and $\gamma = 2.75$ at higher velocities, while the main redshifted outflow have the $\gamma = 1.5$ at low velocities and $\gamma = 3.36$ at higher velocities. In the main redshifted lobe we have studied the restricted area compared to the (Moriarty-Schieven & Snell. 1988), but the blueshifted lobes are spatially identical in both studies. Therefore the difference in M-V slopes illustrates the effects velocity dependent optical depth correction has on the M-V slope. Applying the constant correction for the optical depth underestimates the correction at lower velocities and overestimates correction at higher velocities which results in the shallower M-V slope obtained by Moriarty-Schieven & Snell (1988). In addition, higher spectral resolution data with lower noise level per velocity channel allow us to detect break in the M-V relation, which was erased by the binning performed by Moriarty-Schieven & Snell (1988).

In the L1228 outflow, previous study by Tafalla & Myers (1997) found the M-V slope of the blue- and redshifted outflows to be the same with $\gamma \sim 2.5$, while we find $\gamma \sim 2.5$ for the blueshifted and $\gamma \sim 3.8$ for the redshifted gas. Tafalla & Myers (1997) did very careful mass analysis using the ^{12}CO line in outer wings and ^{13}CO in the inner wings as mass tracers. Therefore agreement of the γ slopes is expected. The difference in the redshifted γ slopes is most likely caused by Tafalla & Myers (1997) coming too close to the line core where ^{13}CO becomes possibly thick and therefore underestimating the mass by assuming thin emission. It is indeed in their M-V plot that this very first mass points departs from the otherwise steeper slope defined by other mass points, and including it in the fit steepens M-V redshifted slope. For the other outflows presented here, there are no published M-V analysis to compared against.

Velocity dependent opacity correction is a good tool to apply when estimating outflow mass. However there are still some uncertainties encountered along the way. Two major uncertainties are (1) the low velocity extent of the ^{13}CO line wing emission which sometimes limits or totally prevents the application of the method and (2) functional form of the fit adopted for ^{12}CO -to- ^{13}CO ratio extrapolation beyond the detected ratio. In the case of L1551, the outflow with the strongest ^{13}CO wing emission, we detect ^{12}CO -to- ^{13}CO ratio up to 10 km s^{-1} from the line core, but use the logarithmic fit to extrapolate for the optical depth up to 25 km s^{-1} from the line core. In L1228 the ^{13}CO emission is stronger in the blue lobe and the ratio can be traced up to $\sim$ 6 km s^{-1} from the line core. Beyond this velocity we checked if the data is consistent with the logarithmic correction for the optical depth by examining the ratio of the integrated intensities in the larger velocity range and we obtained the ratio of 85 $\pm$ 85, which is an inconclusive result. In the case of Haro 6-10 we had very limited velocity coverage of the outflow emission and in that range ^{13}CO emission was too weak to use, so the application of the velocity dependent opacity correction method was not possible.

In the second chapter, we have discussed in detail how the selection for the function that fits the line ratio affect the slopes of the mass spectra. The logarithmic function adopted in L1551 case is more slowly varying function with velocity, than the parabolic fit commonly adopted by other authors and in couple of sources we studied. Logarithmic fit makes larger corrections (more mass) at the higher velocities, which in turn makes the mass spectral slopes shallower.

The amount of mass that remains hidden by the ambient cloud is yet another factor that brings uncertainty in the M-V slope determination and even more to the total outflow mass estimate, given the fact that most of the outflow mass is at low velocities. Since there is no good way to extract outflow emission from the ambient cloud emission, we usually chose to go further away from the v_{LSR} of the cloud to

start accounting for the outflow gas. We were often guided by the channel maps when determining the start velocity of the outflow.

7.3 The Entrainment Model For Molecular Outflow

The focus of this work has been on physical characteristics of the outflows and confronting them with the predictions of the different outflow entrainment models in order to distinguish their relative importance. The γ slope in M-V relations proves to be a useful probe of the entrainment model, assuming that break or steep γ in the M-V identifies jet entrainment. However we have more difficulties using PV plot's spur vs. parabolic structures as a discriminatory tool between entrainment models (Lee et al., 2000). The Hubble law velocity field, i.e. acceleration away from the driving star, has been observed in all outflows, but usually the maximum velocity has been reached very close to the driving source. Only in the case of L1551's blueshifted main outflow, we have seen clear spur structures associated with jet driven bow shock models (Lee et al., 2000, 2001, 2002). Exploring the published literature on the entrainment models we find that the only model that produces PV structure that reaches its maximum close to the driving star is Steven Stahler's turbulent jet model (Stahler, 1994), where the highest velocities are not found at the jet head, but rather laterally with respect to the entraining jet, see Figure 7.1 for comparison of the prompt(bow shock) and turbulent jet PV characteristics. Not only that the entrainment of the gas in these two jet models takes place at the different locations, but the underlying jet is supersonic and under-dense in prompt model, while the Stahler's jet is subsonic or mildly trans-sonic and of similar density as the ambient medium (Bence et al., 1996). However, it has been argues in the literature that Stahler's jet produces too narrow outflow morphology, see Figure 1.4.

Combination of CO and optical data provides morphological relation between different tracers of the shock processes that arise during the interaction of the material

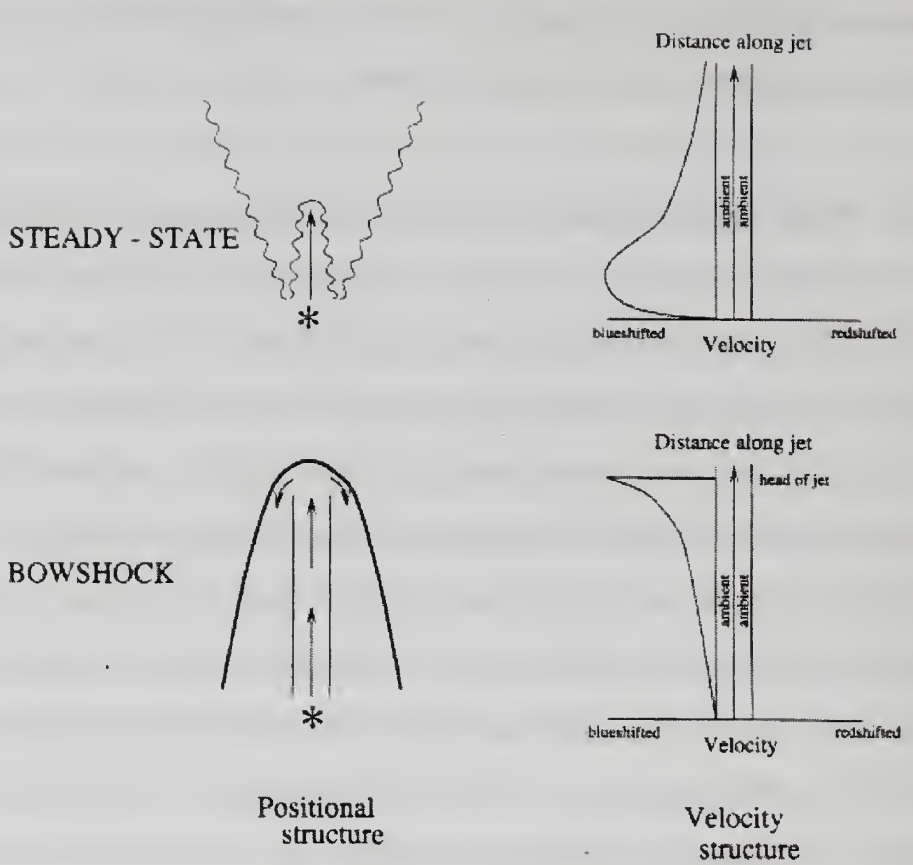

Figure 7.1 PV Structure in Turbulent and Prompt Models. Velocity Structure in the PV diagram for two competing jet models: turbulent or steady-state and prompt or bow-shock jet model. Figure adopted from Bence et al. (1996)

launched from the star with its surrounding ambient cloud. The highest velocity CO outflow gas is expected to be spatially correlated with the optical shocked emission traced by HH objects in bow shock jet models. This spatial correlation of the HH gas and high-velocity gas traditionally cannot be reproduced by any wind entrainment model. Through detailed channel maps in each source presented in the previous chapter, we have seen that the highest moving CO gas is always found close to the jet axis delineated by HH objects and sometimes right on top of the HH object. At the same time shells of lower velocity gas coexist (L1551, L1228). In L1228 redshifted outflow two high velocity peaks are identified, one on top of the HH 199/200 knots at the end of the jet axis and the other high-velocity peak very close to the driving source.

At the same time within the blueshifted lobe, the highest velocity gas is elongated along the jet axis and very collimated. The morphology in the L1228 redshifted lobe can best be explain with the jet model with multiple internal surfaces, such as the bow shock models where jet velocity varies. In Haro 6-10 we have seen that clumpy morphology of the redshifted lobe consist of two emission regions, one close to the source and the other on top of the HH 412. The CO redshifted emission at the HH 412 location has identical morphology as the underlying shocked optically emitting gas: elongated along the jet axis. Also we have seen that even in the structure reach L1551 outflow lobes peak intensity and highest velocity gas is localized close to the HH 259 in blue lobe and close to the HH 262 in red lobe.

Studies of the morphological relation between CO gas and shock tracers such as Hα or H_2 emission could greatly benefit from the better spatial resolution of CO maps. Often the optical emission is of a smaller spatial extent than the CO beam which hampers the comparison. The 22″ beam of HHT 10 m telescope revealed much better structure of the CO emitting gas evident in both channel and PV plots compared to the 45″ FCRAO 14m beam. Using better resolution J=3→2 data we were able to identify tentative outflow from the L1551 NE, better compare CO and Hα emission and identify spur structure of the blueshifted lobe in PV plot. Yet another example is L1228 outflow where interferometric map (Arce & Sargent, 2004) of the region adjacent to the driving source shows symmetrical wide angle outflow emerging from the driving source, while on the larger scale these two lobes are very different. Extending interferometric map to a larger scale would benefit the studies of the collimation of the CO emission in the blueshifted outflow in addition to morphological comparison to optical/IR shock tracers.

The mass spectral indices, the morphological appearance of the position-velocity plots and integrated intensity emission maps of the molecular data, compared with the optical data were used in each source to isolate the entrainment model that best

fits the observations. Table 7.2. We find that most of the studied outflows show some features that are characteristic of the jet-driven models and some features that are characteristic of the wind-driven models.

The outflows that we studied here are not young "simple" flows, as for example HH 211 outflow whose lifetime is estimated to only 750 yr, but rather older, more evolved associated with CLASS I stars whose lifetimes are at least few 10^4 yr. Since most of the stars are born in multiple systems or clustered mode, our outflows are complicated with multiple outflows often overlapping in the same region such as L 1551 NE, IRS 5, EW, HL Tau outflows in L 1551 or HH 199 and HH 200 in L1228. We did our best to isolate these flows and study each of them separately. The multiple ejection episodes from the same driving source are expected at these timescales but theoretical models usually do not account for them, which makes comparison difficult. To make things more complicated due to the unknown ambient properties it is not trivial to translate the observed outflow morphology and kinematics to the physical properties of the driving wind, best illustrated in the case study of the L1228 asymmetric outflow. On the other hand, theoretical models usually assume uniform ambient density distribution decreasing from the driving source as $1/r^2$, when deriving theoretical M-V distribution. In our sample only outflow driven by IRS 1 in NGC 2071 turned out to be amazingly symmetric with respect to the mass content of the outflow lobes, γ slopes that characterize the mass distribution and with respect to the velocity field in the lobes traced by PV plots. Assuming that the jet/wind is symmetric when launched from the star, the environment must play a key role in producing different observables in the outflow lobes.

Nevertheless, the coexistence of wind and jet signatures in most of our outflows suggests two possibilities which are not exclusive: there is a *unified model* for the HH and CO outflows where wind and jet co-exist at all times and/or the *entrainment mechanism evolves* from the more jet dominated in young flows to less collimated

with both jet and wind components being important in older flows. It has been noted in the literature that the youngest flows are usually CO collimated, with H_2 shocked emission closely related to the morphology of the CO flows. Such an example of the HH 212 outflow driven by CLASS 0 protostar where CO emission produced in the wings of the bow surface surrounds the H_2 emission produced near the bow shock surface (Zinnecker et al., 1988). Since this is an embedded source, optical HH emission is not observed, but in the jet model would be expected at the head of the jet/bow shock. The PV diagram along the HH 212 jet axis shows a series of spur structures in both lobes with the highest velocity near the H_2 features (Lee et al., 2001). Therefore this is the clear example of the jet driven flow. In more evolved flows, such as L1551 or L1228, driven by CLASS 0/I stars most of the HH objects and highest velocity CO gas remain on the jet axis, which is also the symmetry axis of the outflow, but CO outflow lobes are laterally expanding and becoming less collimated and PV plot does not show clear jet signatures.

Lately there has been a theoretical tendency toward unified model, since in the past it has been discussed that both jet and wind theoretical models fail to match different aspects of observations. For example, jets without significant wandering cannot produce the observed CO outflow width, while wide-angle winds without strong velocity gradients away from the core cannot produce the observed discrete bow shock structures (Lee et al., 2001). Recent numerical simulation work by Shang et al. (2006) unifies jet and wind formalisms under the framework of Shu et al. (1991) arguing that the unified picture is the consequence of the magnetocentrifugal theory of jet formation (Konigl & Pudritz, 2000; Shu et al., 2000). When jets are launched they must first travel away from the rotational axis before being collimated (Shang et al., 2006). Two component density structure arises: a dense axial jet and a dense closed shell which encases the jet (Shang et al., 2006). During the evolution from CLASS 0 to CLASS I the driving star is accreting more and more mass and the neighboring

Table 7.2. Entrainment Mechanisms For Studied Outflows

Outflow Lobe	Single/Broken	Gamma[a]	PV[b]	Morphology
L 1551				
Main B	B	2, 2.75	Spur	Wide
Main R	B	1.5, 3.4	Jet?	Wide
NB	S	4.85	–	Collimated
HLT R	B	1.35, 2.63	–	–
HLT R	S	3.8	–	–
EW	S	2.85	Spur?	Collimated
L 1228				
Blue	S	2.5	turbulent?	Collimated
Red	S	3.8	turbulent?	Wide
Haro 6-10				
Blue	S	6	Inconclusive	–
Red	S	5.5	Inconclusive	Collimated
NGC 2071				
Main B	S	3.4	turbulent?	Wide
Main R	S	3.5	turbulent?	Wide
North B	B	3.7, 6.4	turbulent?	–
North R	B	2.6, 6.1	turbulent?	–
SE R	B	3, 4.8	turbulent?	Collimated

[a]Two numbers indicate it is a broken power law

[b]PV plots clearly showed *spur* structure only in blueshifted L1551 in J=3→2 transition. There are indication or spur identification in L1551 EW flow where the highest velocity is at the highest distance from driving source and in Haro 6-10 redshifted emission where the velocity maximum is found coincident with HH 412. *turbulent* refers to the PV structure identified in Stahler's turbulent jet model where maximum velocity is reached very close to the driving star.

gas is settling from the envelope to the disk distribution (Andre 1994), producing wider evacuated region around the magnetic pole (Shang et al., 2006). This allows wind driven outflow lobes to widen with time, which is in agreement with the observations. The unified model thus provides a common mechanism for optical and molecular manifestations of the outflow phenomena. Both components are present at all time but the immediate environment to the accreting star plays an important role in determining the morphology (collimation) of the outflow.

Although there have been an increasing number of numerical simulation available in the last year or two on the outflow entrainment models they did not provide M-V or PV predictions to allow direct comparison with observations. Their future work should provide results for these commonly observed outflow features to allow better comparison of the model with the existing observations.

7.4 Outflow Impact On Its Environment

Can stellar winds provide energy sufficient to sustain the turbulence in the molecular clouds (supersonic motions that characterize molecular outflows)? Can outflows through their combined effect input energy at the rate necessary to anull the dissipating turbulence.

In order to study the effects of a molecular outflow on its environment, it is essential to calculate its mass, momentum, and energy in the most precise way possible. The highest uncertainty in mass determination, factor of 2, is related to the N_{H_2} to N_{CO} conversion factor (Frerking et al., 1982). Traditionally uncertainties in mass determination come also from the unknown optical depth of the transition studied and the dependence of this opacity on velocity. These uncertainties have been minimized, with the velocity dependent opacity correction method applied in the study. Lastly, distinguishing amount of outflow mass from the ambient cloud mass remains puzzling. In all cases we studied, we consider the outflow to start at least $\sim$1 km s^{-1} from the host cloud's mean and therefore the effect of the cloud contamination to the low velocity outflow mass is minimal and our mass estimates are lower limits.

Estimating the momentum and energy content of a molecular outflow is subject to great uncertainties from the unknown orientation of the flow with respect to the plane of the sky. We have only accounted for the radial velocity of the outflow and did not correct for the tangential component. Therefore our energy and momentum estimates are only the lower limit. Nevertheless, we find that powerful outflows such as those associated with L1551, L1228 and NGC 2071 have kinetic energies comparable to their host cloud's binding energies, even for no inclination angle correction, and lower $T_{\rm ex}$ assumption. The impact these energetic outflows have on their parent clouds depends on the efficiency in which momentum and energy can be transferred from the outflowing molecular gas to the surrounding cloud material. In some cases outflows can break out from the cloud, carrying the energy and momentum in the

intercloud medium. It has been suggested that outflows can regulate star-formation rate within their host cloud by gas removal or alternatively by shock compressing the cloud material which may trigger the star-formation. The L1551's main blue outflow has broken out of the cloud near HH 256, and significant disruption on the cloud has been imposed. Also, the outflow activity in the IRS 5 region has likely induced star formation in the L1551 NE region and new stars have being triggered to form in the L1551 system as a result of the effects of the multiple outflows in the region.

Multiple outflows through their combined effect within the single cloud can be considered as a potential energy reservoirs to contribute to the dissipating turbulent motions in the cloud. Numerical simulations of MHD turbulence show that it will decay on a molecular cloud crossing timescale (Mac Low, 1999; Vazquez-Semadeni et al., 2000). If clouds are long-lived structures, turbulence is assumed to provide support against molecular cloud collapse and it must be resupplied. Alternatively, molecular clouds are short-lived, transient features. Li & Nakamura (2006) have shown that the decaying turbulence in dense star-forming clusters can be replenished by protostellar outflow driven turbulence. If the outflows are jet driven the energy and momentum deposited are localized around jet working surfaces which occupies very small volume compared to the whole cloud's volume. The energy and momentum in the localized region must be randomized and distributed over many scales, which is best done through the multiple outflow events within the same cloud. Quillen et al. (2005) suggests that outflows couple to the turbulent motions of the parent cloud via fossil outflow cavities after they deceleterate to the velocities comparable to the turbulent velocity. This happens after outflow driving sources have ceased.

In the case of L 1551 and L 1228 we concluded that if a small fraction of the outflow energy could be coupled into cloud turbulence, the outflow could sustain the turbulence for over a million years, much greater than the lifetimes of molecular outflows. Tafalla & Myers (1997) used velocity gradient sensitive tracers and showed

that gas acceleration in L1228 occurs without appreciable line width enhancement, suggesting that outflow has not increased substantially the turbulence of the gas. This may imply extremely inefficient coupling of the outflow momentum and cloud kinematics.

In the past an approximate balance between outflow input from combined outflows in the molecular cloud and turbulent support has been found (Bally et al., 1996; Knee & Sandell, 2000; Matzner, 2002; Warin et al., 1996). The future theoretical work remains to be done to clarify the importance of the outflows to turbulent motions in the clouds.

7.4.1 Conclusions

Conclusions for individual chapters are presented at the end of each chapter. Here we present the global conclusions of this thesis.

Parsec-scale HH flows and associated molecular flows are found to be associated with more evolved CLASS I stars, which have cleared up significant fraction of its surrounding cloud material, and allowed parsec scale HH jets to be seen. Consequently molecular outflow emission is clumpy and sometimes of the smaller extent than parsec-scale HH flows, usually in the situation when the HH objects are found against the strong stellar background outside of the molecular cloud when there is no CO gas to be entrained.

We studied M-V, PV and morphological relation between CO vs. shocked optical gas in order to discriminate between different theoretical models. We find that many parsec-scale outflows show signatures of both jet and wind entrainment. This supports recent theoretical works of unified entrainment models in which both jet and wind component are coexistent at all times of protostellar evolution, with jet being more important in the CLASS 0 protostars and wind or wider-angle component gaining on significance with the more evolved sources. The exact comparison of the properties of

the outflow's PV structure with unified outflow model. remains to be done in future when theoretical predictions are reported for this model.

Finally, we find that the outflows have enough energy to be considered as a potential re-supplier of the decaying turbulence in the molecular clouds and therefore an important player against the collapse of the molecular cloud. The exact nature of the coupling remains to be further explored.

BIBLIOGRAPHY

Adams, F. C. & Fatuzzo, M. 1996, ApJ, 464, 256

Anthony-Twarog, B. J. 1982, AJ, 87, 1213

Arce, H. G. & Goodman, A. A. 2001a, ApJ, 554, 132

—. 2001b, ApJ, 551, L171

—. 2002, ApJ, 575, 928

Arce, H. G. & Sargent, A. I. 2004, ApJ, 612, 342

Arce, H. G., Shepherd, D., Gueth, F., Lee, C.-F., Bachiller, R., Rosen, A., & Beuther, H. 2006, ArXiv Astrophysics e-prints

Aspin, C., Sandell, G., & Walther, D. M. 1992, MNRAS, 258, 684

Bachiller, R. 1996, ARA&A, 34, 111

Bachiller, R., Guilloteau, S., Dutrey, A., Planesas, P., & Martin-Pintado, J. 1995, A&A, 299, 857

Bally, J. 1982, ApJ, 261, 558

Bally, J. & Devine, D. 1994, ApJ, 428, L65

Bally, J., Devine, D., Fesen, R. A., & Lane, A. P. 1995, ApJ, 454, 345

Bally, J., Devine, D., & Reipurth, B. 1996, ApJ, 473, L49+

Bally, J. & Lada, C. J. 1983, ApJ, 265, 824

Bally, J., Langer, W. D., Wilson, R. W., Stark, A. A., & Pound, M. W. 1991, in IAU Symp. 147: Fragmentation of Molecular Clouds and Star Formation, ed. E. Falgarone, F. Boulanger, & G. Duvert, 11–+

Bally, J., Reipurth, B., & Davis, C. 2006, Protostars and Planets V

Bally, J., Reipurth, B., Lada, C. J., & Billawala, Y. 1999, AJ, 117, 410

Bence, S. J., Richer, J. S., & Padman, R. 1996, MNRAS, 279, 866

Beuther, H. & Schilke, P. 2004, Science, 303, 1167

Bieging, J. H. & Cohen, M. 1985, ApJ, 289, L5

Briceño, C., Hartmann, L., Stauffer, J., & Martín, E. 1998, AJ, 115, 2074

Burton, M. G., Geballe, T. R., & Brand, P. W. J. L. 1989, MNRAS, 238, 1513

Butner, H. M., Evans, II, N. J., Harvey, P. M., Mundy, L. G., Natta, A., & Randich, M. S. 1990, ApJ, 364, 164

Campbell, B., Persson, S. E., Strom, S. E., & Grasdalen, G. L. 1988, AJ, 95, 1173

Canto, J. & Raga, A. C. 1991, ApJ, 372, 646

Cantó, J., Raga, A. C., & Riera, A. 2003, Revista Mexicana de Astronomia y Astrofisica, 39, 207

Carr, J. S. 1990, AJ, 100, 1244

Cernicharo, J. & Reipurth, B. 1996, ApJ, 460, L57+

Cerqueira, A. H. & de Gouveia dal Pino, E. M. 1999, ApJ, 510, 828

Cerqueira, A. H. & de Gouveia Dal Pino, E. M. 2001, ApJ, 560, 779

Chandler, C. J., Barsony, M., & Moore, T. J. T. 1998, MNRAS, 299, 789

Chernin, L. M. & Masson, C. R. 1992, ApJ, 396, L35

Chernin, L. M. & Welch, W. J. 1995, ApJ, 440, L21

Codella, C., Welser, R., Henkel, C., Benson, P. J., & Myers, P. C. 1997, A&A, 324, 203

Coppin, K. E. K., Davis, C. J., & Micono, M. 1998, MNRAS, 301, L10

Cunningham, A., Frank, A., Varnière, P., Poludnenko, A., Mitran, S., & Hartmann, L. 2005, Ap&SS, 298, 317

De Young, D. S. 1986, ApJ, 307, 62

Devine, D., Reipurth, B., & Bally, J. 1999a, AJ, 118, 972

Devine, D., Reipurth, B., Bally, J., & Balonek, T. J. 1999b, AJ, 117, 2931

Downes, T. P. & Cabrit, S. 2003, A&A, 403, 135

Downes, T. P. & Ray, T. P. 1999, A&A, 345, 977

Edwards, S., Hartigan, P., Ghandour, L., & Andrulis, C. 1994, AJ, 108, 1056

Edwards, S. & Snell, R. L. 1984, ApJ, 281, 237

Eislöffel, J. 2000, A&A, 354, 236

Eisloffel, J. & Mundt, R. 1997, AJ, 114, 280

Elmegreen, B. G. 2000, ApJ, 539, 342

Emerson, J. P., Harris, S., Jennings, R. E., Beichman, C. A., Baud, B., Beintema, D. A., Wesselius, P. R., & Marsden, P. L. 1984, ApJ, 278, L49

Erickson, N., Grosslein, R. M., Erickson, R. B., & Weinreb, S. 1999, IEEE Trans. Microwave Theory and Tech., 2212

Favata, F., Giardino, G., Micela, G., Sciortino, S., & Damiani, F. 2003, A&A, 403, 187

Frerking, M. A., Langer, W. D., & Wilson, R. W. 1982, ApJ, 262, 590

Fridlund, C. V. M. & Liseau, R. 1998, ApJ, 499, L75+

Gålfalk, M., Olofsson, G., Kaas, A. A., Olofsson, S., Bontemps, S., Nordh, L., Abergel, A., André, P., Boulanger, F., Burgdorf, M., Casali, M. M., Cesarsky, C. J., Davies, J., Falgarone, E., Montmerle, T., Perault, M., Persi, P., Prusti, T., Puget, J. L., & Sibille, F. 2004, A&A, 420, 945

Garay, G., Mardones, D., & Rodríguez, L. F. 2000, ApJ, 545, 861

Garden, R. P., Russell, A. P. G., & Burton, M. G. 1990, ApJ, 354, 232

Gardiner, T. A., Frank, A., & Hartmann, L. 2003, ApJ, 582, 269

Garnavich, P. M., Noriega-Crespo, A., & Green, P. J. 1992, Revista Mexicana de Astronomia y Astrofisica, 24, 99

Gomez, M., Jones, B. F., Hartmann, L., Kenyon, S. J., Stauffer, J. R., Hewett, R., & Reid, I. N. 1992, AJ, 104, 762

Gredel, R. & Reipurth, B. 1994, A&A, 289, L19

Grenier, I. A., Lebrun, F., Arnaud, M., Dame, T. M., & Thaddeus, P. 1989, ApJ, 347, 231

Gueth, F. & Guilloteau, S. 1999, A&A, 343, 571

Haikala, L. K. & Laureijs, R. J. 1989, A&A, 223, 287

Harjunpää, P., Lehtinen, K., & Haikala, L. K. 2004, A&A, 421, 1087

Haro, G. 1952, ApJ, 115, 572

—. 1953, ApJ, 117, 73

Hartigan, P. 1989, ApJ, 339, 987

Hartigan, P., Morse, J., Palunas, P., Bally, J., & Devine, D. 2000, AJ, 119, 1872

Hartmann, L., Hewett, R., & Calvet, N. 1994, ApJ, 426, 669

Hatchell, J., Fuller, G. A., & Ladd, E. F. 1999, A&A, 346, 278

Herbig, G. H. 1950, ApJ, 111, 11

—. 1951, ApJ, 113, 697

—. 1974, Lick Observatory Bulletin, 658, 1

Herbst, T. M., Koresko, C. D., & Leinert, C. 1995, ApJ, 444, L93

Heyer, M. H., Snell, R. L., Goldsmith, P. F., & Myers, P. C. 1987, ApJ, 321, 370

Hodapp, K.-W. 1994, ApJS, 94, 615

Hogerheijde, M. R., van Dishoeck, E. F., Blake, G. A., & van Langevelde, H. J. 1997, ApJ, 489, 293

—. 1998, ApJ, 502, 315

Itoh, Y., Kaifu, N., Hayashi, M., Hayashi, S. S., Yamashita, T., Usuda, T., Noumaru, J., Maihara, T., Iwamuro, F., Motohara, K., Taguchi, T., & Hata, R. 2000, PASJ, 52, 81

Kawabe, R., Kitamura, Y., Ishiguro, M., Hasegawa, T., Chicada, Y., & Okumura, S. K. 1989, in LNP Vol. 350: IAU Colloq. 120: Structure and Dynamics of the Interstellar Medium, ed. G. Tenorio-Tagle, M. Moles, & J. Melnick, 254–+

Keegan, R. & Downes, T. P. 2005, A&A, 437, 517

Kenyon, S. J., Dobrzycka, D., & Hartmann, L. 1994, AJ, 108, 1872

Kitamura, Y., Kawabe, R., Yamashita, T., & Hayashi, M. 1990, ApJ, 363, 180

Knee, L. B. G. & Sandell, G. 2000, A&A, 361, 671

Koenigl, A. 1991, ApJ, 370, L39

Konigl, A. & Pudritz, R. E. 2000, Protostars and Planets IV, 759

Krist, J. E., Stapelfeldt, K. R., Burrows, C. J., Hester, J. J., Watson, A. M., Ballester, G. E., Clarke, J. T., Crisp, D., Evans, R. W., Gallagher, III, J. S., Griffiths, R. E., Hoessel, J. G., Holtzman, J. A., Mould, J. R., Scowen, P. A., & Trauger, J. T. 1999, ApJ, 515, L35

Kun, M. 1998, ApJS, 115, 59

Lada, C. J. 1985, ARA&A, 23, 267

Lada, C. J. & Fich, M. 1996, ApJ, 459, 638

Lane, A. P. & Bally, J. 1986, ApJ, 310, 820

Langer, W. D. & Penzias, A. A. 1993, ApJ, 408, 539

Larson, R. B. 2003, Reports of Progress in Physics, 66, 1651

Lee, C.-F., Mundy, L. G., Reipurth, B., Ostriker, E. C., & Stone, J. M. 2000, ApJ, 542, 925

Lee, C.-F., Mundy, L. G., Stone, J. M., & Ostriker, E. C. 2002, ApJ, 576, 294

Lee, C.-F., Stone, J. M., Ostriker, E. C., & Mundy, L. G. 2001, ApJ, 557, 429

Levreault, R. M. 1988, ApJ, 330, 897

Li, Z.-Y. & Nakamura, F. 2006, ApJ, 640, L187

Li, Z.-Y. & Shu, F. H. 1996, ApJ, 472, 211

Lizano, S. & Giovanardi, C. 1995, ApJ, 447, 742

Looney, L. W., Mundy, L. G., & Welch, W. J. 1997, ApJ, 484, L157+

López, R., Rosado, M., Riera, A., Noriega-Crespo, A., Raga, A. C., Estalella, R., Anglada, G., Le Coarer, E., Langarica, R., Tinoco, S., & Cantó, J. 1998, AJ, 116, 845

Lynds, B. T. 1962, ApJS, 7, 1

Mac Low, M.-M. 1999, ApJ, 524, 169

Masson, C. R. & Chernin, L. M. 1993, ApJ, 414, 230

Matzner, C. D. 2002, ApJ, 566, 302

Matzner, C. D. & McKee, C. F. 1999, ApJ, 526, L109

—. 2000, ApJ, 545, 364

Meyers-Rice, B. A. & Lada, C. J. 1991, ApJ, 368, 445

Micono, M., Bodo, G., Massaglia, S., Rossi, P., Ferrari, A., & Rosner, R. 2000, A&A, 360, 795

Mitchell, G. F., Johnstone, D., Moriarty-Schieven, G., Fich, M., & Tothill, N. F. H. 2001, ApJ, 556, 215

Moriarty-Schieven, G. H., Hughes, V. A., & Snell, R. L. 1989, ApJ, 347, 358

Moriarty-Schieven, G. H., Johnstone, D., Bally, J., & Jenness, T. 2006, ApJ, 645, 357

Moriarty-Schieven, G. H. & Snell, R. L. 1988, ApJ, 332, 364

Moriarty-Schieven, G. H. & Wannier, P. G. 1991, ApJ, 373, L23

Movsessian, T. A. & Magakian, T. Y. 1999, A&A, 347, 266

Mundt, R., Buehrke, T., & Ray, T. P. 1988, ApJ, 333, L69

Mundt, R., Buehrke, T., Solf, J., Ray, T. P., & Raga, A. C. 1990, A&A, 232, 37

Nagar, N. M., Vogel, S. N., Stone, J. M., & Ostriker, E. C. 1997, ApJ, 482, L195+

Narayanan, G., Heyer, M. H., Brunt, C., Goldsmith, P. F., Snell, R., Tang, Y., & Li, D. 2007

Narayanan, G. & Walker, C. K. 1996, ApJ, 466, 844

Ostriker, E. C., Lee, C.-F., Stone, J. M., & Mundy, L. G. 2001, ApJ, 557, 443

O'Sullivan, S. & Ray, T. P. 2000, A&A, 363, 355

Persson, S. E., Geballe, T. R., Simon, T., Lonsdale, C. J., & Baas, F. 1981, ApJ, 251, L85+

Plambeck, R. L. & Snell, R. L. 1995, ApJ, 446, 234

Pound, M. W. & Bally, J. 1991, ApJ, 383, 705

Pudritz, R. E. & Banerjee, R. 2005, in IAU Symposium, ed. R. Cesaroni, M. Felli, E. Churchwell, & M. Walmsley, 163–173

Pudritz, R. E., Ouyed, R., Fendt, C., & Brandenburg, A. 2006, ArXiv Astrophysics e-prints

Quillen, A. C., Thorndike, S. L., Cunningham, A., Frank, A., Gutermuth, R. A., Blackman, E. G., Pipher, J. L., & Ridge, N. 2005, ApJ, 632, 941

Raga, A. & Cabrit, S. 1993, A&A, 278, 267

Raga, A. C., Binette, L., Canto, J., & Calvet, N. 1990, ApJ, 364, 601

Raga, A. C., Noriega-Crespo, A., González, R. F., & Velázquez, P. F. 2004, ApJS, 154, 346

Raga, A. C., Velázquez, P. F., Cantó, J., & Masciadri, E. 2002, A&A, 395, 647

Reipurth, B. & Bally, J. 2001, ARA&A, 39, 403

Reipurth, B., Bally, J., & Devine, D. 1997, AJ, 114, 2708

Reipurth, B., Bally, J., Graham, J. A., Lane, A. P., & Zealey, W. J. 1986, A&A, 164, 51

Reipurth, B., Chini, R., Krugel, E., Kreysa, E., & Sievers, A. 1993, A&A, 273, 221

Reipurth, B., Hartigan, P., Heathcote, S., Morse, J. A., & Bally, J. 1997b, AJ, 114, 757

Reipurth, B. & Olberg, M. 1991, A&A, 246, 535

Reipurth, B., Raga, A. C., & Heathcote, S. 1992, ApJ, 392, 145

Reipurth, B., Rodríguez, L. F., Anglada, G., & Bally, J. 2002, AJ, 124, 1045

—. 2004, AJ, 127, 1736

Reipurth, B., Yu, K. C., Heathcote, S., Bally, J., & Rodríguez, L. F. 2000, AJ, 120, 1449

Reipurth, B., Yu, K. C., Rodríguez, L. F., Heathcote, S., & Bally, J. 1999, A&A, 352, L83

Richer, J. S., Shepherd, D. S., Cabrit, S., Bachiller, R., & Churchwell, E. 2000, Protostars and Planets IV, 867

Rodriguez, L. F., Anglada, G., & Raga, A. 1995, ApJ, 454, L149+

Rodriguez, L. F., Canto, J., Torrelles, J. M., & Ho, P. T. P. 1986, ApJ, 301, L25

Rodriguez, L. F., Carral, P., Moran, J. M., & Ho, P. T. P. 1982, ApJ, 260, 635

Rodriguez, L. F., D'Alessio, P., Wilner, D. J., Ho, P. T. P., Torrelles, J. M., Curiel, S., Gomez, Y., Lizano, S., Pedlar, A., Canto, J., & Raga, A. C. 1998, Nature, 395, 355

Rodríguez, L. F., Porras, A., Claussen, M. J., Curiel, S., Wilner, D. J., & Ho, P. T. P. 2003, ApJ, 586, L137

Rodriguez, L. F. & Reipurth, B. 1994, A&A, 281, 882

Rodríguez, L. F. & Reipurth, B. 1996, Revista Mexicana de Astronomia y Astrofisica, 32, 27

Sandqvist, A. & Bernes, C. 1980, A&A, 89, 187

Scoville, N. Z., Sargent, A. I., Sanders, D. B., Claussen, M. J., Masson, C. R., Lo, K. Y., & Phillips, T. G. 1986, ApJ, 303, 416

Shang, H., Allen, A., Li, Z.-Y., Liu, C.-F., Chou, M.-Y., & Anderson, J. 2006, ApJ, 649, 845

Shu, F. H., Adams, F. C., & Lizano, S. 1987, ARA&A, 25, 23

Shu, F. H., Laughlin, G., Lizano, S., & Galli, D. 2000, ApJ, 535, 190

Shu, F. H., Najita, J., Ostriker, E. C., & Shang, H. 1995, ApJ, 455, L155+

Shu, F. H., Ruden, S. P., Lada, C. J., & Lizano, S. 1991, ApJ, 370, L31

Smith, H. A. & Beck, S. C. 1994, ApJ, 420, 643

Smith, M. D. & Rosen, A. 2003, MNRAS, 339, 133

—. 2005, MNRAS, 357, 579

Smith, M. D., Suttner, G., & Yorke, H. W. 1997, A&A, 323, 223

Snell, R. L. & Bally, J. 1986, ApJ, 303, 683

Snell, R. L., Loren, R. B., & Plambeck, R. L. 1980, ApJ, 239, L17

Snell, R. L., Scoville, N. Z., Sanders, D. B., & Erickson, N. R. 1984, ApJ, 284, 176

Stahler, S. W. 1994, ApJ, 422, 616

Stahler, S. W. & Palla, F. 2005, The Formation of Stars (The Formation of Stars, by Steven W. Stahler, Francesco Palla, pp. 865. ISBN 3-527-40559-3. Wiley-VCH , January 2005.)

Stocke, J. T., Hartigan, P. M., Strom, S. E., Strom, K. M., Anderson, E. R., Hartmann, L. W., & Kenyon, S. J. 1988, ApJS, 68, 229

Stojimirović, I., Narayanan, G., Snell, R. L., & Bally, J. 2006, ApJ, 649, 280

Stone, J. M. & Hardee, P. E. 2000, ApJ, 540, 192

Stone, J. M. & Norman, M. L. 1993a, ApJ, 413, 198

—. 1993b, ApJ, 413, 210

—. 1994, ApJ, 420, 237

Strom, K. M., Strom, S. E., & Vrba, F. J. 1976, AJ, 81, 320

Suttner, G., Smith, M. D., Yorke, H. W., & Zinnecker, H. 1997, A&A, 318, 595

Swift, J. J., Welch, W. J., & Di Francesco, J. 2005, ApJ, 620, 823

Tafalla, M. & Myers, P. C. 1997, ApJ, 491, 653

Torrelles, J. M., Anglada, G., Rodriguez, L. F., Canto, L. F., & Barral, J. F. 1987, A&A, 177, 171

Torrelles, J. M., Gómez, J. F., Rodríguez, L. F., Curiel, S., Anglada, G., & Ho, P. T. P. 1998, ApJ, 505, 756

Vazquez-Semadeni, E., Ostriker, E. C., Passot, T., Gammie, C. F., & Stone, J. M. 2000, Protostars and Planets IV, 3

Velusamy, T. & Langer, W. D. 1998, Nature, 392, 685

Walther, D. M., Robson, E. I., Aspin, C., & Dent, W. R. F. 1993, ApJ, 418, 310

Warin, S., Castets, A., Langer, W. D., Wilson, R. W., & Pagani, L. 1996, A&A, 306, 935

Wu, Y., Wei, Y., Zhao, M., Shi, Y., Yu, W., Qin, S., & Huang, M. 2004, A&A, 426, 503

Yang, J., Ohashi, N., Yan, J., Liu, C., Kaifu, N., & Kimura, H. 1997, ApJ, 475, 683

Yokogawa, S., Kitamura, Y., Momose, M., & Kawabe, R. 2003, ApJ, 595, 266

Yu, K. C., Billawala, Y., & Bally, J. 1999, AJ, 118, 2940

Yu, K. C., Billawala, Y., Smith, M. D., Bally, J., & Butner, H. M. 2000, AJ, 120, 1974

Zhang, Q., Hunter, T. R., Sridharan, T. K., & Ho, P. T. P. 2002, ApJ, 566, 982

Zhang, Q. & Zheng, X. 1997, ApJ, 474, 719

Zhao, B., Wang, M., Yang, J., Wang, H., Deng, L., Yan, J., & Chen, J. 1999, AJ, 118, 1347

Zinnecker, H., Mundt, R., Geballe, T. R., & Zealey, W. J. 1988, NASA STI/Recon Technical Report N, 89, 25085

2195 - 11